EPR studies on defects in semiconducting barium disilicide

SATO　TAKUMA

February 2020

EPR studies on defects in semiconducting barium disilicide

SATO　TAKUMA

Doctoral Program in Nano-Science and Nano-Technology

Submitted to the Graduate School of

Pure and Applied Sciences

in Partial Fulfillment of the Requirements

for the Degree of Doctor of Philosophy in

Engineering

at the

University of Tsukuba

Outline

Abstract ... 1

Chapter 1 Introduction ... 3

1.1. Application of photovoltaic devices ... 3

1.2. Parameters of photovoltaic devices ... 4

1.3. Effect of defects ... 8

Chapter 2 Background ... 12

2.1. Zintl phase ... 12

2.2 Fundamental properties of $BaSi_2$ ... 13

2.3. Growth of $BaSi_2$ thin-film ... 16

2.4. $BaSi_2$ based photovoltaic devices ... 18

2.5. Defects in $BaSi_2$ ... 21

2.6. Magnetism in $BaSi_2$ ... 26

2.7. Aim of this thesis ... 28

Chapter 3 Principle of electron paramagnetic resonance ... 29

3.1. EPR parameters ... 30

3.1.1. Electon Zeeman interaction ... 30

3.1.2. Hyperfine interaction ... 31

3.1.3. Nuclear quadrupole interaction ... 32

3.1.4. Others ... 32

3.2. Relaxation ... 33

Chapter 4 EPR study on $BaSi_2$ film ... 34

4.1. *a*-axis orientated epitaxial $BaSi_2$ films ... 34

4.2. EPR spectra of $BaSi_2$ epitaxial films ... 38

4.3. Temperature and microwave power dependences ... 40

4.3.2. Temperature dependence ... 40

4.3.2. Microwave power dependence ... 41

4.4. Multi-frequency EPR ... 41

Q-band ... 41

High-field (high frequency) ... 43

4.4. Effect of deposition ratio during film growth ... 44

4.5. Effect of atomic hydrogen into $BaSi_2$ film ... 46

4.6. Summary ... 47

Chapter 5 EPR study on $BaSi_2$ bulk ... 48

5.1. Powder ... 48

5.1.1. Samples ... 48

5.1.2. Effect of composition ratio of Ba and Si ... 49

5.1.3. T_1 and T_2 measurements ... 53
5.1.4. Decomposition of the EPR spectra ... 56
5.1.5. Summary ... 61
5.2. Hyperfine spectroscopy ... 62
5.2.1. HYSCORE, ENDOR, ED-NMR ... 62
5.2.2. Results ... 65
5.2.3. Summary ... 72
5.3. Single Crystal ... 75
5.3.1. Sample preparation ... 75
5.3.2. Si-rich Sample ... 76
5.3.3. Ba-rich sample ... 77
5.3.4. Summary ... 78
5.4. Simulation ... 81
5.4.1. Results ... 81
5.4.2. Spin concentrations ... 88
5.4.3. Summary ... 90
5.5. DFT calculations ... 91
5.5.1. Method ... 91
5.5.2. Results ... 92
5.5.3. Summary ... 98
5.6. General discussion ... 103
5.6.1. Comparison: experiments and computations ... 103
5.6.2. Comparison: film and bulk ... 107
Chapter 6 Photoluminescence spectroscopy ... 108
6.1. Sample ... 108
6.2. PL spectra of polycrystalline samples ... 108
6.3. PL spectra of film samples ... 111
6.4. Radiative defects model ... 114
6.5. Comparison with EPR spectra ... 116
Chapter 7 Total summary ... 118
Acknowledgement ... 121
Special thanks ... 123
Appendix ... 124
A. Raman spectroscopy and DFT calculations ... 124
A.1. Sample ... 124
A.2. Lattice constants and residual stress ... 124
A.3. DFT Calculation: vibrational frequency ... 125
A.3.1. Method ... 126

A.3.2. Computed results 127
A.4 Effects of intrinsic defects on Raman spectra 129
List of publications 141
Reference 144

Abstract

In this study, I focused on semiconducting barium disilicide $BaSi_2$. Since $BaSi_2$ is composed of less toxic and earth-abundant elements, this environmental-friendly material takes advantage over other materials in terms of elemental strategies. Our previous researches found its potentials for solar cell applications. For instance, $BaSi_2$ shows a large absorption coefficient (3×10^4 cm^{-1} @ 1.5 eV, whose value larger than crystalline Si by 40 times) in spite of its indirect bandgap because of its characteristic band structure.

So far, we have successfully demonstrated Si-based hetero- and homo-junction solar cells. In order to design devices with higher conversion efficiencies, I investigated intrinsic defects in undoped-$BaSi_2$ films and bulks in this study. This is because the defects promote photogenerated carriers to recombine each other during their travel to electrodes. As a result, photogenerated currents decrease. Therefore, defect control is indispensable to realize the devices with a high conversion efficiency. My previous researches found $BaSi_2$ films grown by molecular beam epitaxy contained the defects while their origins are unknown yet. Electron paramagnetic resonance (EPR) enables me to access microscopic information such as identification of paramagnetic defects, determination of local structures, etc.

First, I performed EPR measurements on *a*-axis orientated $BaSi_2$ epitaxial films. Assessing the observed g value carefully, I succeeded in detection of EPR active defects in this material for the first time. In addition, it was confirmed that the EPR line observed from the film (anisotropic g value: 2.003-2.010) decreased by introducing atomic hydrogens (H). In our previous study, H-passivated $BaSi_2$ films showed significant improvements on photoresponsivity, indicating that such defects can affect optical properties.

Second, I revealed that some different types of defects formed depending on Ba/Si composition ratios through the EPR measurements of powder and single crystal of $BaSi_2$. To accomplish this identification, I adopted a variety of EPR techniques from the multi-frequency cw-EPR to the advanced pulse-EPR. In Si-rich samples, I observed at least two different defects with averaged g values (g_{av}) > 2. Each defect exhibited different behavior on temperature dependence and relaxation time. On the other hand, in Ba-rich samples, other EPR lines ($g_{av} < 2$) appeared. One of the defects had a narrow linewidth and hyperfine structures which may stem from ^{29}Si ($I = 1/2$), ^{135}Ba ($I = 3/2$), or ^{137}Ba ($I = 3/2$). I performed further identification by adopting hyperfine spectroscopy such as ELDOR-detected NMR (ED-NMR). ED-NMR is a technique that has attracted attention in recent years as a new technique for measuring hyperfine coupling constants. The hyperfine coupling constant of $|A| \sim 70$ and 80 MHz was successfully obtained in ED-NMR spectra of Si-rich and Ba-rich, respectively. These values seemed to correspond to those observed in single crystals. The density functional theory (DFT) calculation was also carried out to get a picture of possible defect models. Through simulations of the EPR spectra using the obtained parameters, I suppose that at least and Si vacancies (V_{Si}) were formed as a paramagnetic defect in the Ba-rich sample.

At last, I also conducted photoluminescence (PL) measurements, which is very powerful for determining defect levels. Four PL peaks were observed at almost the same photon energy in each thin film sample and the polycrystalline sample. These results suggest that similar defects are formed in the thin films and the polycrystalline samples. In addition, I compared these results with those obtained by other methods (the deep level transient spectroscopy and temperature dependence of electrical resistivity), enabling me to propose a radiative defect model

in $BaSi_2$. Combining the EPR results with those of PL, I concluded that the definitive defect affected its photoresponsivity originated from V_{Si} with 0.8 or 0.9 eV of the PL peak in the $BaSi_2$ epitaxial films.

As a conclusion, I performed EPR and PL measurements on the $BaSi_2$ films as well as polycrystalline and monocrystalline $BaSi_2$ bulks in order to clarify the defect profiles. In the bulk samples, the EPR measurements revealed that at least V_{Si} tend to be formed under Ba-rich condition. On the other hand, I found that there are other types of defects in Si-rich $BaSi_2$, which relate to relatively deeper defect levels within the bandgap from viewpoints of PL measurements. The defects observed in the $BaSi_2$ films grown by molecular beam are good agreements with those detected in the Si-rich bulk samples.

Chapter 1 Introduction

1.1. Application of photovoltaic devices

The demand for electricity, which has increased due to the recent development of IoT and AI technologies, has further increased the importance of renewable energy such as solar, wind, biomass, hydropower, tides, and geothermal energies, alternative to commonly used fossil fuels, is of great importance.[1] Fossil fuels not only constitute a limited energy source, but also the main reason of increased air pollution and global warming. Photovoltaic (PV) technology, which is known for converting solar energy into electricity through a semiconducting material, plays a key component of decarbonizing electricity.

The first solar cell, which was created by Charles Fritts in 1883, achieved a power conversion efficiency (η) of 1-2% by covering selenium with a thin layer of gold. In 1954, physicists at Bell Laboratories discovered that crystalline silicon c-Si is more efficient than selenium, and created the first practical solar cell with improved η of 6%.[2] Since then, the η has been improved by adopting technologies such as back-surface field (BSF),[3,4] surface passivation,[5,6] texture structure,[7,8] and back contact.[9,10] In recent years, a heterojunction with intrinsic thin-layer (HIT) type solar cell has an *i*-type amorphous Si (a-Si) layer sandwiched between heterojunction interfaces of *p*-type a-Si and *n*-type c-Si. Research on batteries is also advancing, with the same structure having Panasonic's conversion efficiency of 25.6%[11] in 2014 and Kaneka's 26.33%[12] in 2016. Figure 1.1-1 presents the global installed capacity of solar PV system from 2007 to 2017. In 2017, the total PV global capacity increased to over 400 GW, rose by almost 33% compared with the year 2016. The market expansion was mainly due to the increasing competitiveness of solar PV combined with the rising demand for electricity in developing countries, as well as to the increasing awareness of solar PV's potential to alleviate pollution, reduce CO_2 emissions and provide energy access.[13]

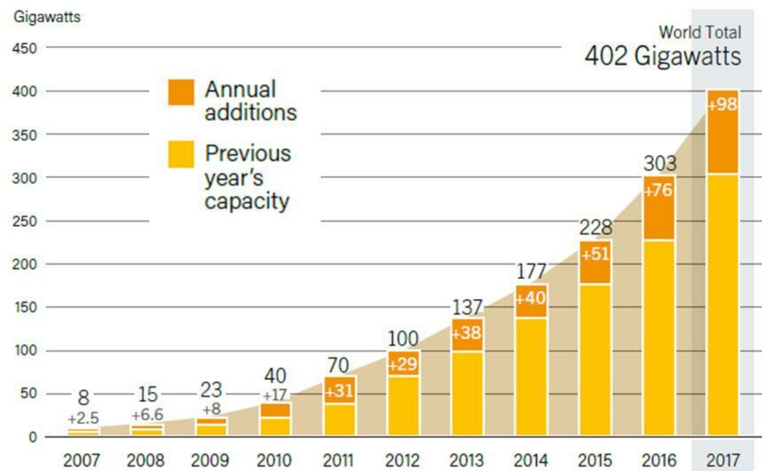

Fig. 1.1-1 Global renewable power capacity, 2007-2017.[13]

At present, the η of c-Si single-junction solar cells, which share about 90% of the solar cell market, reaches around 26%, but the improvement in η has been only 1.5% in the last 20 years. The rest of the market are composed of the third generation PV technologies which use advanced thin-film solar cells modules including cadmium-telluride (CdTe) modules, a-Si modules, and copper indium gallium selenide sulfide $Cu(In,Ga)(S,Se)_2$ (CIGS)

modules.[14] Since sunlight has a wide energy distribution from infrared to ultraviolet, the η of PV is limited by the heat loss (i) due to a loss of transmitted photons through materials with a wide bandgap (E_g), and (ii) due to a heated loss caused be a difference between energy of absorbed photons and E_g in materials with a narrow E_g. In other words, achieving a η of over 30% requires a drastic review of the current solar cell structures. In recent years, multi-junction solar cells have been highly evaluated for their potential as next-generation solar cells. Due to a combination of a material having a wide E_g and a material having a narrow E_g, the present structure, in which absorb sunlight more effectively, can dramatically improve the η. The η of the three-junction solar cell InGaP/GaAs/Ge that has been put into practical use today is as high as 32%. However, since the raw material contains rare and/or toxic elements, it is difficult to significantly expand its use for consumer use, and its use is limited. There is a need for the development of Si-based multi-junction solar cells composed of resource-rich elements.

1.2. Parameters of photovoltaic devices

Solar cell efficiency refers to the portion of energy in the form of sunlight that can be converted via PVs into electricity. The η of a solar cell is considered the most important criterion when assessing a solar cell's quality. The most efficient commercially available solar PV module on the market has an η of 22.5%, whereas the majority are from 15% to 17% efficiency rating. Most relevant for solar energy conversion is the terrestrial solar spectral irradiance on the surface that differs from the extraterrestrial irradiation (AM0) due to the effect of filtering by the atmosphere. Air Mass 1.5 Global (AM1.5G) describes the radiation arriving at earth's surface after passing through 1.5 times a standard air mass, with the sun at 48.2° from zenith with integrated power density of 100 mW/cm^2, including both direct and diffuse radiation. This is the power density that is usually referred to as "one sun". The AM also depends on the position of the sun and can be defined as follows:

$$\mathrm{AM} = \frac{1}{\cos(\theta)}$$

where θ is the elevation angle of the Sun as shown in Fig. 1.2-1.[15] AM1.5G is used as the standard spectral distribution of light to measure a solar cell's efficiency. Generally, 99% of the light that reaches the Earth's surface is at wavelengths of less than 2500 nm in the AM1.5G spectrum, and 88% is less than 1350 nm. To be efficient, a solar cell should be able to absorb the largest number of photons possible. Figure 1.2-2 compares the AM0 and AM1.5G spectra.[16] Figure 1.2-4 shows recent best research-cell efficiencies in the world, measured under standard AM1.5G illumination, which is summarized by national renewable energy laboratory (NREL). Single gallium arsenide (GaAs) junction solar cells (η = 28.9%) are approaching the theoretical limiting power efficiency of 33.7%, noted as the Shockley-Queisser limit.[17] The maximum η of single c-Si solar cells is 27.6% with concentrated area. As for thin-film solar cells, CIGS solar cells reach a maximum η of 23.3%, showing great potential compared with c-Si solar cells. Besides, organic-inorganic hybrid perovskite $CH_3NH_3PbI_3$ solar cell is a rising star in solar cell family. Its efficiency increased dramatically from 3.8% to 23.3% in a few years, catching up with CIGS solar cells.

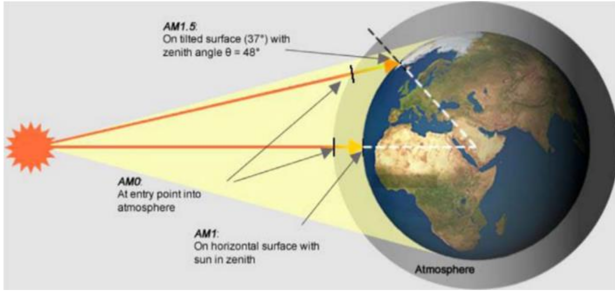

Fig. 1.2-1 Illustration of the air mass concept.[15]

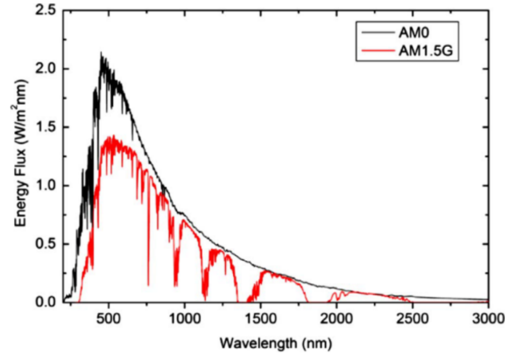

Fig. 1.2-2 AM0 and AM1.5G solar irradiance spectra.[16]

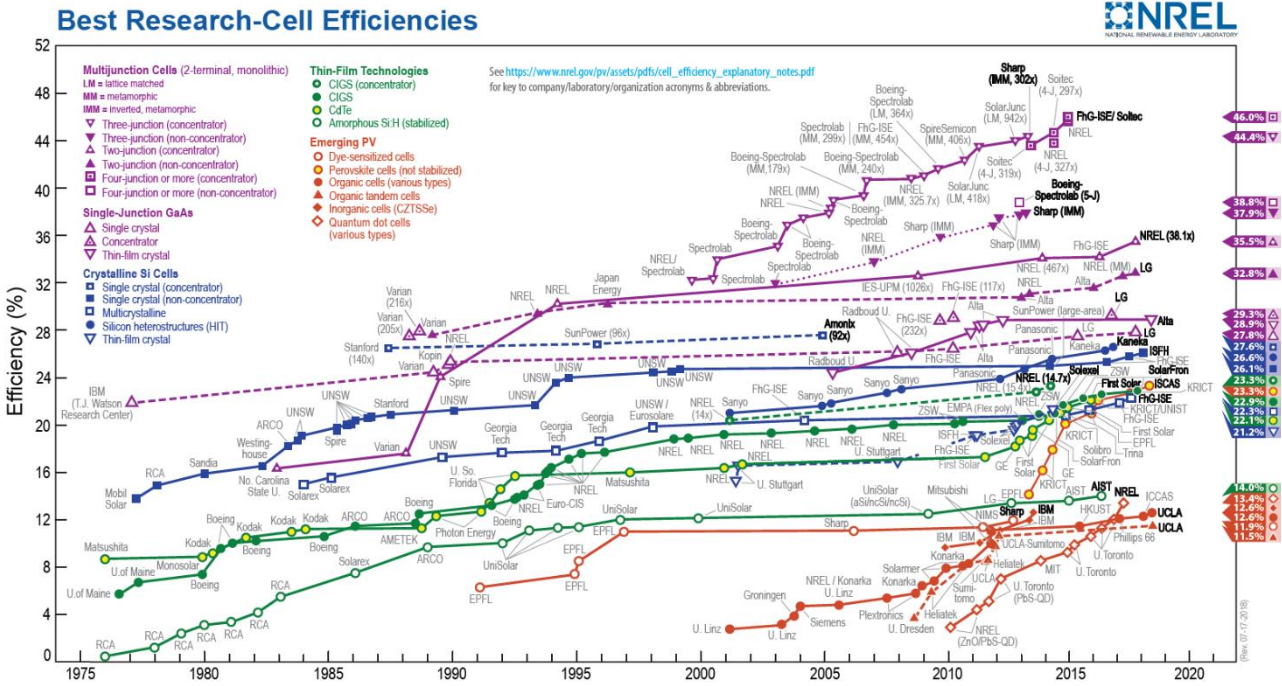

Fig. 1.2-3 Recent best research-cell efficiencies in the world.

I discuss current density-voltage (J-V) characteristics of *pn* junction solar cells during light irradiation. As a simple model, I consider the model of the *pn* junction formed by a p-type semiconductor having a thickness of d and a n-type semiconductor which has sufficiently thicker than its minority carrier (hole) diffusion length L_h. When the solar cell is irradiated with light, the following differential equation holds for the hole density distribution $p_n(x)$ in the n-type neutral region.

$$D_n \frac{d^2 p_n(x)}{dx^2} + G(x) - \frac{p_n(x) - p_{n0}}{\tau} = 0\,.$$

D_n : diffusion coefficient of hole, p_{n0} : hole concentration at thermal equilibrium, τ : minority career lifetime

$G(x)$: electron-hole pair generation rate per unit time and unit volume

Here, assuming that photons of monochromatic light enter the surface of this *pn* junction solar cell by Φ_0 [s/cm^{-2}]. The number of photons $\Phi(x)$ reaching the *n*-type neutral region is described below by using the reflectance at the surface R, and the light absorption coefficient α.

$$\Phi(x) = (1 - R)\Phi_0 e^{-\alpha(x+d)}\,.$$

Since $G(x) = -\mathrm{d}\Phi(x)/\mathrm{d}x$ holds,

$$G(x) = \alpha(1-R)\Phi_0 \mathrm{e}^{-\alpha(x+d)}$$

Given the initial condition of $p_\mathrm{n}(x \to \infty) = p_{\mathrm{n}0}$, $p_\mathrm{n}(x \to W_\mathrm{n}) = p_{\mathrm{n}0}\exp(qV/k_\mathrm{B}T)$ to the differential equation, if D and τ are constant regardless of location assuming that $p_\mathrm{n}(x)$ is obtained as follows.

$$p_n(x) = p_{n0} + \left[p_{n0}\left(\mathrm{e}^{qV/k_\mathrm{B}T} - 1\right) - F\mathrm{e}^{-\alpha W_n}\right]\mathrm{e}^{(W_n - x)/L_\mathrm{h}} + F\mathrm{e}^{\alpha x}.$$

Here,

$$F = \Phi_0(1-R)\frac{\alpha\tau}{1-\alpha^2 L_\mathrm{h}^2},$$

$$L_\mathrm{h} = \sqrt{D_\mathrm{h}\tau}.$$

Therefore, the hole current flowing in n-type neutral region is,

$$J_\mathrm{h} = qD_\mathrm{h}\left.\frac{\mathrm{d}\Delta p_n}{\mathrm{d}x}\right|_{x=W_n} = q\frac{D_\mathrm{h}}{L_\mathrm{h}}p_{n0}\left(\mathrm{e}^{qV/k_\mathrm{B}T} - 1\right) - q\Phi_0(1-R)\mathrm{e}^{-\alpha(W_n+d)}\frac{\alpha L_\mathrm{h}}{1+\alpha L_\mathrm{h}}.$$

The first item of this equation represents the current when no light is irradiated (dark current), and the second item represents the photocurrent. Here, paying attention to the expression included in the photocurrent expression,

If $\alpha L_\mathrm{h} \gg 1$, then $\frac{\alpha L_\mathrm{h}}{1+\alpha L_\mathrm{h}} \sim 1$. Else if $\alpha L_\mathrm{h} \ll 1$, then $\frac{\alpha L_\mathrm{h}}{1+\alpha L_\mathrm{h}} \sim \alpha L_\mathrm{h}$. In other words, in the *pn* junction type solar cell, a larger photocurrent can be obtained as the product of the light absorption coefficient α and the minority carrier diffusion length L_h is larger.

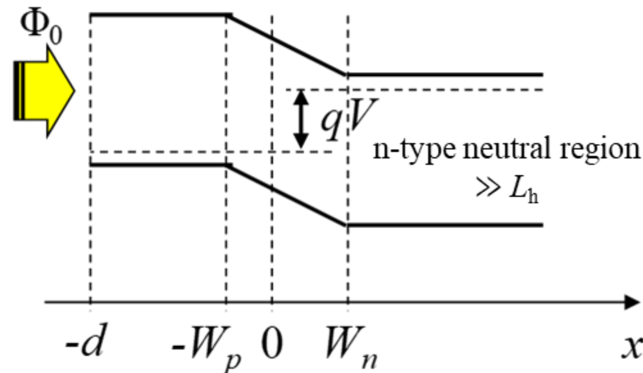

Fig. 1.2-4 A schematic picture of pn junction.

Here, the band structure of a semiconductor is considered. Semiconductors in which the value of the wave vector k at the bottom of the conduction band and the top of the valence band do not match, such as Si, are called indirect band-gap semiconductors. Since this semiconductor requires a change in momentum for carrier transition between bands, the transition probability is low and therefore α is small. The small α of Si is due to this indirect transition. On the other hand, since the momentum change is required even when the carriers recombine, it takes a long time for the recombination, that is, L is long. Semiconductors such as GaAs, in which the bottom of the conduction band and the k at the top of the valence band coincide, are called direct band-gap semiconductors. Such semiconductors have high carrier transition probability and a large α, but also allows recombination without a change in momentum. Therefore, the recombination easily occurs and L is short. Thus, in general, the magnitude of α and the length of L are in a trade-off relationship.

Next, let us consider the *I-V* characteristics during light irradiation in the ideal equivalent circuit of the

solar cell shown in Fig. 1.2-5. In the circuit of Fig. 1.2-5, the constant current I_{ph} due to photo-generated carriers flows in the reverse direction of the diode D_1, so *I-V* characteristic is expressed by,

$$I = I_0 \left\{ \exp\left(\frac{qV}{k_B T}\right) - 1 \right\} - I_{ph} \ .$$

I_0: the reverse saturation current, q: the elementary charge, k_B: the Boltzmann' constant, T: temperature

At this time, the voltage V_{OC} generated when the terminal is open is called an open voltage, and the current density J_{SC} flowing when the terminal is short-circuited is called a short-circuit current density. In the case of a *pn* homojunction, the magnitude of V_{OC} is roughly determined by the built-in potential, that is, the difference of Fermi level between the *p*-type semiconductor and the *n*-type semiconductor. That is, since V_{OC} is considered to be a value proportional to the magnitude of E_g,

$$V_{OC} = \frac{E_g}{q} - \Delta E$$

Therefore, V_{OC} generally increases monotonically with E_g. On the other hand, J_{SC} is determined by the sum of the number of photons having energy larger than E_g in the photon spectrum Φ (E) of AM1.5 that pours into the solar cell, so the maximum value of J_{SC} can be expressed as follows.

$$J_{SC} = q \int_{E_g}^{\infty} \Phi(E)\ \mathrm{d}E$$

Therefore, J_{SC} monotonically decreases with respect to E_g. The conversion efficiency η of a solar cell is given by,

$$\eta = \frac{P_m}{P_{in}} = \frac{V_m \times J_m}{P_{in}} = \frac{FF \times V_{OC} \times J_{SC}}{P_{in}}$$

P_{in} : Incident energy, P_m : Power at optimal operating point, V_m : Voltage at optimal operating point, J_m : Current density at optimal operating point, FF : fill factor

Hence, η has a maximum point for E_g. Generally, the maximum value of η is obtained when E_g = 1.4 to 1.6 eV, but may shift due to the influence of the quality of the crystal, etc.

So far, we have used the equation of the *J-V* characteristic using the ideal equivalent circuit of the solar cell, but in actuality it is necessary to consider the series resistance R_s and the parallel resistance R_{sh} as shown in Fig. 1.2-6. Furthermore, in order to take into account the recombination current, it is necessary to introduce an ideal coefficient γ. The equation of the *J-V* characteristic considering R_s, R_{sh}, and γ is given by,

$$J = J_0 \left\{ \exp\left(\frac{q(V\text{-}SJR_s)}{\gamma k_B T}\right) - 1 \right\} - J_L + \frac{V - SJR_s}{SR_{sh}} \ .$$

S : the area

When $R_s \to 0$ and $R_{sh} \to \infty$ in the above equation, the ideal case is obtained. Fig. 1.2-7 shows the effect of R_s and R_{sh} on the *J-V* characteristics. In the *J-V* characteristics under light irradiation, the slope near V_{OC} indicates $1/R_s$, and the slope near Isc indicates $1/R_{sh}$. That is, the slope of the current near V_{OC} becomes gentler as the R_s increases, and the slope of the current near J_{SC} becomes sharper as R_{sh} decreases. Therefore, since R_s and R_{sh} greatly affect the *FF* of

the solar cell, it is important to reduce R_s and increase R_{sh} to increase the efficiency of the solar cell. R_s includes (1) the resistance of wiring or electrode, (2) the contact resistance at interface between metals and semiconductors, (3) the resistance in the neutral region of *p*- and *n*- type layer, (4) the resistance of depletion layer at the interface of *pn* junction, etc.[18-20] Further, R_{sh} is considered to be a leakage current using a crystal grain boundary, dislocation, or the like as a current path, a sneak current between front and rear electrodes, and the like.

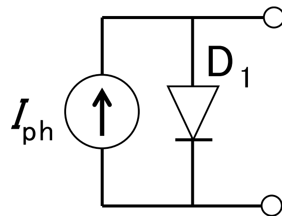

Fig. 1.2-5 Ideal solar cell equivalent circuit.

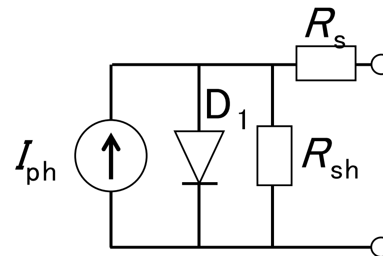

Fig. 1.2-6 Equivalent circuit of solar cell considering series resistance (R_s) and parallel (R_{sh}) resistance.

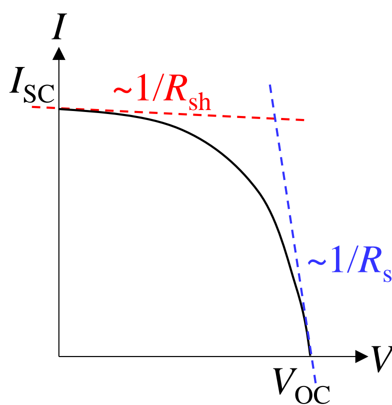

Fig. 1.2-7 Effect of R_s and R_{sh} on the *I*-*V* characteristic of solar cell.

1.3. Effect of defects

Defects that form electronic states in the middle of the bandgap play the most definitive role in semiconductors. To obtain qualitative insights into such defects on the photovoltaic device performances, let us consider a model depicted in Fig. 1.3-1 based on the Shockley-Read-Hall model (SRH model).[21] We assume that a defect having a concentration of n_d with a known defect level E_d and a known capture cross section σ_e for electrons and σ_h for holes.

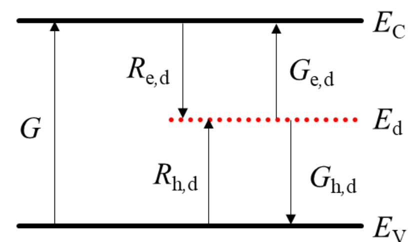

Fig. 1.3-1 Electrons and holes generated via absorption of photon with the generation rate G are captured by defect with the rates $R_{e,d}$ and $R_{h,d}$ at E_d. Then, they are emitted thermally with the rates $G_{e,d}$ and $G_{h,d}$ from the E_d to theconduction band (E_C) or the valence band (E_D).

The electron concentration n_e in the conduction band (CB) changes in time due to the rate of generation $G_e = G_h = G = \alpha(\hbar\omega)\ j_\gamma/d$ by the absorption of photons averaged over the thickness d and it changes by the rate $R_{e,d}$ of capture into defects occupied by holes and by the rate of thermal emission $G_{e,d}$ from defects occupied by electrons. The continuity equations

for the changes in the concentrations of electrons in the CB n_e, of holes in valence band (VB) n_h, and of trapped in defects $n_{e,d}$ as a function of the generation and recombination rates are given by

$$\frac{\partial n_e}{\partial t} = G - R_{e,d} + G_{e,d} ,$$

$$\frac{\partial n_h}{\partial t} = G - R_{h,d} + G_{h,d},$$

$$\frac{\partial n_{e,d}}{\partial t} = R_{e,d} - R_{h,d} - G_{e,d} + G_{h,d} .$$

Since charge neutrality of the semiconductor must prevail even when the different concentrationns are changing, we can rewrite the third formula as

$$e\left(n_D^+ - n_e - n_A^- + n_h - n_{e,d}\right) = 0,$$

where we assume that the defects are negatively charged when they are occupied by electrons, i.e. they are acceptor-type defects.

Regarding the rate of recombination $R_{e,d}$, whenever an electron that moves through the lattice at its thermal velocity v_e comes within a capture cross section σ_e of an defect that is occupied by hole, it will be captured. So, the rate at which capture happens all electrons is

$$R_{e,d} = \sigma_e v_e n_e n_{h,d} ,$$

where $n_{h,d}$ (= $n_d - n_{e,d}$) is the density of defects not occupied by an electron and then occupied by a hole, which are the recombination partners for the electrons. The capture cross sections for electrons, σ_e, and for holes, σ_h, have values of the order in the range of 10^{-18}-10^{-15} cm^2. Similarly, the recombination rate for holes is given by

$$R_{h,d} = \sigma_h v_h n_h n_{e,d} .$$

For the generation rates of electrons or holes from the defects into the CB or VB, it should be proportional to the concentration of $n_{e,d}$ or $n_{h,d}$. Therefore, the generation rates of electrons and holes are

$$G_{e,d} = \beta_e n_{e,d} \text{ and } G_{h,d} = \beta_h n_{h,d} .$$

Here β_e and β_h are derived from the consideration of detailed balance in the dark. In the absence of external excitation ($G = 0$) and in a steady state,

$$\frac{\partial n_e}{\partial t} = \mathrm{G} - R_{e,d} + G_{e,d} = -\sigma_e v_e n_e(n_d - n_{e,d}) + \beta_e n_{e,d},$$

Therefore,

$$N_{e,d} = n_d \frac{1}{\beta_e/(\sigma_e v_e n_e) + 1} = n_d \frac{1}{exp[(E_d - E_F)/k_B T] + 1}$$

With $n_e = N_C \exp[-(E_C - E_F)/k_B T]$, we obtain the coefficient of emission of electrons,

$$\beta_e = \sigma_e v_e N_C \exp\left(-\frac{E_C - E_d}{k_B T}\right) .$$

Similarly, for the coefficient of emission of holes,

$$\beta_h = \sigma_h v_h N_V \exp\left(-\frac{E_d - E_V}{k_B T}\right) .$$

Therefore, we can solve the continuity equations as a function of the external rate of generation G. For the steady-state case, we find the density of defects occupied by electrons,

$$n_{e,d} = \frac{n_d\{\sigma_e v_e n_e + \sigma_h v_h N_V \exp[-(E_d - E_V)/k_B T]\}}{\sigma_e v_e\{n_e + N_C \exp[-(E_C - E_d)/k_B T]\}} + \sigma_h v_h\{n_h + N_V \exp[-(E_d - E_V)/k_B T]\}.$$

and

$$G = \frac{n_e n_h - n_i^2}{\frac{n_e + N_C \exp[-(E_C - E_d)/k_B T]}{n_d \sigma_h v_h} + \frac{n_h + N_V \exp[-(E_d - E_V)/k_B T]}{n_d \sigma_e v_e}}.$$

Here, $n_d\sigma_h v_h$ is the rate of per hole capture if all defects are occupied by electrons and its reciprocal value $\tau_{h,min} = 1/(n_d\sigma_h v_h)$ is defined as the smallest mean lifetime of a hole in the VB. Similarly, $\tau_{e,min} = 1/(n_d\sigma_e v_e)$ is that of electron in the CB.

Since separation of the Fermi levels is the main objective of a photovoltaic devices, it is worthwhile to express G in terms of the Fermi levels.

$$G = \frac{n_i \exp[(E_{FC} - E_{FV})/k_B T] - 1}{\tau_{h,min}\{\exp[(E_{FC} - E_i)/k_B T] + \exp[(E_d - E_i)/k_B T]\} + \tau_{e,min}\{\exp[(E_i - E_{FV})/k_B T] + \exp[(E_i - E_d)/k_B T]\}}.$$

The concentrations of additional electrons and holes due to the external generation rate G can be determined analytically from the above equation for small n_d and weak excitation. Let us consider excess electrons and holes are generated ($n_e = n_e^0 + \Delta n_e$ and $n_h = n_h^0 + \Delta n_h$, where n_e^0 and n_h^0 are those in the dark state). Since we are discussing the case of small n_d, therefore, $n_d << \Delta n_e$, Δn_h, resulting in that the excess concentrations of electrons and holes are equal, i.e. $\Delta n_e = \Delta n_h = \Delta n$. The condition of weak excitation is fullfilled, if $\Delta n << n_e^0 + n_h^0$. Also, we assume that the capture cross sections are not so different for electrons and holes. Then,

$$\Delta n = G\left\{\tau_{h,min}\frac{n_e^0 + N_C \exp[-(E_C - E_d)/k_B T]}{n_e^0 + n_h^0} + \tau_{e,min}\frac{n_h^0 + N_V \exp[-(E_d - E_V)/k_B T]}{n_e^0 + n_h^0}\right\}.$$

The mean lifetime τ of electrons and holes is defined as $\Delta n/G$. Figure 1.3-2 shows the τ in p-$BaSi_2$ as a function of E_d. Figure 1.3-2 indicates that the lifetime τ becomes shorter, in other words, the recombination accordingly more effective as the E_d approaches the E_i, which is in almost the middle of the E_g.

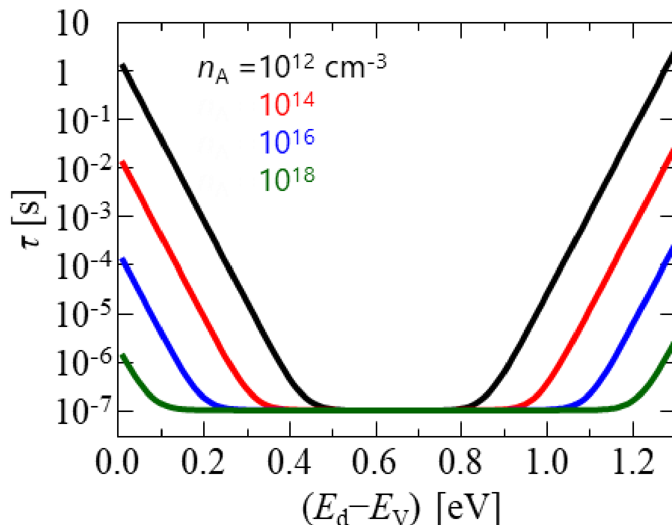

Fig. 1.3-2 Lifetime τ of electron and holes in p-$BaSi_2$ by recombination including defects as a function of the defect level E_d, measured from the VB maximum with the acceptor density n_A of 10^{12}-10^{18} cm^{-3}. The defects have a concentration of $n_d = 10^{15}$ cm^{-3} with equal capture cross sections of electrons and holes of $\sigma = 10^{-15}$ cm^2 and the velocity is $v = 10^7$ cm s^{-1}. The effective density of state in the CB and VB are 2.6×10^{19} cm^{-3} and 2.0×10^{19} cm^{-3}, respectively.

When the defect levels are close to the CB or VB, the defects are less effective. Most of the time the levels are not occupied by electrons or holes because captured carriers are much more frequently emitted back to the CB or VB than annihilated by recombination with a hole or an electron captured from the VB or CB. On the other hand, captured electrons and holes by the defect levels located at the middle of E_g, recombination with each carrier and then annihilations occur for much less time. We have to, therefore, control the defects, especially, “deep” defects in order to extract photogenerated carriers as much as possible.

Chapter 2 Background

2.1. Zintl phase

At room temperature (RT) and under atmospheric pressure, $BaSi_2$ exhibits orthorhombic structure (space group *Pnma* (no. 62)) as shown in Fig. 2.1-1. This material contains 16 Si atoms and 8 barium atoms in its unit cell (Z = 8), and every 4 Si atoms form to a tetrahedral structure. Its lattice constants are 8.9326 Å, 6.7262 Å, 11.5335 Å, respectively.[22] The characteristic crystal structure of $BaSi_2$ is explained by the Zintl-Klemm concept.[23] According to the concept, two valence electrons are supplied one by one from a Ba atom to two Si atoms. Therefore each Si atom possesses five valence electrons following the Octet rule.[24] As a result, each Si atom with five valence electrons bonds with the other three Si atoms. These tetrahedra are found in the allotrope of phosphorus P, which has five valence electrons.[25] As reported by Imai *et al.*,[26] the molecular orbital (MO) diagram of $BaSi_2$ is interpreted to consist of a combination of the density of states distributions (DOS) of Ba atoms and $4Si_4$, and the part of Si_4^{4-} is similar to the occupied MOs of the P_4 tetrahedron.

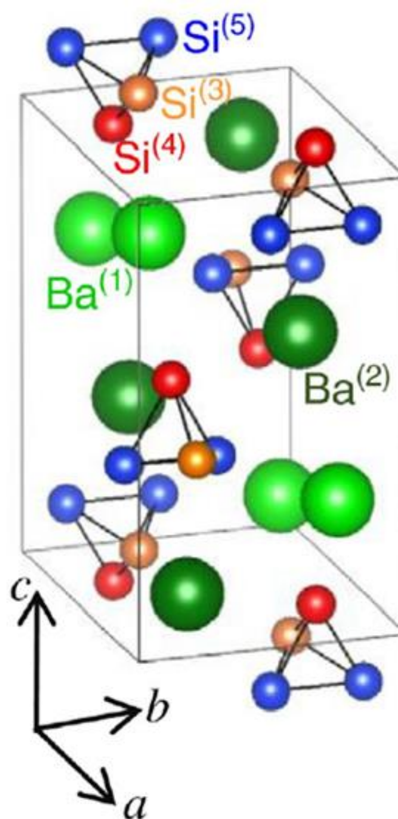

Fig. 2.1-1 Crystal structure of orthorhombic $BaSi_2$.[23]

Figure 2.1-2 shows the phase diagram of the binary system of Ba and Si.[27] Each compound has a crystal structure as shown in the Figs. 2.1-3. Among them, Ba_5Si_3, BaSi, Ba_3Si_4, and $BaSi_2$ follow the Zintl-Klemm concept, that is, electrons are from Ba atoms with low electronegativity to Si atoms with high electronegativity to become cation and anion atoms, respectively. In these materials, the anion atoms are bonded by covalent bonds (Table 2-1).

Table 2-1. Compounds of Ba-Si binary system.

	Ba_2Si	Ba_5Si_3	BaSi	Ba_3Si_4	$BaSi_2$	$Ba_{24}Si_{100}$
Ba/Si	2	1.67	1	0.75	0.5	0.24
Crystal System	Orthorombic	Tetragonal	Orthorhombic	Tetragonal	Orthorhombic	Cubic
Space Group	*Pnma*	*P4/ncc*	*Cmcm*	$P4_2/mnm$	*Pnma*	$P4_132$
Si average charge	−4	−3.33	−2	−1.5	−1	−0.48
Si-Si distance	2.6	2.74	2.502	2.424	2.404	2.415
Si sublattice	1 D	Si_2 dangbel	1D zigzag-chain	Si_4^{6-}: butterfly-shaped	Si_4^{4-}: isolated tetrahedron	

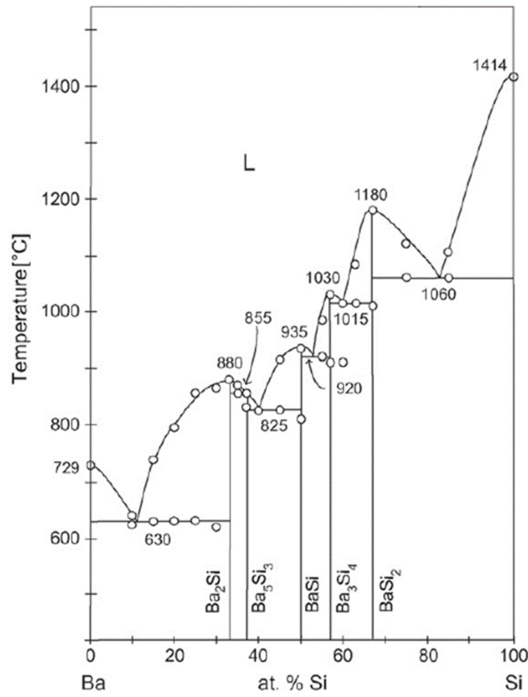

Fig. 2.1-2 The phase diagram of the Ba–Si binary system.[27]

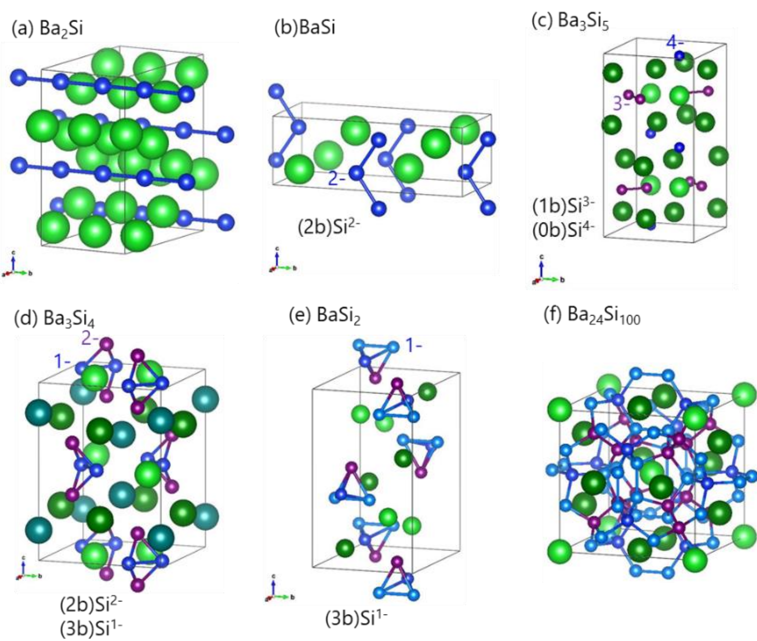

Fig. 2.1-3 Crystal Structure of Ba-Si binary compounds. (a) Ba_2Si,[28] (b) BaSi,[29] (c) Ba_3Si_5,[30] (d) Ba_3Si_4,[31] (e) $BaSi_2$,[22] and (f) $Ba_{24}Si_{100}$.[32] Big and small circle correspond Ba and Si atoms, respectively. (#b) indicate the number of Si bonds with its charge.

2.2 Fundamental properties of $BaSi_2$

Figure 2.2-1(a) shows a band structure of $BaSi_2$. The valence band maximum (VBM) is located at approximately (0, 1/3, 0) along the $\Gamma-\Upsilon$ (0, 1/2, 0) direction and the conduction band minimum (CBM) is located at T(0, 1/2, 1/2), that is, $BaSi_2$ is an indirect semiconductor.[33] Figure 2.2-1 (b) shows the orbital projected partial density of states (p-DOS) of $BaSi_2$.[34] The valence band (VB) of $BaSi_2$ mainly consists of the Si p state and the Ba d state appears dominant in the conduction band (CB). One of the most outstanding characteristics of $BaSi_2$ is its large light absorption coefficient (α) in spit of indirect semiconductor, which might be originated from the fact that the direct transition occurs at c.a. (0, 1/3, 0) located at higher level than that of the indirect one by only 0.1 eV. In the case of Si, the difference between the transitions is about 2.3 eV. The experimental absorption spectrum of $BaSi_2$ was performed using a silicon-on-insulator (SOI) substrate, on which a $BaSi_2$ film was grown. Figure 2.2-2 shows that $BaSi_2$ has an indirect bandgap (E_g) of 1.3 eV, and α reaches 3×10^4 cm^{-1} at 1.5 eV.[35] By replacing some Ba atoms with Sr atoms to form $Ba_{1-x}Sr_xSi_2$, the E_g can be enlarged to 1.4 eV.[36] Meanwhile, by substituting part of Si with isoelectric C, the E_g of $BaSi_{2-x}C_x$ can be continuously increased from 1.3 to 3.0 eV.[37] Recently, the potential of the $BaSi_{2-x}C_x$ fabricated by sputtering was demonstrated experimentally.[38] Therefore, it is possible to tune its E_g to the optimal values derived from the Shockley-Queisser limit[17]. Regarding the α, this value is about 40 times larger than that of c-Si and comparable with other conventional direct E_g absorbers such as $Cu(In,Ga)(S,Se)_2$[39], CdTe[40], etc. Moreover, comparing with those absorbers, a strong onset absorption near the edge of optical absorption can be expected in $BaSi_2$ because we can confirm the band curvature of the lowest CB is flat owing to the localized Ba-d states. For thin-film photovoltaic devices, not only an optimal E_g (~ 1.4 eV[41]) but also the shape of an absorption

spectrum resulting from its band structure and DOS[42,43] are important so as to find "good" candidates for thin-film photovoltaic devices. $BaSi_2$ meets such fundamental requirements for an absorber desirable for thin-film photovoltaic techniques.

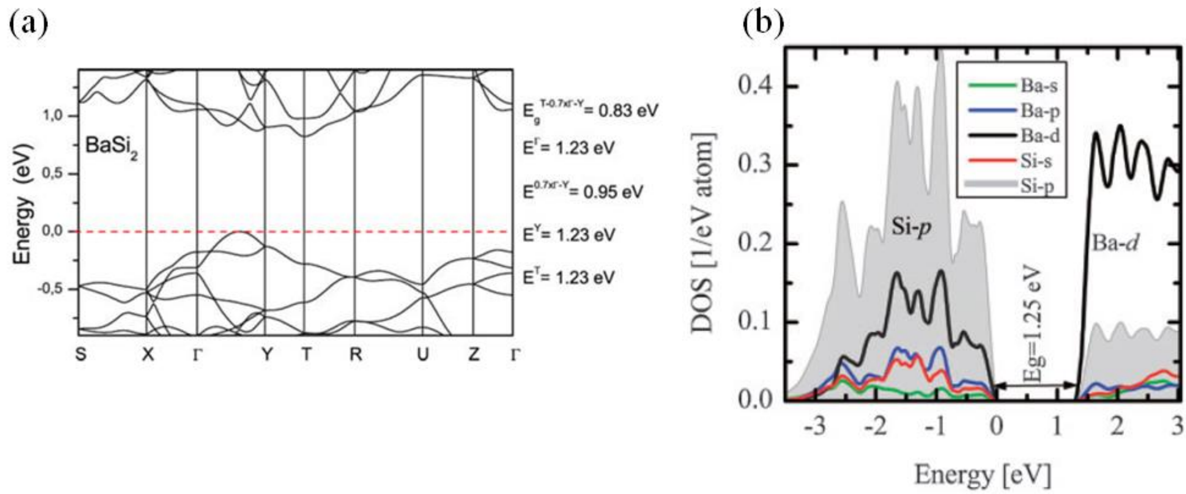

Fig. 2.2-1 (a) Band structure[33] and (b) atomical resolved and orbital projected DOS of $BaSi_2$.[34]

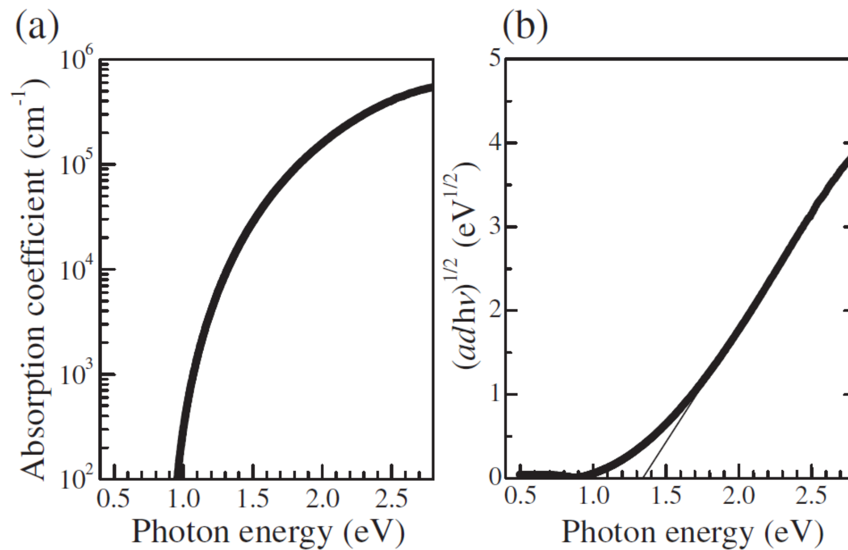

Fig. 2.2-2 (a) Absorption spectrum and (b) $(\alpha dh\nu)^{1/2}$ versus photon energy plotted for $BaSi_2$.[41]

Another promising feature of $BaSi_2$ is its excellent minority carrier properties. For the formation of solar cells, material should have not only suitable E_g and large α, but also large minority carrier diffusion length (L) and lifetime (τ). As for L, a longer L is desirable for photovoltaic devices, which is measurable with electron beam induced current (EBIC) techniques. Figures 2.2-3(a)(b) and 2.2-3(c)(d) show secondary-electron (SE) and electron EBIC results, respectively, with acceleration voltage V_{ac} = 5 kV. Front-side Schottky contacts were formed with Al on the $BaSi_2$ surface via wire bonding, and the back-side ohmic contact was made with sputtered Al. In the EBIC method, carriers generated within the diffusion length in the n-type $BaSi_2$ are collected by the electric field under the Al contact and sensed as a current in the external circuit. In Figs. 2.2-3(c) and 2.2-3(d), the brighter regions show higher collection of electron-beam-induced carriers in the $BaSi_2$. Figure 2.2-3(e) shows the EBIC line-scan data along dotted line AA' in Fig. 2.2-3 (c). The EBIC profile shows an exponential dependence of the distance from the Al contact.

The L was roughly estimated to be approximately 10 μm, assuming that the EBIC profile varies as $\exp(-x/L)$, where x is the distance from the Al edge (point A) along the dotted line, and L is the diffusion length of minority carrier for $BaSi_2$. As can be seen in section 2.3, the L is much larger than a grain size of the $BaSi_2$.[44,45] On the other hand, τ of undoped $BaSi_2$ was measured by means of microwave detected photoconductive decay (μ-PCD), where carriers were generated by a 5 ns laser pulse with a wavelength of 349 nm. Photoconductivity decay was monitored by the reflectivity of microwave with the frequency of 26 GHz. High-sensitivity measurement was realized by the differential detection of the reflected microwave intensity between the areas with and without laser irradiation. Then, τ can be calculated by analyzing the photoconductivity decay curves. The decay curve was assigned three different regions (Fig. 2.2-4(a)). Figure 2.2-4(b) shows film-thickness dependence of lifetime in undoped $BaSi_2$. The bulk lifetime is 14 μs, which is long enough for thin-film solar cell applications.[46,47]

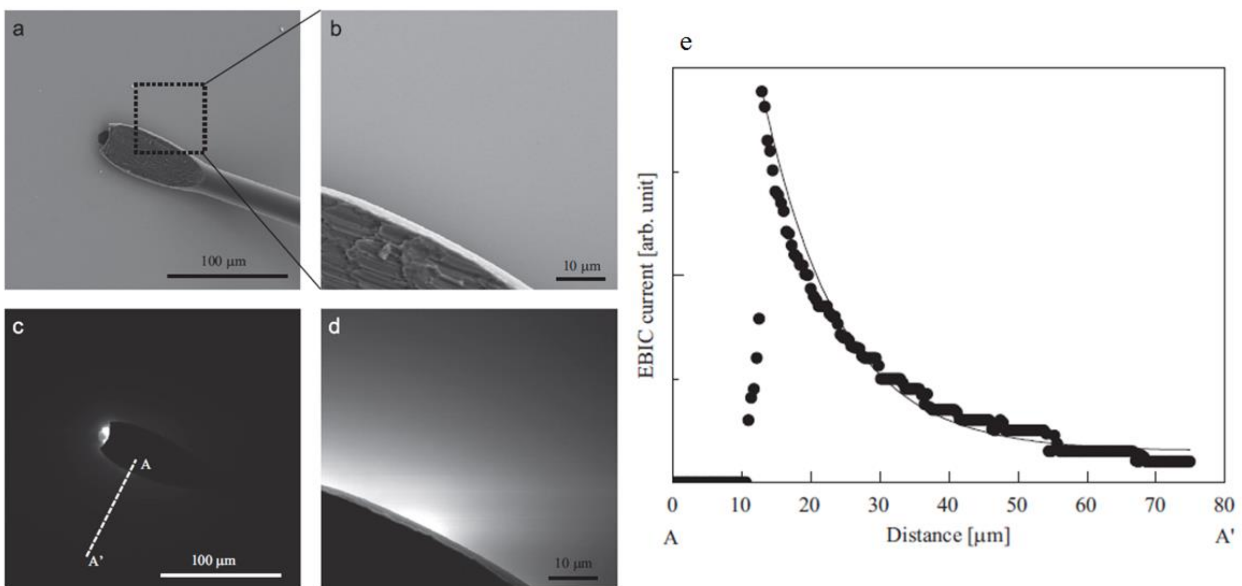

Fig. 2.2-3 (a), (b) SE and (c), (d) EBIC images around Al contact. (e) EBIC line-scan data along dotted line AA'.[44]

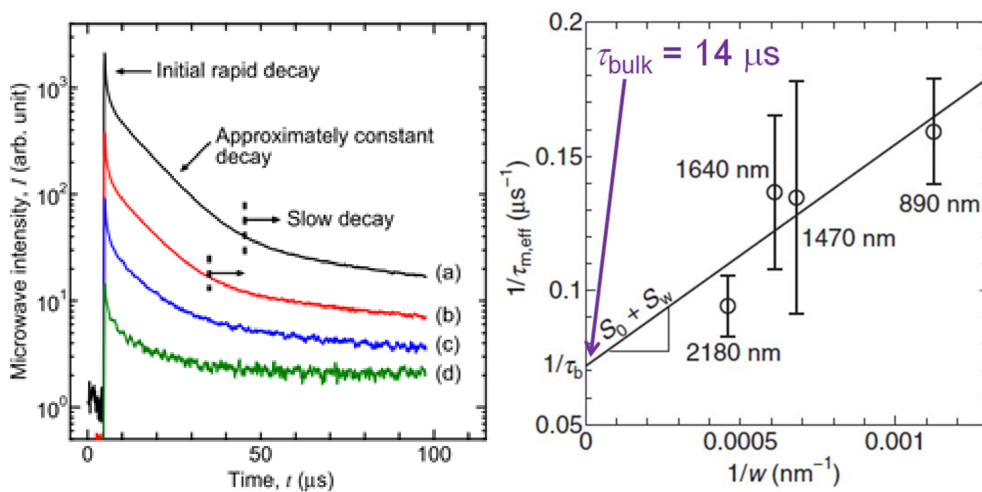

Fig. 2.2-4 (a) Photoconductivity decay curves of $BaSi_2$ films with different laser intensities.[46] (b) Film-thickness dependence of lifetime in undoped n-$BaSi_2$.[47]

Comprehensive investigations on *ex situ* and *in situ* doping had been done. In Ref [48], possible dopants to obtain *n*- and *p*- type $BaSi_2$ are well listed. As can be seen in Fig. 2.2-1(b), the Si *p* state contributes the VBM mainly. Therefore, by the replacement of the Si atoms in $BaSi_2$ with a group 13 (15) element, we can achieve a *p*- (*n*-) type $BaSi_2$.[33,49] This is the same way as that widely used to control the electrical properties of semiconductors such as Si. Table 2-2 lists the conduction types and carrier concentrations by different dopants in $BaSi_2$. In particular, B-doped $BaSi_2$ shows *p*-type conductivity, and the hole concentration *p* can be continuously controlled in the range of 10^{16}~10^{20} cm^{-3}. Therefore, B-doped $BaSi_2$ films are often adopted to design solar cells structures. On the other hand, as for *n*-type $BaSi_2$, various dopants are still being studied. While Sb-doped $BaSi_2$ shows n-type conductivity with *n* controlled between 10^{16} and 10^{20} cm^{-3}, Sb atoms have a large diffusion coefficient in $BaSi_2$.[48] Thereby, a distribution of the Sb atom into undoped $BaSi_2$ after fabricating *p-i-n* device structure is considered to hinder a realization of a steep junction. Therefore, other atoms with small diffusion coefficient in $BaSi_2$ such as As has been under investigations.[50] Thus, we can control the conduction type of $BaSi_2$ while there is room for improvement. The bipolar property is also a good advantage for design high-η $BaSi_2$ homojunction solar cells composed of *p-n* or *p-i-n* device structures.

Table 2-2 Conduction types and carrier concentrations by different dopants in $BaSi_2$.

Dopant	**Conduction type**	**Carrier concentration [cm^{-3}]**	**Notes**	**Reference**
undoped	*n* or *p*	10^{16}	Strongly depend on R_{Ba}/R_{Si}.	51
B	*p*	10^{16}~10^{20}	Continuously control up to p^+.	52
Al	*p*	10^{16}~10^{17}	Diffusion is too strong.	53
Ga	*n*	10^{15}, 10^{20}	Can’t be controlled properly.	54
In	*p*	10^{16}~10^{17}	Can’t be up to p^+.	54
N	*p*	10^{16}~10^{17}	Plasma source.	55
P	*n*	10^{16}~10^{18}	GaP source.	56
As	*n*	~10^{19}	As ion implantation.	57
Sb	*n*	10^{16}~10^{20}	Continuously control up to n^+.	58

2.3. Growth of $BaSi_2$ thin-film

There are three main methods to grow $BaSi_2$ films thicker than 1 μm: molecular beam epitaxy (MBE), magnetron sputtering, and vacuum evaporation. In terms of photovoltaic device applications, the formation of high-quality films is one of the most important points.

$BaSi_2$ can be grown epitaxially on Si (111) and Si (001) substrates by MBE.[59-63] The growth processes will be described well in Section 4.1. The obtained films exhibit a three-fold symmetric domain rotated by 120° on Si (111), and it forms a twice symmetric domain rotated by 90° on Si (001) as shown in Figs. 2.3-1. These domains are randomly formed on the Si substrate (Figs. 2.3-2).[60-63] Noted that MBE is the best method to examine a potential of $BaSi_2$ for photovoltaic devices because it is easier to control the atomic ratio of Ba and Si during the film growth.

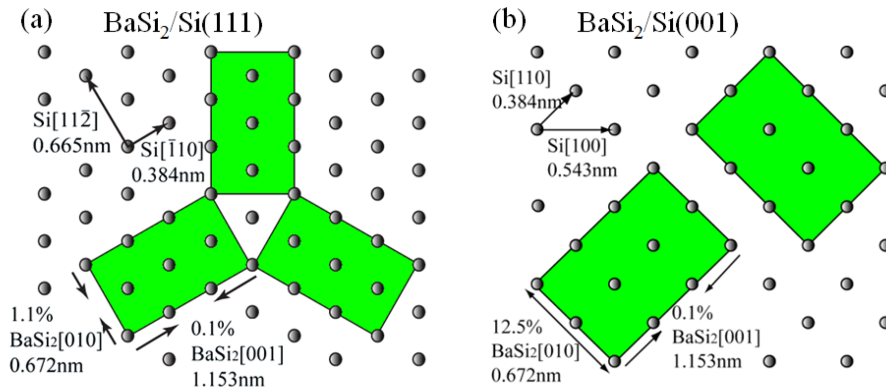

Fig. 2.3-1 Epitaxial relationship of $BaSi_2$ on (a) Si(111) and (b) Si(001).[61,62]

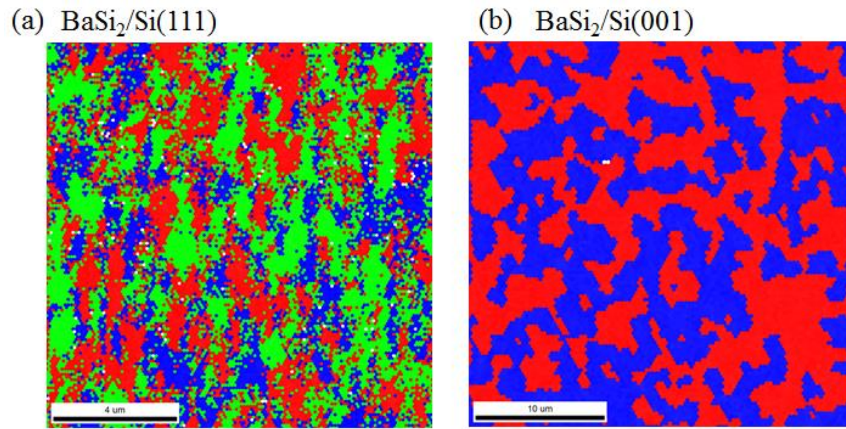

Fig. 2.3-2 EBSD maps of $BaSi_2$ films on (a) Si(111) and (b) Si(001).[61,63]

The magnetron sputtering is a practical method to form large area devices. Matsuno *et al.* formed single phase polycrystalline $BaSi_2$ films on Si(111) by helicon-wave excited plasma (HWP) sputtering, using a stoichiometric $BaSi_2$ target.[64,65] As the HWP has a higher plasma density, uniform in a large volume,[66] and lower ion energy than those of usual capacitive-coupled plasmas, substrate damage can be greatly reduced. As a result, a typical value of $n = 2 \times 10^{16}$ cm^{-3} was obtained at RT. The photoresponsivity rapidly increased for photon energies larger than the band gap of $BaSi_2$, and reached 0.75 A/W at a photon energy of 2.0 eV and $V_{bias} = -0.5$V applied to the indium-tin-oxide (ITO) electrode with respect to the Al electrode. Recently, a marked enhancement of photoresponsivity was achieved in C-doped $BaSi_2$ films due to the increase of minority carrier lifetime.[38]

Vacuum evaporation is another feasible method. An UHV is not a prerequisite; therefore, the equipment can be simple and inexpensive. Trinh *et al.* used $BaSi_2$ granules to form $BaSi_2$ films by vacuum evaporation, and achieved a large τ of 4.8 μs in the films grown at 500 °C. Evaporated undoped-$BaSi_2$ films show n-type conductivity with n varies from 10^{17} to 10^{22} cm^{-3} at different substrate temperature. The maximum value of photocurrent was obtained at a photon energy of 1.9 eV, corresponding to an *EQE* of 22% at a reverse applied voltage of 2.0 V.[67] One problem of the evaporated films was cracking due to the mismatch in thermal expansion coefficient between $BaSi_2$ and c-Si. Moreover, the grown films contained metallic phases such as Ba_2Si and Ba_5Si_3.[68,69] Hara et al., however, found out that the source premelting procedure suppressed the oxidation and made the films homogeneous.[70] Recently, a theoretical basis of thermal evaporation of $BaSi_2$ had reported based on the calculation from relative partial molar enthalpies of Ba and Si.[71]

2.4. $BaSi_2$ based photovoltaic devices

Attractive features suggest that $BaSi_2$ is a very promising material for thin-film photovoltaic devices. According to device simulations by Suemasu, we can expect up to 25% of η with 2-μm-thick $BaSi_2$ homojunction diodes,[72] whose value is comparable to that of the Si-based photovoltaic devices. To realize such high η, it is very important to take the band alignment of $BaSi_2$ and Si into account. Suemasu *et al.* revealed that $BaSi_2$ has an electron affinity of 3.2 eV,[73] which is about 0.8 eV smaller than the electron affinity of Si (4.05 eV). Therefore, we have to adjust the device structure such that the transport of photogenerated carriers is not blocked at the band offset as seen in Fig. 2.4-1. Based on this understandings, several studies have already been conducted and demonstrated their potential for device applications. Here, I summarize several structures of $BaSi_2$-based solar cells and make clear current issues and trials under investigations .

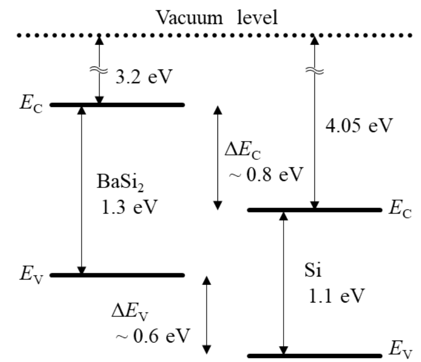

Fig. 2.4-1 Band alignment of $BaSi_2$ and Si with respect to the vacuum level.

(a) *p*-$BaSi_2$/*n*-Si heterojunction

The first operation of $BaSi_2$-based photovoltaic devices were operated in this structure. Figure 2.4-2(a) shows the band alignment of a *p*-$BaSi_2$/*n*-Si(111) junction diode when p is 2×10^{18} cm^{-3} for *p*-$BaSi_2$ and n is 2×10^{15} cm^{-3} for *n*-Si. The band offsets ΔE_C and ΔE_V in Fig. 2.4-2(a) promote the separation of photogenerated electrons and holes in p-$BaSi_2$, as well as those in n-Si, leading to the operation of a solar cell. η of approaching 10% are achieved based on this structure.[74,75] This is a champion value ever reported for photovoltaic devices fabricated with semiconducting silicides. Figure 2.4-2(b) shows a dependence of *p*-$BaSi_2$ layer thickness on *J*–*V* curves under AM1.5G illumination. The J_{SC} reaches a maximum of 35.8 mA/cm^2, and V_{OC} increases with the thickness of *p*-$BaSi_2$ and reaches a maximum of 0.47 V at 20 nm.[76] Deng *et al.* also demonstrated the operation of solar cells of *p*-$BaSi_2$/*n*-Si(001) junction diode with $p \sim 1 \times 10^{18}$ cm^{-3} for *p*-$BaSi_2$. The J_{SC} reaches a maximum of 37.0 mA/cm^2, a maximum V_{OC} of 0.44 V was obtained at 40 nm with $\eta \sim 9.8\%$.[77] In the structure of *p*-$BaSi_2$/*n*-Si(111), we can expect J_{SC} = 39.0 mA/cm^2, VOC = 0.63 V, and η = 15.7 % at maximam according to numerical simulations based on Silvaco ATLAS.[78] This deviation between the simulated results and the measured ones were explained by contributions of band tails of 1.2×10^{18} cm^{-3} eV^{-1} with its decay energy of 0.1 eV and a density of defects localized at 0.45 eV from the VBM with 3.5×10^{18} cm^{-3} eV^{-1} which is distributed with a width of 0.04 eV.[79]

(b) *n*-$BaSi_2$/*p*-Si heterojunction

In contrast to the band alignment of the *p*-$BaSi_2$/*n*-Si(111) or *n*-Si(001) structures, the band offsets at the n^+-$BaSi_2$/*p*-Si interface hinder the transport of photogenerated carriers, promoting the recombination of accumulated electrons and holes via defects at the heterointerface as seen in Fig. 2.4-3(a). Figure 2.4-3(b) shows a typical example of rectifying current–density versus voltage *J*–*V* characteristics under AM1.5G illumination for the n^+-$BaSi_2$/*p*-Si

diode. While J_{SC} of 11.8 mA/cm^2, V_{OC} = 0.22 V, and η = 1.5% were obtained from Fig. 2.4-3(b), these values are much smaller than those obtained in B-doped p-BaSi$_2$/n-Si heterojunction solar cell.[80]

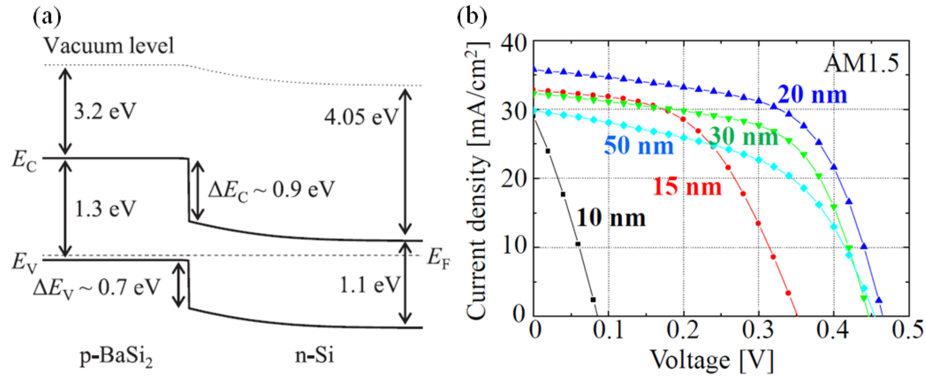

Fig. 2.4-2 (a) Band alignment and (b) J–V characteristics of p-BaSi$_2$/n-Si heterojunction solar cell.[74,76]

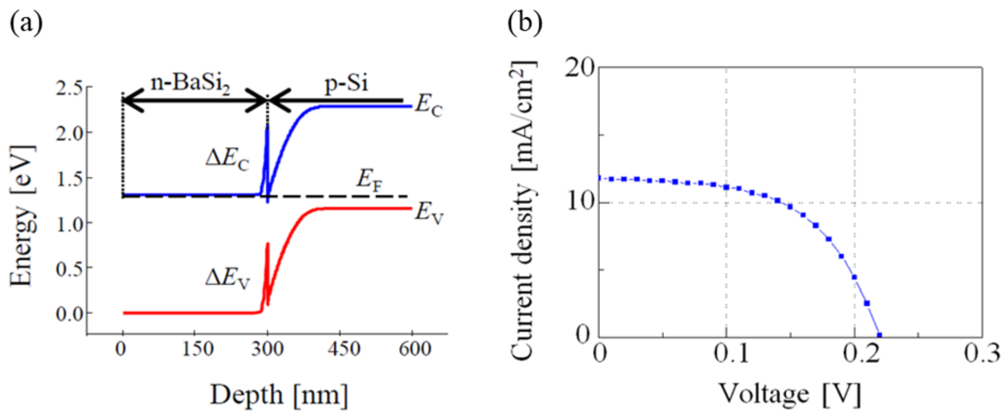

Fig. 2.4-3 (a) Band alignment and (b) J–V characteristics under AM1.5G illumination for n^+-BaSi$_2$/p-Si diode.[80]

(c) BaSi$_2$ homojunction on a tunnel junction

The contributions of BaSi$_2$ layers to the measured J_{SC} was low for heterojunction structures (in the case of p-BaSi$_2$/n-Si(111), it was estimated to be less than 20%).[74] In other words, we are not yet to be able to make full use of advantage of BaSi$_2$ properties in heterojunction structures. Therefore, we have examined to realize BaSi$_2$ homojunction diode, in which we can expect an increase of V_{OC} due to a larger difference of Fermi levels between n- and p-type regions. The only obstacle is large conduction and valence band discontinuities at the BaSi$_2$/Si heterointerface since we grow the BaSi$_2$ films on Si substrates. So, we tried to overcome this respect by forming a tunnel junction (TJ) to assist current flow in a BaSi$_2$ *pn* junction diode on a Si substrate. In previous works, an Sb-doped n^+-BaSi$_2$/p^+-Si TJ and clear photoresponsivity in undoped p-BaSi$_2$ overlayers formed on the TJ were achieved.[81-83] Recently, Kodama *et al.* first demonstrated the operation of BaSi$_2$ homojunction solar cells. Figure 2.4-4(a) shows the band alignment of proposed n^+-BaSi$_2$ (20 nm, $n = 1 \times 10^{19}$ cm^{-3})/p-BaSi$_2$ (500 nm, $p = 1 \times 10^{17}$ cm^{-3})/p^+-BaSi$_2$ (50 nm, $p = 1 \times 10^{19}$ cm^{-3})/p^+-Si(111) ($\rho < 0.01\Omega$cm) diodes. The influence of a large ΔE_V at the p^+-BaSi$_2$/p^+-Si interface was diminished by using the heavily doped p^+-Si substrate. Figures 2.4-4(b) and (c) are J–V characteristics under AM1.5G illumination and *IQE* spectra for the n^+-BaSi$_2$ (20 nm)/p-BaSi$_2$ (500 nm)/p^+-BaSi$_2$ (50 nm) diodes. The J–V curve in Fig. 2.4-4(b) is for the sample with $p = 1 \times 10^{16}$ cm^{-3}. As shown in the figure, leakage

current was large in the homojunction diode as expected. The *IQE* became pronounced at $\lambda < 800$ nm in Fig. 2.4-4(c), while the *IQE* was very small at $\lambda > 800$ nm because the photogenerated electrons in the p^+-Si recombined with holes before reaching the built-in field region. On the other hand, the *IQE* exceeded 30% at $\lambda = 500$ nm. Considering that the absorption length ($3/\alpha$) at $\lambda = 500$ nm is approximately 100 nm in $BaSi_2$,[35] so the *IQE* spectrum in Fig. 2.4-4 (c) was attributed to the photogenerated carriers originating from the *p*-$BaSi_2$ layer and then they were separated by the built-in electric field in the $BaSi_2$ *pn* junction diode. The *IQE* value distinctly increased as the *p* of the *p*-$BaSi_2$ layer decreased from 1×10^{17} to 1×10^{16} cm^{-3}, while the J_{SC} values were 1.3 and 3.6 mA/cm^2, respectively. On the basis of these results, the operation of a $BaSi_2$ homojunction solar cell was achieved for the first time.[80] η was as small as ~0.1% because of large leakage currents caused by defects resulting from step bunching at the p^+-$BaSi_2$/p^+-Si interface.[84] After the first operation, we improved the η up to 0.28% by considering optimum carrier concentrations and thickness at each layers. The most largest η was realized in n^+-$BaSi_2$ (20 nm, n ~ 10^{19} cm^{-3})/p-$BaSi_2$ (500 nm, p ~ 10^{16} cm^{-3})/p^+-$BaSi_2$ (20 nm, p ~ 10^{19} cm^{-3}) diodes on the B implanted p^+-Si/*p*-Si(111).[85]

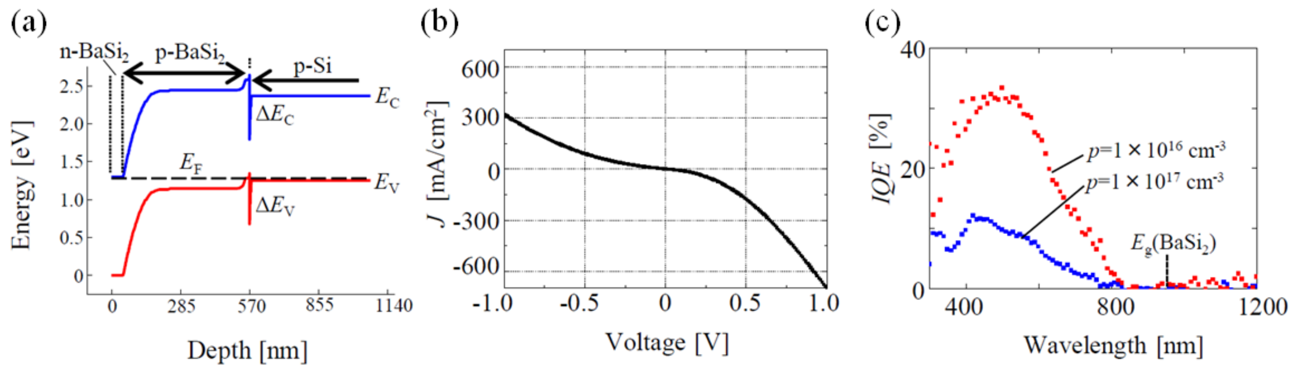

Fig. 2.4-3 (a) Band alignment; (b) *J–V* characteristics under AM1.5G illumination and (c) *IQE* spectrum for n^+-$BaSi_2$/*p*-$BaSi_2$/p^+-$BaSi_2$/p^+-Si diodes.[80]

As described above, we are at the next stage to improve η of homojunction solar cells. We had revealed much a lot of electric and optical characteristics and successfully demonstrated the potential of $BaSi_2$ for photovoltaic device applications. Moreover, as the future perspective, the realization of $BaSi_2$ homojunction solar cells enables us to design Si-based tandem PV devices which $BaSi_2$ *p-n* or *p-i-n* structures work as top cells. According to Deng, we can achieve above 30% of η by using BaC_xSi_{2-x} as its absorption layer.[86] To achieve such next generated PV devices, the remaining and unknown issue is “defect” in $BaSi_2$, which plays the most important role in conversion efficiency.

2.5. Defects in $BaSi_2$

Temperature dependence of electrical conductivity

From the temperature dependence of the electrical conductivity, activation energies (E_a) are given by,

$\sigma = \sigma_0 \exp(-E_a/k_B T)$.

The first report on the electrical conductivity was performed by Evers and Weiss using the four-probe method.[87] Then, Imai and Hirano reported electrical conductivity of the bulk $BaSi_2$ measured by the same method as Ref.[87] in the temperature range 80-290 K.[88] As it is clear from Fig. 2.5-1, $BaSi_2$ showed temperature dependence of semiconducting electrical conductivity. Based on the thermoelectric measurements, the sample in their research was considered to be *n*-type semeconductor. Therefore, the obtained activation energy by using the above equation corresponded to defect levels from the conduction band edge. At higher temperature range between room temperature to 1200 K, activation energies of 0.13 and 0.26 eV were also assigned defect levels from the donor levels by Nakamura *et. al.*[89] They evaluated the energies by using $\sigma = \sigma_0 \exp(-E_a/2k_B T)$ instead of $\sigma = \sigma_0 \exp(-E_a/k_B T)$. because the temperature region in their measurement corresponded almost the intrinsic region, where the activation energy is about a half of the energy gap.

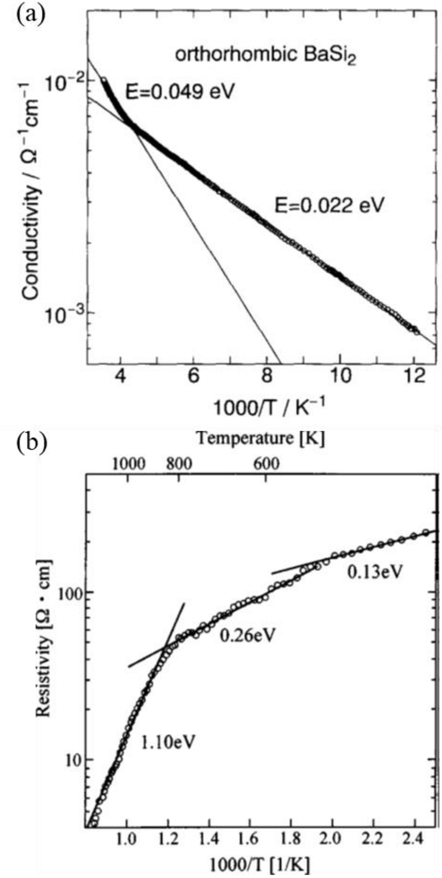

Fig. 2.5-1 Electrica conductivity of $BaSi_2$ as a function of reciptocal tempweature, 1/T in the temperature region (a) 80-290 K,[88] and (b) RT-1200 K.[89]

Photoluminescence

Kishino *et al*. reported photoluminescence spectra of $BaSi_2$, wherein Ba:Si ratios of 36:64 (Ba-rich) and 30:70 (Si-rich) of single crystals grown by the vertical Bridgman method. They observed two emissions at 1.143 and 1.052 eV for the Ba-rich sample (Fig. 2.5-2(a)).[90] On the other hand, four emissions were observed in the Si-rich sample with the energy of 1.138-1.141, 1.045-1.052, 0.831, and 0.672 eV (Fig. 2.1-2(a)). They pointed out that band-related emissions such as band-to-band or band-to-bound were assigned to the emissions observed at 1.143 eV in the Ba-rich sample and 1.138-1.141 eV in the Si-rich sample. This supposition was based on the fact that the indirect band gap energy of their samples at RT from absorption measurements was estimated to be equal to 1.13 eV. I note that Suemasu *et al.* measured the temperature dependence of the indirect band gap energy up to 8K.[91] According to them, the band gap became wide as decreasing temperature and the difference between that of room temperature and

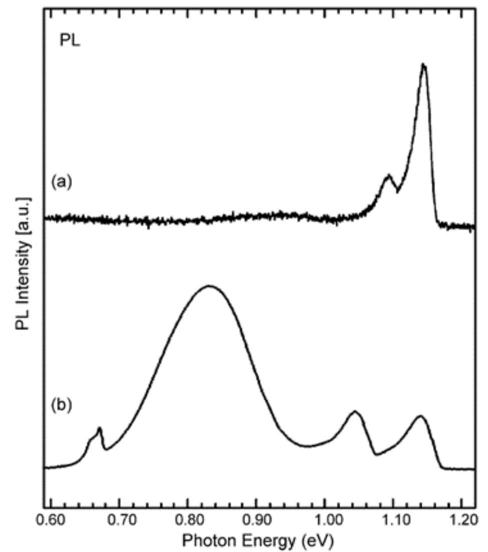

Fig. 2.5-2 Photoluminescence spectra of (a) Ba-rich and (b) Si-rich single crystals.[90]

that of below 50 K was 0.1 eV, while their polycrystalline film showed 1.3 eV of the indirect band gap at room temperature. Therefore, the assignments of such emissions should be completed from additional point of view including the Stokes shift, etc. As for the emissions of the 0.831 and 0.672 eV, Kishino *et al.* mentioned their dependence of the PL properties on the excitation laser power. Since the intensities of the emissions tended to saturate as the excitation laser power increased, they pointed out the emissions were related to defects in $BaSi_2$.

Deep level transient spectroscopy (DLTS)

Deep level transient spectroscopy (DLTS) is one of the defect detection methods for which there are relatively many reports.[84,92-95] The DLTS requires junctions such as Schottky junction or *pn*-junction. Among the researches, we had founded a few defects in $BaSi_2$ bulk region. Figures 2.5-3(a)-(c) showed DLTS profiles of $BaSi_2$ epitaxial films grown by MBE. Each sample had a junction at the interface between undoped $BaSi_2$ and Si(111). In Ref. [93], the DLTS profile of p-type $BaSi_2$ film (Fig. 2.5-3(a)) showed a minority carrier trap of 0.27 eV (H1) with a defect density (N_T) of 1×10^{13} cm^{-3}. Recently, we could improve the photoresponsivity of the films by changing an atomic ratio of Ba and Si more precisely during the MBE growth.[95] In such films, narrower DLTS peaks were observed as seen in Figs. 2.5-3(b) and (c), suggesting that the decrease in kind of defects in those films compared with those in Fig. 2.5-3(a). Although we observed majority carrier traps in both films, since the conductivity type was different in each sample, we concluded that two trap levels were hole traps (H2 and H3) as seen in Fig. 2.5-3(b) and two others were electron traps (E1 and E2) as seen in Fig. Fig. 2.5-3(c). Table 2-3 summarizes the trap levels detected by DLTS so far.

Table 2-3 Trap levels and defect densities (N_T) observed in DLTS. H# (E#) indicate a hole (electron) trap. The trap level of H# (E#) is defined from the valence band maximum (the conduction band minimum).

	H1 [93]	H2 [95]	H3 [95]	E1 [95]	E2 [95]
Trap Level [eV]	0.27	0.45	0.64	0.14	0.25
N_T [cm^{-3}]	1×10^{13}	8.3×10^{13}	1.7×10^{14}	4.7×10^{14}	1.1×10^{14}

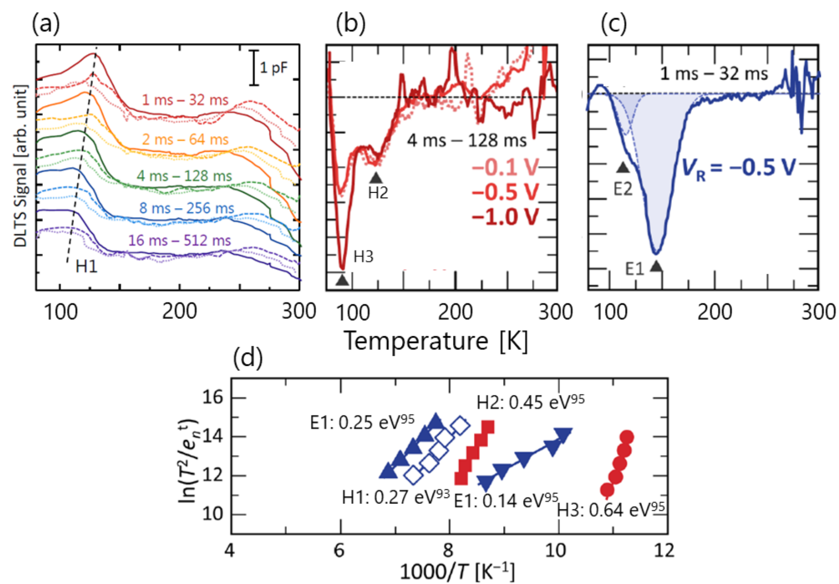

Fig. 2.5-3 (a)-(c) show DLTS profiles of undoped $BaSi_2$ films on Si(111) substrates with different MBE growth condition and/or method. (d) Arrhenius plots for electron (E1 and E2) and hole (H1, H2, and H3) trap levels.[93,95]

Raman spectroscopy

In my first year as a Ph. D student, I tried to assign Raman peaks on local vibrations originated from intrinsic defects in $BaSi_2$ films. Combined with DFT calculations (Figs. 2.5-4(a) and (b)), I clarified that a local vibration of Si vacancy made full width at half maximum of the most intense Raman peak (A_g mode) broad as a function of a deposition ratio (R_{Ba}/R_{Si}) during the MBE growth (Fig. 2.5-4(c)) . This interpretation was examined by Polarized Raman scattering measurements as seen in the inserted figure of Fig. 2.5-4(c). See Appendix A for the detailed discussions.

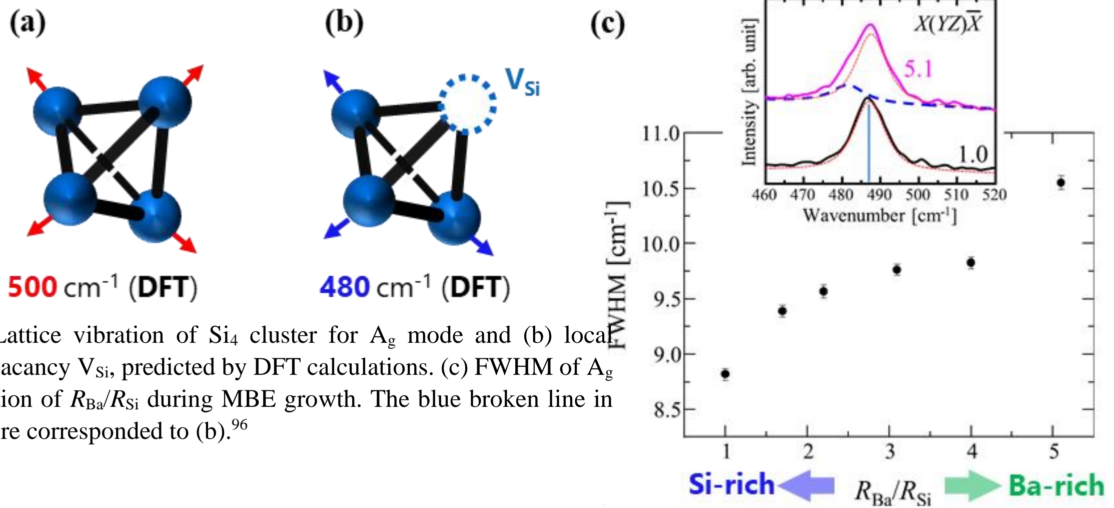

Fig. 2.5-4 (a) Lattice vibration of Si_4 cluster for A_g mode and (b) local vibration of Si vacancy V_{Si}, predicted by DFT calculations. (c) FWHM of A_g mode as a function of R_{Ba}/R_{Si} during MBE growth. The blue broken line in the inserted figure corresponded to (b).[96]

Positron annihilation spectroscopy

We performed the positron annihilation spectroscopy (PAS) on 500-nm-thick undoped $BaSi_2$ epitaxial films.[97] The PAS is known as the detection method for vacancy-type defects. In general, the characteristic value of S related to the annihilation of positrons increases because of their trapping by the vacancies.[98] Figure 2.5-5 show the S parameter and carrier concentration on $BaSi_2$ with different R_{Ba}/R_{Si} during MBE growth. Interestingly, the S parameter showed the same tendency against R_{Ba}/R_{Si} as that of the carrier concentration. Since the S parameter increases as increasing the vacancy-type defects, our results indicated the existence of the such defects. To compare the S parameter between films, the same thickness is preferable. However, it was hard to control the thickness of the film as accurate as required by the PAS. The PAS measurements were also performed by the group of Dr. O. Isabella. According to their results, single vacancy or divacancy were likely to be formed in the films.[99]

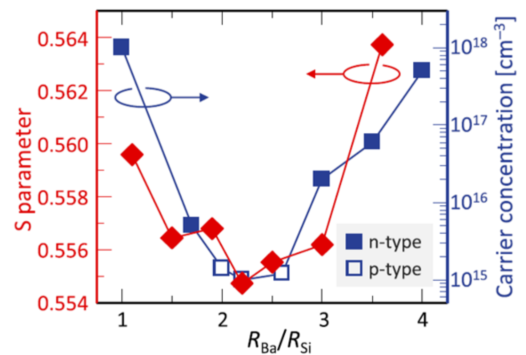

Fig. 2.5-5 Dependences of the S parameter and carrier concentration on $BaSi_2$ films.[97]

Photoreflectance

H. Hoshida *et al.* measured photoreflectance spectra of $BaSi_2$ epitaxial films with different R_{Ba}/R_{Si} (Fig. 2.5-6).[100] According to them, the third derivative spectra were observed in all the films in the photon energy range 1.5-1.7 eV, which corresponded to the photo modulated signal of the direct transition edge. The first derivative spectra

observed at 1.25 eV was related to the defect level with strong localization. That signal reached a minimum at R_{Ba}/R_{Si} =2.2 where carrier concentration became a minimum. Thus, they concluded that there was the defect level of 1.25 eV from the band.

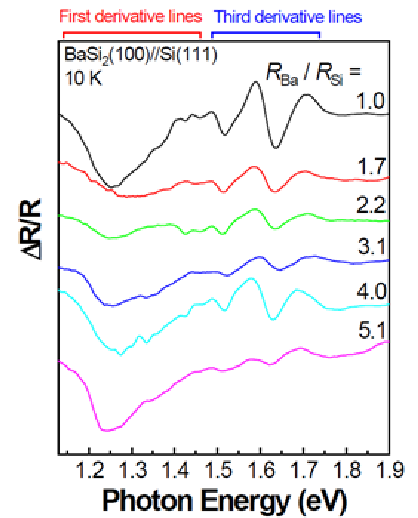

Fig. 2.5-6. Photoreflectance spectra of $BaSi_2$ epitaxial films.[100]

Grain boundary

As I showed in Figs 2.3-1, $BaSi_2$ can be epitaxially grown on Si (111) and Si (001) substrates by MBE,[59-63,101,102] and we confirmed $BaSi_2$ on Si (111) formed a three-fold symmetric domain rotated by 120°, while $BaSi_2$ on Si (001) forms a two-fold symmetric domain rotated by 90°. Since these domains are randomly arranged on the Si substrate, the $BaSi_2$ films are not uniform films like a single crystal but grow epitaxially while forming grain boundaries. Therefore, there are many grain boundaries that can be recombination centers in the $BaSi_2$ film. We had already studied the properties of such grain boundaries by Kelvin probe force microscopy (KFM). Thereby, we revealed that undoped n-$BaSi_2$ on the Si (111) substrate showed a downwardly convex band lineup at the grain boundaries (Fig 2.5-7(a)).[103] Hence, we could expect that the minority carriers (holes) recoil at the grain boundaries, and it is considered that the grain boundary is unlikely to act as a recombination center. This experimental fact was also confirmed from the fact that minority carrier lifetime of the $BaSi_2$ films didn't change even when the grain area was changed.[104,105] On the other hand, undoped n-$BaSi_2$ on Si (001) substrate showed an upwardly convex band lineup at the grain boundaries (Fig 2.5-7(b)).[103] Therefore, it is conceivable that the minority carriers (holes) easily accumulate in the grain boundary portion and easily work as a recombination center. In fact, the minority carrier diffusion length, L, of undoped $BaSi_2$/Si (111) measured by the EBIC was L = 10 µm, whereas L was 1.5 µm in undoped n-$BaSi_2$ / Si (001) (Fig. 2.5-7(c)).[45]

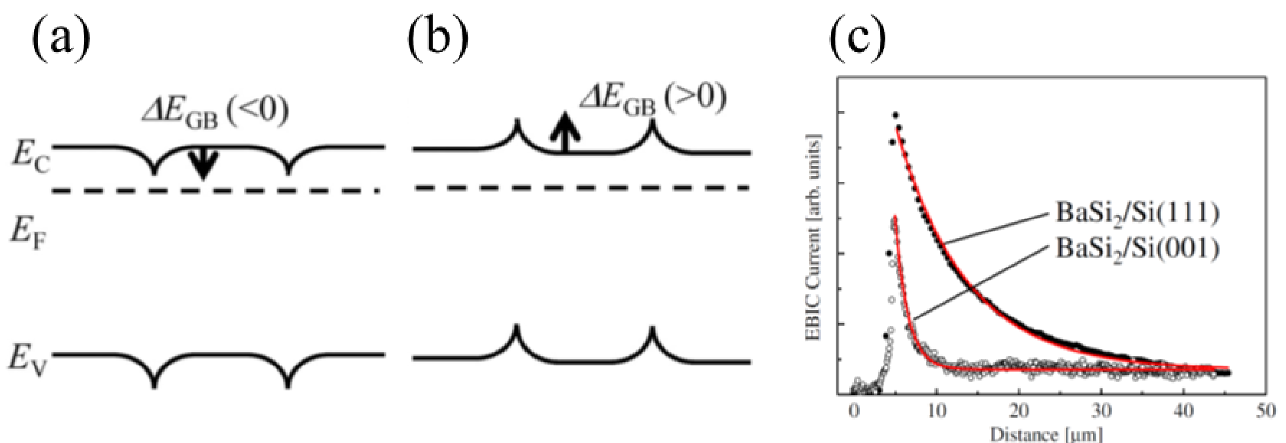

Fig. 2.5-7 Band alignment around grain boundaries of (a) $BaSi_2$/Si (111) and (b) $BaSi_2$/Si (001).[103] (c) EBIC current line profiles for $BaSi_2$/Si (111) and $BaSi_2$/Si (001).[45]

DFT calculations

In 2017, Kumar *et al.* reported possible intrinsic defects in $BaSi_2$ systerm systematicaly for the first time.[106] Before their researches, Y. Imai and A. Watanabe investigated the most probable insersion sites for Ga and In.[49] Based on their results, D. Tsukahara *et al*. calculated effect of interstitial dopant such as Sb, B, Al.[107] In Ref. [106], Kumar *et al*. also adopted the probable site, the 4c site, interstitial Si (Si_i) and Ba (Ba_i) as their initial configuration, where an impurity atom is surrounded by three Si atoms, one of which is at a corner of one of the Si-tetrahedrons while the other two make up one of the edges of the other Si-tetrahedron. Regarding the vacancy- and antisite-type defects (Si vacancy (V_{Si}), Ba vacancy (V_{Ba}), antisite Ba substituted for Si (Si_{Ba}), and antisite Si substituted for Ba (Si_{Ba})) were introduced at the position of Ba1 and Si3, respectively (Fig. 2.1-1). Figures 2.5-8 shows the results of formation energy of each defect as a function of Fermi Energy under Si-rich and Ba-rich condition. From Fig 2.5-8(a) and (b), they pointed out that V_{Si}^+ is the most likely to be formed in undoped $BaSi_2$ under both Si-rich and Ba-rich conditions. Addition to the formation energies, they also showed thermodynamic transition levels for the intrinsic defects as seen in Fig. 2.5-9. I note that the Fig. 2.5-9 is the case of DFT band gap calculated by DFT calculation.

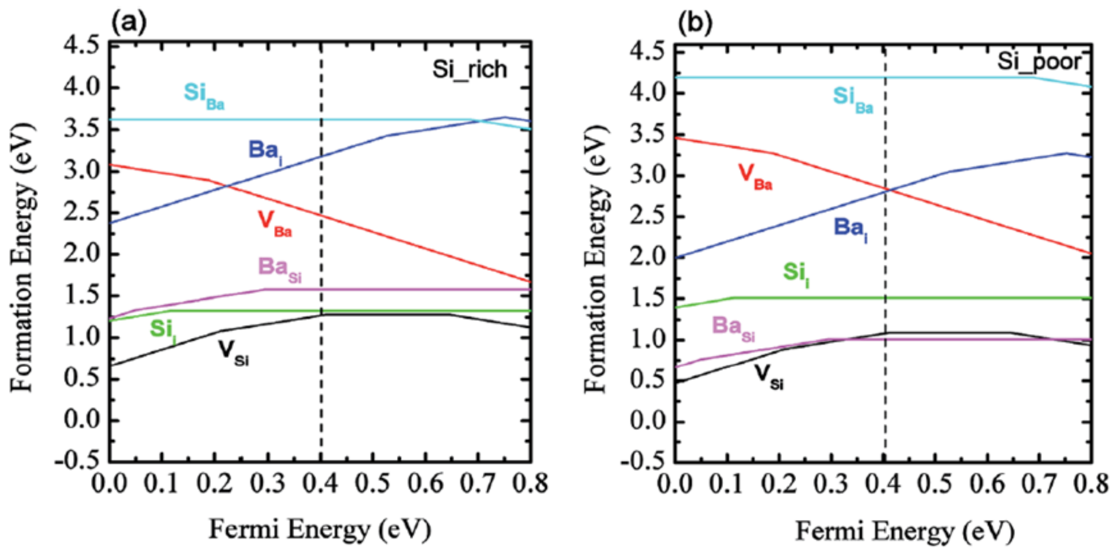

Fig. 2.5-8 Calculated formation energies as a function of the Fermi energy of the intrinsic point defects in $BaSi_2$ under (a) Si-rich and (b) Ba-rich conditions.[106]

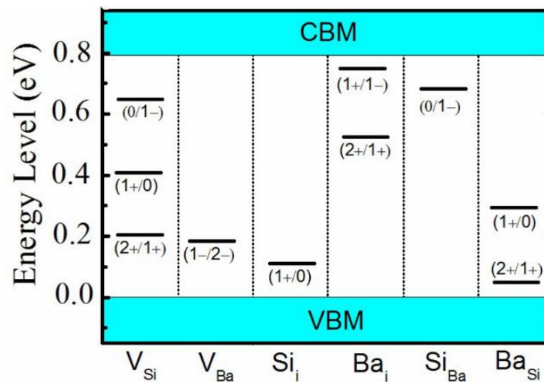

Fig. 2.5-9 The ionization levels of intrinsic defects in the DFT band gap (~0.8 eV).[106] The initial and final charge states are labeled in parenthes.

2.6. Magnetism in $BaSi_2$

Magnetic susceptibility

Orthorhombic $BaSi_2$ exhibit diamagnetic property. That was reported by Evers in 1978.[108] He measured the magnetic mass susceptibility χ_g of $BaSi_2$ by the Faraday balance under high vacuum conditions between 25 and 580 °C. He didn't report the measured value of orthorhombic $BaSi_2$ at, for instance, RT because he focus on a metal-semiconductor transition[109] in the literature. He only mentioned that the results of susceptibility showed horizonal slope against reciprocal magnetic field and reported the susceptibility of -0.41- -0.43×10^{-6} emu/g above 415 °C, at which the phase transition from metal phase (trigonal $BaSi_2$).

Nuclear magnetic resonance (NMR)

Regarding the magnetic resonance, there is a report by Goebel *et al.*[110] Their interest was chemical bonding in intermetallic compounds because the nature of idealized ionic and covalent bonding was relatively well understood whereas there was still a lack of knowledge about that of intermetallic one. They considered the Zintl phase as a model system, for the Zintl phase are polar intermetallic phases dominated by covalent and ionic bonding.[111] Since ^{29}Si is contained with low natural abundance (~ 4.68 %)[112], they prepared the ^{29}Si enriched samples for the measurements. Figure 2.5-10 shows the ^{29}Si Magic angle spinning (MAS) NMR signals. The MAS NMR signal of $BaSi_2$ seen at the bottom of Fig. 2.5-10 corresponded to three crystallographically different Si sites in $BaSi_2$. The isotropic shift was negative and between −50.2 and −365.5 ppm, which corresponded to those of being diamagnetic or non-metallic materials (in the range of −50.2 - −365.5 ppm). Furthermore, they also confirmed the temperature dependence of the shift, concluding that the dominant interaction was chemical shielding. Besides, based on quantum mechanical calculations, the intensities of the signals from Si3 and Si4 site (in Fig. 2.1-1) were equal because of equal multiplicity of the occupied sites. Since chemical shielding is the dominant mechanism, they evaluate the anisotropic shift (δ_{aniso}) and asymmetric parameter to get a picture of the electron distribution in the vicinity of the silicon atoms (Table 2-4). In the literature, they reported static NMR signals of cations while there was no data for Ba. Table 2-5 shows the quantum chemical caluculation results of electron counts of silicon atoms. According to the Zintl-Klemm concept, the charge transfer should be complete in the materials. On the other hand, they found the real material doens't follow the concept perfectly. Also, the electron count of Si3 site differs significantly from that of Si4 and Si5 site as seen in Table 2-5. While there was no magnetic resonance study on $BaSi_2$ except for the above mentioned one as long as I know, investigations on bare Zintl anion clusters such as Si_4^{4-} tend to increase in the field of material science.[111,113-115]

Table 2-4 Experimental and quantum mechanically calculatied NMR spectroscopic parameters of $BaSi_2$.[110]

Ba_2Si_4					
Si1	NMR	−99.9	144.3	0.82	1
	QM	−91.4	−143.8	0.85	
Si2	NMR	−50.2	−27.7	0.25	1
	QM	−37.8	−27.5	0.25	
Si3	NMR	−84.3	192.7	0.18	2.2
	QM	−67.1	194.4	0.26	

Table 2-5 Electron counts of silicon atoms in $BaSi_2$ (q in electrons per atom).[110]

	q(QTAIM)		
	Si1	Si2	Si3
Na_4Si_4	14.72	14.74	–
K_4Si_4	14.65	14.65	–
Rb_4Si_4	14.62	14.62	–
Cs_4Si_4	14.59	14.59	–
Ba_2Si_4	14.62	14.42	14.61

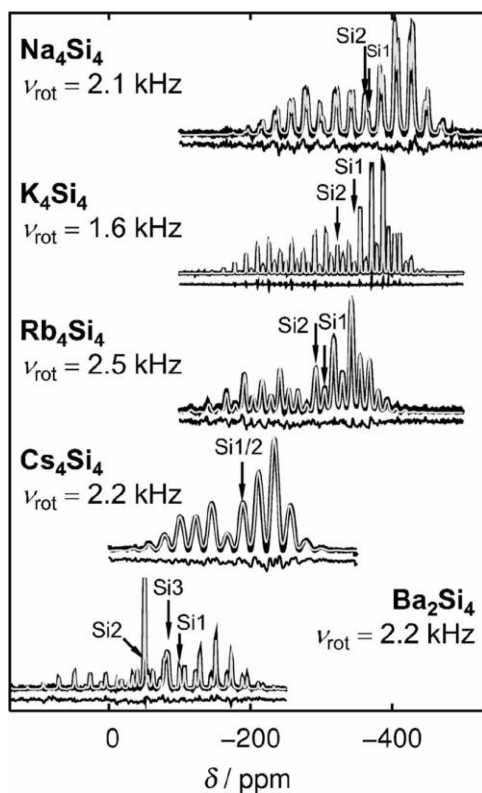

Fig. 2.5-10 ^{29}Si MAS NMR signal. The positions of the isotropic shifts are marked by arrows.[110]

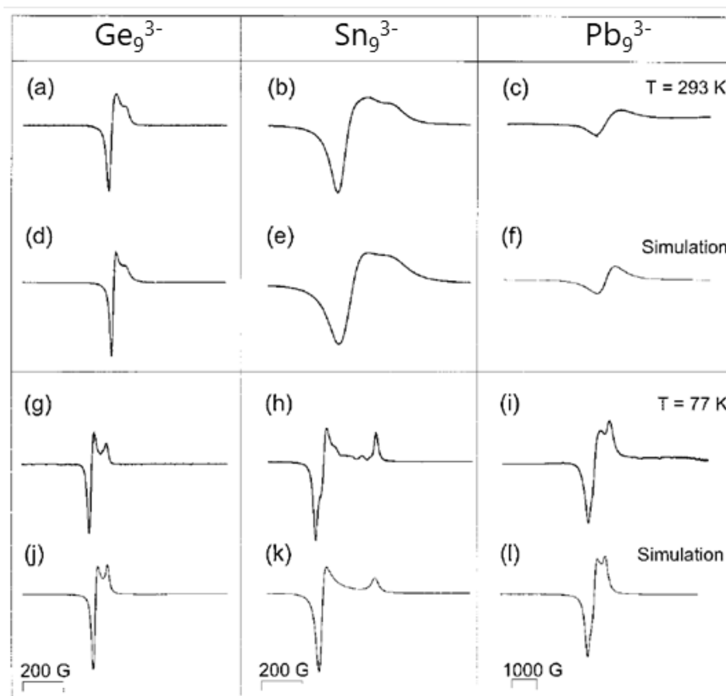

Fig. 2.5-11 EPR spectra of powder samples of Ge_9^{3-}, Sn_9^{3-}, and Pb_9^{3-} at 297 K (a-c) and 77 K (g-i). The spectra (d-f) and (j-l) were simulated using three different *g* tensor components (Table 2-4).[111]

Electron paramagnetic resonance (EPR)

Contrast to NMR, there is no EPR study about $BaSi_2$ as far as I know. On the other hand, some studies on other materials containing Zintl anions (E_9^{3-}, E = Si, Ge, Sn, and Pb)[111, 116-118] were reported. The EPR spectra originated from E_9^{3-} (E = Ge, Sn, and Pb). In Table 2-6, the parameter for the simulation are listed.

Table 2-6 g tensors and line width (LB) in Gauss for the simulation of Fig. 2.5-10.[111]

	Pulver					Einkristall		Lösung c)	
	298 K	LB a)	77 K	LB a)		298 K	77 K	298 K	77 K d)
1	2.04 2.04 1.99	28, 14 h)	2.04 2.03 1.99	10, 14 h)	**1 a** b)	2.08 2.06 2.02	2.06 2.00 1.99	– e)	2.00 f)
2	2.07 2.07 1.93	120, 80 h)	2.08 2.05 1.93	20	**2 c**	2.04 2.01 1.93	2.01 1.99 1.94	2.03 f)	2.03 2.02 2.00
3	1.68 f)	600	1.88 1.74 1.55	120	**3 a**	1.52 i)	1.76 i)	– g)	– g)

From the value of *g*-tensors, the anisotropy and the line width became large as increase atomic number. Figure 2.5-12 shows the EPR spectra of $[Si_{2.4}Ge_{6.6}]^{3-}$ reported by Waibel and Fassler. They mentioned that the EPR line width seemed (3 mT) Ge_9^{3-},[116] while the *g* value corresponded Si_9^{3-} of $g = 2.004(2)$.[117]

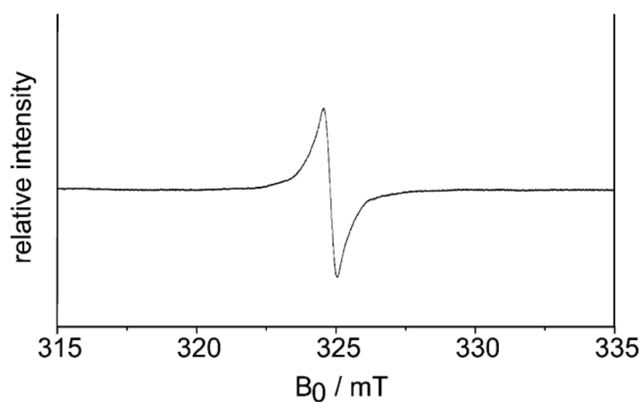

Fig. 2.1-12. X-band EPR spectrum at 150 K (g = 2.004(2)) of the sample containg $[Si_{2.4}Ge_{6.6}]^{3-}$. [116]

2.7. Aim of this thesis

As described above, $BaSi_2$ has physical properties suitable for solar cell applications. In addition, we had already demonstrated operation of solar cells by using $BaSi_2$, and the maximum conversion efficiency of silicide-based heterojunction solar cells with crystalline Si of ~ 10% has been achieved. More recently, a homojunction solar cell device that can be expected to further improvement on conversion efficiency has been successfully operated. On the other hand, investigation of defects that greatly affect conversion efficiency is still limited. It is clear that the defect exists, but its identity remains unknown. Therefore, the purpose of this study is to detect and clarify defects from a microscopic viewpoint using the electron paramagnetic resonance.

Chapter 3 Principle of electron paramagnetic resonance

Electron paramagnetic resonance (EPR) is a powerful experimental method for studying systems with unpaired electrons. In systems with unpaired electrons, irradiation with electromagnetic waves causes a dipole transition. As a result, an absorption spectrum, i.e., the EPR spectrum are obtained. Examples of EPR applications include free radicals in solids, liquids and gases, transition metal ions, photogenerated species, and point defects in solids. Especially, regarding point defects in solids, EPR provides us fruitful information on their microscopic structures as well as their dynamics as a faction of temperature. For instance, EPR has revealed the defect symmetry and its chemical identity in various semiconductors such as Si, SiC, etc.

A dipole magnetic field (***B***) created by the magnetic dipole ($\boldsymbol{\mu}$) is given by the following equation.

$$\mathrm{B} = \frac{1}{r^3}\left[\frac{3(\boldsymbol{\mu}\cdot\boldsymbol{r})}{r^2} - \mu\right].$$

Thus, all magnetic moment always accompanies the angular mementum ***G***.

$$\boldsymbol{G} = \boldsymbol{r}\times\boldsymbol{p}$$

Where ***r*** is the radius vector and ***p*** is the momentum. The ratio of the magnetic moment to the angular momentum is called the magnetogyric ratio ($\gamma = \mu/G$). If the magnetic moment is parallel or antiparallel to the angular momentum,

$$\mu = \frac{1}{c}IS, I = \frac{q}{2\pi R}v.$$

Here q is the charge, R is the loop radius, v is the velocity of the charge, and $S = \pi R^2$. Therefore, the magnitude of the magnetogyric ratio is given by,

$$\gamma = \frac{\mu}{G} = \left(\frac{qvR}{2c}\right)/\left(m_q vR\right) = \frac{q}{2m_q c}.$$

In quantum mechanical descriptions, the angular momentum is written as $\boldsymbol{G} = \hbar\boldsymbol{L}$, then the orbital magnetic moment of electron $\boldsymbol{\mu}_L$ is given by

$$\boldsymbol{\mu}_L = \gamma\boldsymbol{G} = -\frac{\mathrm{e}\hbar}{2\mathrm{m}_q\mathrm{c}}\boldsymbol{L} = -\beta\boldsymbol{L}.$$

Here β is called the Bohr magneton. In radio spectroscopy a dimensionless quantity named the g-factor is introduced instead of the magnetogyric ratio, then it can be written as $\boldsymbol{\mu}_L = -g_\mathrm{L}\beta\boldsymbol{L}\ (g_L = 1)$. Similarly, $\boldsymbol{\mu}_S = -g_S\beta\boldsymbol{S}$ (g_S= 2.0023 ... 1). Now, the Hamiltonian when the magnetic moment is placed in a magnetic field is given by $\mathcal{H} = -\boldsymbol{\mu}\cdot\boldsymbol{B}$, so the spin magnetic moment is spitted into following two energies.

$$E_\pm = -\boldsymbol{\mu}\cdot\mathbf{B} = \pm(1/2)g_S\mu_\mathrm{B}B_0$$

This is called the Zeeman effect. EPR observes the microwave absorption spectrum corresponding to the energy difference due to Zeeman splitting (Zeeman energy). In other words, as resonance conditions

$$hv = g_S\beta B_0$$

In practice, if we extend the two-level model to N spins, the emission of photons will occur as well. The characteristic quantity is then the population difference of N, which follows a Boltzmann distribution in thermal equilibrium. In the high-temperature approximation $E \ll k_\mathrm{B}T$, one obtains the population difference $n = Ng_S\beta B_0/2k_\mathrm{B}T$, where k_B denotes the Boltzmann's factor, and T the temperature. Therefore, the sensitivity of the spectrometer increases with

the total number of spins, for larger magnetic fields and at lower temperatures. Due to the proportionality of the magnetic field and the frequency, we would now suspect that the sensitivity improves with larger frequencies as well. But in this case, the corresponding waveguides become smaller, which means that the samples have to be smaller too. Consequently, they also contain fewer detectable spins *N*. In a scheme of EPR, a spin polarization is bigger, resulting in expecting an increase of sensitivity. This parameter is usually the more important one in real materials. Besides that, several aspects restrict the used frequency range to the microwave region. For example, in the high-frequency regime, it is difficult to produce sufficiently homogeneous magnetic fields and it is expensive to shrink the microwave components. On the other hand, in a real material system, not all of the EPR-detectable mechanisms are field-dependent (i.e. frequency-dependent).

3.1. EPR parameters

We now turn to the formal description of the relevant processes which affect the EPR spectrum. First, for conventional EPR, it is sufficient to consider only the electronic ground state, since the energy difference between the ground and excited states of the defect system (on the order of eV) is significantly higher than the one between the dipole transitions (in the range of eV-meV). The effective spin Hamiltonian characterizing the defects are described below.

$$\mathcal{H}(r) \equiv \mathcal{H} = \mathcal{H}^{\mathcal{Z}} + \mathcal{H}^{\mathcal{FS}} + \mathcal{H}^{\mathcal{HF}} + \mathcal{H}^{\mathcal{NZ}} + \mathcal{H}^{\mathcal{Q}}$$

$\mathcal{H}^{\mathcal{Z}} = \mu_{B\boldsymbol{B}^T} \cdot \boldsymbol{g} \cdot \boldsymbol{S}$ ... electronZeeman interaction
$\mathcal{H}^{\mathcal{FS}} = \boldsymbol{S}^T \cdot \boldsymbol{D} \cdot \boldsymbol{S}$... fine-structure interaction
$\mathcal{H}^{\mathcal{HF}} = \boldsymbol{S}^T \cdot \boldsymbol{A} \cdot \boldsymbol{I}$... hyperfine interaction
$\mathcal{H}^{\mathcal{NZ}} = -\mu_{n\boldsymbol{B}^T} \cdot \boldsymbol{g}_n \cdot \boldsymbol{I}$ ... nuclear Zeeman interaction
$\mathcal{H}^{\mathcal{Q}} = \boldsymbol{I}^T \cdot \boldsymbol{P} \cdot \boldsymbol{I}$ ... nuclear quadrupole interaction

where g, D, A, g_n, and P are effective g tensor, fine structure tensor, hysymmetrical, three-dimensional matrices, which can be diagonalized and are characterized by their principal values and eigenvectors. In experiments, it is easier to obtain the relative signs for the matrix elements (e.g. g_{ij}) than the overall one (e.g. $\boldsymbol{g}$) [31]. From the above equations, we see that $\mathcal{H}^{\mathcal{Z}}$ depends on the magnetic field but not $\mathcal{H}^{\mathrm{HF}}$. In the presence of *g*-strain (broadening of the *g*-values in a frozen solution), it is better to obtain the hyperfine tensor at low magnetic fields and corresponding frequencies (S- and X-band), whereas the *g*-tensor is measured at high frequencies (Q- and W-band).

3.1.1. Electon Zeeman interaction

In this subsection, I focus on the term in the spin Hamiltonian that represents the interaction of the electron spin with the external magnetic field B, i.e., electronic Zeeman term;

$$\mathcal{H}^{\mathcal{Z}} = \beta \boldsymbol{B}^T \cdot \boldsymbol{g} \cdot \boldsymbol{S} .$$

In the description of the spin Hamiltonian, all spatial information is aggregated in the g-tensor (3×3 matrix). In the principal axes system (X, Y, Z) of g-tensor, the spin Hamiltonian becomes,

$$\mathcal{H}^{\mathcal{Z}} = \beta \mathrm{B}(n_X n_Y n_Z) \begin{pmatrix} g_X & 0 & 0 \\ 0 & g_Y & 0 \\ 0 & 0 & g_Z \end{pmatrix} \begin{pmatrix} S_X \\ S_Y \\ S_Z \end{pmatrix}$$

Here, the spin operator is defined as $\mathrm{S} \equiv 1/2\mathrm{h}\sigma$ using a Pauli matrix. Where each component of the Pauli matrix is

$$\sigma_x = \begin{pmatrix} 0 & 1 \\ 1 & 0 \end{pmatrix}, \sigma_y = \begin{pmatrix} 0 & -i \\ -i & 0 \end{pmatrix}, \sigma_x = \begin{pmatrix} 1 & 0 \\ 0 & -1 \end{pmatrix}.$$

Therefore,

$$\mathcal{H}^Z = \frac{1}{2}\beta B \begin{pmatrix} n_Z g_Z & n_X g_X - i n_Y g_Y \\ n_X g_X + i n_Y g_Y & -n_Z g_Z \end{pmatrix}$$

by diagonalizing the matrix,

$$E(\pm) = \pm\frac{1}{2}\beta B\left(\sum_i n_i^2 g_i^2\right)^{1/2} = \pm\frac{1}{2}\beta\left[B(n^T g)(g^T n)B\right]^{1/2},$$

Thus, we can obtain eigen energies, $E(+1/2) - E(-1/2) = (|g^T n|)\beta B \equiv g\beta B$. We often use the principal axes of the *g*-tensor introduced on the right side of the equation. Single crystal makes possible to determine the complete g-tensor, the principal values and direction of the principal axes. In contrast to single crystal, we can observe only these principal values of the g-tensor in non-orientated samples such as powders.

As seen in Fig. , g-tensor is anisotropc in generall. This deviation from the value of free electron (g_e) is ascribed to the current induced by moving around the spin, which is called the spin-orbit-coupling ($\mathcal{H}^{SO} = \beta \boldsymbol{B}^T \cdot \boldsymbol{g} \cdot \boldsymbol{S}$). As a result of the spin-orbit-coupling, in real system,

$$g = g_{e\mathbf{1}} - 2\lambda\boldsymbol{\Lambda}.$$

The λ is spin-orbit-coupling constant and tend to larger in heaver nuclei.
Here,the elements of Λ are given by

$$\Lambda_{ij} = \sum_{n\neq 0}\frac{< 0|L_i|n > < n|L_i|0 >}{E_n - E0}(i,j = x,y,z)$$

where 0 and n are the atomic orbitals that are singly occupied in the ground and the *n*-th excited states. In aspect of spectroscopy, it is easier to observe the contribution of the *g*-tensor. From the respect of DFT calculations, it is much more difficult to calculate the *g*-tensor because we have to take all excited states into the accounts.

Overall, we can distinguish between,

- $\Delta g \approx 10^{-5}$– 10^{-2}: typical for defects with a weak spin-orbit coupling ($\lambda \approx 1 - 100 cm^{-1}$) in a strong crystal field. This applies for example to light impurity atoms in ionic crystals and defects with an s-ground state, which in principle do not have a spin-orbit coupling at all.
- $\Delta g \approx 10^{-2} -$ a few 10^{-1}: typical for transition-metal ions with a $3d^n$-configuration ($\lambda \approx 10^2$– $10^3 cm^{-1}$) in a strong crystal field (e.g. ionic crystals).
- $\Delta g \approx 1$: the concept of a g-shift is no longer applicable. This is for example the case for rare-earth ions with a $4f^n$-orbital configuration.

3.1.2. Hyperfine interaction

In this subsection, I focus on the term in the spin Hamiltonian that represents the interaction between electron spin, $\boldsymbol{S}$, and nuclear spin, $\boldsymbol{I}$, i.e., hyperfine coupling term;

$$\mathcal{H}^{\mathcal{HF}} = \boldsymbol{S}^T \cdot \boldsymbol{A} \cdot \boldsymbol{I}$$

The hyperfine tensor are divided int two parts; an isotropic part (a_{iso}) and an anisotropic part ($\boldsymbol{T}$). The *A* tensor, therefore, is given by,

$$\boldsymbol{A} = a_{\mathrm{iso}}\boldsymbol{1} + \boldsymbol{T}$$

Formally, the isotropic hyperfine interaction is defined by the Hamiltonian,

$$\mathcal{H}_{\mathrm{iso}}^{HF} = \frac{8\pi}{3} g_n g \mu_n \mu_B |\psi(\boldsymbol{R} = 0)|^2 \boldsymbol{S}^T \cdot \boldsymbol{I}$$

where$\psi(\boldsymbol{r})$ stands for the one-particle wavefunction at the atomic site $\boldsymbol{R}$. This means that it is proportional to the probability of presence at the position of the nucleus. Since only s-wavefunctions don't vanish at the position of the nucleus ($|\psi(\boldsymbol{R}=0)|^2 \neq 0$).

The anisotropic dipole interaction is described by the following Hamiltonian

$$\mathcal{H}_{dip}^{\mathcal{HF}}(r) = g_n g \mu_n \mu_B \left[\frac{3(I^T \cdot r)(S^T \cdot r)}{r^5} - \frac{S^T \cdot I}{r^3}\right]$$

where r is the distance vector between the electron and nucleus, which is averaged over the wave function of unpaired electrons. In contrast to the Zeeman interaction, the hyperfine interactions is more local interactions ($r < 1$ nm). The most important characteristics from the aspect of spectroscopy is that the A-tensor doesn't depend on the applied field (or the applied frequency).

3.1.3. Nuclear quadrupole interaction

The nuclear quadrupole interaction is not directly observed in EPR because this is the results of the interaction of electric quadrupole moment of an atomic nucleus with the electric-field gradient at its lacation. The Hamiltonian of this interaction is given by

$$\mathcal{H}^{Q} = \boldsymbol{I}^T \cdot \boldsymbol{P} \cdot \boldsymbol{I}$$

As it is clear from the Hamiltonian, electronic spin are not included. Hence, in standard EPR measurement, we don't take it into the acccount. This effect only shows up on the spectra when we measure the NMR transition containg $I > 1/2$ via the ESR such as ESSEM, ENDOR, and EDNMR etc. In its principal axes, the nuclear quadrupole tensor is defined as

$$\boldsymbol{P} = \begin{pmatrix} P_x & 0 & 0 \\ 0 & P_y & 0 \\ 0 & 0 & P_z \end{pmatrix} = \begin{pmatrix} K(-1+\eta) & 0 & 0 \\ 0 & K(-1-\eta) & 0 \\ 0 & 0 & 2K \end{pmatrix}$$

where $K = e^2Qq/4\mathrm{I}(2\mathrm{I}-1)h$ is the parameter directly related to the size of the observed spectral shifts and splittings. The η represent its asymmetry of the electric-field-gradient. The nuclear quadrupole moment, Q, is related to the shape of charge distribution of atomic nuclei. The Q is propotional to the charge of Z of the nucleus. On the other hand, the electric-field inhomogeneity at the position of a nucleaus is describede as e$\boldsymbol{q}$ which stems from the second derivatives of electrostatic potential at the nucleus, $V(\boldsymbol{R})$.

3.1.4. Others

The nuclear Zeeman term is the same concept as the electron Zeeman term. The only difference between two is the range of the resonances. In the case of nuclei, the resonance occurs in the region of radio frequency (~ MHz) due to the mass of the nuclei. The ratio of the nuclei to electron is around 2000, resulting in the magnetogyric ratio become small. This means that the energy splitting is smaller than that of the electron. The absorption of the radio frequency corresponding to the nuclear Zeeman energy is called the nuclear magnetic resonance (NMR). In comparison with EPR, its sensitivity is low so that the spin polarization of the nuclei is small at thermal equilibrium. However, since each nuclei possesses specific magnetogyric ratio, the

applicable field over almost whole materials as well as atomic selectivity. Their fine-structure term is explained in the same manner as the nuclear quadrupole term. This interaction should be taken into the account in the system with $S > 1/2$. One consequence of this contribution is the fine structures which are important to understand zero field splitting. Furthermore, in the coupled spins system, the exchange interaction term ($\mathcal{H}^{\mathcal{J}} = -2\mathrm{J}s_1 \cdot s_2$) is also needed to be paid careful attentions to understand the spectra.

3.2. Relaxation

EPR is caused by the difference in the occupation number of states with different spin numbers. Therefore, the continuous wave EPR, which is widely used at present, often observes the saturation of the EPR signal due to the strong microwave irradiation. In a spin system that has changed from a ground state to an excited state due to microwave absorption, the energy returns to the ground state by transferring energy to the lattice system. The relaxation time is defined as a physical quantity characterizing the transition from the excited state to the ground state. The exchange of energy between the spin system and the lattice system is called spin-lattice relaxation time (T_1), and is an important parameter that determines the microwave intensity dependence. The spin-spin relaxation time (T_2) that governs coherence and decoherence between unpaired electrons also affects microwave intensity dependence. In EPR measurement using continuous microwave, the saturation factor s is defined by the following equation.

$$\mathrm{S} = \frac{1}{1 + \gamma^2 B_1^2 T_1 T_2}$$

When $s < 1$, the amplitude of the cw EPR signal decreases and broadening of the signal may be observed. In practice, by plotting the EPR amplitude as a function of square root of microwave power P_{mw}, one can confirmed whether the EPR line is saturated or not. Deviation from linearity means microwave saturation.

On the other hand, since T_1 and T_2 are unique physical quantities at each paramagnetic center, if T_1 and/or T_2 are significantly different at each paramagnetic center, one of them is measured in a saturated state, and the other is EPR. Helps you understand the outline of the line. Generally, T_2 does not depend much on temperature, whereas T_1 has a strong temperature dependency. Clarifying the physics governing matter through the temperature dependence of T_1 is one of the real thrills of magnetic resonance. However, it is difficult to separate T_1 and T_2 by the currently widely used CW method. A promising method is EPR measurement using pulse microwave.

Chapter 4 EPR study on $BaSi_2$ film

In this chapter, I show the results obtained on *a*-axes-orientated epitaxial $BaSi_2$ films. The films are fabricated on Si substrates by molecular beam epitaxy (MBE).[59-63, 101,102] My final goal is to evaluate defects in $BaSi_2$ thin-films, which are expected to act as light absorbing layers. Since this is the first EPR study on $BaSi_2$, it was not known whether an EPR line was actually observed. However, if an EPR line could be observed in thin-films directly, that is the shortest and most efficient route. A point to be noted here is that it is extremely difficult to separate the EPR lines of $BaSi_2$ from those of the Si substrate because a $BaSi_2$ thin-film of about 500 nm is deposited on the 625μm-thick Si substrate at 625 μm. In order to suppress the EPR line derived from the Si substrate, Si substrates (Floating-Zone (FZ) Si substrate) having a high resistivity, i.e., low carrier density was used. Therefore, even if the origin of the paramagnetic center in the Si substrate is observed, it is highly likely that the origin of the paramagnetic center is an isotropic one having no crystal symmetry. On the other hand, the $BaSi_2$ thin-film is an epitaxial film that is uniaxially oriented in *a* direction perpendicular to the plane. Hence, the origin of the anisotropic EPR line can be ascribed to the $BaSi_2$ thin film. The above is the strategy in this chapter.

4.1. *a*-axis orientated epitaxial $BaSi_2$ films

A crystal growth of $BaSi_2$ was performed using a molecular beam epitaxy (MBE) chamber having a maximum ultrahigh vacuum of about 10^{-8} Pa. The MBE chamber is equipped with a Knudsen cell (K-cell) for supplying Ba and an EB gun for supplying Si. Further, the deposition rate R_{Si} of Si is controlled by a feedback system using an electron impact emission spectroscopy (EIES) sensor. The procedure for preparing a sample is described below.

In this study, Si (111) substrate was used to fabricate a $BaSi_2$ epitaxial film. On the surface of the Si substrate, there is a natural oxide film of about 1 nm and organic pollutants, metal pollutants, and particles. Therefore, before growing $BaSi_2$, it is necessary to remove them and obtain a clean surface. The substrate pre-pretreatment shown in Table 4-1 was performed. First, in order to remove organic contamination on the Si surface, organic cleaning with acetone / methanol / pure water was performed. Next, the native oxide layer was removed with a 5% aqueous hydrofluoric acid (HF) solution. Further, it was immersed in an aqueous hydrochloric acid (HCl) solution for 5 mins for the purpose of removing metal contamination. At this time, hydrogen peroxide solution (H_2O_2) was also simultaneously added to form a protective oxide layer on the Si surface. Then, the protective oxide layer was removed again with the 5% HF aqueous solution, and then immersed in an aqueous ammonia solution (NH_4OH) to remove particles and organic substances. Note that the H_2O_2 was also added into this NH_4OH aqueous solution to form a protective oxide film. Finally, the substrate was transferred into the ultrahigh vacuum chamber after removing moistures. The substrate was heated at 900 °C in the chamber for 30 min to remove the protective oxide film and obtain a clean surface of Si (thermal cleaning, TC).

After obtaining a clean surface of the Si substrate, a 5-nm-thick $BaSi_2$ template layer was deposited on the Si substrate heated at 500 °C by supplying Ba atoms (reactive deposition epitaxy, RDE). This template layer serves as a seed crystal for a layer laminated thereon.[119] Next, a $BaSi_2$ thin-film having a thickness of about 450 nm was grown by MBE in which Ba and Si were simultaneously supplied and reacted on the template layer heated to 580 °C. During the MBE growth, the deposition rate of Si (R_{Si}) was fixed at R_{Si} = 0.9 nm/min and the deposition rate of Ba (R_{Ba}) was changed from 1.0 nm/min to 3.2 nm/min, resulting in the films with R_{Ba}/R_{Si} = 1.1 to 3.6 were obtained.[51,97] Thereafter, a 5-nm-thick amorphous Si (a-Si) was deposited in situ as a surface passivation layer on undoped $BaSi_2$ thin-films heated to 180 °C.[104,120,121] Table 4-2 shows the details of the sample growth conditions.

Table 4-1 Pretreatment method for Si substrate

	Process	Time	Purpose
1	Ultrasonic cleaning with acetone	10 min	Removal of organic materials and particles
2	Ultrasonic cleaning with methanol	10 min	
3	Ultrasonic cleaning with ultrapure water	5 min	
4	5% HF	30 s	Removal of natural oxide film
5	HCl : H_2O_2 : H_2O = 1 : 1 : 4	5 min	Removal of metal contaminations Formation of protective oxide film
6	5% HF	30 s	Removal of protective oxide film
7	NH_4OH : H_2O_2 : H_2O = 1 : 1 : 4	5 min	Removal of organic materials and particles Removal of protective oxide film
8	N_2 blowing	-	Removal of moistures
9	Thermal cleaning in ultrahigh chamber 900 °C	30 min	Removal of protective oxide film

Table 4-2 The details of MBE growth conditions

Label	MBE				
	R_{Si} (nm/min)	R_{Ba} (nm/min)	R_{Ba}/R_{Si}	Time (h)	Thickness (nm)
A	0.9	1.0	1.1	8	450
B		1.4	1.5	8	430
C		1.7	1.9	8	380
D		2.0	2.2	8	450
E		2.3	2.5	8	440
F		2.7	3.0	8	450
G		3.2	3.6	8	480

In this study, FZ undoped *n*-Si (111) substrates (ρ = 1000-10000 Ω cm) were used to suppress the EPR line from the Si substrate. RHEED, XRD, and Raman spectroscopy were performed for characterizations of the films. In the XRD measurement, out-of-plane θ–2θ measurement was performed to determine an *a*-axis lattice constant, and in-plane φ-$2\theta_\chi$ measurement was performed to determine the *b*- and *c*-axis lattice constants. An Nd: YAG laser (532 nm) was used for Raman spectroscopy.

Figure 4.1-1 shows the RHEED pattern after Thermal Cleaning (TC), RDE, and MBE growth. After TC in all samples, clear RHEED patterns along with Si $[11\bar{2}]$ were confirmed. It can also be seen that the $BaSi_2$ template layer was formed in all samples by the RDE method. After MBE growth, a streak pattern indicating that the film was grown epitaxially when R_{Ba}/R_{Si} = 1.5-2.5. On the other hand, a halo pattern was observed in R_{Ba}/R_{Si} = 1.1, which

indicates that a vicinity of the grown film surface is amorphous. Spot patterns seen in R_{Ba}/R_{Si} = 3.0 and 3.6 suggests that their surface are rough.

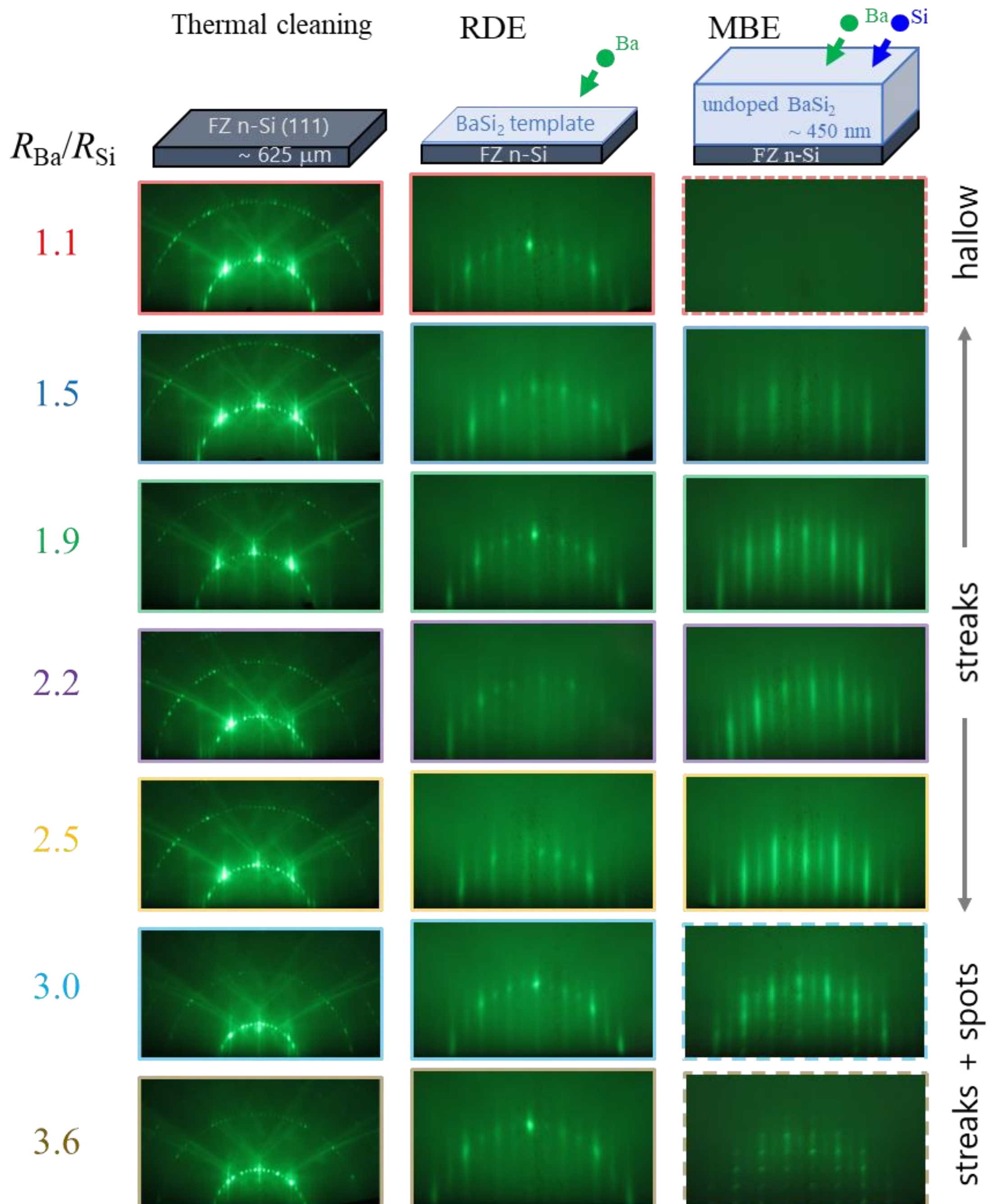

Fig. 4.1-1. RHEED patterns after TC, RDE, and MBE. The clear Si [1$\bar{1}$0] patterns on the Si substrate can be confirmed, indicating that the clean surfaces were obtained by TC in all samples. After the RDE, a clear streak pattern of $BaSi_2$ along Si [11$\bar{2}$] was observed in all samples, whereas after MBE growth, halo, streaks, and streak + spots patterns were observed depending on R_{Ba}/R_{Si}.

Streak RHEED patterns indicate epitaxial $BaSi_2$ films growth with flat surfaces.

Subsequently, all the films were evaluated using XRD. As shown in Figs. 4.1-2, the *a*-axis oriented $BaSi_2$ epitaxial thin-films were obtained in all samples. However, when R_{Ba}/R_{Si} = 1.1, the intensities of $BaSi_2$ (200) were weak by out-of-plane measurement, and any peak could not be confirmed by in-plane measurements. Furthermore, in the out-of-plane measurement, a peak from a precipitate in the film was confirmed at around 2θ = 32 deg. In the sample with R_{Ba}/R_{Si} = 3.6, the peak of $BaSi_2$ was confirmed, while the appearance of a peak from a precipitate in the film was also confirmed at 2θ = 24.5 deg by in-plane measurement. Figure 4.1-3 shows the lattice constant of each sample evaluated by XRD using the Nelson-Riley relationship.[122]

XRD results show all the films were grown epitaxitialy (*a*-axis-oriented).

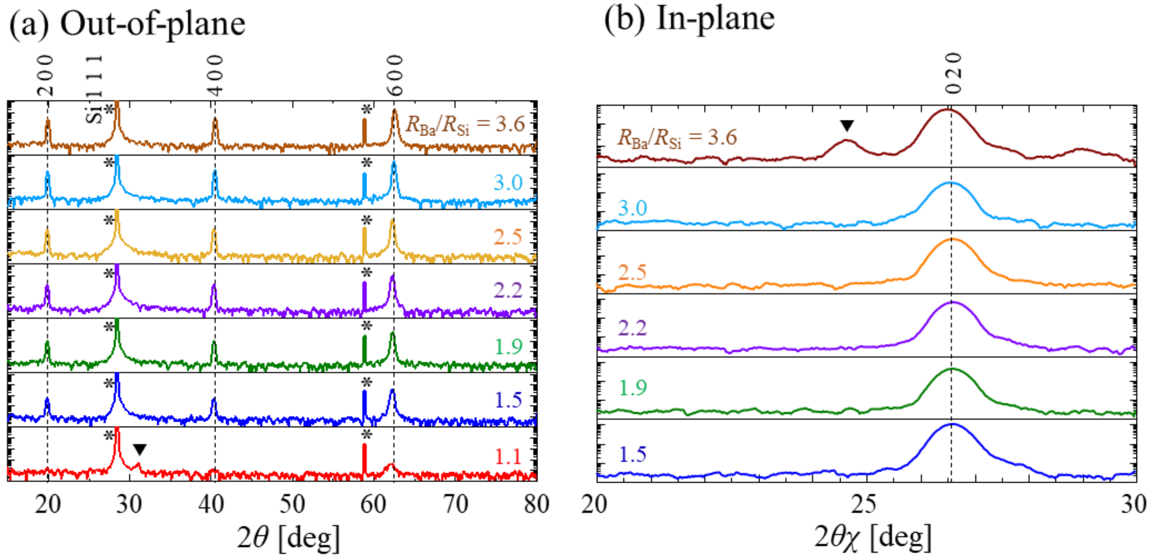

Fig. 4.1-2. (a) Out-of-plane and (b) in-plane XRD patterns. The a-axis oriented $BaSi_2$ epitaxial films (parallel to Si <111>) were formed. In the films with RBa/RSi =1.1 and 3.6, peaks from precipitates (▼) were observed.

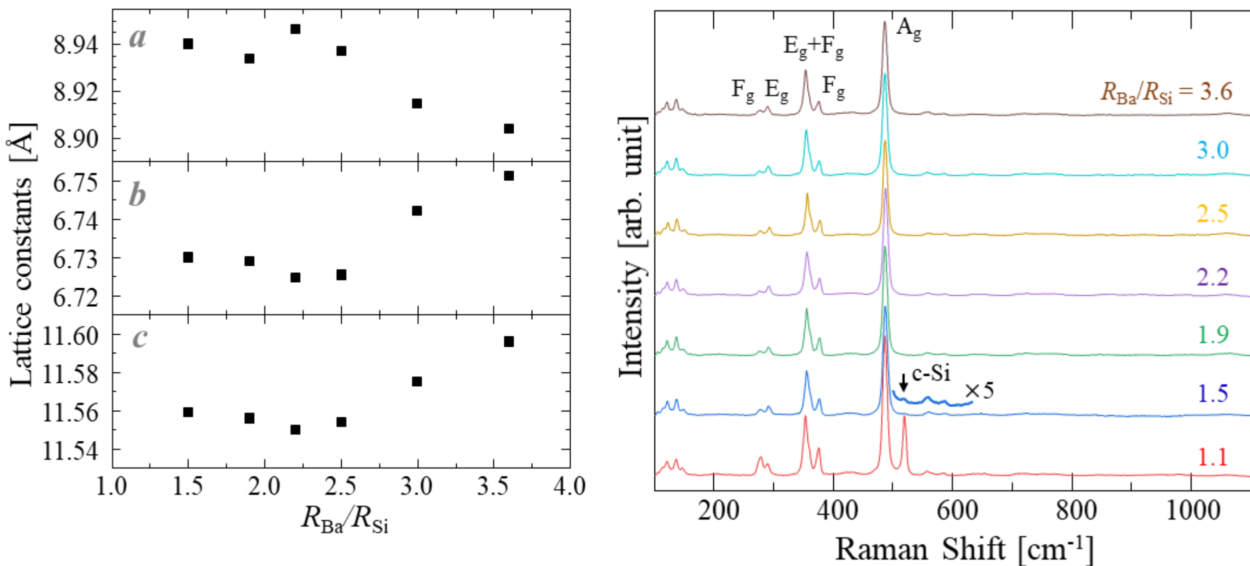

Fig. 4.1-3. The lattice constants (*a*, *b*, and *c*) of the films. Each constant was determined by the Nelson-Riley relationship.[122]

Fig. 4.1-4. Raman spectra of $BaSi_2$ epitaxial films. The peaks originated from Si_4 cluster were observed in the range of 250-500 cm^{-1}. The samples with R_{Ba}/R_{Si} = 1.5 and 1.1 are containing c-Si precipitation (Si TO phonon appers at 520.2 cm^{-1}).

Next, Raman spectra of the films are shown in Fig. 4.1-4. *In all the samples, the Raman spectra due to Si_4 tetrahedra constituting $BaSi_2$ were observed in a region between 250-500 cm^{-1}* with T_h symmetry in the lattice of $BaSi_2$.[96,123-127] On the other hand, at R_{Ba}/R_{Si} = 1.1 and 1.5, a Raman spectrum derived from c-Si precipitated in the film was observed at 520 cm^{-1}. The wavelength of the incident light used in this time was 532 nm, and considering the light absorption coefficient of $BaSi_2$, it can be said that these samples contained c-Si precipitated within 3α ~ 100 nm from the surface.[35]

Raman spectra also show growth of $BaSi_2$.

The atomic ratio of Ba and Si in the films were not evaluated by the Rutherford backscattering method, etc. However, from the previous reports, the atomic ratio closest to its stoichiometry was considered to be R_{Ba}/R_{Si} = 2.2.[51]

The point to be noted for thin-film samples used in this study are summarized below.

- **R_{Ba}/R_{Si} = 1.1**:
  Crystalline Si precipitate were detected within 100 nm from the surface. XRD results also showed the peak derived from the precipitate. The crystallinity was significantly worse than the other samples, and it is presumed that the vicinity of the surface was amorphous.
- **R_{Ba}/R_{Si} = 1.5**:
  Crystalline Si precipitate were detected within 100 nm from the surface, but not as bad as R_{Ba}/R_{Si} = 1.1. The crystallinity was considered to be relatively good from the RHEED pattern after MBE growth.
- **R_{Ba}/R_{Si} = 1.9-2.5**:
  Both surface condition and crystallinity were good. $BaSi_2$ single phase.
- **R_{Ba}/R_{Si} = 3.0**:
  After MBE growth, a spot pattern was confirmed, while no precipitate was confirmed by neither XRD nor Raman spectroscopy, suggesting that it was a $BaSi_2$ single phase.
- **R_{Ba}/R_{Si} = 3.6**:
  After MBE growth, a spot pattern was confirmed, and a peak derived from the precipitate was confirmed in XRD.

4.2. EPR spectra of $BaSi_2$ epitaxial films

For the measurements, the samples have been cut to pieces with typical dimensions of 20 mm × 2 mm × 0.0625 μm and were transferred into EPR tubes. The details of their size are listed in Table 4-3. These tubes were sealed under Ar atmosphere.

Table 4-3 The size of samples for EPR studies.

Label	R_{Ba}/R_{Si}	l (mm)	w (mm)	d (μm)	Volume (10^{-6} cm^{-3})
A	1.1	10.32	2.20	0.45	10.22
B	1.5	6.68	2.04	0.43	6.02
C	1.9	5.47 [4.12]	1.84 [1.66]	0.38	6.42
D	2.2	10.10	2.57	0.45	11.68
E	2.5	9.78	2.49	0.44	10.71
F	3.0	7.83	1.92	0.45	6.77
G	3.6	7.32	2.32	0.48	8.15
H	FZ-Si	9.71	2.00	(625)	12.14×10^3

Figures 4.2-1 shows the EPR line results for the sample with R_{Ba}/R_{Si} = 2.2, together with the result for the Si substrate measured as a reference. In EPR measurements, sample arrangements where the static magnetic field and the normal of the substrate surface (corresponding to the a-axis of $BaSi_2$ thin-film) are parallel is defined as 0 deg. The measurement were carried out by changing the angles at every 15 deg up to 90 deg where the static magnetic field and the a-axis are perpendicular (Fig. 4.2-1 (a)).

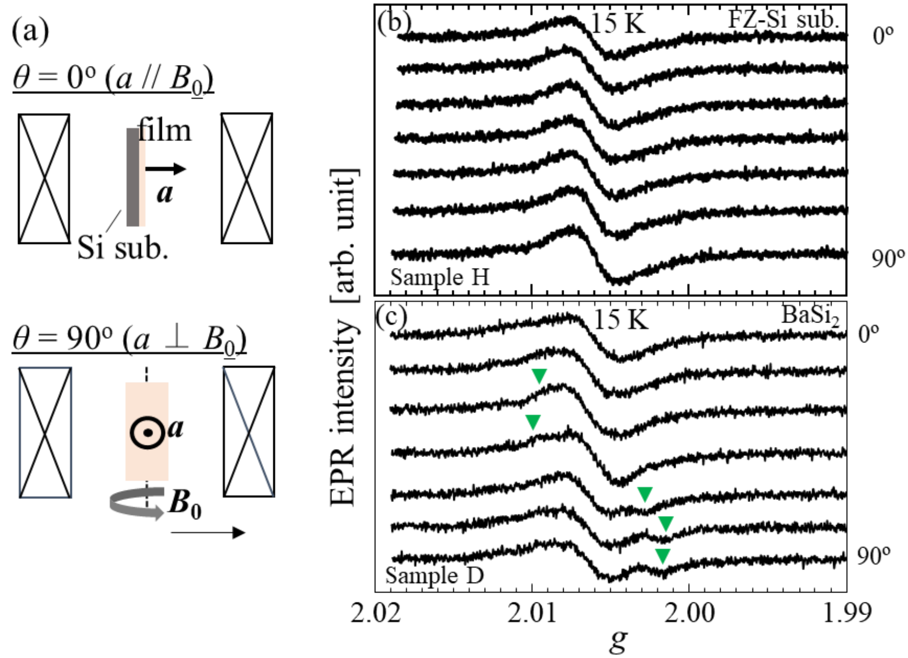

Fig. 4.2-1. (a) A schematic picture of sample arrangements. EPR spectra of (b) FZ-Si substrate and (c) $BaSi_2$ thin-films fabricated on the FZ-Si substrate. In the $BaSi_2$ films, anisotropic EPR lines were obserbed (marked as green triangles in figure) while only isotropic EPR line was observed in FZ-Si substrate.

I observed an isotropic EPR line from Si substrate with different angles. On the other hand, I observed *anisotropic* EPR lines with different angles, which was apparent at θ = 75 deg. In order to obtain a *g* profile of EPR lines from the $BaSi_2$ film, I reproduce the EPR spectra at all the angels, assuming three different Lorentzian derivatives. Figure 4.2-2(a) shows typical fitting results and Fig. 4.2-2(b) shows the fitting *g* value of each paramagnetic center as a function of the angle. One of these species corresponded to the isotropic line from the substrate (red line) while the two others (the Defects A and B, orange and blue lines, respectively) correspond to defects in the $BaSi_2$ film. At 20 K (Fig. 4.1-2(a)) the Defect B is easy to follow on the complete angular range and show a pronounced *g* anisotropy (from 2.003 to 2.010). The Defect A was more difficult to detect and its angular variation was more difficult to analyze. It must be noted that the Defect A and the Defect B anisotropy can be easily understood: even if $BaSi_2$ domains exhibit disordered *b* and *c* axes orientation in plane, all *a* axes are orientated perpendicular to the $BaSi_2$ epitaxial film.[61] Thus, it is possible to detect *g* variation in these systems with an angular dependence from a static magnetic field parallel to *a*-axis to a static magnetic field perpendicular to *a*-axis. This anisotropy is thus in complete agreement with the origin of these line corresponding defects in the $BaSi_2$ epitaxial film.

Regarding the EPR lines from the Si substrates, a large number of EPR lines have been reported.[128-136] However, it is sufficient to consider only P_b center,[130] E' center,[134] P_{s0} and P_{s1} centers,[135] and damaged Si-surface center[136] because FZ-Si(111) substrates were adopt in this work. Among them, it can be concluded that the EPR line observed from the Si substrate originates from damaged Si-surface centers because of its anisotropy and its *g* value.[136] These centers are caused by microcracks of a Si substrate on its cleavage planes. Note here that we did not observe P_b centers in the Si substrates used. P_b center is well known as a paramagnetic center caused by dangling bonds on Si surfaces. Present results indicate that the number of P_b center were too small to be detected.[130]

- Isotropic EPR line from Si substrate
- Additional anisotropic EPR lines for $BaSi_2$ paramagnetic defects.

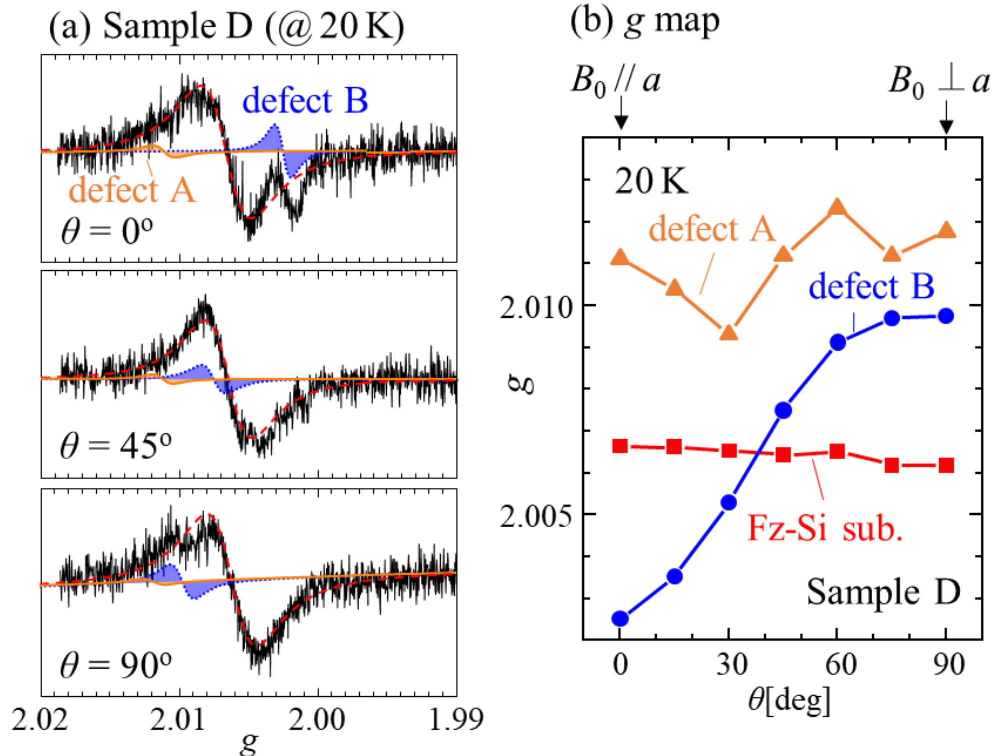

Fig. 4.2-2 (a) Angle dependent EPR spectra measured at 20 K on sample E at $\theta = 0$ deg (top), $\theta = 45$ deg (middle), and $\theta = 90$ deg (bottom). Red broken line, blue dot line, and orange solid line are fitting curve. (b) Variations of paramagnetic centers against B_0. Each origin is discussed in the text.

4.3. Temperature and microwave power dependences

To characterize the observed paramagnetic centers in the $BaSi_2$ films, I tried to decompose the lines which stem from the films from that of Si substrate. Since each paramagnetic center possesses different relaxation times (T_1: spin-lattice relaxation time, T_2: spin-spin relaxation time), I expected to separate each spectrum by changing either measuring at different temperatures or applied microwave power.

4.3.2. Temperature dependence

In order to separate the EPR lines of the $BaSi_2$ thin film from that of the Si substrate, the temperature dependence was measured at $P_{MW} = 1$ mW and $\theta = 0$ deg. As I shown in Fig. 4.3-1, the EPR line (red line) derived from the Si substrate and *the paramagnetic center (blue line) in the $BaSi_2$ thin-film clearly have different temperature dependences.* Because the paramagnetic center in the $BaSi_2$ thin-film is clearly observed in the high-temperature region, it is considered that the center in $BaSi_2$ has a relatively long relaxation time. On the other hand, the signal to noise (S/N) ratio decreased with increasing the temperature. Eventually, the two EPR lines could not be completely separated. In the subsequent measurements, the measurement was performed at $T = 15$ or 20 K in consideration of the separation of the EPR line in the $BaSi_2$ thin film and the S/N ratio.

Comfirmed $BaSi_2$ film: different temperature dependence behavior for Si substrate and $BaSi_2$ films.

- $BaSi_2$: high T → longer relaxation time
- Si : → shorter relaxation time

4.3.2. Microwave power dependence

In order to separate the EPR line from the $BaSi_2$ thin-film from that of the Si substrate, the microwave intensity dependence was measured at T = 10 K, θ = 0 deg. *The EPR line from the $BaSi_2$ film was clearly visible at low microwave power, while, at high microwave power, the line was buried at the foot of the EPR line from the Si substrate.* As with the temperature dependence, the EPR lines could not be separated by changing microwave power. However, from this experiment, it can be said that *the paramagnetic center in the $BaSi_2$ film is easily saturated compared with that from the Si substrate.* That is, it is presumed that a paramagnetic center having a relatively long relaxation time exists in the $BaSi_2$ thin film. This is consistent with the above-mentioned temperature dependence.

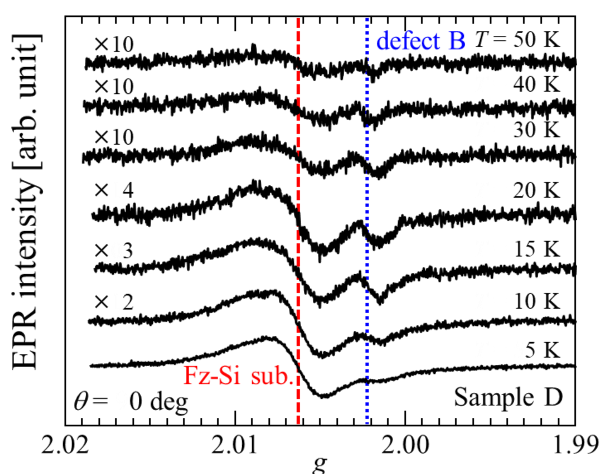

Fig. 4.3-1. Temperature dependence of the EPR spectra from 5 to 50 K at θ = 0 deg. The EPR line from the $BaSi_2$ films (blue dot line) seems to possess a reratively long relaxation time.

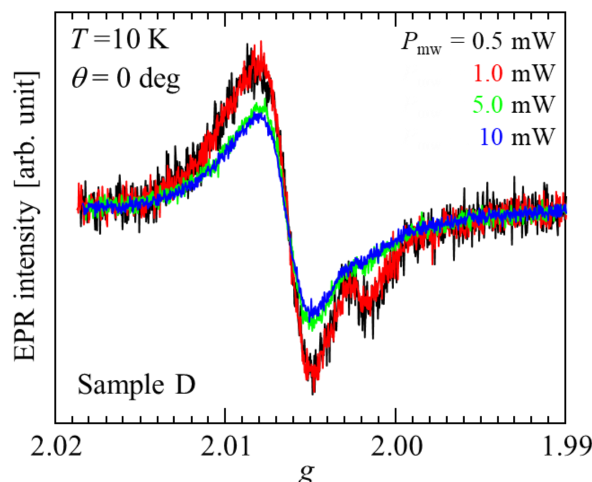

Fig. 4.3-2. Microwave power (P_{MW}) dependence of the EPR spectra recorded at 10 K with θ = 0 deg.

Comfirmed $BaSi_2$ film of paramagnetic defects – easily saturated

4.4. Multi-frequency EPR

Since each paramagnetic center is characterized by specific g value, EPR line will be separated under magnetic field due to Zeeman interaction. Therefore, I can expect that EPR lines originating from different centers are more separable at higher magnetic field (in other words, at higher microwave frequency).[137-140]

Q-band

First I performed EPR experiments by using around 34 GHz (Q-band). A ratio to X-band is 34/9.7 ~ 3.5. Hence, in an ideal case (width of its line is enough narrow),[138] resolution of spectra can be improved. Figure 4.4-1(a) shows the result of cw-Q-band, performed on the same sample as that measured in the X-band. Due to the overlap with the signal from EPR tube, it was not possible to determine whether the EPR line from the $BaSi_2$ thin film could be observed. Since the signal from the tube is considered to be the color center (E') in SiO_2,[134] I annealed the the EPR tube overnight. As a result, the E' center decreased as I show in Fig. 4.4-1 (b). However, even after annealing,

a slight EPR line (▼) was observed from the tube. Although the origin of this signal is unknown, it is suggested that it has an hyperfine structure with Mn^{2+} indicated as stars (*) in the Fig. 4.4-1(b). Figure 4.4-2 shows the results of measuring the EPR spectra of the $BaSi_2$ thin-film and the Si substrate using the annealed EPR tube. The observed EPR line from the $BaSi_2$ films in the X-band could not be confirmed in the Q-band. This is due to the fact that the sample size in a Q-band tube (inner diameter ~ 1 mm) should be decreased to about one-fifth of that in the X band.

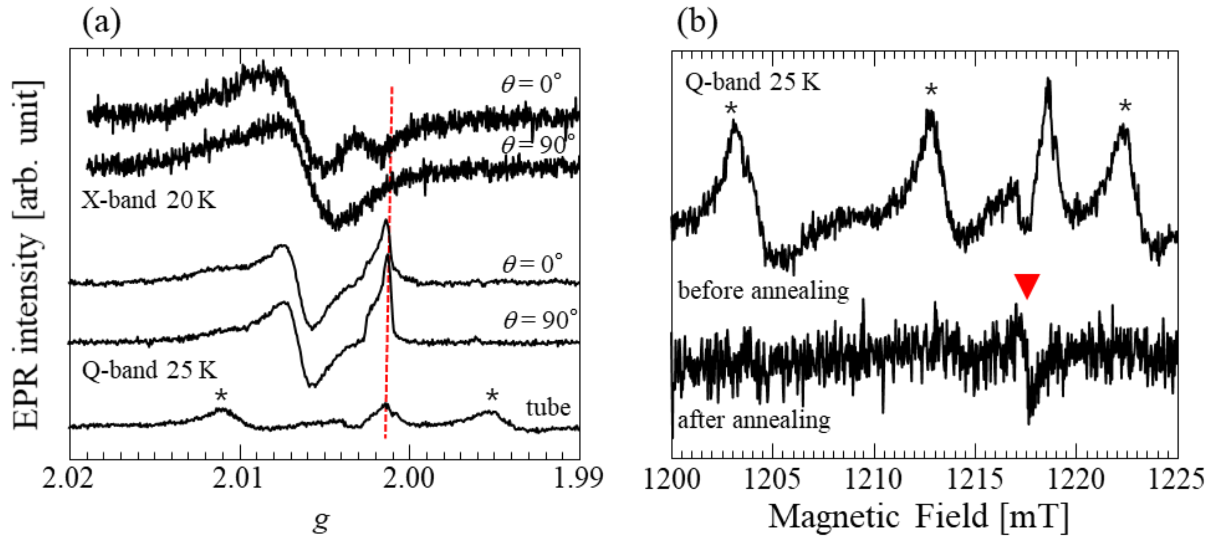

Fig. 4.4-1. (a) EPR spectra observed in X-band and Q-band of $BaSi_2$ thin-film. In the Q-band, the E' center in the EPR tube (red dotted line) was observed at the position where the EPR line from $BaSi_2$ thin-film was expected. (b) EPR spectra of Q-band EPR tubes before annealing and after annealing at $T = 1000$ °C over night. Because of annealing, the E' center decreased. However, another signal indicated by ▼ in the figure remained even after annealing. In addition, this signal is considered to have hyperfine structures with Mn^{2+} (marked as *).

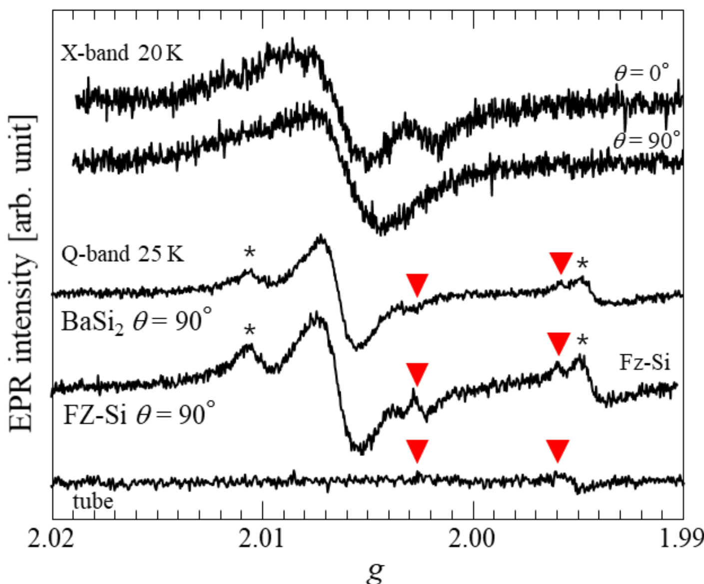

Fig. 4.4-2 The EPR spectra of $BaSi_2$ film, FZ-Si substrate, and the annealed EPR tube. Even after annealing the tube, a few paramagnetic centers (▼) remained.

The EPR lines of $BaSi_2$:

- ✓ visible by cw-X-band
- ✓ not visible by cw-Qband (due to sensitivity)

High-field (high frequency)

In order to increase its resolution, I also performed EPR measurements under high-field (high-frequency) in which the recorded signal is the absorption of the light delivered by on optically-pumped far infrared waveguide laser providing emission lines at several wavelengths between 570 μm and 2mm. In this setup, since no resonator is used, it is possible to pile the samples.[139-141] The samples were cut to typically 2×2×2 mm and put into a tube with teflon tube which suppress for samples to move during the measurements as shown in Fig. 4.4-3(a). Figure 4.4-3(b) shows results of the high-field EPR measurements on the $BaSi_2$ films and the only Si substrates using a microwave frequency of 225.36 GHz. Since no resonator is used, there is no resonant magnetic field sample position. Instead of that, since the measurement is performed in a high magnetic field, the spin polarization should be higher. As a result, in principle, the same sensitivity as in X- and Q-band measurement using a resonator can be expected. The EPR line can be confirmed at g ~ 2. However, due to the convolution of the EPR derived from the Si substrate and the signal of Mn^{2+} contained probably in the Si substrate as natural abundance, *the EPR line from the relatively small amount of the BaSi₂ films could not be observed.*

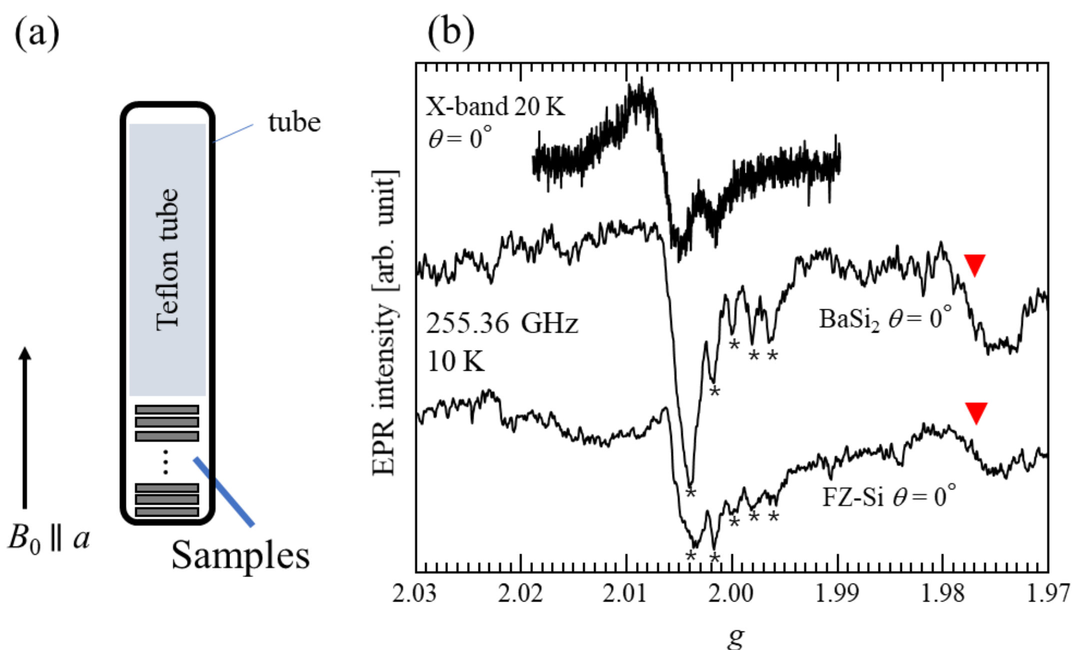

Fig. 4.4-3 (a) A schematic image of a sample arrangement. A static magnetic field is applied to the direction parallel to a-axis of the films, which direction corresponds to $\theta = 0$ deg in X- and Q-band. The samples are sealed under Ar atmosphere together with a teflon tube. The teflon tube prevent the samples from vibrations during the measurements. (b) EPR spectra of the $BaSi_2$ films and FZ-Si substrates recorded at 10 K with 255.36 GHz of microwave frequency. Hyperfine structures with Mn^{2+} were observed in addition to the EPR line from the Si substrates. The red triangle indicates another center from the tube.

No EPR line obtained for $BaSi_2$ film at very high field (255.36 GHz)

4.4. Effect of deposition ratio during film growth

In recent years, theoretical calculation results have reported that different defects may be formed in $BaSi_2$ (See Figs. 2.5-8 and -9)[106]. In addition, our previous studies have found that the difference in the deposition rate ratio of Ba to Si (R_{Ba}/R_{Si}) during the MBE growth affected the electrical and optical characteristics.[95,101] Assuming that different defects are generated due to the different R_{Ba}/R_{Si}, observation of different EPR spectra (different g values) are expected. Therefore, the measurements performed on the $R_{Ba}/R_{Si} = 2.2$ thin-film were carried out on other samples with various values of R_{Ba}/R_{Si} (Fig. 4.5-1). In the films with $R_{Ba}/R_{Si} = 1.9$, 2.5, and 2.9, *anisotropic EPR lines were observed*, while relatively isotropic EPR lines were observed in the others.

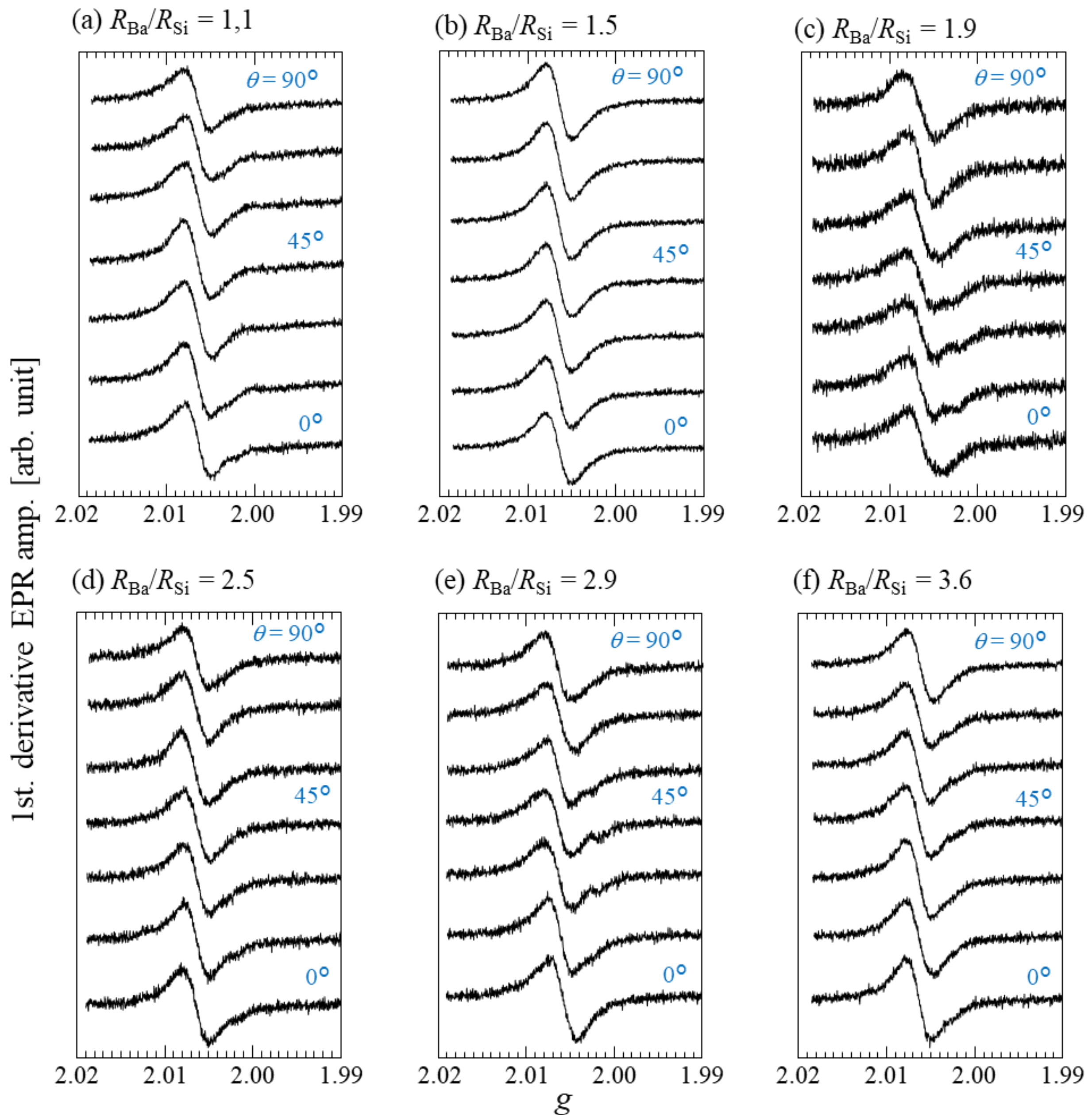

Fig. 4.5-1. Angular dependence of EPR spectra of films with various R_{Ba}/R_{Si}. The measurements were carried out in the same condition as that in $R_{Ba}/R_{Si} = 2.2$ as I already described in section 4.2.

To understand these results, I evaluated their number of spins (N_{spin}). In this study, I used TEMPO with various concentrations (~ 10^{-1}-10^{-5} mol/L) as references (see section 5.4 for the details of analysis). As I discussed in the section 4.2, the EPR line from the substrate was considered to originate from the paramagnetic center at their cleavage faces.[136] Therefore, I estimated contributions of the substrates from their cleavage faces and subtracted them from the N_{spin}. Evaluated N_{spin} are listed in Table 4-4 and plotted as a function of R_{Ba}/R_{Si} in Fig. 4.5-2. As can be seen from Fig. 4.5-2, *the estimated N_{spin} was minimum at R_{Ba}/R_{Si} = 2.2, where is considered to be the most stoichiometric.* Since the intensity of the EPR line is proportional to the number of unpaired electrons, it is expected that the number of defects is smallest when $R_{Ba}/R_{Si} = 2.2$. At R_{Ba}/R_{Si} = 1.1 and 3.6, the precipitates were confirmed in the section 4.1, which is presumed to be the reason for the different tendencies in the EPR line intensity.

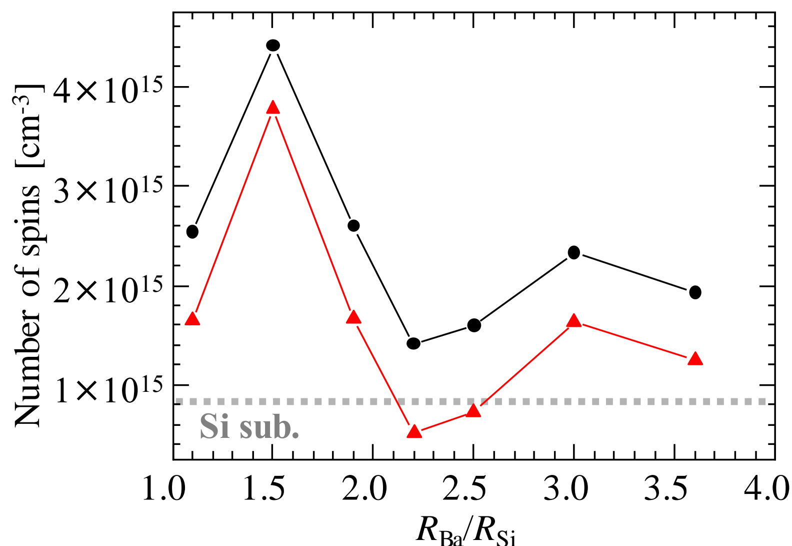

Fig. 4.5-2 A number of spins (assumed $S = 1/2$) per cubic centimeter. The experimental values (black) is re-evaluated by subtracting the contribution of the Si substrate based on the discussion in section 5.4.

Table 4-4 Number of spins in each film.

Label	R_{Ba}/R_{Si}	Volume (10^{-6} cm^{-3})	Surface area of cleavage face(10^{-2} cm^2)	Total number of spins (spins/cm^{-3})	Estimated number of spins (spins/cm^{-3})
A	1.1	10.22	15.65	2.54×10^{15}	1.65×10^{15}
B	1.5	6.02	11.11	4.41×10^{15}	3.78×10^{15}
C	1.9	6.42	16.36	2.60×10^{15}	1.47×10^{15}
D	2.2	11.68	15.84	1.42×10^{15}	5.17×10^{14}
E	2.5	10.71	15.34	1.60×10^{15}	7.30×10^{14}
F	3.0	6.77	12.19	2.33×10^{15}	1.63×10^{15}
G	3.6	8.15	12.05	1.93×10^{15}	1.24×10^{15}
H	FZ-Si	12.14×10^3	14.64	8.34×10^{15}	-

✓ Minimal number of spins near stoichiometry

✓ Maxima for R_{Ba}/R_{Si} = 1.5 (Si-rich)

= 3.0 (Ba-rich)

4.5. Effect of atomic hydrogen into $BaSi_2$ film

According to our results, an introduction of atomic hydrogens (H) into a $BaSi_2$ thin-film significantly improves photoresponsivity.[142,143] Therefore, the EPR measurement was also performed on the film into which atomic hydrogen (H) was introduced. Atomic H produced by a radio-frequency plasma gun was supplied for 15 min after MBE growth of the $BaSi_2$ layer in the chamber, and EPR spectrum was measured in the same conditions as that without H. In the sample into which H was introduced, the EPR line of the Defect B in Fig. 4.2-2 was decreased as seen in Fig. 4.6-1(a).

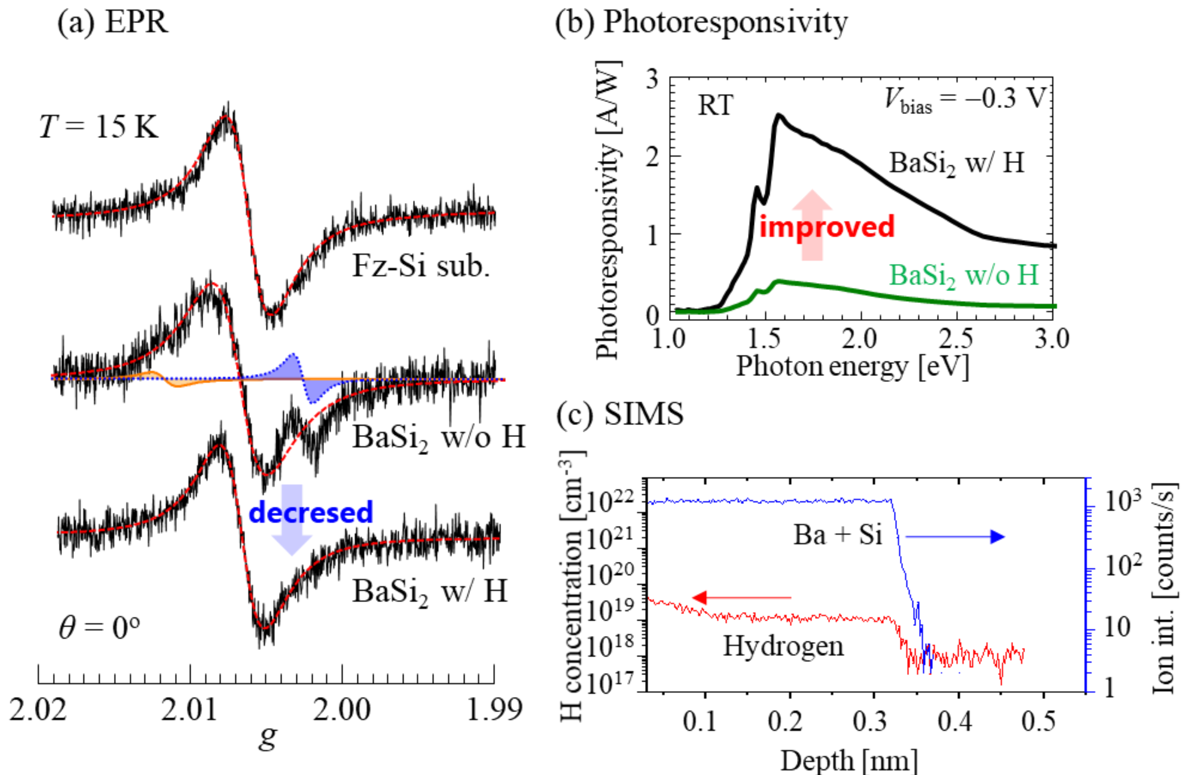

Fig. 4.6-1. (a) X-band EPR spectra recorded at 15 K on FZ-Si substrate, $BaSi_2$ film without and with atomic hydrogen (H). The decrease of the EPR line of the Defect B was confirmed. (b) Photoresponsivity was drastically improved on the film with H. (c) SIMS result indicates that the supplied H are introduded only into the films.

It is considered that *Si vacancy is most likely to be formed as an intrinsic defect in $BaSi_2$* thin-film. In fact, vacancies were found in our thin-films made with different R_{Ba}/R_{Si} by positron annihilation spectroscopy.[97,99] It is well known that hydrogens deactivate Si dangling bonds (what are called P_b centers), resulting in a decrease of the corresponding EPR line after introduction of hydrogen in crystalline Si.[144,145] Therefore, it can be inferred that the *hydrogens similarly deactivated some defects*, probably vacancies Si, in the $BaSi_2$ film.[146] In addition to the EPR results, the significant improvement on photoresponsivity was confirmed on the film with H (Fig. 4.6-1(b)). A result of secondary ion mass spectrometry (SIMS) seems to support my interpretation because I confirmed the introduction of H into the $BaSi_2$ film as I show in Fig. 4.6-1(c).

Introduction of atomic H:
- ✓ Improved photoresponsivity
- ✓ Deactivated defects

4.6. Summary

I observed different paramagnetic centers in a Si substrate and $BaSi_2$ epitaxial films as I listed below.

The Defect A in $BaSi_2$ film : 2.010-2.013
The Defect B in $BaSi_2$ film : 2.003-2.010 (anisotropic)
Paramagnetic center from Si substrate on its cleavage planes. : isotropic

To characterize the paramagnetic centers in $BaSi_2$, I performed multi-frequency EPR measurements. However, no obvious EPR signal for $BaSi_2$ was obtained. This is probably because the amount of the paramagnetic center is too low to detect. In addition, judging from the microwave power and temperature dependencies, the paramagnetic centers in $BaSi_2$ are considered to have longer relaxation times. As a result, the observations were difficult at Q-band and high field. On the other hand, the EPR measurements for w/ and w/o atomic H revealed that the Defect B is likely to affect photoresponsivity.

Chapter 5 EPR study on $BaSi_2$ bulk

In chapter 4, I successfully observed the EPR lines from the $BaSi_2$ thin-film for the first time, suggesting that the observed EPR lines may be closely related to the photoresponsivity based on the research on the effect of atomic hydrogens. In order to identify the origin of this EPR lines, it is strongly required to separate them from the EPR lines derived for the Si substrate. Therefore, I tried to separate each EPR line by means of various EPR techniques such as multi-frequency EPR measurements, etc. Unfortunately, all the trials failed. This was because $BaSi_2$ is too sensitive toward moistures to perform wet etching for removals of the paramagnetic center of Si substrate.[147] The electrically detected EPR (EDMR) might be one of the solutions because the EDMR has much better sensitivities for the defect detections.[148-152] On the other hand, further complicating the study is the lack of EPR studies on $BaSi_2$. Therefore, we decided to conduct EPR measurements on bulks to get insights on intrinsic defects of $BaSi_2$ bulks, first of all.

5.1. Powder

First, we performed EPR on powder samples. Compared to single crystals, the powder samples can only provide principal values of EPR parameters, such as g-tensors and/or hyperfine tensors. However, because it is relatively easy to prepare and the volume can be increased, it is considered to be the best as a first step of EPR studies in $BaSi_2$. In addition, by appropriately changing the composition ratio of Ba and Si during sample preparation, it is possible to systematically investigate the effects of the composition ratio on defect formation. The primary goal is to take a bird's-eye view of intrinsic defects in $BaSi_2$.

5.1.1. Samples

Polycrystalline $BaSi_2$ bulk samples were provided by Dr. Imai (NIMS) and Mr. Mesuda (Tosoh Corp.). All the samples were prepared by Ar–arc melting of 1 : x_s (x_s = 2.10, 1.90, 2.06, 2.00, 1.94, and 1.88) molar mixture of Ba (3N, Furuuchi Chem. Corp.) and Si (10N, Furuuchi Chem. Corp.). The chemical compositions of synthesized polycrystalline samples were determined by inductively coupled-plasma optical emission spectroscopy (ICP-OES). Table 5-1 lists the Si–to–Ba ratio of the starting materials x_s and that of synthesized samples (N_{Si}/N_{Ba}).

Table 5-1 Atomic ratio of powder samples. Actual values were determined by ICP-OES.

Label	I	J	K	L	M	N
Starting material Ba : Si = 1 : x_s	2.10	1.90	2.06	2.00	1.94	1.88
$x = N_{Si}/N_{Ba}$	2.404	2.087	2.134	2.054	1.987	1.916

Hereafter, from the viewpoint of composition ratio of Ba and Si, I divide 6 different samples into 2 following groups.

Group1: Si-rich ($x > 2.00$)

Group2: Ba-rich ($x < 2.00$)

I note that samples I and J and samples K–N were provided by different research groups. Table 5-1 shows the order different from N_{Si}/N_{Ba} obtained by ICP-OES based on the results of EPR and photoluminescence described later.

Figures 5.1-1 shows XRD powder patterns of samples I-N. Focusing on the region between 2θ = 40-60 deg (Fig. 5.1-1(b)), the observed patterns are in well agreements with previous reports.[88,90] Thereby, I confirmed that *$BaSi_2$ was obtained in all samples*. However, in Sample I, which is the most Si-rich, extra peaks derived from crystalline Si (c-Si) were observed at 2θ = 47.5 deg and 2θ = 56 deg. It is inferred that the composition ratio $BaSi_2$ of Sample I is smaller than the value obtained by ICP-OES due to the amount of Si precipitated. Similarly, in sample N, which is the most Ba-rich sample, a peak of a precipitate (judging from the phase diagram,[27] probably Ba_3Si_4[31]) was observed at 2θ ~ 48 deg as shown by a triangle (▼) in Fig. 5.1-1 (b).

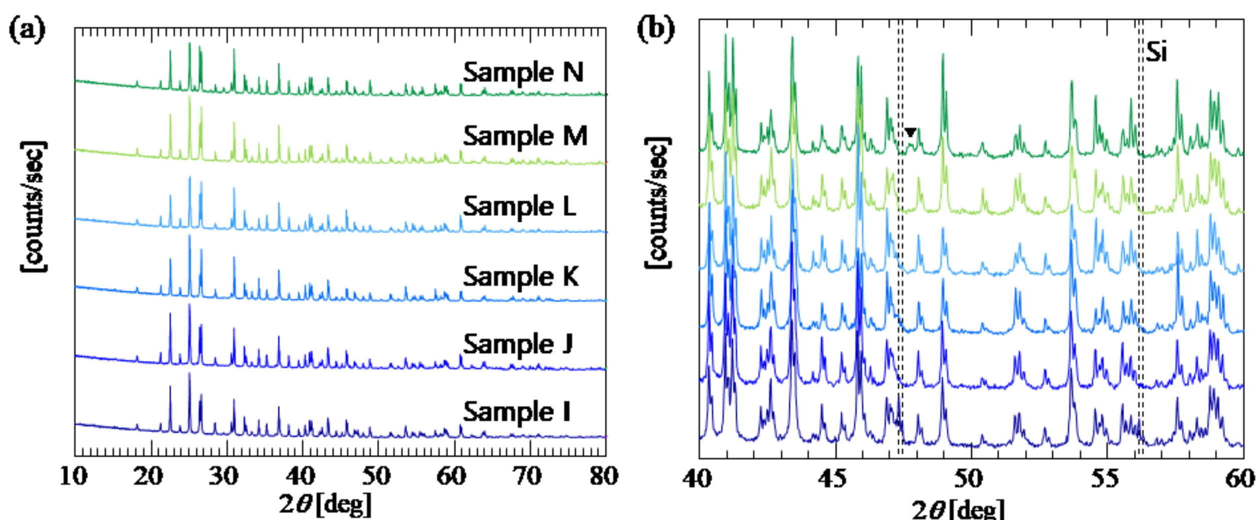

Fig. 5.1-1 (a) Powder XRD pattern of sample I-N. (b) Enlarged the results of (a) between 2θ = 40-60 deg. In sample I, at 2θ = 47.5 and 56 deg, the peaks of crystalized Si were observed. In sample N, the peak of precipitation (probably Ba_3Si_4[31]) was confirmed at 2θ = 48 deg (as shown as a triangle, ▼).

$BaSi_2$ was obtained for all samples

✓ Some crystalline Si (I) or precipitate Ba_3Si_4 (N) were observed in extreme conditions.

5.1.2. Effect of composition ratio of Ba and Si

Polycrystalline $BaSi_2$ were powdered by using an agate in a glove box in order to avoid the generation of new defects due to a reaction with moistures and oxygens in the air. Then, the powdered samples were put into X-band tube (inner diameter is 3 mm) and Q-band tube (Inner diameter is 2 mm) to a height of approximately 1 cm, and sealed in a glove box.

cw-X- and Q-band spectra

Figure 5.1-2(a) shows the powder cw-EPR spectrum measured at ν ~ 9.7 GHz (X-band), P_{MW} = 0.005-0.02 mW, and T = 10 K. Table 5-2 shows more detailed measurement conditions. Figure 5.1-2(b) shows the powder cw-EPR spectrum measured at ν ~ 34 GHz (Q-band), $P_{MW} = 5\times10^{-2}$ mW, and T = 15 K. More detailed measurement

conditions are shown in Table 5-3.

Pulse-X- and Q-band spectra

Electron spin echo-detected field-swept spectra were mesured using pulse sequence: t_p-τ-2t_p-τ-echo. Figure 5.1-3(a) shows the powder pulse-EPR spectrum measured at ν ~ 9.7 GHz (X-band) at T = 10 K. More detailed measurement conditions are shown in Table 5-4. Figure 5.1-3(b) shows the powder pulse-EPR spectrum measured at ν ~ 34 GHz (Q-band) at T = 8 K. More detailed measurement conditions are shown in Table 5-5.

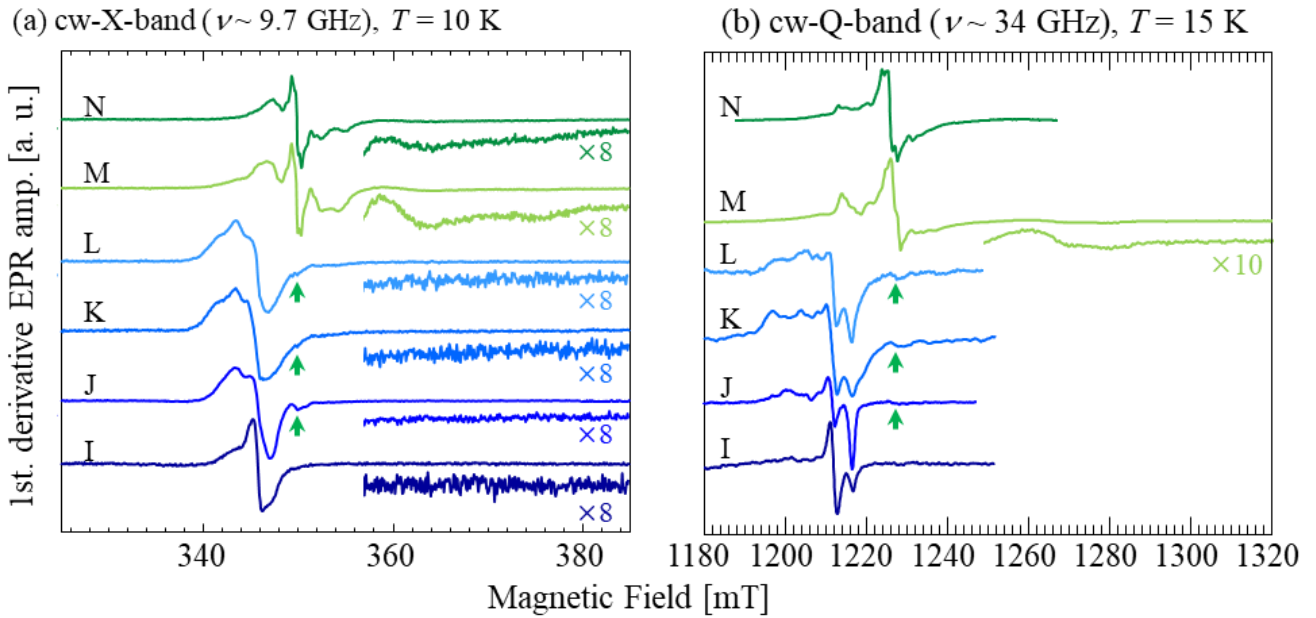

Fig. 5.1-2 EPR spectra of Samples I-N measured in (a) cw-X-band at 10K and (b) cw-Q-band at 15K. The EPR line observed in Ba-rich sampes are contained in Si-rich samples (green arrows in the figure).

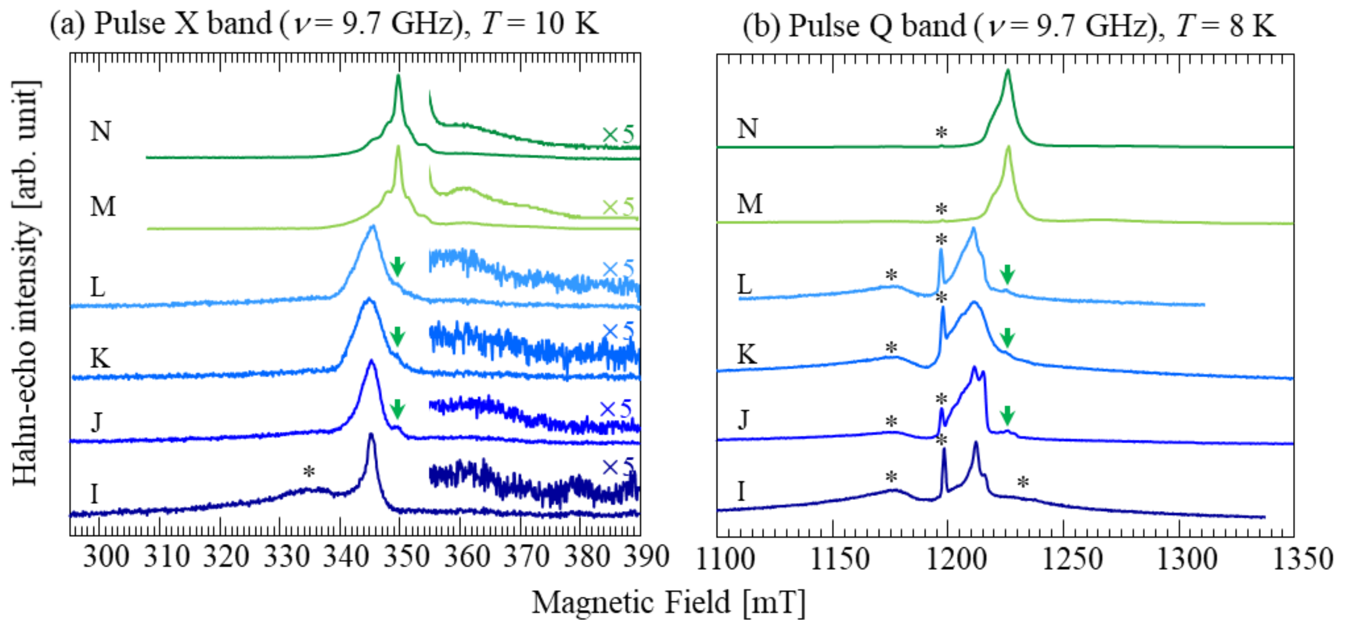

Fig. 5.1-3 EPR spectra of Samples I-N measured in (a) pulse-X-band at 10K and (b) pulse-Q-band at 8K. The EPR line observed in Ba-rich sampes are contained in Si-rich samples (green arrows in the figure). In the pulse measurements, some spectra from the cavity were observed as I marked by stars (*) in the figures.

Table 5-2 Experimental conditions of cw-X-band. The Q value of the cavity, the microwave frequency (ν_{MW}) in MHz, the microwave power (P_{MW}) in mW, the modulation frequency (ν_m) in kHz, the modulation amplitude (B_m) in mT, the time constant (TC) in msec, the conversion time (CT) in msec, the accumulations, and the receiver gain (R.G.) are listed.

Label	Q	ν_{MW}	P_{MW}	ν_m	B_m	TC	CT	acc	R.G.
I	2100	9.6526	2×10^{-2}	100	0.2	81.92	163.84	74	5×10^{5}
J	4000	9.6556	$5\times1\ 0^{-3}$					82	
K	4300	9.6571						60	
L		9.6554						100	
M		9.6554			0.05			51	
N	2500	9.6536						51	

Table 5-3. Experimental conditions of cw-Q-band. The Q value of the cavity, the microwave frequency (ν_{MW}) in MHz, the microwave power (P_{MW}) in mW, the modulation frequency (ν_m) in kHz, the modulation amplitude (B_m) in mT, the time constant (TC) in msec, the conversion time (CT) in msec, the accumulations (acc) , and the receiver gain (R.G.) in dB are listed.

Label	Q	ν_{MW}	P_{MW}	ν_m	B_m	TC	CT	acc	R.G.
I	N/A	34.1310	5×10^{-2}	100	0.25	83.89	81.92	79	60
J		33.9209						20	
K		33.9310						81	
L		34.0177						25	
M		33.9129						9	
N		34.0560						24	

Table 5-4. Experimental conditions of pulse-X-band. The microwave frequency (ν_{MW}) in MHz, the microwave pulse power (P_{MW}) in mW, the details of the pulse sequence: t_p [nsec] – τ [nsec] – $2t_p$ [nsec] – τ – echo, the detection window of the echo [nsec], the pulse shot reputation time of the sequence (srt) in msec, the accumulations, and the video gain for the pulse detection (V.G.) in dB.

Label	ν_{MW}	P_{MW}	t_p	τ	window	srt	acc	V.G.
I	9.6970	6.69×10^{-1}	16	200	200	20	130	51
J	9.6971	6.76×10^{-1}						45
K	9.6970	6.70×10^{-1}						51
L	9.7012	2.12×10^{-4}					135	48
M	9.6957	2.12×10^{-4}					45	27
N	9.7014	2.11×10^{-4}					20	24

Table 5-5. Experimental conditions of pulse-Q-band. The microwave frequency (ν_{MW}) in MHz, the microwave pulse power (P_{MW}) in mW, the details of the pulse sequence: t_p [nsec] - τ [nsec] - $2t_p$ [nsec] - τ - echo, the detection window of the echo [nsec], the pulse shot reputation time of the sequence (srt) in msec, the accumulations, and the video gain for the pulse detection (V.G.) in dB.

Label	ν_{MW}	P_{MW}	t_p	τ	window	srt	acc	V.G.
I	33.8247	6.69×10^{-1}	16	200	200	20	75	33
J	33.4878	6.76×10^{-1}					20	24
K	33.6412	6.70×10^{-1}					25	27
L	33.5439	2.12×10^{-4}					20	24
M	33.5304	2.12×10^{-4}					5	30
N	33.5280	2.11×10^{-4}					20	6

General comparison

For comparison of the EPR spectra, cw- and pulse-EPR spectra of each sample plotted against magnetic field and g are shown in Appendix B (Figs. B-1 and B-2, respectively.) Here, pseudo-modulation differential were carried out to the pulse-EPR spectra for the comparison. As is clear from the comparison of the g values in Fig. B-1 and Fig. B-2, dominant EPR spectra were observed at different positions in the Si-rich samples and the Ba-rich samples. In the Si-rich samples, the average g value (g_{av}) of the dominant EPR line is greater than 2. On the other hand, in the Ba-rich group, the dominant EPR line were observed at $g_{av} < 2$. As shown by the green arrows in Figs. 5.1-2 and 5.1-3, it can be confirmed that a slight amount of those observed in the Ba-rich samples were formed even in the Si-rich sample. Figure 5.1-4 (a) shows the superimposed cw-X-band spectra of samples M and N recorded at 50 K. It can be seen that the two spectra agree well at $g < 2$ or less. On the other hand, the spectrum is slightly different at $g > 2$. Figure 5.1-4(b) shows the difference between samples M and N. From Fig. 5.1-4(b), it is inferred that the sample M has a small amount of a different paramagnetic center having $g_{av} > 2$, which seemed to correspond to the dominant center in the Si-rich group from the comparison of the g values. Thus, I concluded that the defects from different origins were likely predominant in the Si-rich and the Ba-rich samples, whose threshhold seemed to be at their stoichiometric ratio (i.e., $x = 2$).

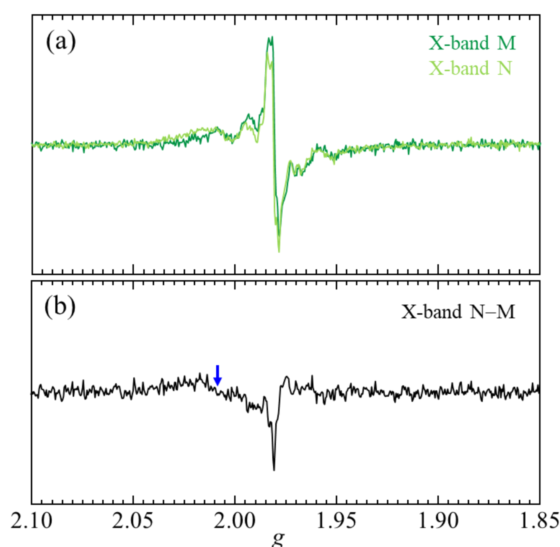

Fig. 5.1-4 (a) EPR spectra of Sample M and N recorded with X-band frequency at 50 K. (b) A Subtracted spectrum (Sample N – Sample M). I speculated that a line placed at blue arrow corresponded to that observed in Si-rich samples.

- Si-rich samples → $g_{av} > 2$ (I-L)
- Ba-rich samples → $g_{av} < 2$ (M and N)

Threshold is stoichiometric ratio

5.1.3. T_1 and T_2 measurements

The observed powder spectra were very broad. In particular, in Si-rich samples, it is hard to think that the powder spectra were caused by only one g-tensor. Since the relaxation time generally differs at each paramagnetic center, T_1 and T_2 were measured and compared at characteristic positions of the spectra (Appendix, Figs. B-3-8.). T_1 and T_2 were each performed at 8K using the pulse sequence shown in Fig. 5.1-5.

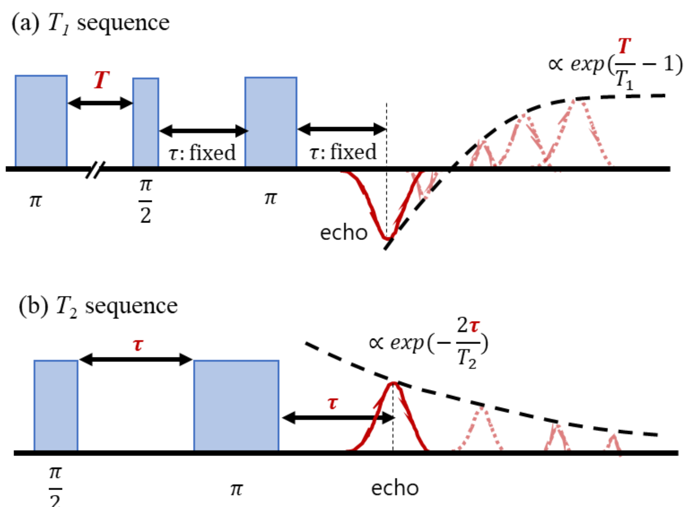

Fig. 5.1-5. Pulse sequences to measure (a) T_1 and (b) T_2. In the T_1 sequence, the fist pulse are used to invert the spins. Hahn-echo detection was adopted after a varibale delay time T (so called inversion recovery method). In the T_2 sequence, Hahn echo intensity is recorded with changing interval between detection pulses τ.

T_1 and T_2 can be fitted by following equations in ideal cases.[153,154]

$$T_1 = \sum_i S_0^{(i)} \left[2 \times exp\left(\frac{T}{T_1^{(i)}} - 1 \right) \right]$$

$$T_2 = \sum_i S_0^{(i)} exp\left\{ -\frac{2\tau}{T_2^{(i)}} \right\}$$

where, the subscript i indicates the number of different paramagnetic centers.

About analyses of T_1 measurements, it was difficult to fit correctly using the above equation. This is because the sample used here were powders and the line width of the EPR spectra was broad because of their inhomogeneity. Microwave pulses cause only ESR transitions and do not contribute to NMR transitions in principle. However, since amplitudes of the irradiated microwave pulse are strong, the surrounding nuclei are flipped after the irradiation of the pulses. The electron spin existing around the flipped nucleus can feel such effect, so the Larmor frequency of the electron spins changes slightly. Such a phenomenon is called the spectral diffusion[155] and makes it difficult to analyze the relaxation time in the measurement of a sample having an inhomogeneous line width. As a result, normalized Hahn-echo intensities didn't reach to −1 even at $T \sim 0$ μs regardless that the electron spins were inverted by using π pulse as I could observe in Fig. B-3-8,. For the above reasons, T_1 summarized in Table 5-6 are provisional values, which were estimated by fitting the result following the above equation.

Next, I analyzed T_2 according to the following procedure. Figures 5.1-6 shows the result of Q-band of Sample K at 1209 mT (which corresponded to $g \sim 2.010$) as an example. All the results are listed on Table 5-6.

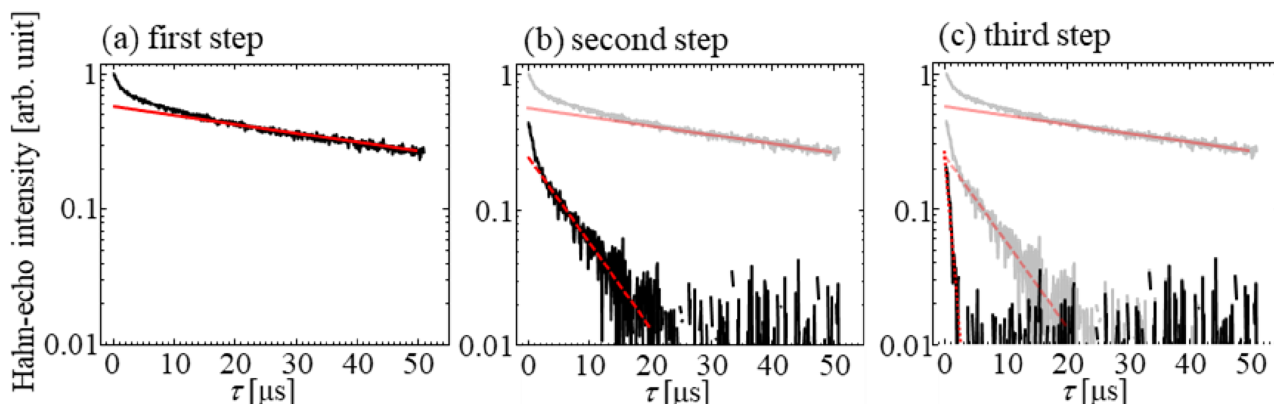

Fig. 5.1-6 The procedures of T_2 analysis.

[Procedures]

i. The result normalized by its maximum value is semilogarithmically plotted with respect to τ, and a linear region is fitted with the component having the longest T_2 using the above equation (i = 1) (Fig. 5.1-6(a)).

ii. Subtract components fitted in the procedure i from the measurement results. The linear area resulting from the subtraction is fitted in the same way as the procedure i. (Fig. 5.1-6(b)).

iii. The same procedure as in the procedure ii. (Fig. 5.1-6(c)).

As it is clear from Table 5-6 and 5-7, the *at least two deffent relaxation mechanism* are needed to explain the results, suggesting that each sample contains a few paramagnetic centers. In the tables, I marked stars (*) at the positions observed signals from the cavity. Especially, in the Si-rich samples, it made the measurements difficult. For the future works I note that our Q-band cavity contains paramagnetic centers with long T_1 at the possision with g ~ 2.028 while I didn't listed the value on the table. Although the relaxation times depend on spin concentration, it will be useful for the following discussions to evaluate T_1 and T_2 of each paramagnetic center relatively, based on the positions where a few relaxation times are observed. In the Si-rich samples, relaxation times reached minimum at the postion observed the narrower line (g ~ 2.005) except for those oberved the signal from the cavity. In the Ba-rich samples, the broader line (more visible at $g < 1.93$) has show shorter T_2. I also determined the initial pulse sequences for hyperfine spectroscopy experiments as I described in the next section.

Different relaxation times by one-two order of magnitude

✓ Different paramagnetic centers

Table 5-6 Fitted results of T_1. The stars (*) indicate positions observed signals from the cavity.

Sample		**2.138***	**2.063 - 2.070***	**2.036**	**2.017 - 2.028**	**2.004 - 2.010**	**1.998**	**1.981 - 1.984**	**1.913 - 1.921**
T_1 [μs]									
I	X	63.6 ± 23.1	51.6 ± 30.1 486 ± 107	—	—	29.0 ± 5.0 574 ± 29.7	—	—	—
	Q	—	—	—	—	16.8 ± 1.9 121 ± 8	—	—	—
J	X	—	35.6 ± 10.0	—	—	167 ± 26 3413 ± 453	15.2 ± 2.6	8.6 ± 2.6	—
	Q	—	—	—	125 ± 5	15.6 ± 2.2 193 ± 16	unable	62.7 ± 2.8	—
K	X	—	—	—	—	40.3 ± 15.1 625 ± 69	—	—	—
	Q	—	—	—	23.6 ± 4.2 232 ± 29	31.6 ± 4.3 289 ± 57	—	30.4 ± 8.2 212 ± 79	—
L	X	—	44.9 ± 9.6	—	—	84.5 ± 13.9 1440 ± 532	—	33.1 ± 19.6 1115 ± 318	10.3 ± 3.5
M	g	**2.011**	**1.997**	**1.993**	**1.983**	**1.973**	**1.954**	**1.921**	**1.868**
	X	88.3 ± 10.7 771 ± 155	62.9 ± 2.9 637 ± 18	59.3 ± 1.6 513 ± 7	64.7 ± 1.7 745 ± 9	57.3 ± 1.8 531 ± 10	67.3 ± 7.0 1138 ± 220	7.4 ± 0.5	6.0 ± 0.7
N	X	—	—	36.2 ± 5.6 376 ± 33	—	56.4 ± 2.2 585 ± 16	—	59.4 ± 1.3 632 ± 7	524 ± 51
	Q	—	—	—	—	—	—	27.9 ± 0.2 536 ± 4	—

Table 5-7 Fitted results of T_2. The stars (*) indicate positions observed signals from the cavity.

Sample		**2.138***	**2.063 - 2.070***	**2.036**	**2.017 - 2.028**	**2.004 - 2.010**	**1.998**	**1.981 - 1.984**	**1.913 - 1.921**
T_2 [μs]									
I	X	0.8 ± 0.1, 16.3 ± 1.0	1.0 ± 0.1, 14.7± 1.2	—	—	1.5 ± 0.1, 58.0 ± 2.7	—	—	—
	Q	—	2.0 ± 0.1, 4.0 ± 0.4, 124 ± 8	—	2.1 ± 0.04, 4.4 ± 0.3, 110 ± 8	1.6 ± 0.08 74.9 ± 1.5	1.8 ± 0.07 5.0 ± 1.1 85.3 ± 15	—	—
J	X	—	1.0 ± 0.20 10.6 ± 1.5	—	—	1.2 ± 0.14 54.8 ± 0.7	1.2 ± 0.15 25.8 ± 3.9	2.0 ± 0.27 27.6 ± 3.9	—
	Q	—	—	—	2.2 ± 0.24 13.3 ± 3.0 458 ± 191	2.8 ± 0.78 13.3 ± 7.3 163 ± 4	1.6 ± 0.22 9.8 ± 1.3 159 ± 3	5.4 ± 1.4 171 ± 3	—
K	X	—	2.8 ± 0.23	—	—	1.7 ± 0.12 12.3 ± 8.7	—	0.9 ± 0.15 36.5 ± 7.8	—
	Q	—	—	—	2.7 ± 0.23 63.4 ± 1.9 148 ± 2	1.6 ± 0.11 13.7 ± 0.8 133 ± 3	—	1.3 ± 0.13 12.3 ± 2.1 199 ± 11	—
L	X	—	1.2 ± 0.15 73.1 ± 31.0	—	—	1.6 ± 0.09 76.6 ± 2.7	—	1.4 ± 0.15 65.8 ± 5.3	0.7 ± 0.14 18.5 ± 3.2
M	g	**2.011**	**1.997**	**1.993**	**1.983**	**1.973**	**1.954**	**1.921**	**1.868**
	X	1.1 ± 0.07 40.5 ± 13.6	1.1 ± 0.04 24.5± 3.0	3.3 ± 0.3 31.4 ± 1.3	5.4 ± 0.07 26.1 ± 0.5	2.3 ± 0.05 22.1 ± 0.1	2.7 ± 0.06 23.3 ± 0.3	4.8 ± 0.08 31.1 ±1.1	5.2 ± 0.2 31.3 ± 1.1
N	X	—	—	3.2 ± 0.08 172 ± 9	—	3.7 ± 0.03 55.8 ± 2.0	—	4.2 ± 0.06 27.8 ± 1.1	0.6 ± 0.04 62 ± 5.0
	Q	—	—	—	0.6 ± 0.2* 125 ± 1*	—	—	3.1 ± 0.03 7.9 ± 0.1 271 ± 9	1.3 ± 0.15 728 ± 77

5.1.4. Decomposition of the EPR spectra

Based on the results in the previous section, $BaSi_2$ has different families of defects depending on the composition ratio. In this section, the paramagnetic centers induced the different EPR lines observed in the Si-rich group and the Ba-rich group were separated from the viewpoints of temperature dependence, microwave dependence and relaxation time. In this section, I set its goal to classifying such centers.

Si-rich group

Figures 5.1-7 shows the temperature dependence of cw-X- and Q-band powder EPR spectra of the Si-rich samples plotted against *g*. Comparing the results of X-band and Q-band at each sample and each temperature, the powder pattern of the Si-rich samples seemed to be explained by *g* anisotropy and/or a few different *g* originated from different centers. However, since the spectra were very broad, I have to keep the possibility in mind that unresolved hyperfine structures are included. On the other hand, as it is clear when I focus on the X-band results, the shape of spectra was changed with varying temperatures. Since at least two different relaxation times were confirmed in the T_1 and T_2 experiments, I suppose that, in the Si-rich samples, the EPR spectra are constituted of two different paramagnetic centers with different relaxation times.

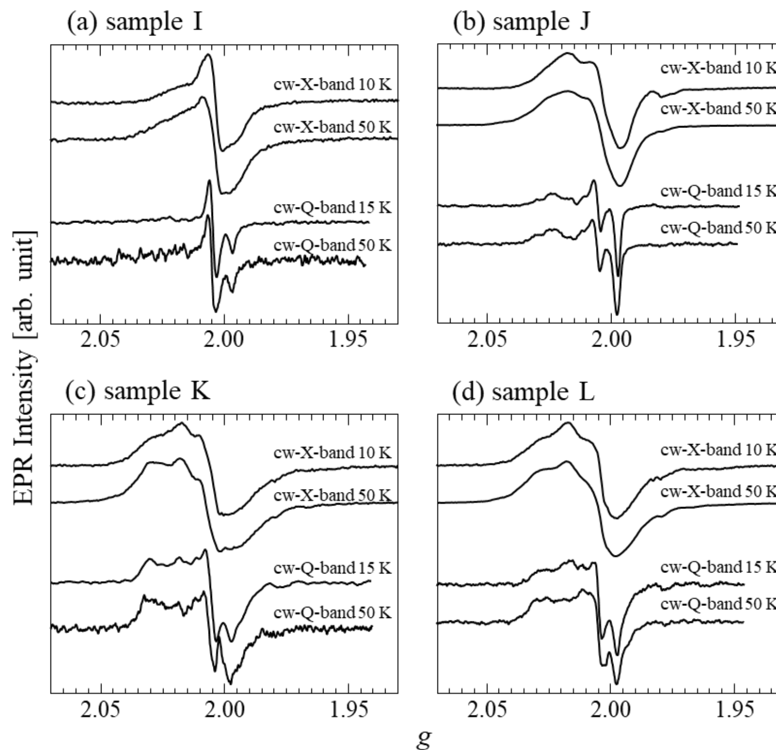

Fig. 5.1-7 Temperature dependence of cw-X- and cw-Q-band EPR spectra of (a) Sample I, (b) Sample J, (c) Sample K, and (d) Sample L.

A relatively narrow EPR lines sclearly observed in Sample I were confirmed in all other Si-rich samples. As N_{Ba}/N_{Si} aproaches stoichiometry, a new broader lines seemed to show up on the spectra. To decompose these two (or more) centers, I measured microwave power dependence of the lines for all samples at X-band (Figs. 5.1-8). Since the shape of the EPR spectrum differs between the maximum P_{MW} and the minimum P_{MW} in each sample, it is highly

possible that a plurality of paramagnetic centers are included.

From the results both of the microwave power dependence and the temperature dependence, it can be said that at least two paramagnetic defects exist in the Si-rich sample. However, due to the broadness of the EPR line, cw-EPR could not clearly separate the centers.

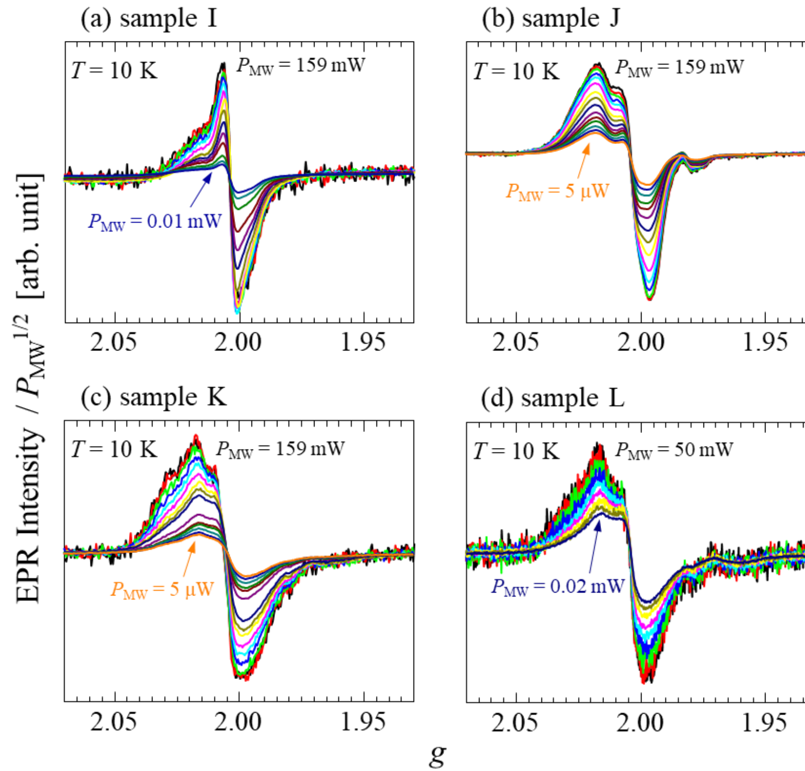

Fig. 5.1-8 Microwave power dependence of the EPR spectra measured in cw-X-band at 10 K.

The Si-rich samples contains two different paramagnetic centers
Defect 1 : very broad and large anisotropic line
Defect 2 : relatively narrow line centered at $g \sim 2.005$

Ba-rich group

First, I show the cw X- and Q-band powder EPR spectra of Samples M and N plotted against g. In Figs. 5.1-9, broad EPR lines were observed. Taking it into the account that the samples are powder, one of the principal values of g-tensor should be $g_3 = 1.855$. On the other hand, there are two possibilities for other two principal values.

① From the cw-Q-band spectrum, $g_1 = 1.930$ and $g_2 = 1.905$ as shown by the blue horizontal lines in Fig. 5.1-7(a).

② Because an origin of a line with $g = 1.95$-1.98 is not clear (it is impossible to separate it from others as I described later), g_1 component can be imposed in this region.

In the following, I will proceed with discussion from the standpoint of ① because I observed the “trace” in Fig. 5.1-9(a) although it was too unclear to identify it as g_1.

Next, I pay attention to the EPR line observed at $g \sim 2.00$. Figure 5.1-10(a) shows the temperature dependence of the cw-X- and cw-Q-band spectra. At 50 K, the EPR line at $g \sim 2.00$ and 1.965 (as I dipicted red horizonal lines in the figures) decreased drastically. Also, as shown in Figs.5.1-10(b), it is only possible to detect in

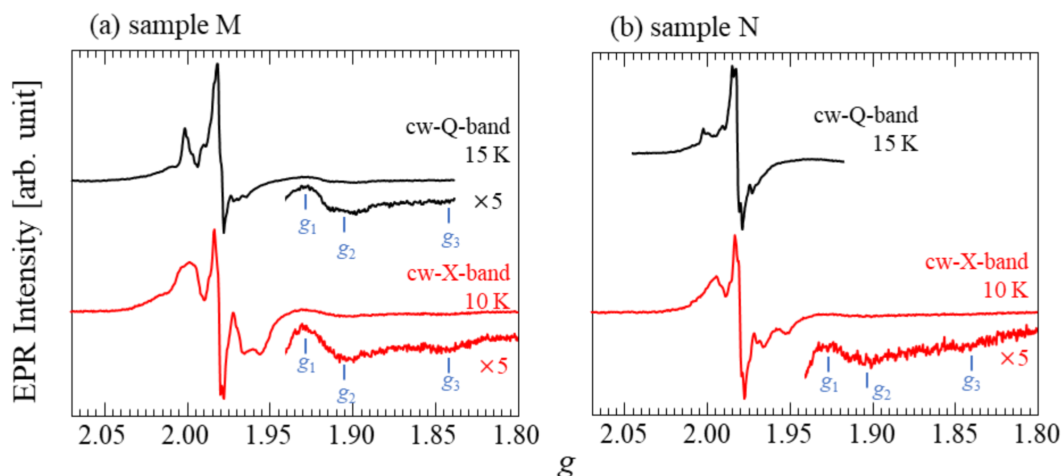

Fig. 5.1-9 cw-EPR spectra of (a) Sample M and (b) N. The cw-X- and cw-Q-band spectra were recorded at 10 and 15 K, respectively. The blue horizonal lines are the principal value of the broad EPR line observed only at low temperature (the one of two possibilities).

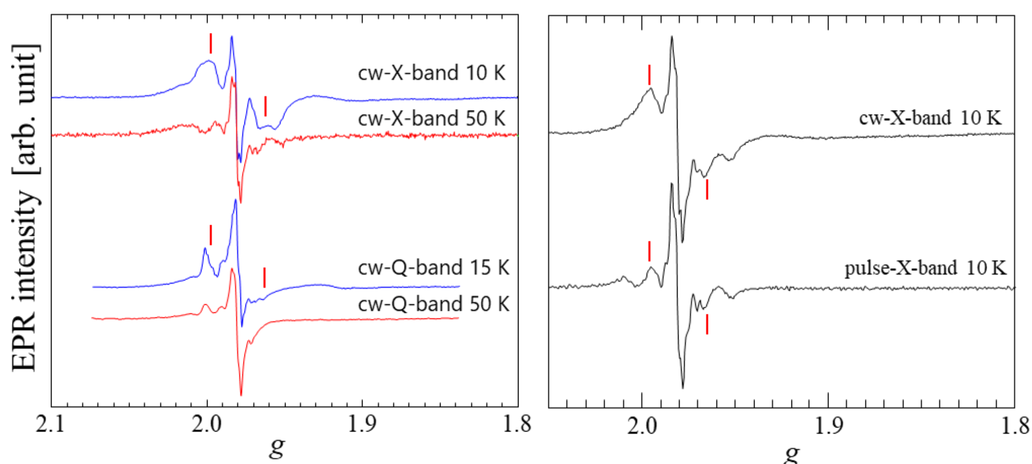

Fig. 5.1-10 (a) Temperature dependence of cw-EPR spectra of Sample M. (b) Comparison between cw- and pulse-EPR spectra of Sample M. The strange EPR line were observed at the position of red horizonal lines.

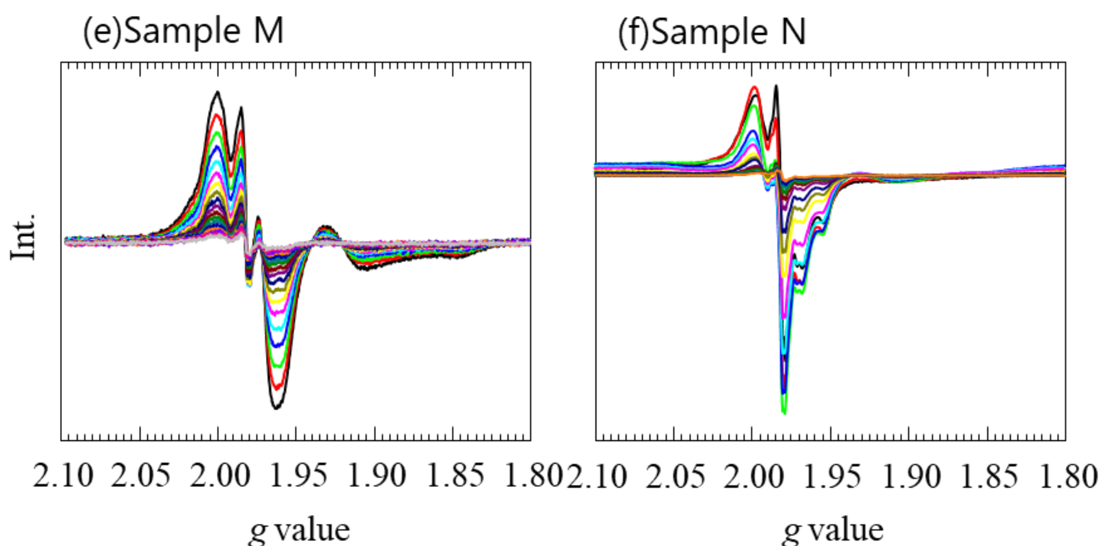

Fig. 5.1-11 Microwave power dependence of cw-X-EPR spectra of (a) Sample M and (b) N. The EPR lines placed at g ~ 2.00 and 1.965 depend on the power strongly.

cw-EPR measurements. Taking the fact into account that, in pulse-EPR, it is impossible to detect the paramagnetic center with very short T_2 due to the mechanical limits. Therefore, the origin of this EPR line possesses very short T_2. Furthermore, the intensity of g ~ 2.00 increased as the microwave power increased (Figs. 5.1-11). Although the main contribution to the microwave saturation is T_1, T_2 is shorter than T_1, in principle. Thus, all experimental results support the interpretation that the EPR line originates from the center with short T_2. One can often observe such short T_2 in a $S > 1/2$ system, where a symmetric spectra can be observed.[156-158] The best choice to determine its spin number, S, is a nutation measurements[158,159] by pulse EPR. However, in my study, it was impossible to perform it as I described just before. Another possibility to confirm S is the half-field resonance expriment by cw-EPR.[156,157] When S is superior than 1/2, forbidden transitions ($\Delta m_S = \pm$ 2, 3, ...) can be observed in addition to the EPR allowed transitions ($\Delta m_S = \pm$ 1) due to spin-spin coupling, for instance. In such cases, as shown in Fig. 5.1-12 (a), an EPR line of forbidden transition is observed at the half resonance position (1/2 H_{res}). However, no such signal was observed in the half resonance condition in this study (Fig. 5.1-12(b) and its insert). Therefore, the possibility of the center of $S \geq 1$ as the origin of this spectrum can be excluded. Thus, I suppose that this EPR possesses $S = 1/2$. However, I am not sure that what is the origin of this strange EPR lines for the moment.

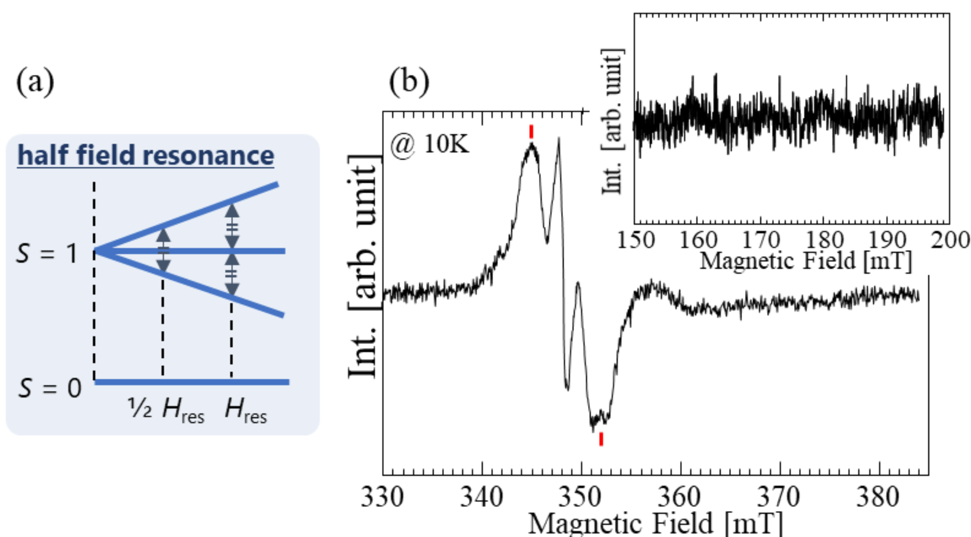

Fig. 5.1-12 (a) A schematic image of evergy level for S =1 spin system. (b) The EPR spectrum of Sample M at 10 K with high microwave power. There was no EPR spectrum at its half field condition.

Next, I focus on the EPR line, which has a complicated structure centered on g ~ 1.981. As can be seen from Figs. 5.1-9, these structures cannot be explained solely by g. Figures 5.1-13 show the cw-EPR spectrum plotted against the magnetic field. As described above, when paying attention to the 50 K spectrum of the X-band, the symmetrical structure toward the narrow EPR line ($B - B_0 = 0$) can be confirmed. Table 5-8 shows the isotopes of Ba and Si with the nuclear spin number, I, and their natural abundance. Although the natural abundance ratios are small, it can be inferred that the complex EPR spectrum is formed by hyperfine interactions with Ba or Si nuclei (As I discuss the details later in section 5.4). In this case, the central narrow EPR line is presumed to correspond to the case where the unpaired electron exists near the nucleus at $I = 0$.

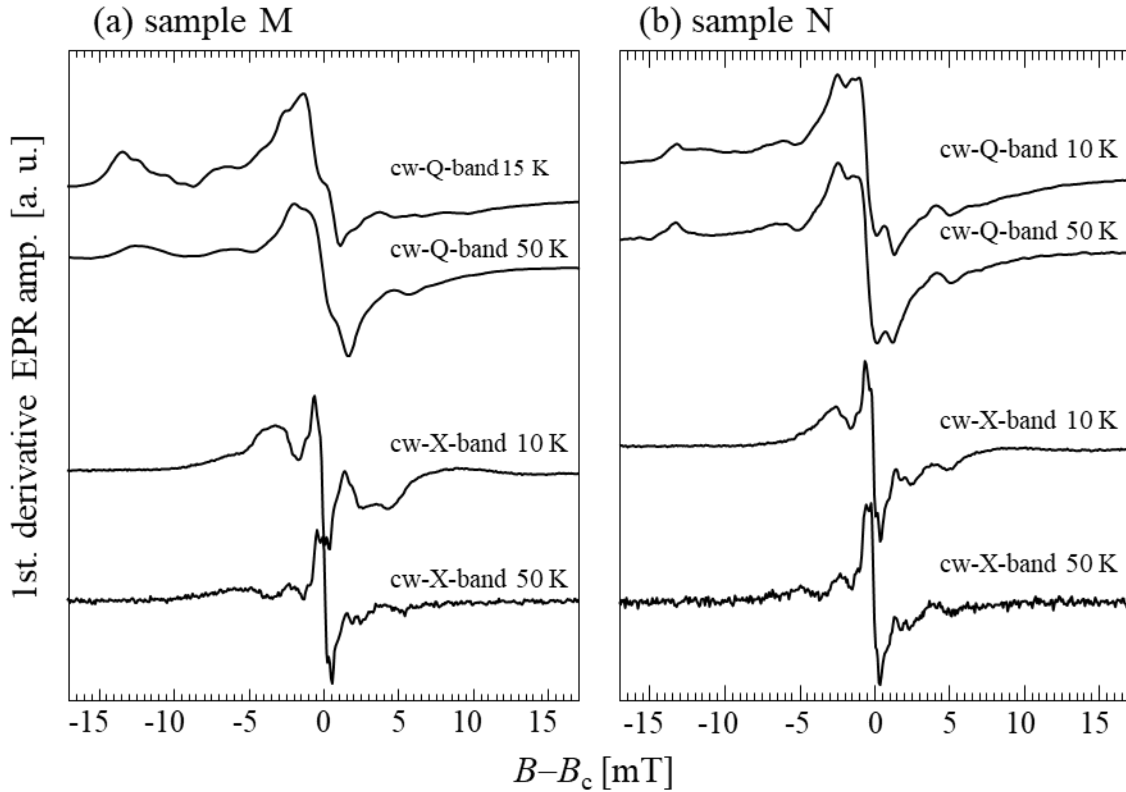

Fig. 5.1-13 Temperature dependence of EPR spectra on (a) Sample M and (b) Sample N. For each sample, cw-X- and Q-band spectra were measured at different temperatures.

Table 5-8 Isotope of Ba and Si.[103]

Isotope	Nuclear spin number	g_N	Natural abundance [%]
^{28}Si	0	0	92.2297
^{29}Si	1/2	-1.11058	4.6832
^{30}Si	0	0	3.0872
^{130}Ba	0	0	0.106
^{132}Ba	0	0	0.101
^{134}Ba	0	0	2.417
^{135}Ba	3/2	0.55863	6.592
^{136}Ba	0	0	7.854
^{137}Ba	3/2	0.62491	11.232
^{138}Ba	0	0	71.698

Ba-rich samples contains three different paramagnetic centers.
Defect 3 : very broad line observed at low temperature
Defect 4 : only visible by cw-EPR, suggesting it has very short T_2
Defect 5 : almost anisotropic line with hyperfine structure

5.1.5. Summary

The different paramagnetic defects are formed in $BaSi_2$ depending on the composition ratio of Ba and Si (Table 5-9).

Table 5-9 Defects in $BaSi_2$.

Label	N_{Si}/N_{Ba}	Defect1	Defect2	Defect3	Defect4	Defect5
I	2.404	◎	○	-	-	-
J	2.087	◎	○	-	-	△
K	2.134	◎	○	-	-	△
L	2.054	◎	○	-	-	△
M	1.987	△	-	△	◎	○
N	1.916	△	-	△	◎	○

◎：Observable (dominant), ○：Observable, △：Observable (weak), －：Unobservable

● Defect 1 [Si-rich]

Shape：Broad and anisotropic EPR line (g ~ 2.04-1.98)

Relaxation：Inferred to have a long T_1 due to insensitivity toward temperature rise

Others：EPR line dominant with Si-rich samples

● Defect 2 [Si-rich]

Shape：Relatively narrow line centered at g ~ 2.005

Relaxation：Relative intensity of the spectra decreases with increasing temperature

Others：-

● Defect 3 [Ba-rich]

Shape：Broad and anisotropic EPR line （$g_1 = 1.930$, $g_2 = 1.905$, $g_3 = 1.855$）

Relaxation：Observed at low temperature ($T < 25$ K) and under strong P_{MW}

Others：Observed only in Ba-rich samples

● Defect 4 [Ba-rich]

Shape：Observed EPR lines at g ~ 2.000 and 1.995

Relaxation：T_2 short enough not to be observed in pulse-EPR

Others：B Observed only in Ba-rich samples

● Defect 5 [Ba-rich]

Shape：Hyperfine structure centered on g ~ 1.982

Relaxation：Most saturable defect observed in Ba-rich sample

Others：EPR line dominant with Si-rich samples

5.2. Hyperfine spectroscopy

The selection rule of EPR is $|\Delta m_S| = 1,\ |\Delta m_I| = 0$ where Δm_S and Δm_I is the change in the magnetic quantum number of the electron and the nuclear spin. When there are some interactions such as hyperfine, quadrupole, spin-spin, spin exchange, … interactions, their states are mixed to an observable extent and the "forbidden" transition which doesn't obey the selection rule of EPR is observed. In a field of magnetic resonance, such conditions are often met. This is probably because the energy difference is not too large comparing with the interactions in contrast to, for instance, optical transition.

Hyperfine interaction is a local interaction between electron spin and nuclear spin. Therefore, by determining the hyperfine coupling tensor, it is possible to obtain extremely useful information about each paramagnetic center, for examples, the type of defect and the local structure. In this section, I aimed to measure the types and structures of paramagnetic centers observed in Si-rich and Ba-rich samples using various methods. In Hyperfine spectroscopies, it is mandatory to have relaxation time of each paramagnetic center to be investigated. For example, in ED-NMR, the detection pulses should be applied after 5 T_2 in order to exclude the influence of T_2 after HTA-pulse. On the other hand, the hole burning created by HTA-pulse recovers according to T_1. In a general semiconductor, T_2 has a weak temperature dependency and T_1 has a strong one. Therefore, by changing the temperature, it is possible to search for the optimum measurement condition of each paramagnetic center. In section 5.1.3, I had already studied the relaxation times (T_1 and T_2). Based on those results, I optimized experimental conditions for each hyperfine spectroscopies.

5.2.1. HYSCORE, ENDOR, ED-NMR

Compared to g-tensor, it often requires sophisticated techniques to measure the hyperfine structures. Once the hyperfine structures are observed, we can compare the experimental results with those theoretically computed by DFT, etc.[145-147] This is because the hyperfine interaction basically considers only the ground state of unpaired electrons, while the theoretical g-tensor considers excited states as well as the ground state. The simplest measurements of the hyperfine structures are to perform multi-frequency EPR[137,160] by using continuous microwaves. Since the hyperfine tensor is field independent, we can separate each component of the observed EPR spectra by comparing with g-tensor which is field-dependent. In complicated or disordered spin system like this study, the advanced EPR spectroscopies are needed to get a whole picture as I listed on the Table 5.10. These three pulse EPR sequences possess merits and demerits. Therefore, it is the best way to choose which sequence is appropriate for each study after trials of all sequences.

Table 5-10. Three different hyperfine spectroscopies.

HYSCORE (ESEEM)[161,162]	ENDOR[163]	ED-NMR[164]
Electron spin echo envelope modulation	Electron-nuclear double resonance	Electron-electron double resonance detected NMR
One frequency	Two frequency	Two frequency
MW	RF and MW	MW

.

HYSCORE

HYSCORE is one of the techniques of electron spin echo envelope modulation (ESEEM) spectroscopy. An irradiation of microwave induces only EPR transition ($|\Delta m_S| = 1$, $|\Delta m_I| = 0$) in principle. However, since there is a finite probability that the nuclear spin is simultaneously inverted by the microwave pulses, the observed echo contains a contribution of nuclei which has hyperfine interaction with the flipped electron spin. I show the typical sequence of HYSCORE in Fig. 5.2-1(a).

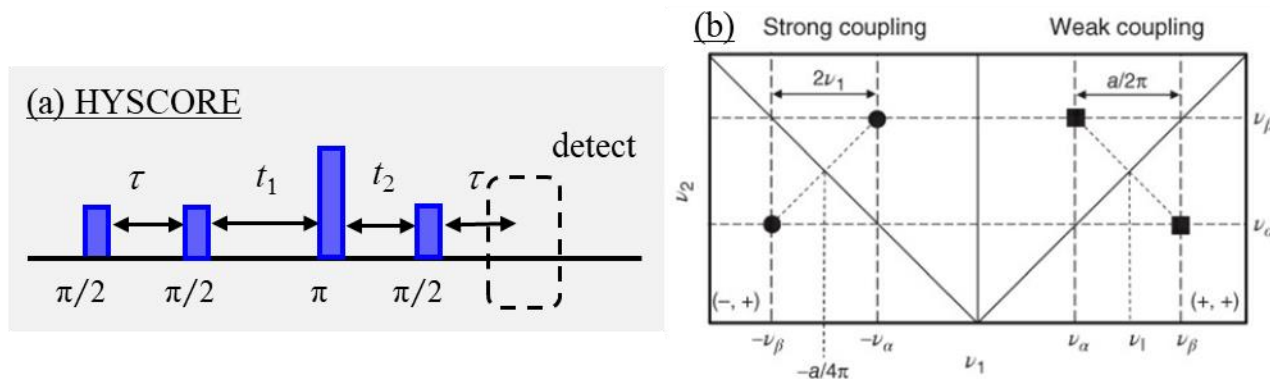

Fig. 5.2-1 (a) Pulse sequence of HYSCORE. The two intervals t_1 and t_2 are independently varied. Therefore, 2-dimmentional results are obtained. (b) After 2-dimmentional Fourier transformation of the results, we get 2D spectra including nuclear frequency (ν_I) together with hyperfine coupling constant. The peak positions depend on the strong coupling or weak coupling.

As can be seen in Fig. 5.2-1(b), the Fourier transferred spectra are observed in different 2 dimensional regions depending on weak coupling or strong coupling. In both cases, ***HYSCORE provides us the type of nuclei and hyperfine coupling constant at the same time***. On the other hand, ***low-frequency transitions (< 5 MHz)*** are best detected by ESSEM (and HYSCORE).

Electron Nuclear DOuble Resonance (ENDOR)

Electron-nuclear double resonance (ENDOR) is one of the main techniques to measure hyperfine coupling. ENDOR sequences take advantage of radio frequency to induce nuclear transitions, i.e., NMR transitions. Although there are many ENDOR pulse sequences, the Davies[165] and Mims[166] type ENDOR are basic sequences (Figs. 5.2-2).

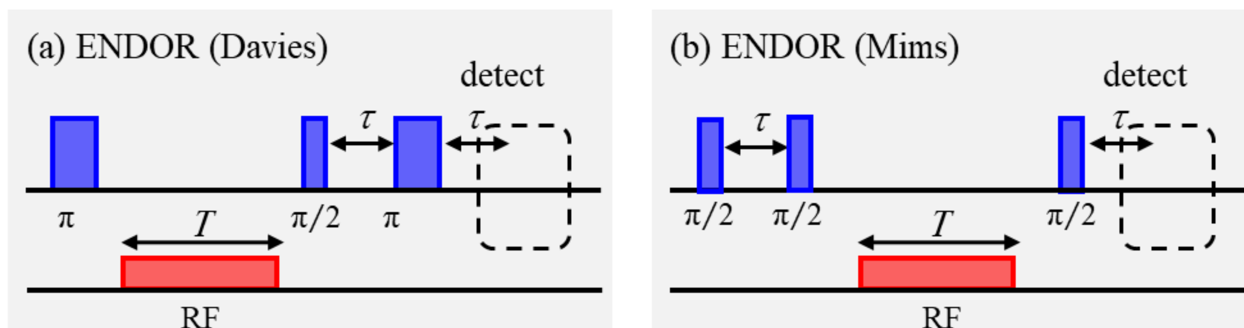

Fig. 5.2-2 Pulse sequences of (a) Davies ENDOR and (b) Mims ENDOR. By inverting the polarization of a partiular EPR transition via NMR transition, two pulse Hahn echo are utilized in Davies ENDOR while a stimulated echo sequences are adopted in Mims ENDOR.

Comparing Mims and Davies ENDOR, Mims ENDOR is specialized in detecting small coupling while Davies ENDOR is the best choice for strong coupling detection. However, to maximize the intensity of Davies ENDOR, the selective π pulse is required. The simplest understandings of ED-NMR sequence are given in a spin system with $S = 1/2$, $I = 1/2$ (Fig. 5.2-3). In such cases, beside EPR transitions 1→3 (ν_{13}) and 2→4 (ν_{24}) ($|\Delta m_S| = 1$, $|\Delta m_I| = 0$), there are NMR transitions 1→2 (ν_{12}) and 3→4 (ν_{13}) ($|\Delta m_S| = 0$, $|\Delta m_I| = 1$). Figure As I show in Fig. 5.2-4(a), first π pulse flip electron spins. When RF pulse corresponds to NMR transition, the polarization is inverted. Then, in the sequences of detection parts, one can observe the difference in the intensity between NMR on resonance and NMR off resonance. Therefore, if the first pulse is nonselective, the intensity of observable intensity becomes

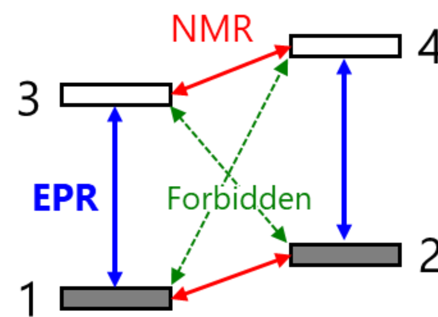

Fig. 5.2-3 Schematic images of energy level of $S = 1/2$, $I = 1/2$ system.

(a) Davies ENDOR

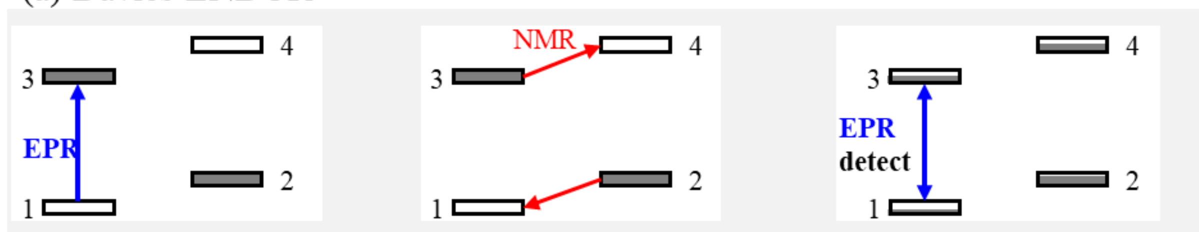

(a) EDNMR

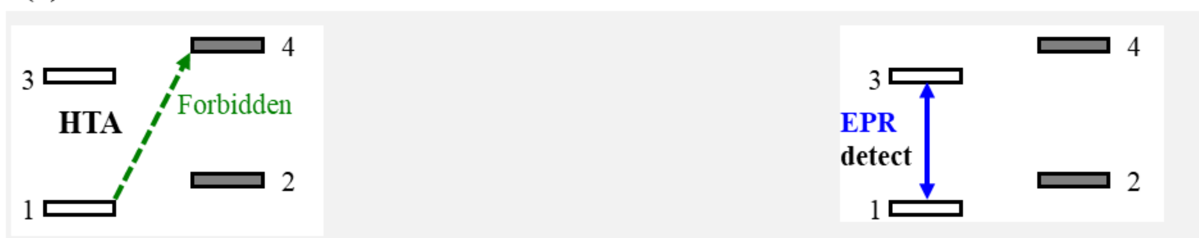

Fig. 5.2-4 Schematic energy level diagram of $S = 1/2$, $I = 1/2$ during (a) Davies ENDOR and (b) ED-NMR sequences.

less because there is less difference between 1 and 3 states in the Fig. 5.2-4(a) after the pulse, resulting in NMR transition, if any, hardly to change each population. Thus, in ***ENDOR enables us to investigate precisely*** while it is ***always difficult to optimize the experimental conditions***. From the viewpoint of relaxation time, the ENDOR sequences require a long phase memory time T_m greater than the dead time of spectrometer and T_1 should be longer than the ENDOR pulse sequence.

ELDOR-detected NMR (ED-NMR)

Electron-electron double resonance (ELDOR)-detected NMR (ED-NMR) is the most newest among three different hyperfine spectroscopies. Therefore, a whole theoretical background is not yet established in contrast to HYSCORE and ENDOR. However, this new sequence has attracted many EPR researchers recently due to its great potentials.[167] As I showed in Fig. 5.2-3, in the spin system with $S = 1/2$ and $I = 1/2$, there are also the so-called

forbidden EPR transitions 1→4 (ν_{14}) and 2→3(ν_{23}). The forbidden transition probabilities are usually low but finite. Therefore, a strong and long microwave pulse (so-called high-turning-angle, HTA, pulse) make the probabilities higher, resulting in, as shown in Fig. 5.2-4(b), the population of the level 1 and 4 change. These concepts underlie ED-NMR, which concept is the same as Davies ENDOR (Fig. 5.2-5(b)). In practice, we use 2 microwave pulses with different frequencies. One of two is set at the position of detection (Fig. 5.2-5), and the other's frequency is swept around the detected position. When the frequency of the HTA pulse matches the forbidden transitions, the intensity observed signal is considerably decreased with the situation where no HTA pulse was applied. Under these conditions, the difference between the frequency for detection and HTA corresponds to the half of hyperfine coupling constant in strong coupling case.

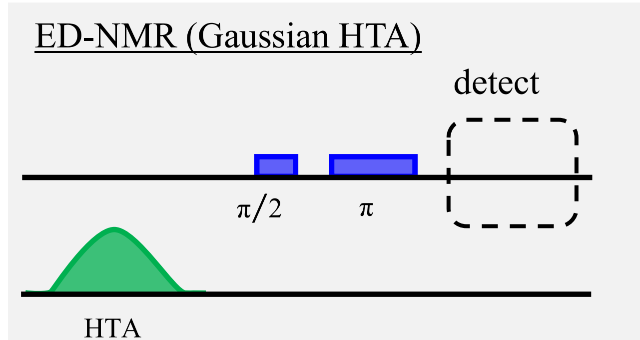

Fig. 5.2-5 Pulse sequence of ED-NMR with Gaussian high-turning-angle (HTA) pulse.

Three different hyperfine spectroscopy specialize in;

- HYSCORE : weak hyperfine coupling
- Davies ENDOR : strong hyperfine coupling
- ED-NMR : strong hyperfine coupling

5.2.2. Results

In this study, HYSCORE, ENDOR, and ED-NMR were performed on Si-rich and Ba-rich samples, respectively. This section focuses on whether each paramagnetic center has a strong hyperfine coupling constant. For simple discussion, I consider isotropic hyperfine interaction, A_{iso}, which is given by the following equation.

$$A_{iso} = \frac{8\pi}{3} g_S \beta g_I \mu_N \left| \Psi_{ns}(0) \right|$$

where g_S, β, g_I, μ_N, $\Psi_{ns}(0)$ are g-factor of electron spin, Bohr magneton (= $9.2740100783\times10^{-24}$ J T^{-1}), g-facor of nulear spin, nuclear magneton (= $5.050783699\times10^{-27}$ J T^{-1}), and wave function of n-th s-orbital, respectively. Since all parameters are known valuses except for $\Psi_{ns}(0)$, I can estimate the charge density of unpaired electrons by measuring hyperfine constant, which are considered to be generated by defects in $BaSi_2$. In the case of small hyperfine coupling $|A_{iso}|$, the charge density can be low, which corresponds to the delocalization of electrons (see Fig. 5.2-6 (a)). On the other hand, in the case of large hyperfine coupling, it is assumed that the charge density is high and it means that the electrons are localized near the nucleus causing hyperfine interaction (if $I \neq 0$). Furthermore, in terms of defect levels in the bandgap, the delocalized, or more mobile defects, correspond to shallow defects such as band tails, and the localized defects correspond to defects with deep levels in the bandgap. Thus, since deep levels promote recombinations of photogenerated carriers more than shallow levels, identifications and decrease of such deep defects, that is, the defects with large hyperfine coupling constants are much more interesting in this study from

the viewpoint of solar cell devices (Fig. 5.5-6(a)). Noted that although hyperfine tensor doesn't depends on the magnetic field, however, the regime of weak and strong coupling can change. This is because each scheme is defined for nuclear Lamor frequency, ν_I (Fig. 5.2-6(b)).

Large hyperfine coupling is much more interesting in this study

Si-rich sample

First, HYSCORE in the X-band by pulse EPR was measured (Table 5-10). As shown in the Figs. 5.2-7, weak hyperfine interaction with ^{29}Si at $|A|$ ~ 2-3 MHz was observed at B = 343 and 345 mT, but no signal of ^{135}Ba (^{137}Ba) was observed (Figs. 5.2-7(b) and (c)).

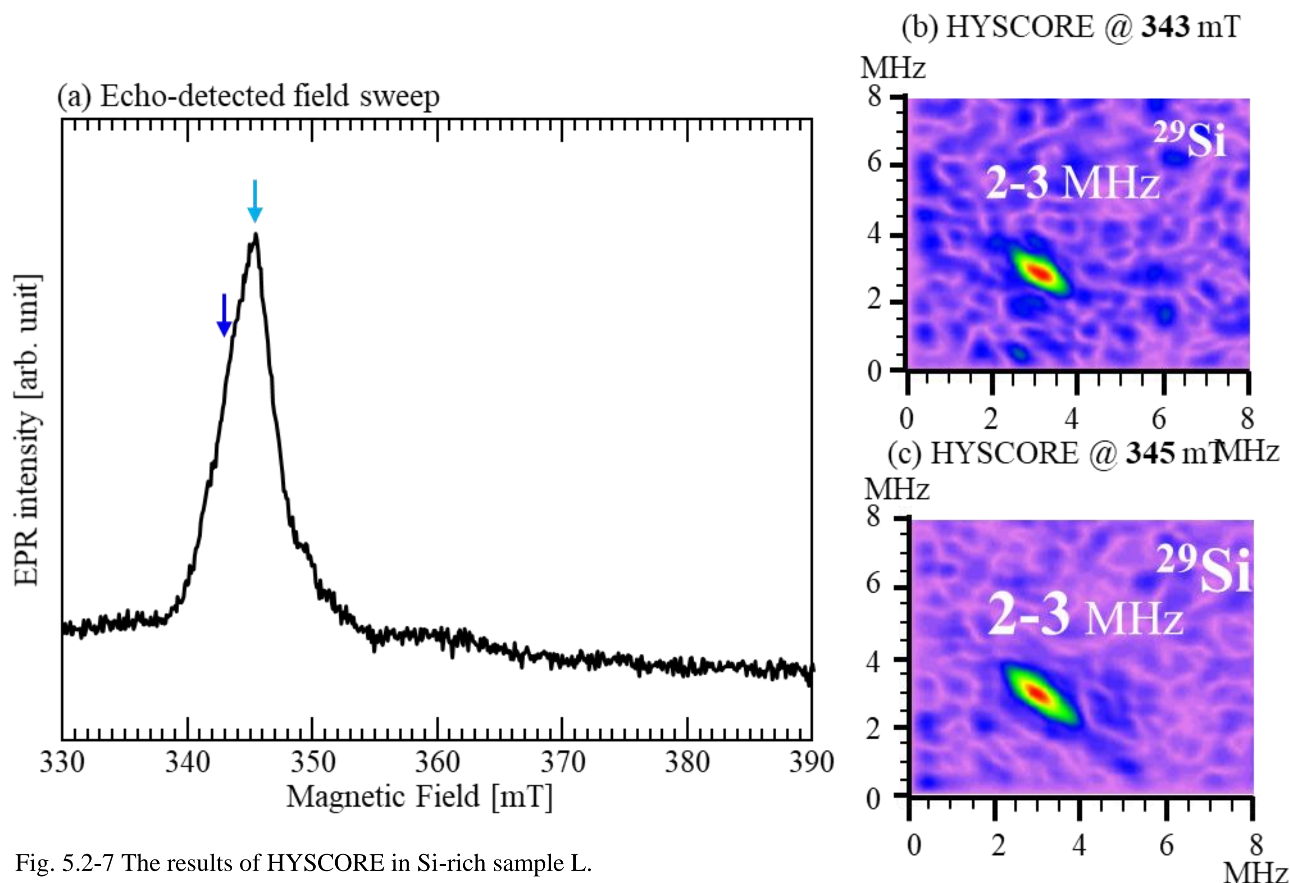

Fig. 5.2-7 The results of HYSCORE in Si-rich sample L.

Table 5-10. HYSCORE pulse sequence for Si-rich Sample L (X-band).

Sample L	P0	P2	Pg	D1	D2	D3	D30	points	srt
343 mT 345mT	16 ns	16 ns	40 ns	140 ns	200 ns	200 ns	24 ns	128×128	10 ms

HYSCORE is the technique specialized for measuring relatively small hyperfine coupling constants. As I mentioned above, however, defects with strong hyperfine interactions are more interesting in this study. Therefore, I tried to measure large hyperfine coupling constant by pulse-ENDOR (Davies type) in a strong coupling regime (Table 5-11).

Table 5-11. Davies ENDOR pulse sequence for Sample L (Q-band).

Sample	Inversion π pulse	delay	RF		delay	detection		srt
			time	range		t_p	τ	
L	32 ns	1 μs	20 μs	1-100 MHz	25 μs	16 ns	200 ns	1 ms

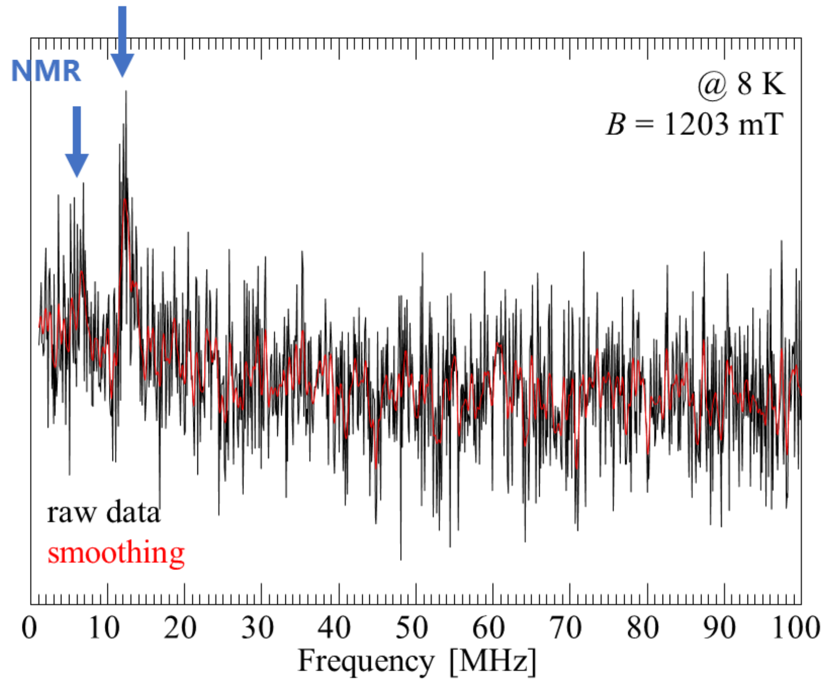

Fig. 5.2-8. The results of Davies ENDOR spectrum in Si-rich sample L.

As shown in the Fig. 5.2-8, I observed peaks at 6.75 and 12.20 MHz after integrating overnight. Reffering Table 2-6, NMR frequencies are given by $|\nu_{29\mathrm{Si}}| = 10.18$, $|\nu_{135\mathrm{Ba}}| = 5.12$, and $|\nu_{137\mathrm{Ba}}| = 5.73$ MHz, respectively. The calculated values seem to correspond to those observed in ENDOR spectra. The deviation from the calculations come from the first π pulse. I used the 32-ns-width pulse to invert the spins. Therefore, it is hard to detect the NMR transition and hyperfine couplings less than $\Delta\nu \sim 1/(1.6578 \times t_p) \sim 19$ MHz.[155] For similar reasons, I could not observed samll hyperfine couplings which observed in HYSCORE. In principle, one can improve the resolution of ENDOR spectra by using more selective pulse as the firs invertion pulse. In this case, however, it wasn't a appropriate approach to optimize the ENDOR sequences because of its poor S/N ratio.

Since the ENDOR measurement requires radiofrequency to induce NMR transitions, it is extremely difficult to optimize experimental conditions combining with the microwave cavity. Therefore, poor S/N ratios have been reported among many systems in ENDOR. Instead of ENDOR, in order to improve the S/N ratio, I tried to perform the ED-NMR measurements which has recently attracted attention as new hyperfine spectroscopy (Table 5-12). Figure 5.2-9 shows the ED-NMR spectrum measured at 1195 mT (Q-band). A clear ED-NMR signal can be confirmed at $\nu_1' - \nu_1 = -33, +34$ MHz. As is clear from the value calculated above, I should consider these values in the strong coupling regime, i.e $|\nu_I| < |A/2|$.

Table 5-12. ED-NMR pulse sequence (Q-band).

Sample	HTA			delay	Detection			srt
	Amp	length	Range		t_p	τ	Integration	
L	5 %	5 μs	± 256 MHz	15 μs	400 ns	2.2 μs	2.5 μs	10 ms

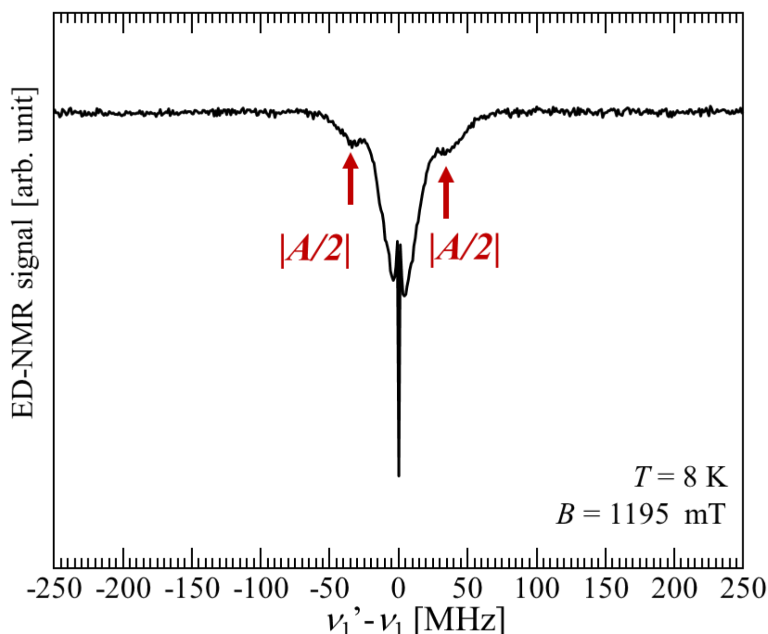

Fig. 5.2-9 The results of ED-NMR in Si-rich sample L.

Hyperfine coupling (Si-rich):	HYSCORE	→ small |A| = 2-3 MHz with ^{29}Si
	ENDOR	→ non cnclusive
	ED-NMR	→ large |A| ~ 70 MHz

Ba-rich sample

I also performed hyperfine spectroscopies on the Ba-rich samples. Figures 5.2-10 show the result of HYSCORE in the X-band by pulse EPR. The details of the pulse sequence are summarized in Table 5-13. Small hyperfine coupling constants with ^{29}Si of $|A|$ ~ 2-3 MHz were observed at the positions of the Defect4 and the Defect5 in the Ba-rich samples (Figs. 5.2-10(b) and (c)). On the other hand, hyperfine interaction with ^{135}Ba and/or ^{137}Ba was not observed in this measurement, as in the Si-rich samples.

In the following, I focus more on the Defect 5. As shown in Fig. 5.2-10(a), the EPR spectra considered to be hyperfine structures of the Defect 5 were observed symmetrically around g ~ 1.982. If these are hyperfine interactions with ^{29}Si, their $|A|$ are roughly estimated at 60, 120, and 230 MHz, respectively. On the other hand, the hyperfine coupling constant obtained by HYSCORE was from 2 to 3 MHz, so it can be said that the hyperfine coupling constant observed in HYSCORE does not correspond to those observed in Fig. 5.2-10(a). I also have to keep their natural abundance in my mind (natural abundance of ^{29}Si is only 4.68%). To get a tip for an origin of the hyperfine structures observed in Fig. 5.2-10(a), the Davies ENDOR was performed (Tabel 5-14). After overnight integration, a very broad ENDOR spectrum with a maximum at ~ 40 MHz was finally observed, as shown in the Fig. 5.2-11.

Table 5-13 HYSCORE (X-band)

Sample L	P0	P2	Pg	D1	D2	D3	D30		srt
343 mT	16	16	40	140	200	200	24	128*128	10
345mT	ns	ns	ns	ns	ns	ns	ns		ms

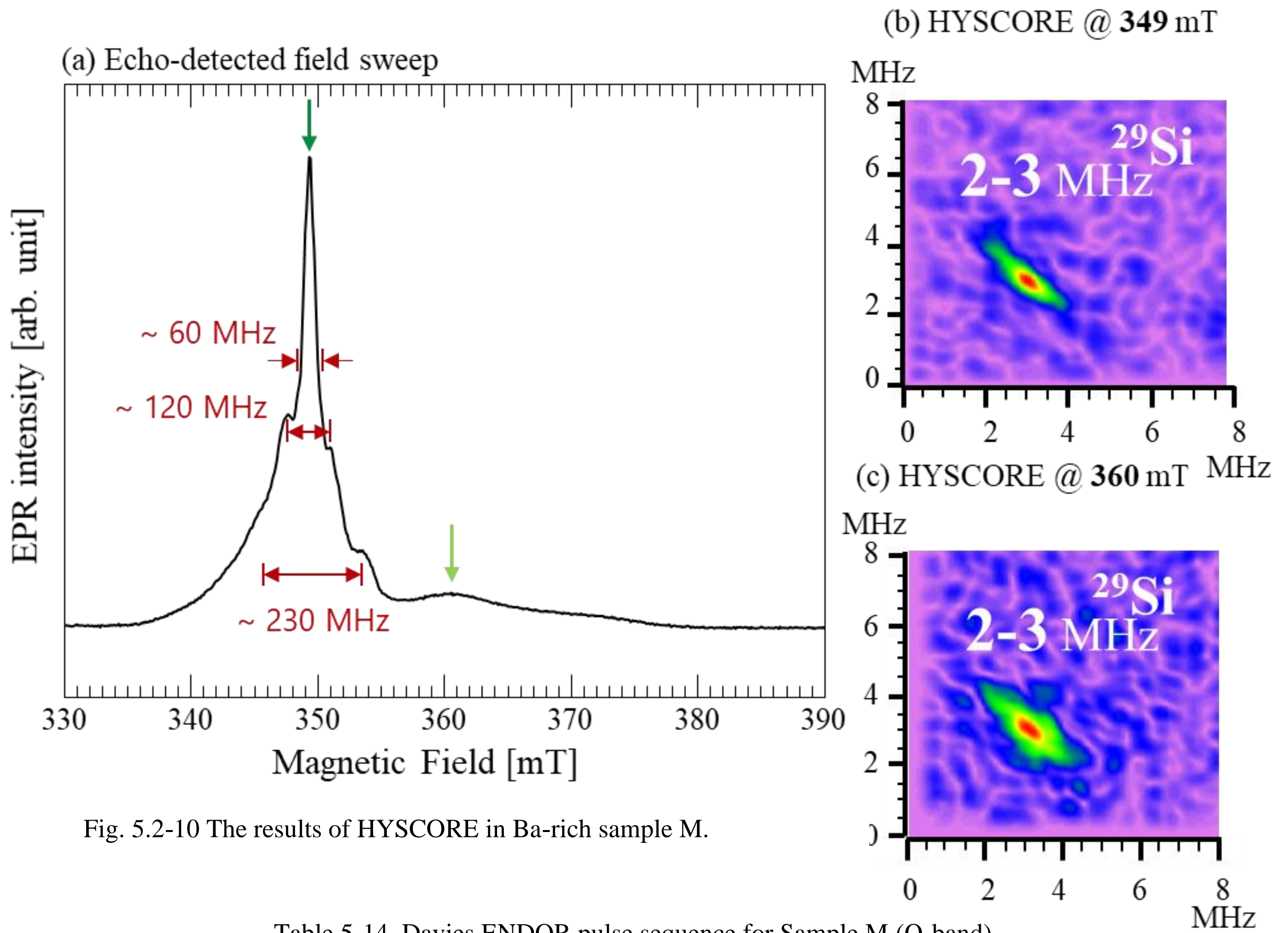

Fig. 5.2-10 The results of HYSCORE in Ba-rich sample M.

Table 5-14. Davies ENDOR pulse sequence for Sample M (Q-band).

Sample	Inversion π pulse	delay	RF		delay	detection		srt
			time	range		t_p	τ	
N	40 ns	1 μs	1 μs	1-195 MHz	25 μs	20 ns	200 ns	1 ms

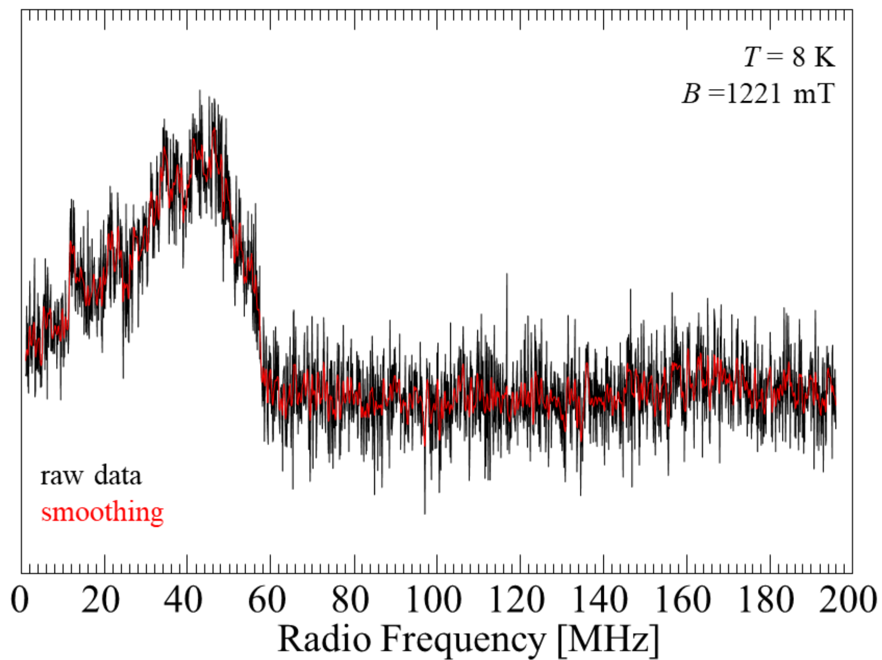

Fig. 5.2-11. The results of ENDOR in Ba-rich sample M.

For the purpose of further improving the sensitivity, the hyperfine coupling constant was measured by ED-NMR measurement as in the case of the Si-rich sample (Table 5-15). As a result, as shown in Fig. 5.2-12(a), the ED-NMR peaks at 30-40 MHz were observed, which almost matches that observed in the ENDOR spectrum. It should be noted that compared with the ENDOR spectrum, the S/N ratio was significantly improved in a relatively short experimental time of 1-2 hours. Also, I show an ED-NMR spectrum recorded at the same position as Fig. 5.2-12(a) with a shoter shot repetition time (srt) of 1 ms in Fig. 5.2-12(b). In addition to the ED-NMR peaks observed at srt = 10 ms, ED-NMR peaks of 80-100 MHz and 150-165 MHz were also detected. These values almost coincide with the values of the hyperfine coupling constants shown in Fig. 5.2-10(a). In particular, the ED-NMR peak at 30-40 MHz agrees well with the ENDOR result. On the other hand, as for the peaks at 80-100 and 150-165 MHz, further experiments are needed while these signals are likely to correspond to hyperfine constants of paramagnetic center(s) with shorter T_1 based on the fact that they were detected when shot repitition time was set to shorter value. I note that no such shot repetition time dependent signal was observed in Si-rich samples.

Table 5-15 ED-NMR pulse sequence for Ba-rich Sample N (Q-band).

Sample	HTA			delay	Detection			srt
	Amp	length	Range		t_p	τ	Integration	
M	5 %	10 μs	± 256 MHz	10 μs	400 ns	2.5 μs	2 μs	10 & 1 ms

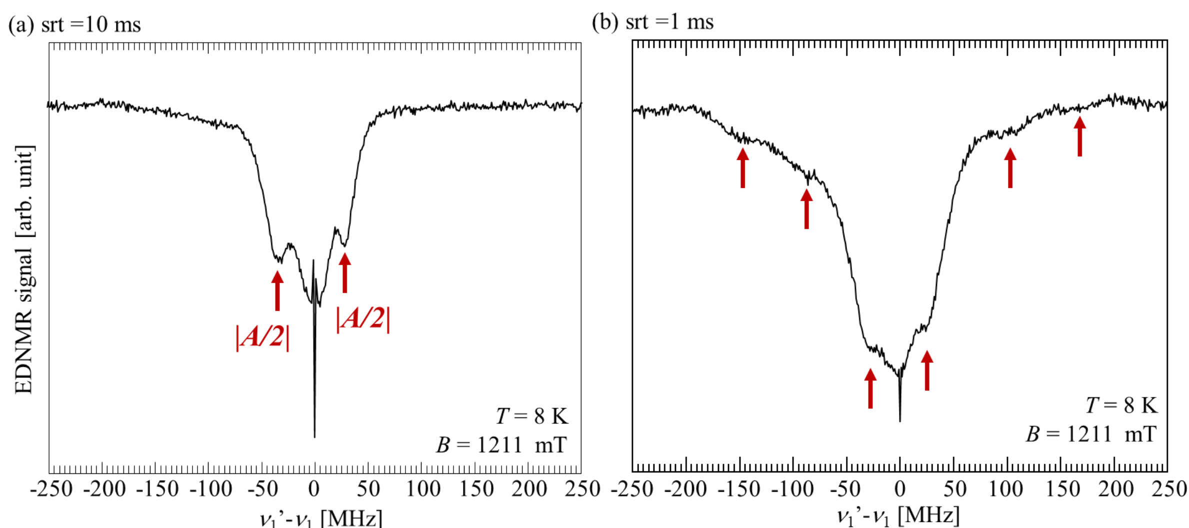

Fig. 5.2-12 The results of ED-NMR for Ba-rich sample N with shot repetition time (srt), (a) srt = 10 ms and (b) srt = 1 ms.

Hyperfine coupling (Ba-rich): HYSCORE → small $|A|$ = 2-3 MHz with ^{29}Si
ENDOR → a broad spectrum, $|A|$ ~ 80 MHz
ED-NMR → large $|A|$ ~ 70–80 (and more) MHz

5.2.3. Summary

Figures 5.2-13-18. show the result of ED-NMR performed to measure the strong hyperfine coupling constant of Sample I-N. Table 5-16 summarizes the observed ED-NMR peak positions.

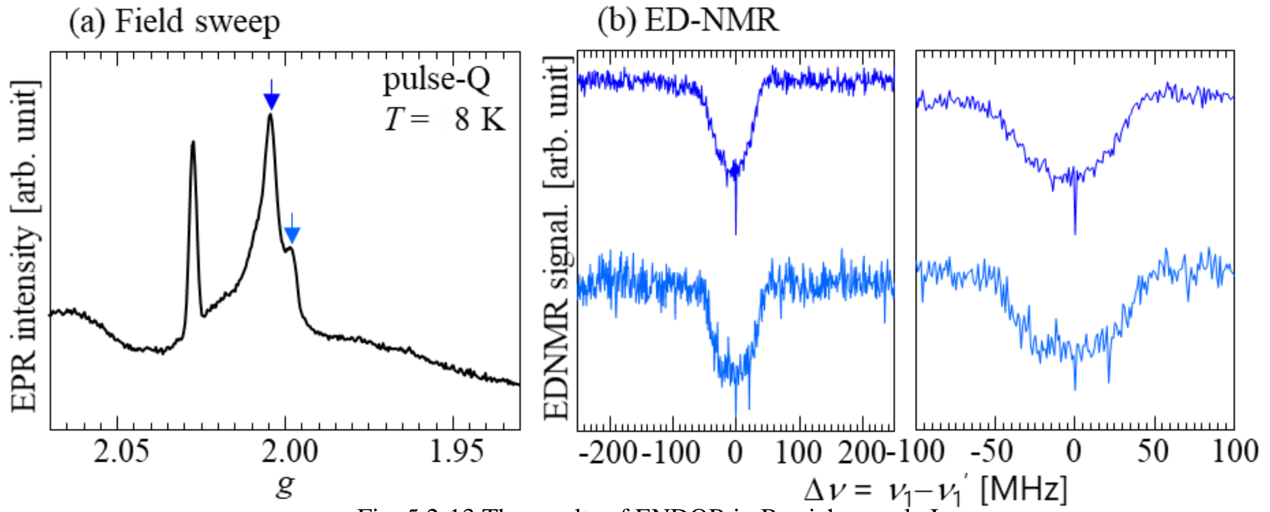

Fig. 5.2-13 The results of ENDOR in Ba-rich sample I.

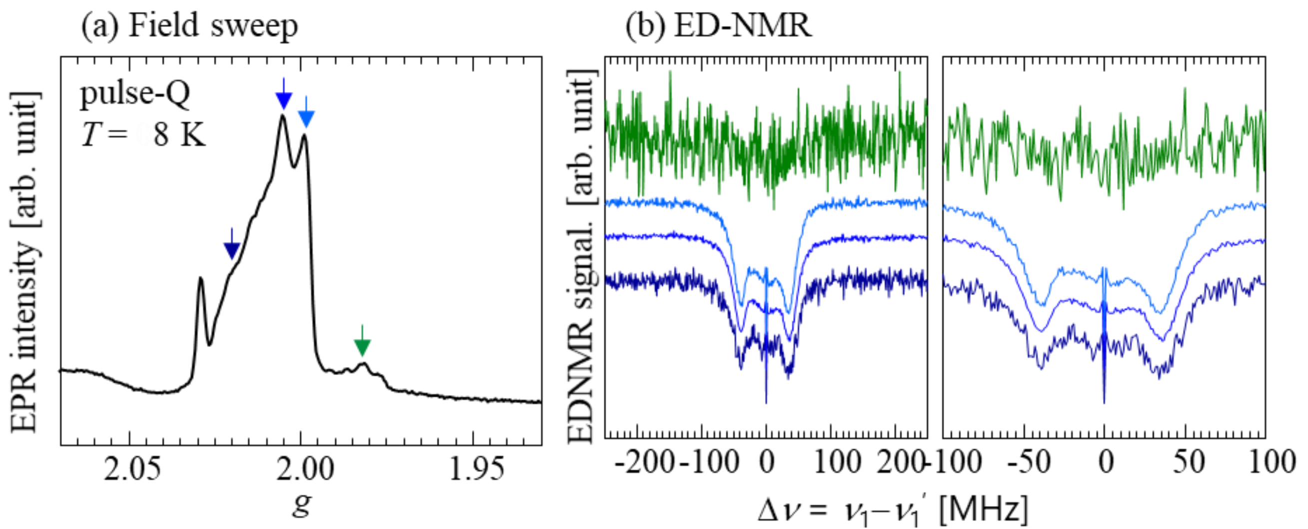

Fig. 5.2-14 The results of ENDOR in Ba-rich sample J.

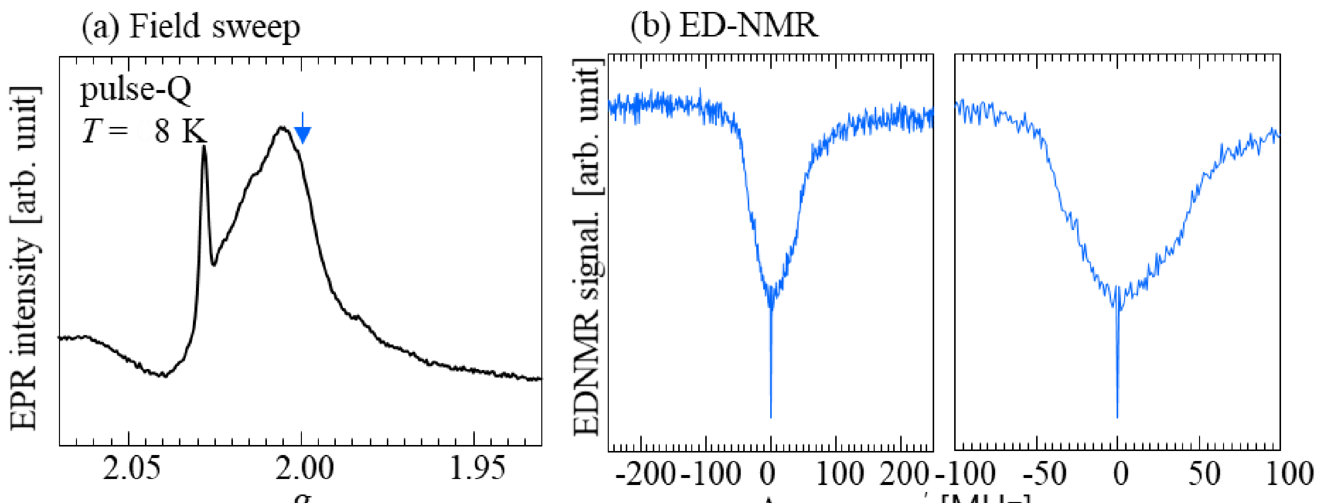

Fig. 5.2-15 The results of ENDOR in Ba-rich sample K.

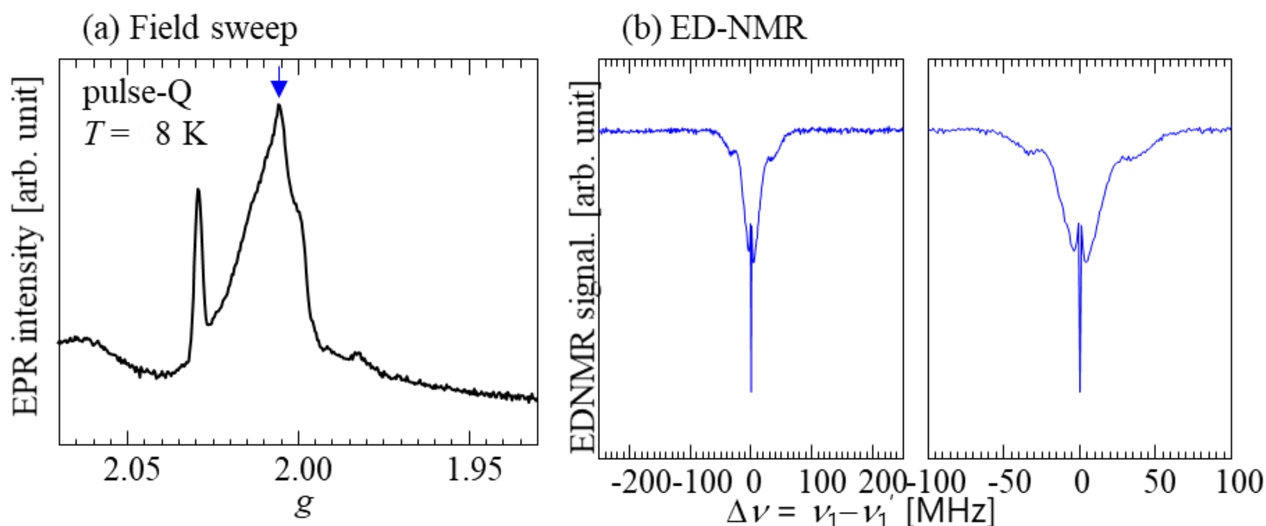

Fig. 5.2-16 The results of ENDOR in Ba-rich sample L.

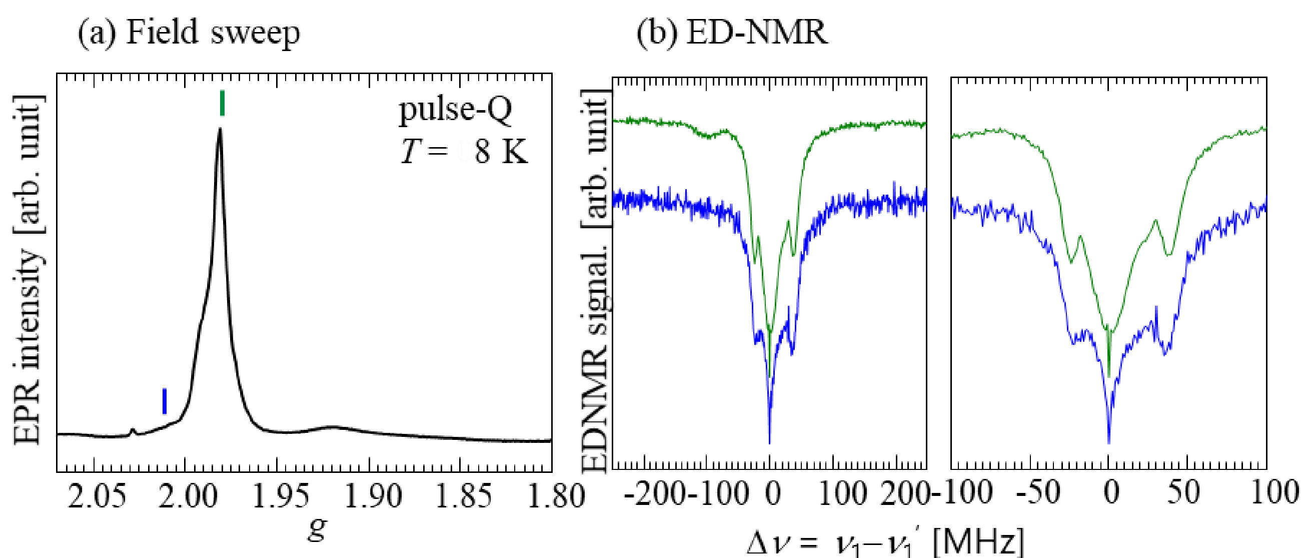

Fig. 5.2-17 The results of ENDOR in Ba-rich sample M.

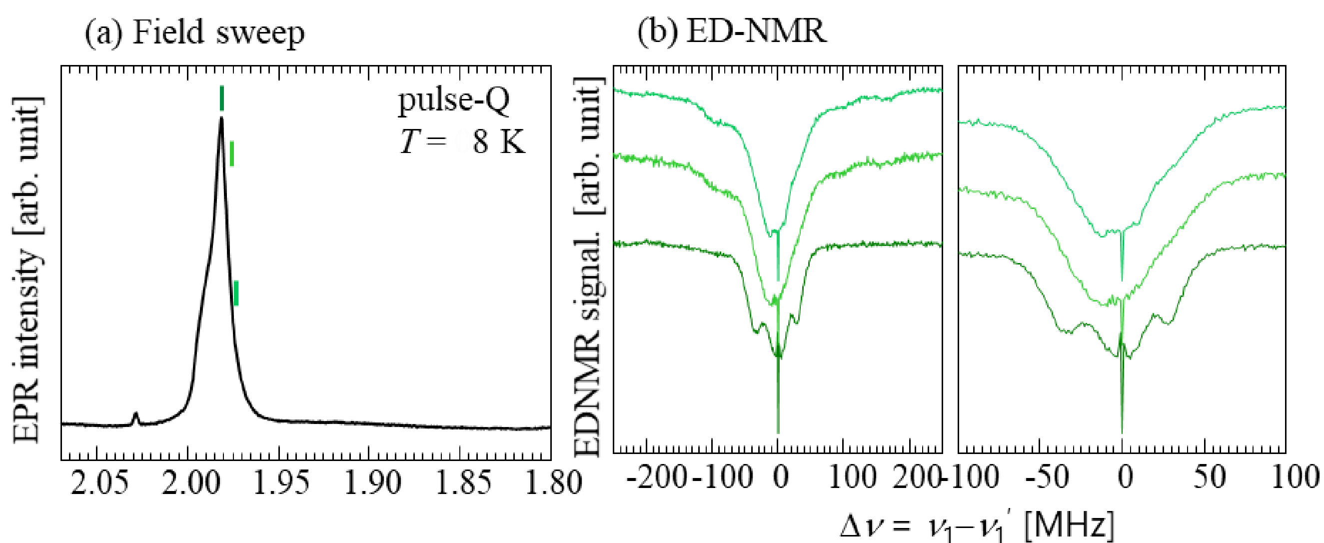

Fig. 5.2-18 The results of ENDOR in Ba-rich sample N.

Table 5-16. ED-NMR peak positons for Sample I-N at different magnetic field (Q-band).

Sample	ED-NMR peak position [MHz]					
	2.02	2.01	2.00	1.98		
I	-	-25, +20	-25, +20	-	-	-
J	-39, +35	-39, +35	-39, +35	low S/N	-	-
K	-	-	-28 +35	-	-	-
L	-	-33, +34	-	-	-	-
M	-	-22, +35	-	-98, -24, +24, +38	-	-
N	-	-	-	-35, +29	-89, -14, +29, +92, +162	-165, -88, -16, +29, +95, +164

ED-NMR spectra indicate the large hyperfine couplings in $BaSi_2$.

This time, often asymmetric ED-NMR spectra were observed. In previous reports, ED-NMR spectra have been observed at symmetric positions.[168-170] Also, the observed ED-NMR signals in this study are very broad compared to previous reports. It may be considered that one of the factors of such asymmetry is that a plurality of ED-NMR signals are superimposed to form an apparently asymmetric shape. Regarding this point, improvement of resolution is expected by ED-NMR measurement in W-band (~ 94 GHz).[168] Since ^{135}Ba (or ^{137}Ba) has $I > 1/2$, it is also necessary to consider the influence of the nuclear quadrupolar interactions. Judging from the nuclear Zeeman frequencies of ^{29}Si, ^{135}Ba, and ^{137}Ba, almost all the ED-NMR peaks are consider to correspond to the value of $|A/2|$. However, since there is no information on quadrupole tensors of Ba nuclei in this material, I don't state that the ED-NMR peak positions are equal to $|A/2|$. I will discuss these results based on the DFT results later in section 5.6.

In this section, we succeeded in observing the hyperfine coupling constants in $BaSi_2$ for the first time by applying ED-NMR. At the same time, there are many unclear points as described above. It is necessary to carry out additional experiments and further research based on simulations.

5.3. Single Crystal

In order to determine principal axes of g-tensors and hyperfine tensors, I performed EPR studies on single crystals of $BaSi_2$. However, it was hard to obtain 'pure' single crystals with enough amount to detect EPR spectra. After much considerations, I managed to measure the spectra of (probably) single crystals. Although the studies in this section are still under investigation, I have already gotten some interesting results as I describe below.

5.3.1. Sample preparation

Monocrystalline $BaSi_2$ were obtained fromAr-arc melted samples with different atomic ratios, Ba-rich and Si-rich. The samples prepared by the Ar-melting method were crushed and then I picked a small piece of samples. I also tried to prepare "pure" crystals by the vertical Bridgeman methods by using the Ar-arc melted samples as a precursor (Ba : Si = 1: 2.06 for Si-rich, 1.94 for Ba-rich). Unfortunately, the samples made by this method were unstable.

Optical microscopic images of the samples are shown in Figs. 5.3-1. As can seen from Figs. 5.3-1, their cleavage faces are not flat, especially for Ba-rich. Hence, I am not sure they are pure single crystals. Further experiments such as XRD meaurements are needed for the certifications. In this study, I define samples' dirrections A, B, and C tentatively.

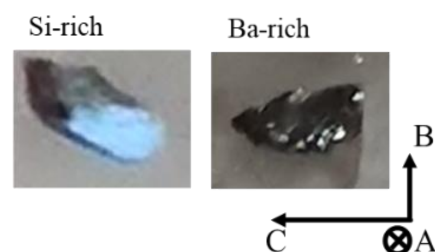

Fig. 5.3-1. Optical microscopic images of Si-rich (left) and Ba-rich (right). Dirrections A, B, and C are difined tentatively.

The picked samples were set on the plastic sheet by a glue (cyanoacrylate) which is inactive with $BaSi_2$ and possess no paramagnetic centers. After being glued on the holder, I put it into an EPR tube. The sample arrangements toward static magnetic field B_0 are also shown in Fig. 5.3-2.

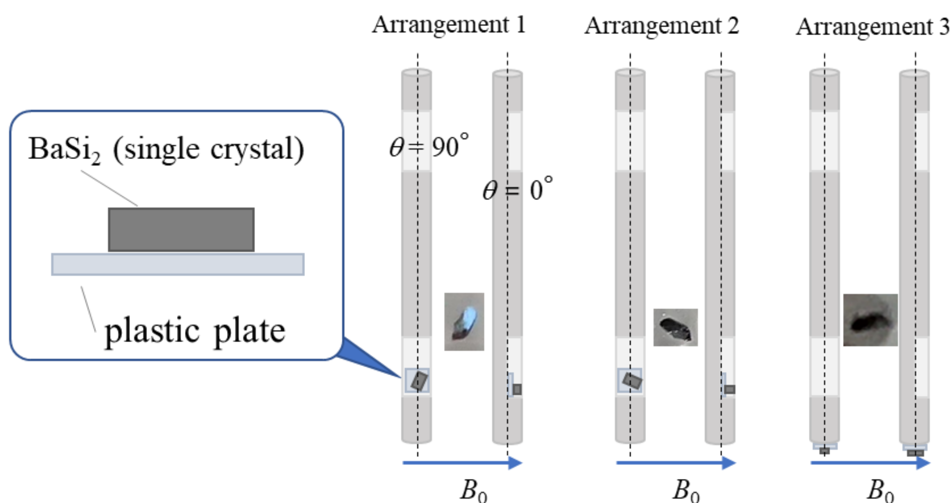

Fig. 5.3-2. Arrangement of samples. In arrangement 1, I define the angle (θ) toward static magetic field (B_0) is equal to 0 deg when direction A // B_0 and direction A and B become perpendicular and parallel toward B_0 at θ = 90 deg. Similarly, in arrangement 2, ϕ= 0 (A // B_0) and ϕ = 90 (A $\perp$ B_0, C // B_0) deg, and also, in arrangement 3, ψ = 0 (B // B_0) and ψ = 90 (C $\perp$ B_0, B // B_0) deg.

5.3.2. Si-rich Sample

In order to reveal the full components of g-tensor and hyperfine tensors, I measured angular dependence by using cw-X-band EPR at three different arrangements. As I show in Figs. 5.3-3, I observed the EPR lines move as I change the angles toward to the applied magnetic field. The range I observed the EPR line of single crystal (SC) were within those of the powder samples (Fig. 5.3-4). Comparing with the powder patterns, each EPR line was narrow and made the spectra more complicated. This indicated that there were hyperfine interactions even in Si-rich samples.

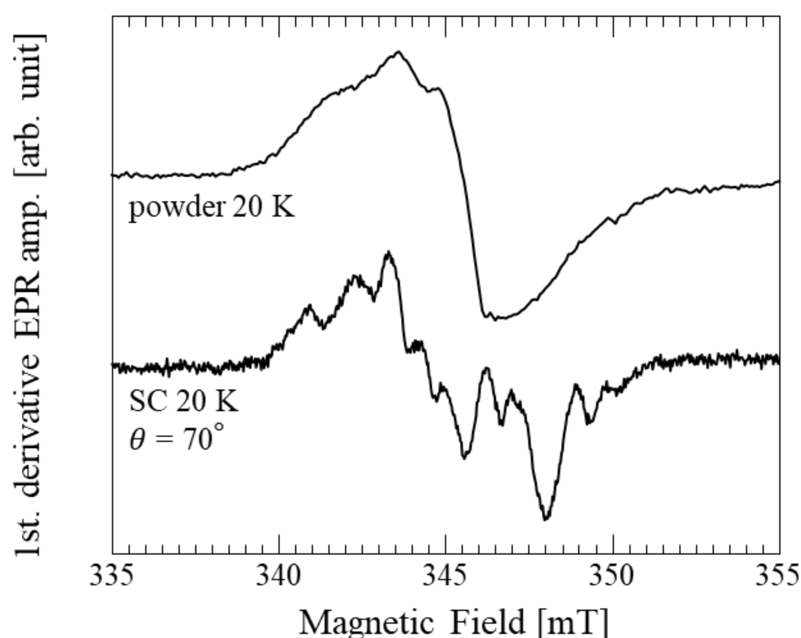

Fig. 5.3-4. EPR spectra of Si-rich powder (Sample K) and single crystal (SC) samples (θ = 70 deg) at 20K. Complicate structures in the SC sample indicate hyperfine interactions due to decrease of each EPR line width.

I focused on a few angles where I observed the ralatively symmetric spectra (Figs. 5.3-5). When hyperfine stuructures were observed in this study, the EPR line without the hyperfine structures should be observed due to the natural abundance of Si and Ba atoms. Also, I have to keep it in my mind that the Si-rich samples contain at least two different paramagnetic centers as I discussed in previous sections. It was difficult to complete analysis of the spectra because it is unknown how the crystal axes (*a*, *b*, *c*) correspond to each arrangement (A, B, C). However, Figs. 5.3-5 show some interesting information about the hyperfine coupling constant. Two symmetric structures were observed in Fig. 5.3-5(a) as I indicated by different marks (●, ▲). Each spectrum was separated by 3.49 (●) and 1.89 (▲) mT with their center at 344.4 (●) and 344.3 (▲) mT. One of these values ($|A|$ = 53 MHz) seems to correspond to that detected by ED-NMR measurements (Table 5-16). The difference between the two is due to their anisotropy. The anisotropic hyperfine components are also predicted from the comparison of the spectra recorded at different angles and arrangements. As it is clear in Fig. 5.3-5(b), much more complicated structures were confirmed.

Single crystal of the Si-rich sample has

- much angular dependence (g-tensors and/or hyperfine tensors are anisotropic)
- complicated spectra than powder (hyperfine structures become visible)

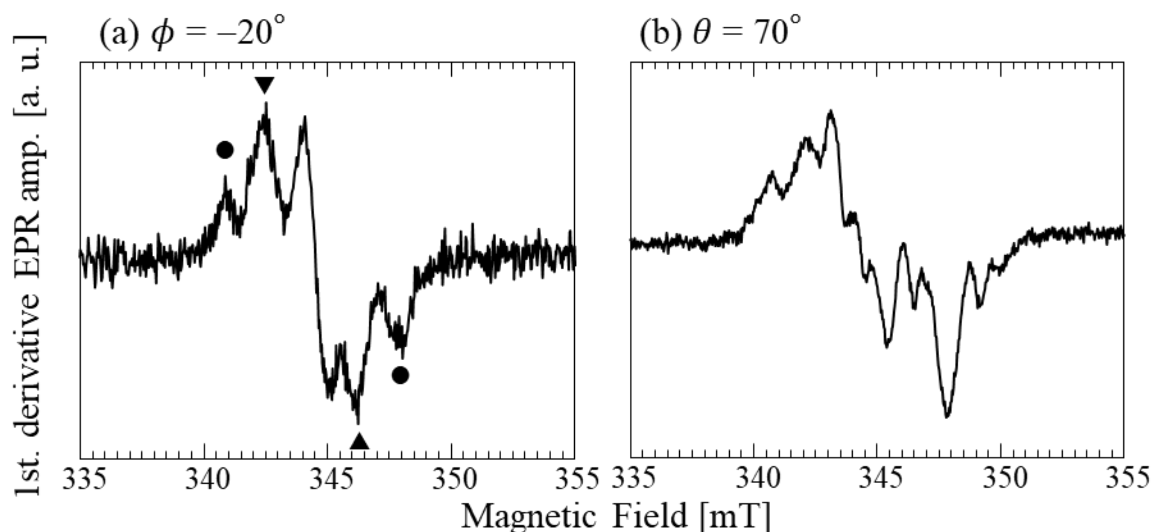

Fig. 5.3-5. EPR spectra of Si-rich single crystal at (a) $\phi = -20$ deg and (b) $\theta = 70$ deg. The substractures marked circles and triangles in (a) are separated by 3.49 (●) and 1.89 (▲) mT, respectively. Much more complicated spectrum was observed in (b).

5.3.3. Ba-rich sample

For the Ba-rich samples, the same EPR measurments were performed as the Si-rich sample. In contrast to Si-rich sample, the observed spectra were less anisotropic (Fig. 5.3-6). Furthemore, each EPR line was well resolved because of their narrow line width (Fig. 5.3-7).

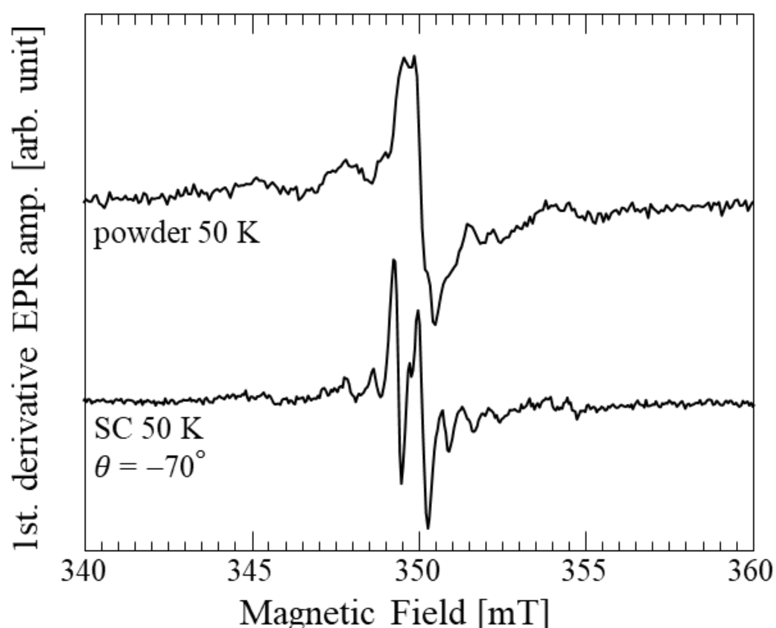

Fig. 5.3-7. EPR spectra of Ba-rich powder (Sample N) and single crystal (SC) samples ($\theta = -70$ deg) at 20K.

For the same reason as the Si-rich sample, I focus on one of the symmetric spectra (Fig. 5.3-8(a)). Assuming the central line without hyperfine interactions, the spectrum is explained by hyperfine interactions with one ^{29}Si and two ^{137}Ba (or ^{135}Ba) as I show each component of the whole spectra schematically in Fig. 5.3-8(b). The value observed in SC are 22 MHz for ^{29}Si, 45 and 84 MHz for Ba whose values are aggrements with those detected in ED-NMR.

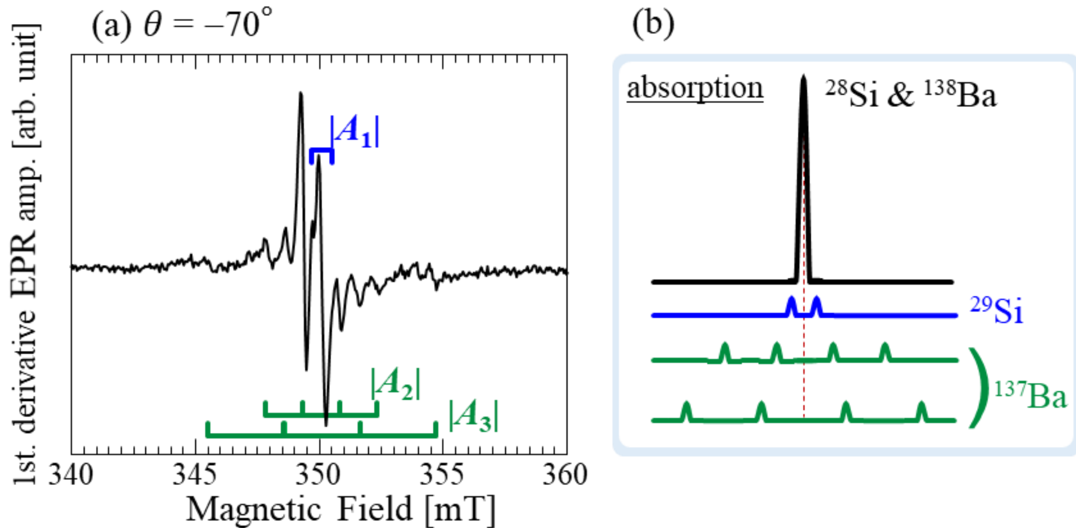

Fig. 5.3-8. (a) EPR spectra of Ba-rich single crystal at θ = −70 deg. Each line is explained by three different hyperfine couplings as depicted in (b) schematically. The central line contains no hyperfine coupling following natural abundance of Si and Ba isotopes.

Single crystal of the Ba-rich sample has

- less angular dependence (*g*-tensors and/or hyperfine tensors are anisotropic)
- clearer hyperfine structure with ^{29}Si and ^{135,137}Ba ($|A|$ ~ 22, 45, 84 MHz)

5.3.4. Summary

I measured the angular dependence of EPR for Si-rich and Ba-rich samples in order to determine their g- and hyperfine tensors. In the Si-rich sample, I found there are some hyperfine structures that were not resolved in the powder samples due to inhomogeneous broadening. Also, the EPR spectra changed drastically upon varying the angles and arrangements, suggesting that the paramagnetic centers in Si-rich have anisotropic g- and/or hyperfine tensors. In Contrast to the Si-rich sample, I observed less anisotropic EPR spectra in Ba-rich sample. Because of narrow line width, I could explain that the spectra are constituted by some hyperfine couplings with ^{29}Si and two ^{135}Ba (and/or ^{137}Ba). The values of 22, 45, 84 MHz seem to correspond to those detected in ED-NMR spectra.

In order to complete assignments the observed EPR lines to each paramagnetic center, further experiments such as XRD are under examining.

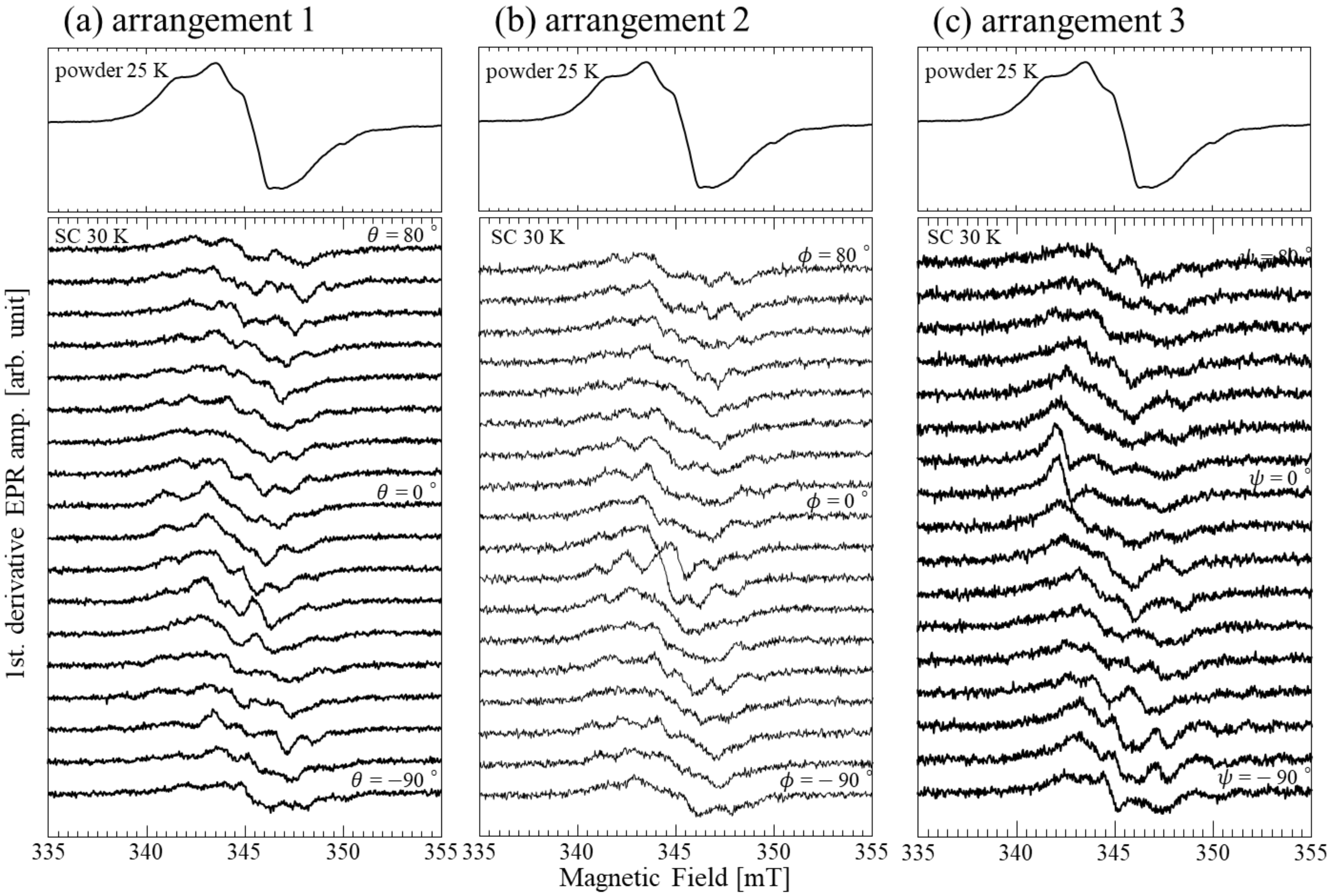

Fig. 5.3-3 Angular dependence of EPR spectra on Si-rich sample at (a) arrangement 1, (b) arrangement 2, and (c) arrangement 3.

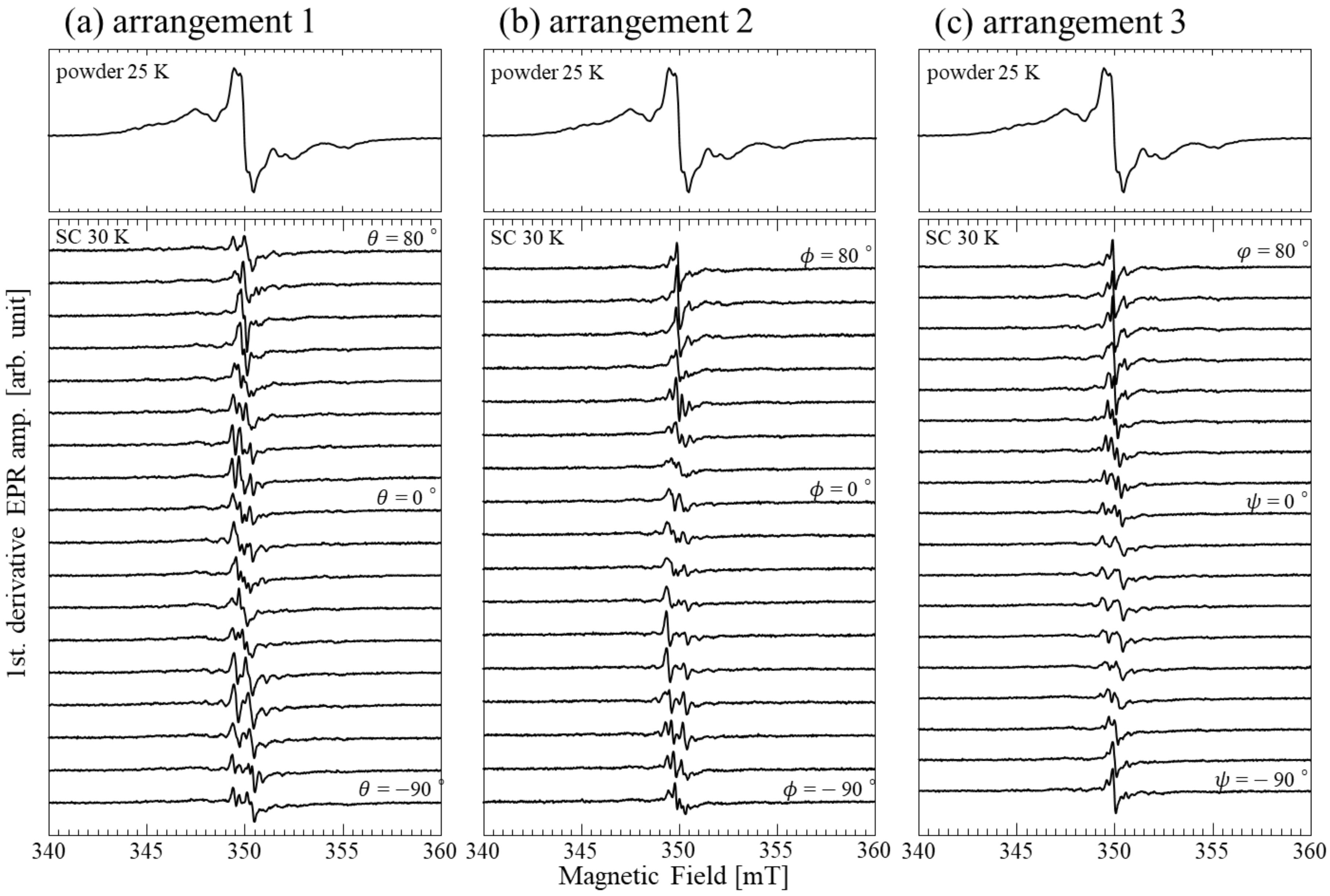

Fig. 5.3-6 Angular dependence of EPR spectra on Ba-rich sample at (a) arrangement 1, (b) arrangement 2, and (c) arrangement 3.

5.4. Simulation

In this section, I show the results of EPR spectrum simulated by using Easyspin (Matlab).[171] As described above, I confirmed that a plurality of paramagnetic centers existed in each of the Si-rich and Ba-rich samples. Attempts to separate each paramagnetic center through temperature dependence, microwave power dependence, and pulsed EPR measurements did not result in complete separation. Therefore, based on these experimental results, I tried to separate EPR spectra through the simulation of experimental results using thinkable paramagnetic centers.

5.4.1. Results

In this study, the reliability of the simulation was improved by fitting the experimental results of cw-X-band and Q-band simultaneously.

Si-rich sample

The Si-rich samples have broader EPR spectra than those of Ba-rich samples. Strong hyperfine couplings of about 30-40 MHz were observed by ED-NMR measurements, but I couldn't see such hyperfine structures on the results of cw-X-band and Q-band spectra because of their line width. Therefore, I focused on g value in the simulation, and considered the contribution of unresolved hyperfine coupling as Hstrain.

The temperature dependence and microwave power dependence of the EPR spectrum of the Si-rich samples indicate that the relatively sharp EPR line (the Defect 2) exists at g ~ 2.005. Therefore, the initial value of principle values of the g-tensor of the Defect 2 were determined first. From the result of cw-Q-band, I could easily anticipate that $g_1' = 2.005$ and $g_2' = 1.997$. Using these values, I tryed to reproduce the experimetal results, assuming the defect has an axial g-tensor ($g_{\parallel} = g_1$, $g_{\perp} = g_2$). As seen in Figs. 5.4-1, however, it was impossible to explain the experimental results, suggesting the Defect 2 possesses a biaxial anisotropy.

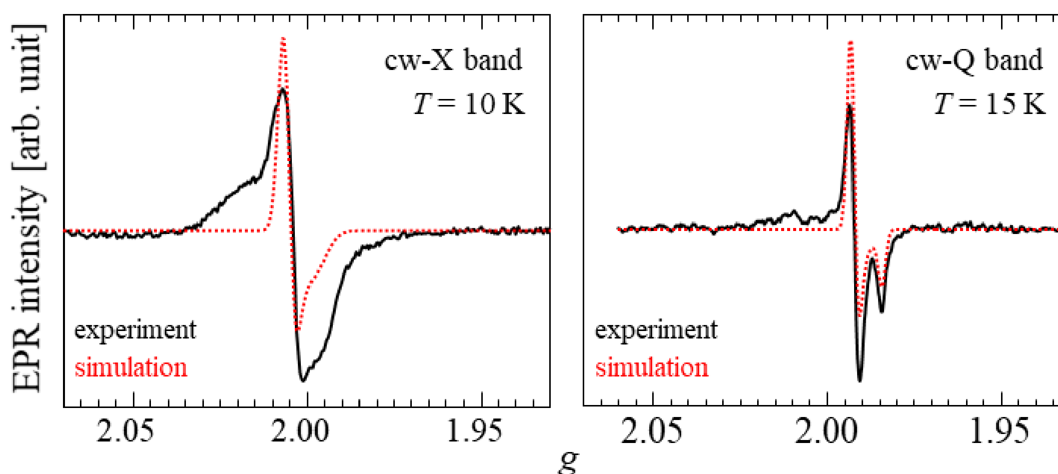

Fig. 5.4-1 Experimental and simulated spectra of Sample I.

Although another main value of the g-tensor $g_3' = 2.0178$ was considered as its candidate, it should be excluded due to the temperature dependence and the microwave power dependence. On the other hand, from the results of pulse-Q-band magnetic field sweep (Fig. 5.4-2), a shoulder was observed at g ~ 2.009. The results of fitting the pulse-Q-band magnetic field sweep spectrum with these values ($g_1 = 2.009$, $g_2 = 2.005$, $g_3 = 1.998$) as initial values are the red dotted lines in Figure 5.4-2.

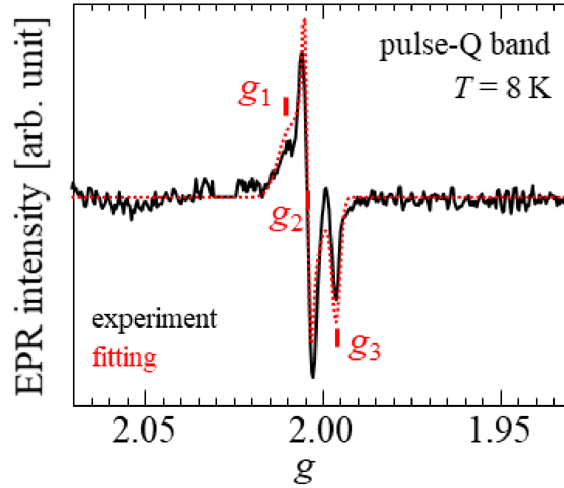

Fig. 5.4-2 Filed sweep spectrum of Sample I. A red dot line indicates a fitting spectra of the Defect 2, assuming the principle values of g-tensor were set g_1 = 2.009, g_2 = 2.005, g_3 = 1.998 as initial values.

Next, I discuss initial values of the Defect 1. The EPR line intensity of the Defect 1 increases as atomic ratio of Ba to Si, x, approaches 2. Therefore, the initial values of the principle values of the g-tensor of the Defect 1 were determined based on samples K and L as shown in Fig. 5.4-3. Here, g_2 was taken into account by considering the overlap with the Defect 2 and widening the constraint conditions for fitting.

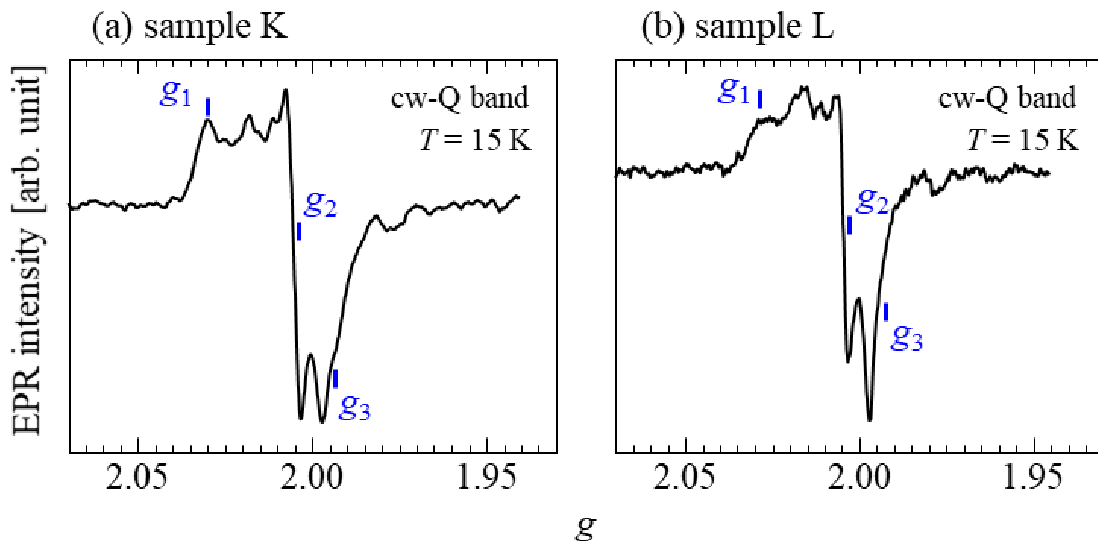

Fig. 5.4-3 EPR spectra of (a) Sample K and (b) L. In these samples, principle values of g-tensor of the Defect 1 seemed clear.

Finally, each EPR line width was evaluated by g strains and H strains. First, I determined g strains based on the result of cw-Q-band, and then the initial value of H strains were determined so that the results of cw-X-band could be reproduced. The results of the fitting performed on each sample based on the above initial values are shown in the fig. 5.4-4. The obtained fitting parameters are as shown in Table 5-17.

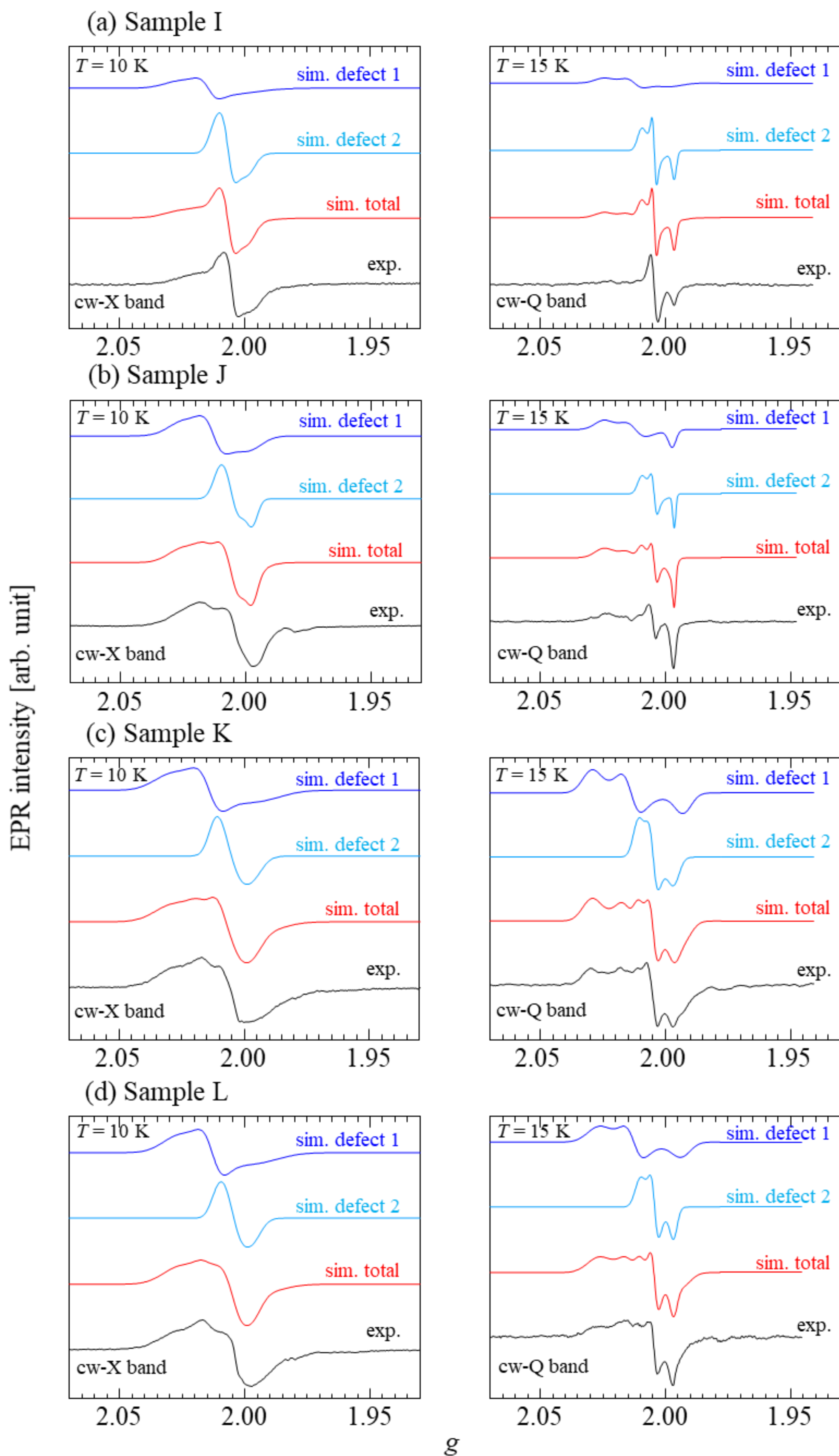

Fig. 5.4-4 EPR spectra of (a) Sample I - (d) L. Simulation EPR line of the Defect 1, the Defect 2, total (the Defect1 + the Defect2), and experimental data are shown as blue, light blue, red, and black solid lines, respectively.

Table 5-17 Fitted values for simulation of Si-rich samples.

Label	I	J	K	L
Defect 1				
g	(2.0249, 2.0121, 1.9975)	(2.0251, 2.0121, 1.9975)	(2.0297, 2.0138, 1.9929)	(2.0271, 2.0126, 1.9935)
g strain	(0.0075, 0.0065, 0.0100)	(0.0075, 0.0075, 3.05×10^{-6})	(0.0075, 0.0066, 0.0060)	(0.0100, 0.0070, 0.0062)
H strain [MHz]	(61, 10, 87)	(55, 15, 60)	(70, 27, 100)	(55, 16, 100)
Defect 2				
g	(2.0098, 2.0046, 1.9966)	(2.0098, 2.0046, 1.9966)	(2.0111, 2.0049, 1.9966)	(2.0103, 2.0043, 1.9966)
g strain	(0.0035, 0.001, 0.0005)	(0.0035, 0.0015, 5.83×10^{-6})	(0.0045, 0.0028, 0.0047)	(0.0045, 0.0023, 0.0027)
H strain [MHz]	(25, 22, 34)	(25, 29, 24)	(25, 40, 40)	(25, 34, 37)
Ratio of the Defect 1 to the Defect 2				
	1.14	2.50	2.83	2.86

Simulation of powder pattern of the Si-rich:

- Defect 1: g_1 = 1.993-1.998, g_2 = 2.012-2.014, g_3 = 2.025-2.030
- Defect 2: g_1 = 1.997, g_2 = 2.004-2.005, g_3 = 2.010-2.011

Ba-rich sample

First, I determined the initial values of the Defect 3 as g_1 = 1.930, g_2 = 1.910, g_3 = 1.844 from the what is observed in the cw-Xband and cw-Q-band spectra. The line width was set to initial values in the same manner as in the procedure used for the Si-rich samples.

Next, the narrow and less anisotropic EPR line at g ~ 1.998 has hyperfine coupling based on its temperature dependence and cw- and pulse- spectra (the Defect 5). Prior to the simulation, possible EPR lines were considered from the viewpoint of Si and Ba isotopes. Figures 5.4-5 shows how many ^{29}Si are likely to be present in a system with N Si atoms based on the natural abundance of ^{29}Si. As can be seen from the figure, when I focus on one Si_4 tetrahedron constituting $BaSi_2$, the probability that two or more ^{29}Si are included in one Si_4 tetrahedron is about 1% . In an unit cell, the probability of two ^{29}S is increases to 14%. In the 2×2×2 supercell, it is most likely that there are 6 or 7 ^{29}Si atoms in the system. What is important now is that by arranging the histogram symmetrically, I can imagine the outline of EPR lines which should be observed in real experiments. Since at least three hyperfine structures are observed in the cw-X-band EPR spectra, if the unpaired electrons have a charge distribution spanning at least about 16 Si atoms, I can interprit that the three hyperfine structures stem from the interactions with three different ^{29}Si. However, considering that the hyperfine interaction is a local interaction between the electron spin and the nuclear spin, if the charge distribution covers 16 Si atoms, the hyperfine coupling constant itself should be small even in X-band. Therefore, it can be difficult to expect a value as large as those observed in experiments. Thus, I also have to consider the contributions of ^{135}Ba and/or ^{137}Ba as well as ^{29}Si.

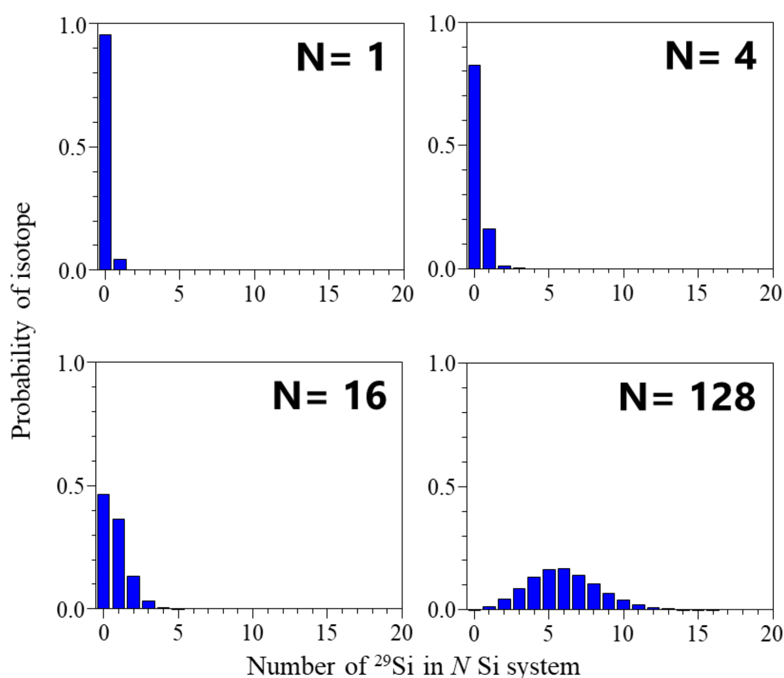

Fig. 5.4-5 Histograms of isotope Si in *N* atoms system (^{29}Si: I =1/2, 4.68 % in natural abundance). N = 1, 4, 16, and 128 correspond to one Si atom, one Si_4 tetrahedron contituting $BaSi_2$, unitcell of $BaSi_2$, and 2×2×2 supercell, respectively.

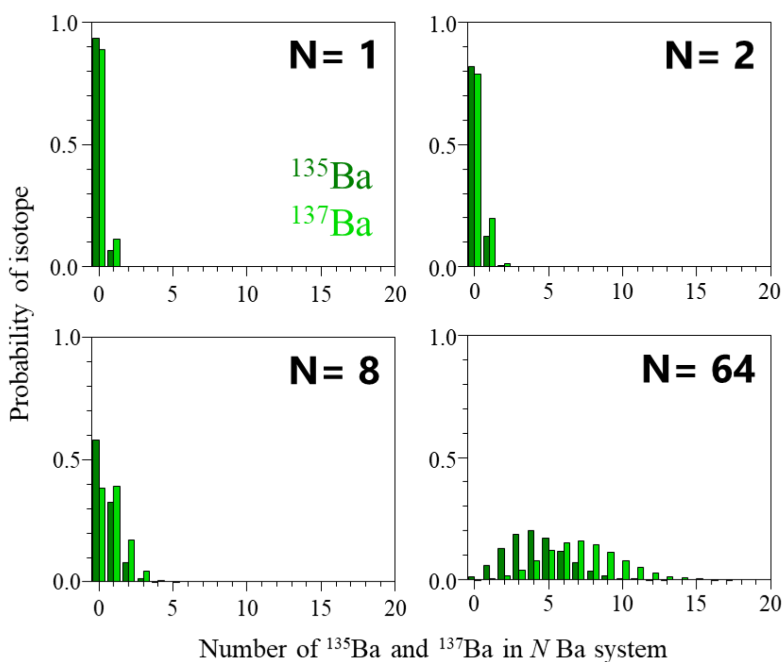

Fig. 5.4-6 Histograms of isotope Ba in *N* atoms system (^{135}Ba: I =3/2, 6.59 % and ^{137}Ba: I = 3/2, 11.23 % in natural abundance). N = 1, 2, 8, and 64 corresponded to one Ba atom, Ba atoms surrounding one Si_4 tetrahedron, unitcell of $BaSi_2$, and 2×2×2 supercell, respectively.

From the above considerations, the following two are considered as the origins of the hyperfine structures observed in Ba-rich samples.

1. One of the three hyperfine structures might come from the interaction between unpaired electrons and ^{29}Si. However, it is difficult to imagine all the three structures originate from only ^{29}Si atoms.

2. ^{135}Ba and ^{137}Ba both have I = 3/2, and their natural abundances are 6.59 and 11.23%, respectively. Figures 5.4-6 show a histogram similar to that made with ^{29}Si. Unlike the case of Si, in the case of hyperfine interaction with Ba, 4 (= 2×3/2 + 1) hyperfine structures are expected. Some of the structures can be explained in such way. In smaller systems, unpaired electrons are more localized, and as a result, a strong hyperfine coupling constant is expected.

I focus on the results of cw-X-band and Q-band at 50 K. Figures. 5.4-7 show simulation results based on the value of |A| which I obtained from DFT calculations for Si vacancy (V_{Si}^{-}). Here, I assumed $|A_{Si}|$ = 22, $|A_{Ba}|$ = 45 and 84 MHz because I observed at least 3 different ED-NMR signals whose values almost correspond to those of the single crystal.

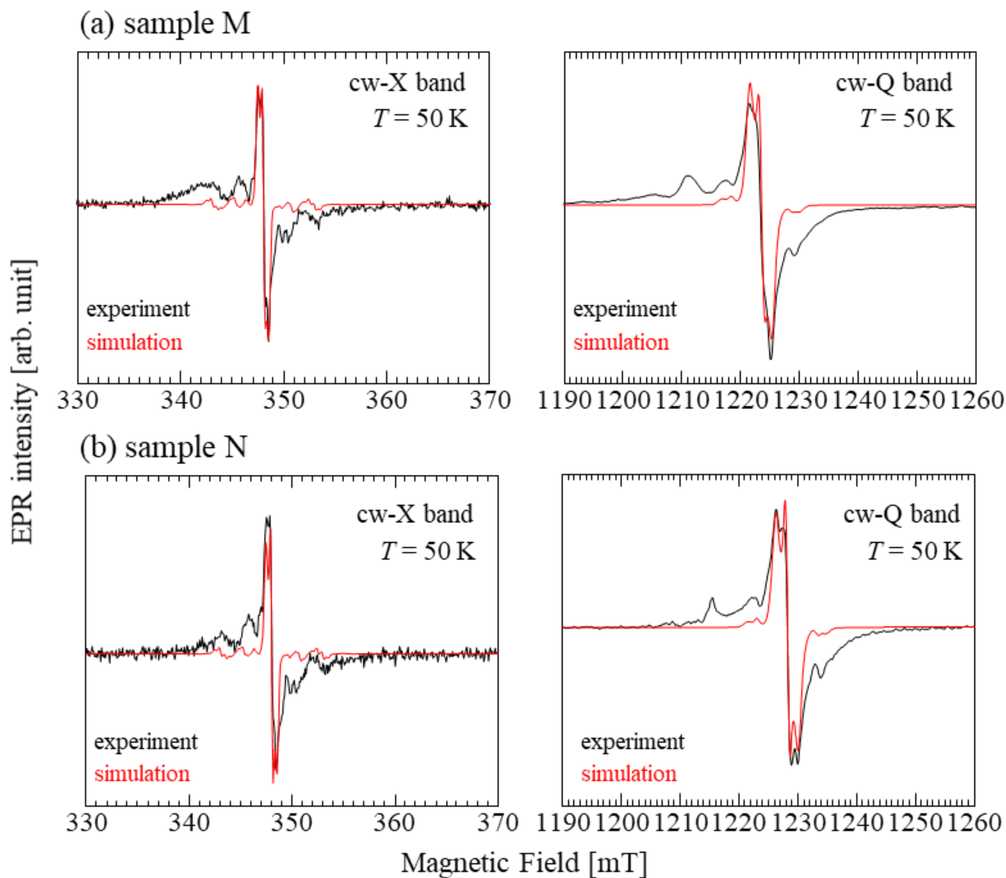

Fig. 5.4-7 Cw-EPR spectra of (a) Sample M and (b) N measured at 50 K. A red dot line indicates simulated spectra of the Defect 5. The initial values are listed in Table 5-18.

From Fig. 5.4-7, peak positions are in very good agreements with the experimental results while the intensities should be improved. On the other hand, as I show the cw-X-band EPR spectra measured at 10 K in Figs. 5.4-8, the intensities divergence from the simulations further increase at positions as indicated by arrows in fig. 5.4-8.

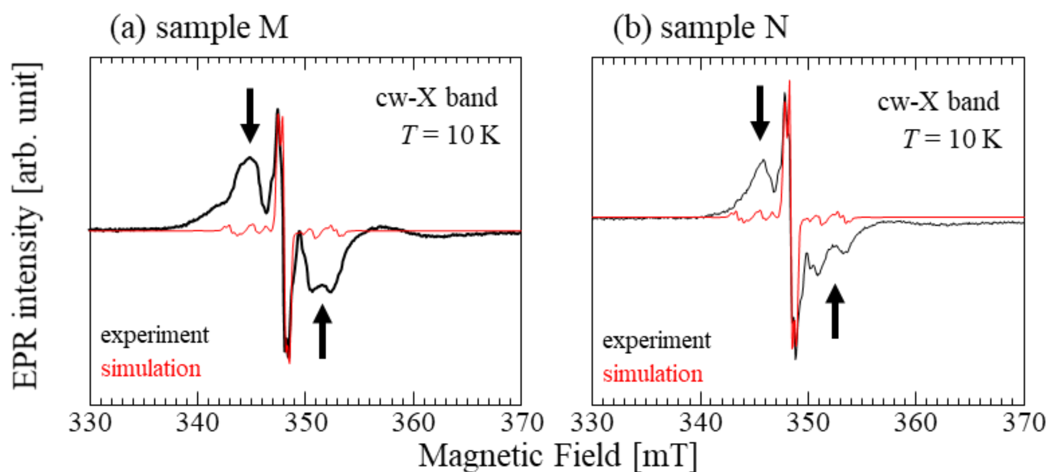

Fig. 5.4-8 Cw-EPR spectra of (a) Sample M and (b) N measured at 10 K. A red dot line indicates simulated spectra of the Defect 5. Large deviations from experimental spectra were confirmed at the positions of black arrows.

From the temperature dependency and the microwave power dependency, it is inferred that this is the contribution of the Defect 4. As I discussed in the previous chapter, the Defect 4 possesses the shorter relaxation times with $S = 1/2$. I couldn't, however, simulate the EPR line from the Defect 4 for the moment.

Taking the existance of the Defect 1 (see in the previous chapter) into the account, I simulated the cw-X-band EPR spectra instead of fitting the spectra (fig. 5.4-9). The set parameters are listed in Table 5-18.

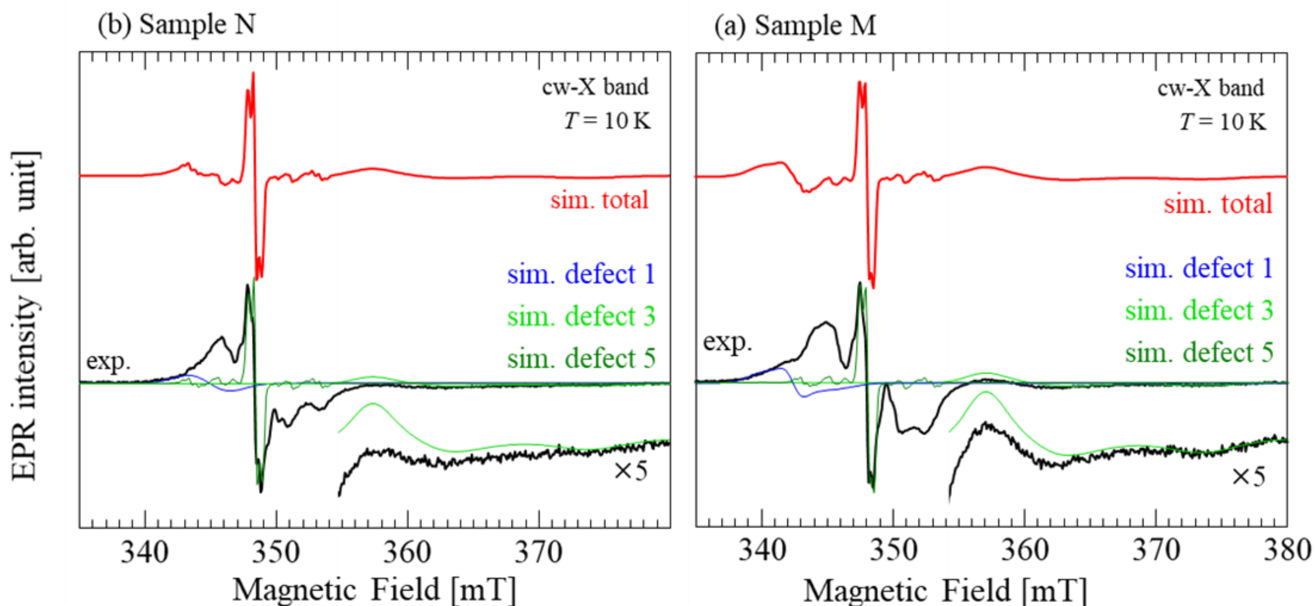

Fig. 5.4-9 EPR spectra of (a) Sample M and (b) N. Simulation EPR line of the Defect 1, the Defect 3, the Defect 5, total (the Defect 1 + the Defect 3 + the Defect 5), and experimental data are shown as light blue, light green, green, red and black solid lines, respectively.

Table 5-18 Initial values for simulation of Ba-rich samples.

Label	M	N
	Defect 1	
g	(2.0271, 2.0126, 1.9935)	(2.0271, 2.0126, 1.9935)
g strain	(0.01, 0.007, 0.006243)	(0.01, 0.007, 0.006243)
H strain	(55, 16, 100)	(55, 16, 100)
	Defect 3	
g	(1.930, 1.910, 1.844)	(1.930, 1.910, 1.844)
g strain	(0.0125, 0.025, 0.02)	(0.0125, 0.025, 0.02)
HF	A_{Si} = 22, A_{Ba} = 45, A_{Ba} = 84	A_{Si} = 22, A_{Ba} = 45, A_{Ba} = 84
	Defect 5	
g	(1.9836, 1.9802, 1.9773)	(1.9832, 1.99798, 1.9768)
g strain	(0.002, 0.0015, 0.002)	(0.002, 0.0012, 0.002)
H strain	(60, 60, 100)	(60, 60, 100)
Ratio of each defect (Defect 2 : Defect 3 : efect 5)		
	1.9 : 5 : 1	0.3 : 4 : 1

Simulation of powder pattern of the Ba-rich:

- Defect 3 : g_1 = 1.844, g_2 = 1.910, g_3 = (1.930)
- Defect 4 : tentative, g_{av} ~ 1.975 at X-band
- Defect 5 : g_1 = 1.977, g_2 = 1.980, g_3 = 1.983-1.984, large hyperfine coupling of 22, 45, 84 MHz

5.4.2. Spin concentrations

The spin concentrations of the powder samples (Samples I-N) were evaluated by using a sample having a known spin concentration. In this study, five TEMPO disolved in orthoterphenyl with different mol/L were used as standard data. Spin concentrations, N_S, are given the following equation, [172,173]

$$N_S = \frac{\mathrm{DI} \cdot V}{\sqrt{P} \cdot B_{\mathrm{m}} \cdot Q \cdot c \cdot S(S+1) \cdot n_{\mathrm{B}} \cdot f(B_1, B_{\mathrm{m}})}.$$

where, DI, V, P, B_m, n_B, Q, c, S, and f are double integrations, volume of sample, microwave power, modulation amplitude, Boltzmann factor, resonator factor, resonator calibraion factor, electron spin, and resonator filled profile, respectively. Also, TEMPO changes magnetization as function of temperatures according to the Curie's law.

$M = C/T$, C : Curie constant

TEMPO dissolved in orthoterphenyl were introduced into an X-band EPR tube at the same height as powdered $BaSi_2$, and measured at the center position of cavity where the spectrum intensity reaches its maximum. In order to correctly estimate the spin concentrations, the measurement were performed at a microwave power of 5 µW at which the EPR spectrum was unsaturated from. The obtained EPR spectra was subtracted the baselines, and then integrated twice to evaluate DI. The obtained from DI were normalized based on the experimental conditions,

Normalized DI $= \frac{DI \cdot T}{\sqrt{P} \cdot B_m \cdot Q \cdot acc. \cdot R.G.}$ by applying the above equation, where acc. and R.G. are accumulations of scans and receiver gain, respectively. In Fig. 5.4-10, I show the normalized DI as a function of mol/L.

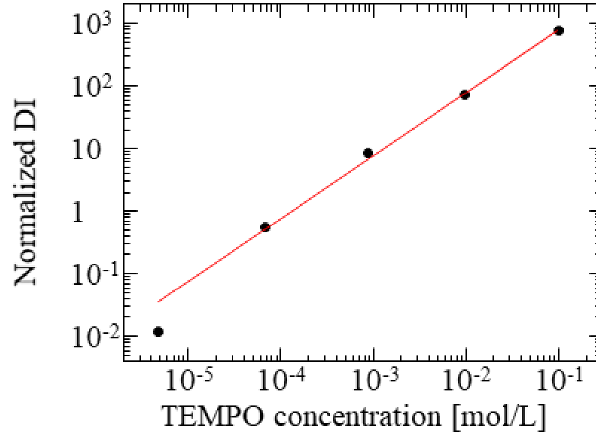

Fig. 5.4-10 Normalized double integration of cw-X-band spectra.

Table 5-19 Experimental conditions

P_{mw} [μW]	B_m [Gauss]	Q	acc.	R.G.	T [K]
5	2	4700	4	$10^3 - 10^6$	10

The same measurement as TEMPO was performed on Samples I-N, and their corresponded mol/L were evaluated from the Normalized DI obtained by comparing with the Fig. 5.4-10. Then, the total spin concentrations, N_{total} were calculated by the following equation in consideration of the filling factor, η. Tabled 5-20 shows the spin densities obtained for each sample.

$$N_{total} = (N_S \text{ [mol/L]}) \times \eta^{-1} \times n_A \times 10^{-3} \text{ [spins/cm}^{-3}\text{]}$$

where n_A is Avogadro's constant. In this evaluations, η was set to 0.5, tentatively. $BaSi_2$ contains a plurality of paramagnetic centers. Therefore, based on the discussion in section 5.4.1, I calculated each spin concentration (Table 5-20) and plotted the concentrations of the provisionally separated EPR lines in fig. 5.4-11.

Table 5-20 Experimental conditions

	Spin concentrations [spins/cm^{-3}]					
	Total	Defect 1	Defect 2	Defect 3	Defect 4	Defect 5
I	4.91×10^{16}	2.62×10^{16}	2.29×10^{16}	–	–	–
J	1.39×10^{17}	9.28×10^{16}	3.71×10^{16}	–	–	8.97×10^{15}
K	1.21×10^{17}	7.99×10^{16}	2.82×10^{16}	–	–	1.32×10^{16}
L	9.72×10^{16}	6.35×10^{16}	2.22×10^{16}	–	–	1.15×10^{16}
M	1.44×10^{18}	8.02×10^{16}	–	4.22×10^{16}	1.11×10^{18}	2.11×10^{17}
N	1.04×10^{18}	2.27×10^{16}	–	7.56×10^{16}	6.43×10^{17}	3.02×10^{17}

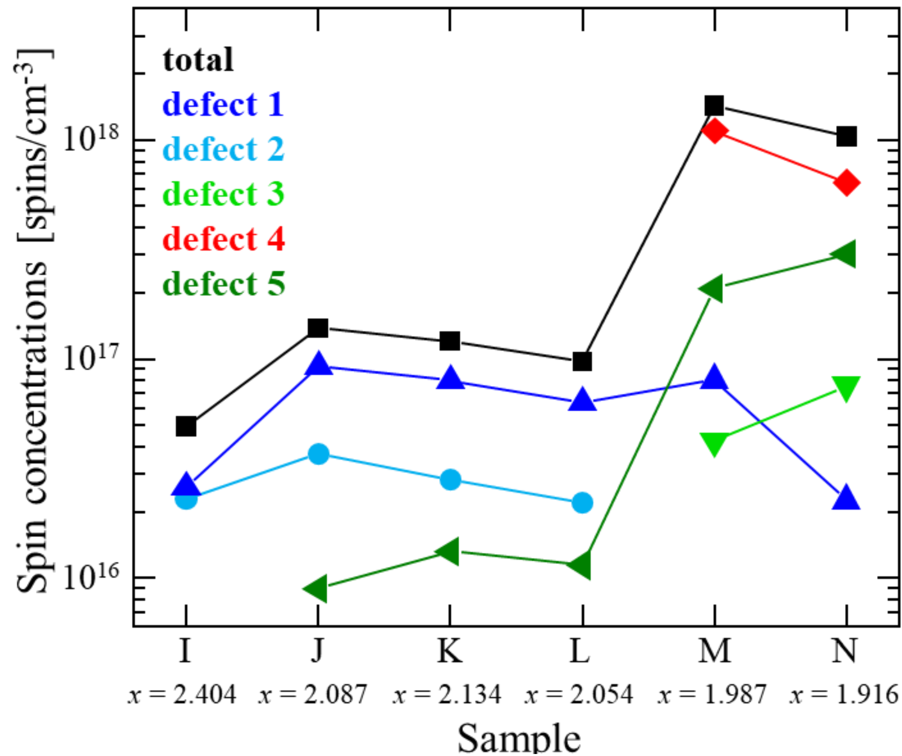

Fig. 5.4-11 Spin concentrations of Sample I-N.

Spin concentration [spins/cm^{-3}] of paramagnetic centers in $BaSi_2$

- Si-rich samples : Total ~ 10^{17}, Defect 5 < Defect 2 < Defect 1
- Ba-rich samples : Total ~ 10^{18}, Defect1 and Defect 3 < Defect 5 << Defect 4

5.4.3. Summary

In this chapter, I tried to separate paramagnetic centers in Si-rich and Ba-rich samples by the simulations with Easyspin. In order to obtain the initial values, I put together the all results I got in cw- and pulse- EPR, and hyperfine spectroscopies. Each center was separated and evaluated tentatively by using Easyspin.

5.5. DFT calculations

I successfully observed the complicated EPR spectra in this study. It is fruitful to clarify the origin of each EPR line because there has been no EPR study in $BaSi_2$ system so far. The paramagnetic centers in $BaSi_2$ are considered to relate to intrinsic defects. To obtain tips for further understandings, the first principle calculation based on density functional theory (DFT) is one of the most powerful tools.[140,179-182] Therefore, I tried to obtain EPR parameters (g-tensor, hyperfine tensor, and electric field gradient tensor) by DFT in order to establish models of the defects. All results in this chapter are collaboration with Ph.D J.-M. Mouesca.

5.5.1. Method

The crystal structure of orthorhombic $BaSi_2$ (Z = 8) is shown in Fig. 5.5-1. $BaSi_2$ belongs to the *Pnma* space group, and its unit cell contains eight formula units. The stoichiometric description of the unit cell is Ba_8Si_{16}. In the unit cell of $BaSi_2$, there are two crystallographically inequivalent sites for Ba [Ba(1) and Ba(2)] and three inequivalent sites for Si [Si(3), Si(4), and Si(5)]. In addition, there are four distinct Si tetrahedra with varying directions and positions that can be mutually translated by symmetric operations. In each Si tetrahedron, the two Si(5) atoms (blue spheres in Fig. 5.5-1) and the single Si(4) atom (red sphere in fig. 5.5-1) have similar a-axis coordinates. I considered six possible intrinsic defects in $BaSi_2$: Ba vacancy (V_{Ba}), interstitial Si (Si_i), antisite Si substituted for Ba (Si_{Ba}), Si vacancy (V_{Si}), interstitial Ba (Ba_i), and antisite Ba substituted for Si (Ba_{Si}). Two intrinsic point defects, V_{Si} and Ba_{Si}, were introduced into one of the four Si3 sites as previously reported.[51,106] We adopted a previously reported interstitial site, the fractional coordinate of which is (0.5841, 0.25, 0.2251), as initial configurations for Si_i and Ba_i.[107,174] As initial configurations for two intrinsic defects of V_{Ba} and Si_{Ba}, the position of Ba(1) was chosen. The EPR parameters' calculation was performed with QUANTUM ESPRESSO (QE) code[175] with the QE subroutine of Gauge-Including Projector-Augmented Wave (GIPAW).[176] Perdew−Burke−Ernzerhof version of the generalized gradient approximation of the exchange-correlation functional (GGA-PBE)[177] and the pseudopotentials prepared by A. Dal Crso[178] were employed. The kinetic energy cutoff for wavefunctions has been set to 30 Ry and the kinetic energy cutoff for charge density and potential has been set to 240 Ry. After the geometry-optimization and the conversion of self-consistant-field (SCF) calculation, additional calculation have been performed to obtain EPR parameters. Confirming the effect of the cell size on the parameters, I computed 2×2×1 supercell as well as unitcell (1×1×1).

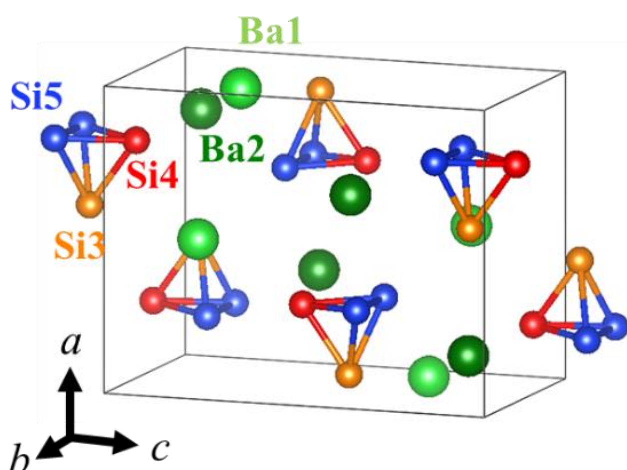

Fig. 5.5-1 Crystal structure of $BaSi_2$ (Z = 8) . There are two crystallographically inequivalent sites for Ba [Ba(1) and Ba(2)] and three inequivalent sites for Si [Si(3), Si(4), and Si(5)] in orthorhomic unit cell with its space group of *Pnma*.[22]

5.5.2. Results

The first three defects are likely to be formed in Si-rich samples, and the remaining three are likely to be formed in Ba-rich samples (fig. 5.5-2).

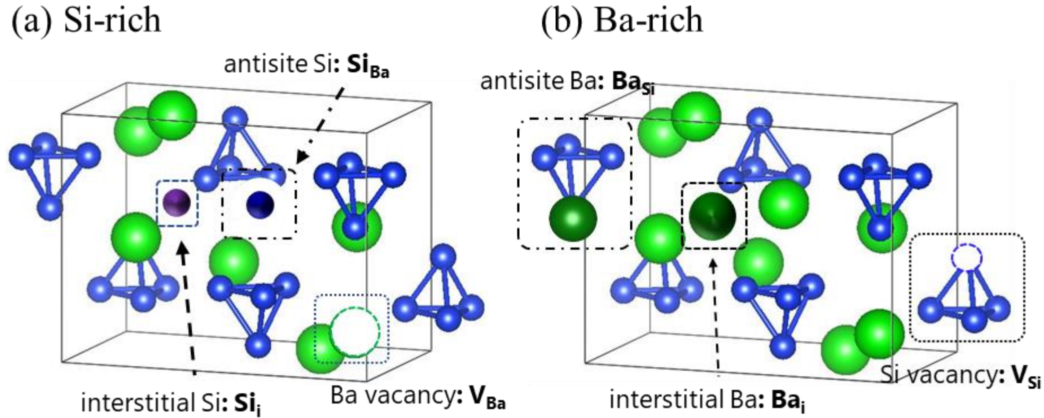

Fig. 5.5-2 Intrinsic point defects considered to be formed in $BaSi_2$ under (a) Si-rich and (b) Ba-rich conditions.

For these six defects, the paramagnetic states observable by EPR were considered as follows. For example, starting from the (24 atoms) diamagnetic state (i.e. even total number of electrons), we create two paramagnetic (here 23 atoms) V_{Si} states by formally removing one $[Si]^-$ anion (and therefore one electron), resulting into a cell of total charge (q = +1) called V_{Si}. This first model can be then twice reduced, resulting into V_{Si} of total charge (q = −1). However, in real systems, after introducing an intrinsic defect, the stable charging state of the defects should be determined by calculating the formation energy of each charged defect and plotting it as a function of Fermi energy. All the defects considered in this study are listed in Table 5-21.

Table 5-21 Paramagnetic defects considered in this study.

Models	Si-rich	Ba-rich
Vacancies	V_{Ba} ($q = -3$)	V_{Si} ($q = -1$)
	V_{Ba} ($q = -1$)	V_{Si} ($q = +1$)
Interstitial	Si_i ($q = -1$)	Ba_i ($q = +1$)
	Si_i ($q = +1$)	Ba_i ($q = +3$)
Antisite	Si_{Ba} ($q = -3$)	Ba_{Si} ($q = +1$)
	Si_{Ba} ($q = -1$)	Ba_{Si} ($q = +3$)

Hyperfine coupling tensor

I started to calculate hyperfine coupling tensor for each defect. Effects of the calculated crystal size on hyperfine-tensor were confirmed. I show the calculated isotropic hyperfine component for V_{Si} ($q = -1$) obtained after geometry-optimizations in Table 5-22. I listeed the values greater than 20 MHz because large hyperfine coupling are much more interesting as I mentioned the in previous section.

Table 5-22 Calculated isotropic part of hyperfine-tensor for V_{Si} ($q = -1$).

Size of cell	Hyperfine tensor [MHz]
1×1×1	Ba → −76, −50, −33, −22, −21 Si → +34×2
2×2×1	Ba → +92×2, +50×2, −46 Si → +23×2
2×2× 2	Ba → +109×2, +63×2, −50 Si → +22×2

It can be seen from this example that no great change occurs anymore between 2×2×1 and 2×2×2 models for DFT hyperfine data, showing that four cells are large enough to accomodate the defect. We therefore propose to harmonize all following results at the 2×2×1 (i.e. four cells) level.

The isotropic part of hyperfine tensor is given by

$$a_{\mathrm{iso}} = \frac{8\pi}{3} g_{\mathrm{n}} g_{\mathrm{eff}} \mu_{\mathrm{n}} \beta |\psi(\boldsymbol{R}=0)|^2 \boldsymbol{S}\cdot\boldsymbol{I}$$

where ψ (R =0) stands for the one-particle wavefunction at the atomic site $\boldsymbol{R}$. The nuclear g-factor, the effective g-factor, the nuclear magneton, and the Bohr magneton are denoted as g_n, g_{eff}, μ_n, and β, respectively. As is clear from the above equation, the wavefunction of the ground state is a factor which causes the differences. When the size of the cell is too small to be delocalized, unpaired electrons are localized at near the defects. Thus, in too small size of the cell, isotropic hyperfine tensor is overestimated. Furthermore, it is readily to imagine that, as shown later, anisotoropy of g-tensor became larger in a smaller sized cell because of a strong spin-orbit interaction. Therefore, I have to use a large enogh cell for unpaired electrons to delocalize. In subsequent calculations, I compared the hyperfine tensor calculated by 2×2×1 supercells. From Figs. 5.5-3 and 5.5-4, some atoms can have strong hyperfine interactions (for instance, Si_i^- has large a_{iso} as seen in Fig. 5.5-3(c)) while almost all atoms show small ones less than 10 MHz. On the other hand, in practical, I have to take their anisotropic part into accounts in order to compare the calculated values with those by experiments. The whole hyperfine tensor is given by $A = a_{iso} + T$, where a_{iso} and T are isotropic and anisotropic parts of hyperfine tensor. In a system of principal axes, the principal values of the tensor are described as (A_{11}, A_{22}, A_{33}) = ($a_{iso} - T_{11}(1 + \delta)$, $a_{iso} - T_{22}(1 - \delta)$, $a_{iso} + 2T_{33}$). I can observe only the principal values by means of the hyperfine spectroscopies because I used powder samples in this study. I show histgrams of the principal values including the contributions of the anisotropic parts for each defect (Figs. 5.5-5 and 5.5-6). Comparing among the results, almost all defects such as V_{Si} ($q = -1$) contain strong anisotropic hyperfine coupling with ^{29}Si as I marked by arrows in Figs. 5.5-5 and 5.5-6. This might be due to a contribution of Si-2p-orbital electrons. On the other hand, large hyperfine couplings are often stemed from Ba atoms except for Si_i (q = -1) and Si_{Ba} (q = -1).

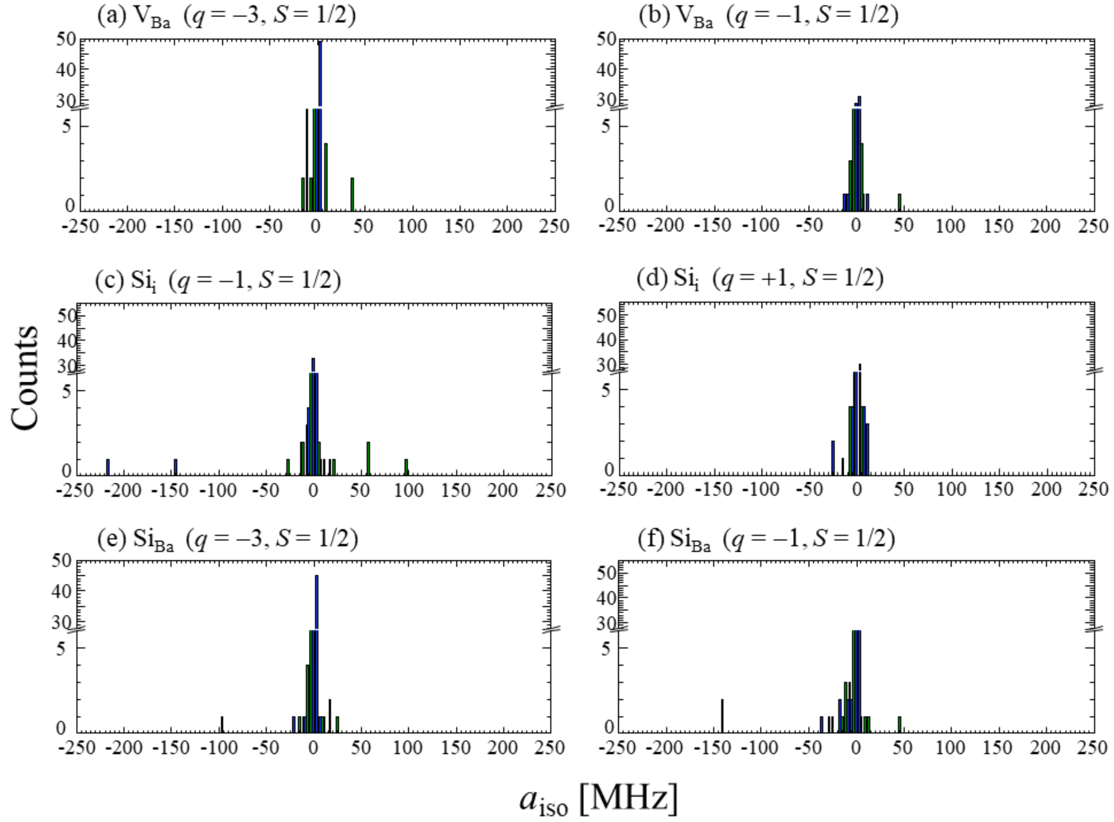

Fig. 5.5-3 Isotropic part of hyperfine tensor for the defects under Si-rich condition. Blue and green bars correspond to ^{29}Si and ^{135}Ba (^{137}Ba) atoms, respectively.

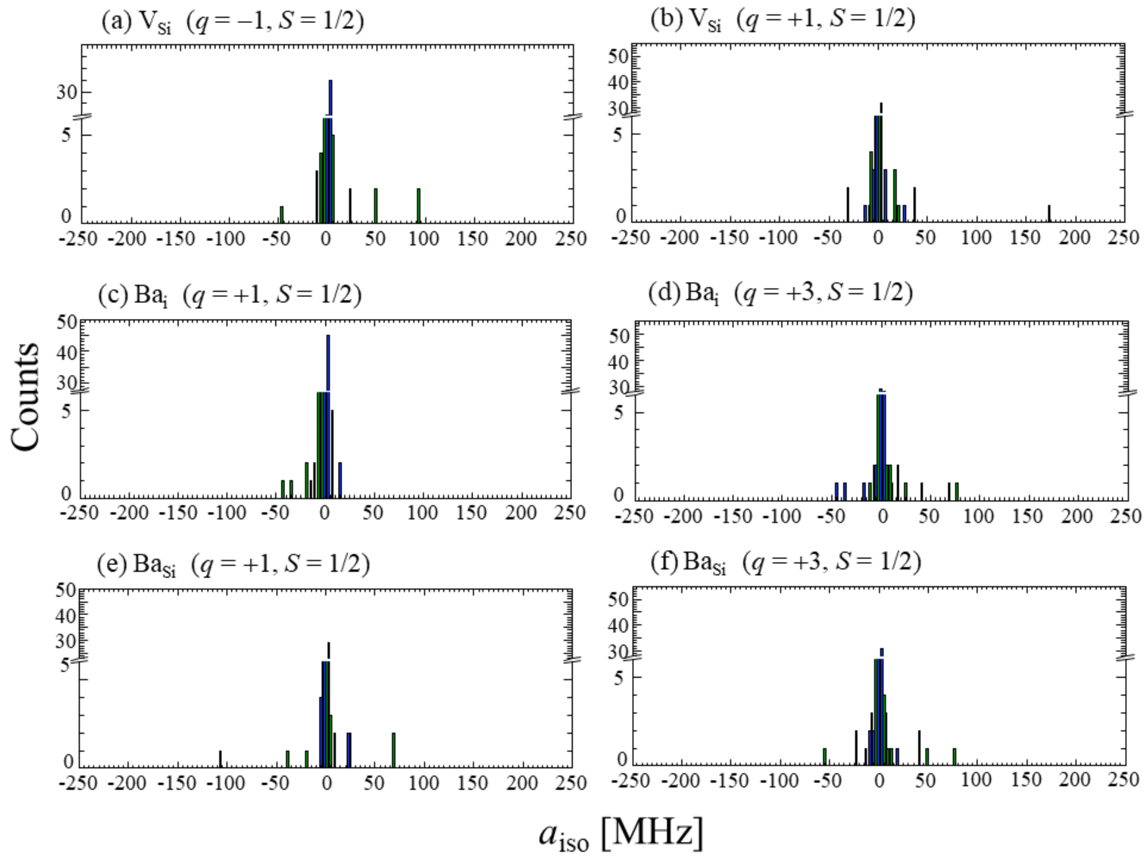

Fig. 5.5-4 Isotropic part of hyperfine tensor for the defects under Ba-rich condition. Blue and green bars correspond to ^{29}Si and ^{135}Ba (^{137}Ba) atoms, respectively.

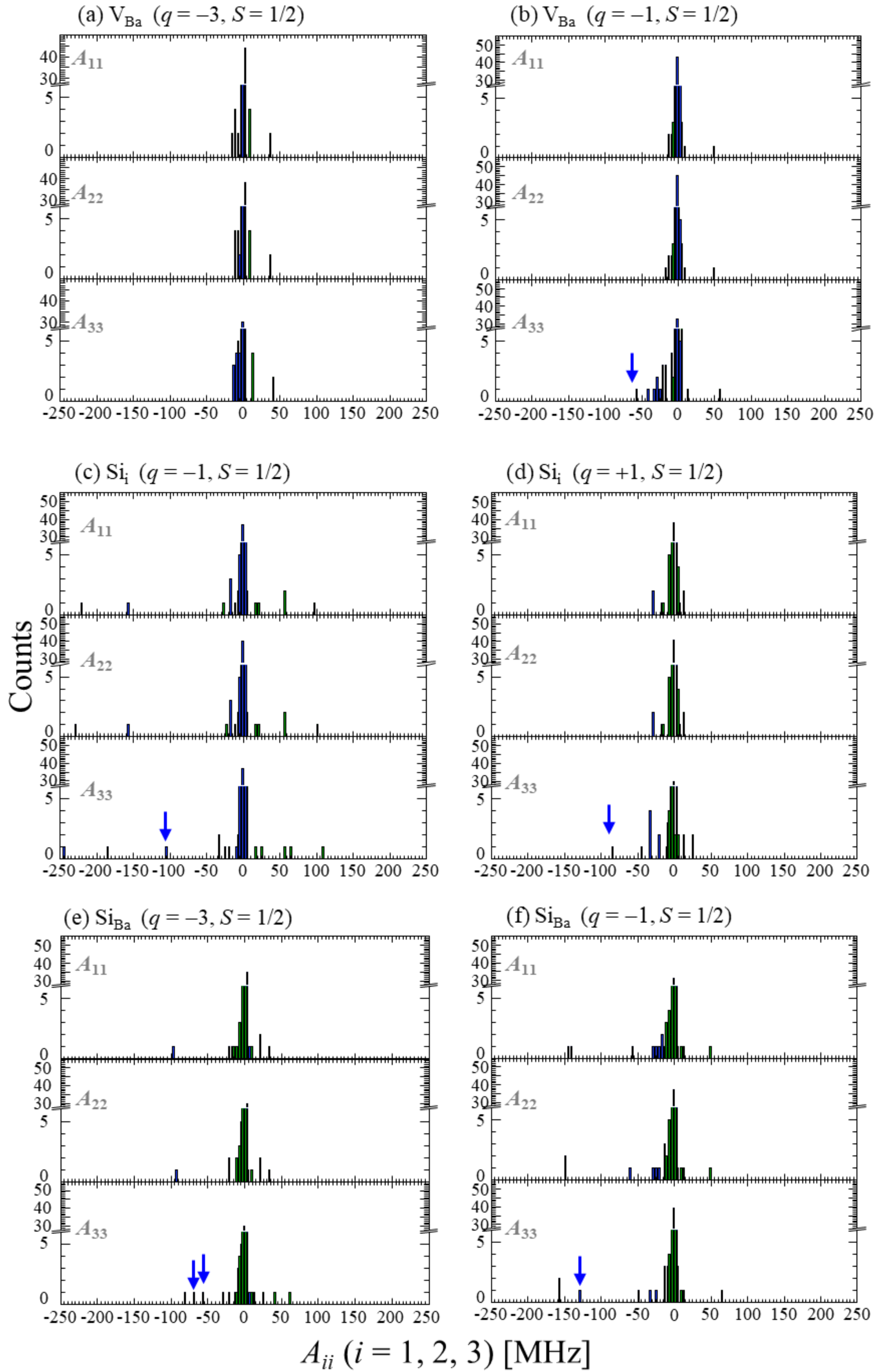

Fig. 5.5-5 Principal values of hyperfine tensor ($a_{iso} + T$) for each defects in Si-rich condition. Blue and green bars correspond to ^{29}Si and ^{135}Ba (^{137}Ba) atoms, respectively. Arrows indicate large anisotropy.

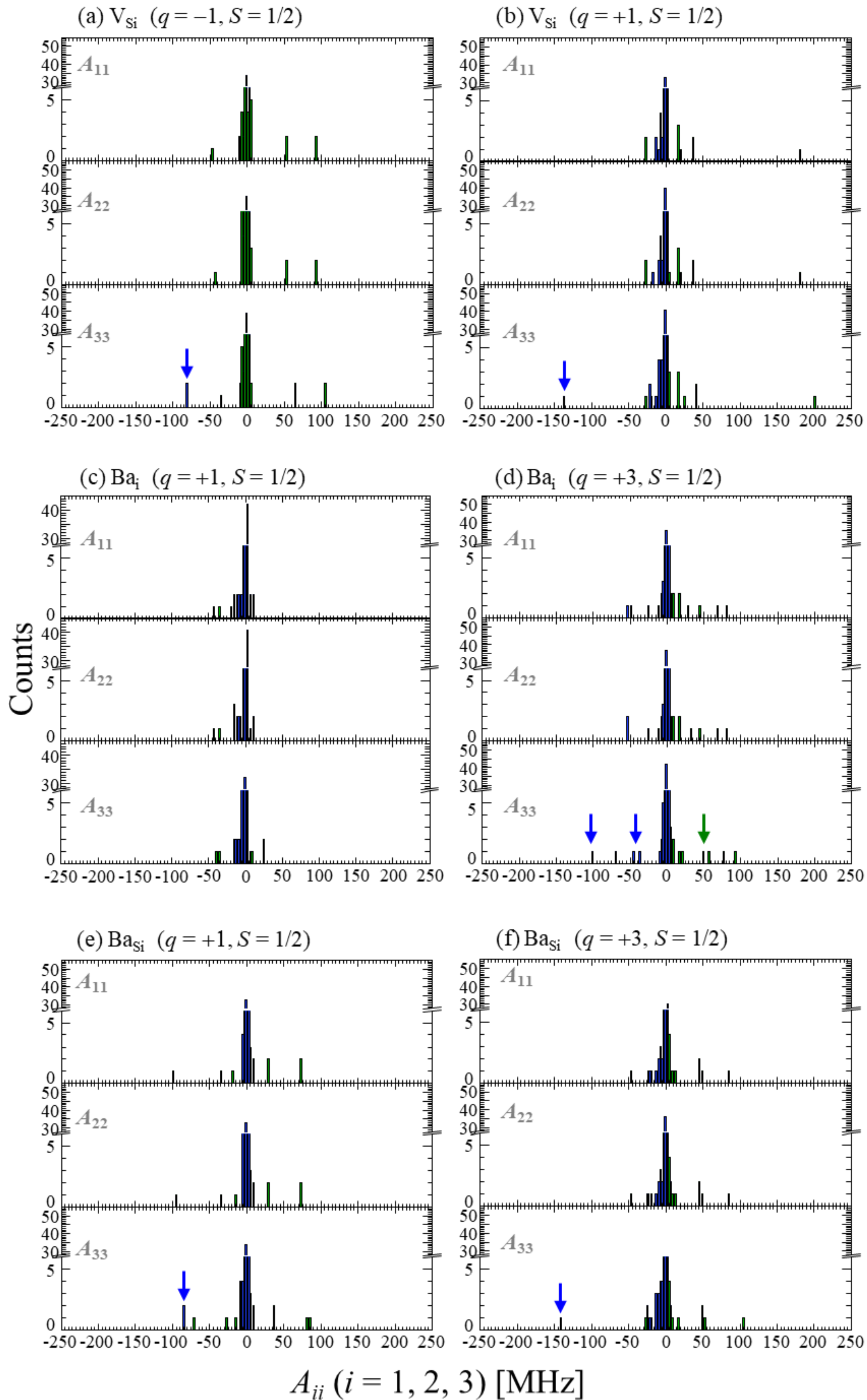

Fig. 5.5-6 Principal values of hyperfine tensor (a_{iso} + T) for each defects in Ba-rich condition. Blue and green bars correspond to ^{29}Si and ^{135}Ba (^{137}Ba) atoms, respectively. Arrows indicate large anisotropy.

g-tensor

Next, I computed g-tensors of each defects. I listeed an effect of the calculated crystal size on g-tensor on Table 5-23, which are results for V_{Si} ($q = -1$) obtained after geometry-optimizations.

Table 5-23 Calculated g-tensor V_{Si} (q = -1).

Size of cell	g_1	g_2	g_3	g_{av}
1×1×1	1.835	1.952	1.996	1.928
2×2×1	1.974	1.985	2.001	1.987

It can be seen that the anisotropy decreases as the cell size increases. In subsequent calculations, I compared the g-tensor calculated in 2×2×1 supercells for each defect (Table 5-24).

Table 5-24 Calculated principal values of g-tensor and their average, g_{av}.

	g_1	g_2	g_3	g_{av}
Si-rich				
V_{Ba}(q = -3)	1.878	2.023	2.047	1.983
V_{Ba}(q = -1)	1.676	1.969	2.042	1.896
Si_i (q = -1)	1.934	1.989	2.005	1.976
Si_i (q = +1)	1.933	2.030	2.078	2.014
Si_{Ba} (q = -3)	1.957	2.003	2.057	2.006
Si_{Ba} (q = -1)	1.936	2.004	2.134	2.025
Ba-rich				
V_{Si}(q = -1)	1.974	1.985	2.001	1.987
V_{Si}(q = +1)	2.013	2.042	2.047	2.034
Ba_i (q = +1)	1.951	1.992	1.996	1.980
Ba_i (q = +3)	1.958	2.027	2.051	2.012
Ba_{Si} (q = +1)	1.958	1.983	2.023	1.994
Ba_{Si} (q = +3)	1.995	2.031	2.051	2.026

Nuclear quadrupole tensor

In ^{135}Ba and ^{137}Ba atom which possess I = 3/2 (> 1/2), the quadrupole interaction has to be taken into account. The Electric field gradient at the position of nucleus causes energy splitting depending on the direction of nulear spin. Hence, I also evaluate the quadrupole coupling constant, $K = e^2Qq/12h$ (in the case of I = 3/2), where e, eq, Q, and h are the elementary charge, the largest magnitude component of electric field gradient at the nucleus, the electric quadrupole moment of the nuleus, the Plank's constant, respectively.

The principal values of the nuclear quadrupole tensor are given by,

$Q_1 = -K(1 - \eta)$, $Q_2 = -K(1 + \eta)$, $Q_3 = 2K$.

Here, the nuclear quadrupole tensor is traceless ($Q_1 + Q_2 + Q_3 = 0$) and η are described as,

$$\eta = \frac{Q_1 - Q_2}{Q_3}.$$

If the value of K is close to the value of $\nu_{eff}(-)$ ($= |\nu_n - |A|/2||$) in a strong hyperfine situation, the quadrupole resonance frequencies are broadened as ν_{eff}/K deviates from 0, which the ENDOR and ED-NMR spectra make broaden.

In practical, the most strongest hyperfine interaction in Ba_i (q = +1), (A_{11}, A_{22}, A_{33}) = (-43, -42, -38), I obtained the value K = 84 MHz and η = 0.04. By using these calculated values, I can evaluate principal values Q_1 = -81, Q_2 = -87, and Q_3 = +168 MHz. In the same way, the most strongest hyperfine nteraction in V_{Si} ($q = -1$), (A_{11}, A_{22}, A_{33}) = (96, 96, 107), I obtained the value K = -12 MHz and η = 0.24. I can evaluate the principal values, (Q_1, Q_2, Q_3) = (-9.1, -14.9, +24) in MHz.

5.5.3. Summary

As a conclusion, the following summarizes the characteristics of defects that can be considered in the case of Si-rich and Ba-rich $BaSi_2$ bulk samples.In each supercell, the defect is dipicted by a red color. Highlighted atoms have hyperfine interactions greater than 20 MHz. Also, the largest hyperfine couplings are listed with their principal axes in the supercell for Ba and Si, respectively. In a term of quadrupole tensor, I simply categorized them into three regimes: high field regime ($|\nu_{eff}/K/ >> 1$), low field regime ($|\nu_{eff}/K/ << 1$), and intermediate regime ($|\nu_{eff}/K/ \sim 1$). In case that the values of $|\nu_{eff}/K/$ depends on its site, I denoted that “depends on sites”and the regime for the largest hyperfine coupling, $|\nu_{eff}/K|$, is shown in parentheses.The information such as g-tensor, hyperfine tensor, and quadrupole tensor are listed for each defect in Tables 5-25 and 5-26. In the tables, the A_{ii} (i = 1, 2, 3) greater than 20 MHz are only listed.

The defects considered to likely to be formed in Si-rich condition are following.

(a) V_{Ba} ($q = -3$, $S = 1/2$)

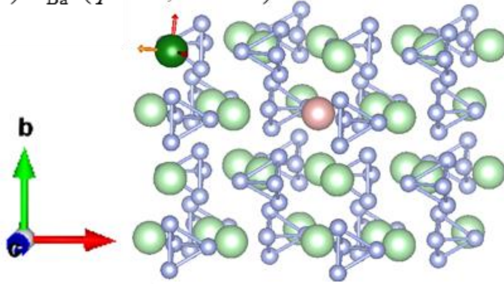

g-tensor : **strong anisotropy**, (1.878, 2.023, 2.047), $g_{av} = 1.983$

hyperfine tensor : **only** with **Ba**
$A_{max}^{(Ba)} = (37.8, 38.0, 43.1)$ MHz
$A_{max}^{(Si)} =$ --- MHz

quadrupole tensor: Intermediate regime

(b) V_{Ba} ($q = -1$, $S = 1/2$)

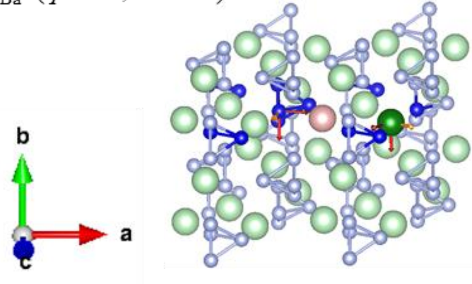

g-tensor : **strong anisotropy**, (1.676, 1.969, 2.042), $g_{av} = 1.896$

hyperfine tensor : almost with **Si**
$A_{max}^{(Ba)} = (48.8, 49.3, 58.2)$ MHz
$A_{max}^{(Si)} = (-8.0, -8.6, -59.3)$ MHz

quadrupole tensor: **High** field regime

(c) Si_i ($q = -1$, $S = 1/2$)

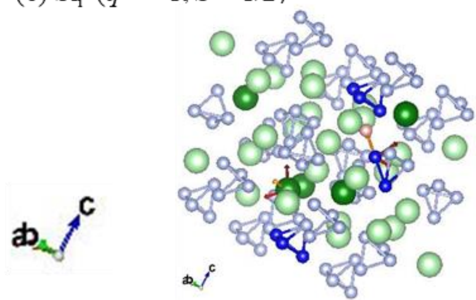

g-tensor : **anisotropy**, (1.934, 1.989, 2.005), $g_{av} = 1.976$

hyperfine tensor : **large coupling** with **Si** and **Ba**
$A_{max}^{(Ba)} = (99.8, 101, 109)$ MHz
$A_{max}^{(Si)} = (-220, -232, -247)$ MHz

quadrupole tensor: Depends on sites (**High** field regime)

(d) Si_i ($q = +1$, $S = 1/2$)

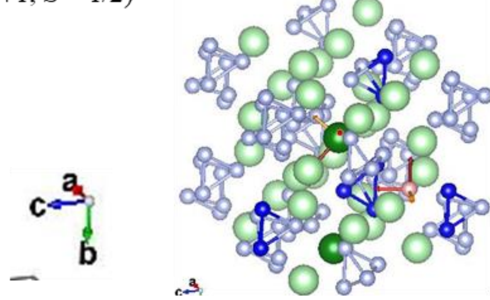

g-tensor : **anisotropy**, (1.933, 2.030, 2.078), $g_{av} = 2.014$

hyperfine tensor : almost with **Si**
$A_{max}^{(Ba)} = (13.9, 14.2, 24.5)$ MHz
$A_{max}^{(Si)} = (-16.5, -17.9, -84.3)$ MHz

quadrupole tensor: **Low** field regime

(f) Si_{Ba} ($q = -3$, $S = 1/2$)

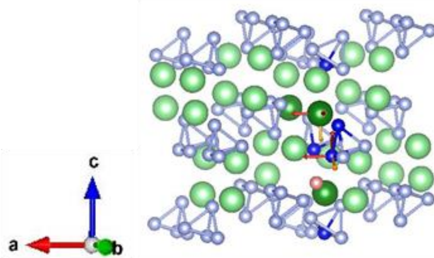

g-tensor : **anisotropy**, (1.957, 2.003, 2.057), $g_{av} = 2.006$

hyperfine tensor : $A_{max}^{(Ba)} = (34.9, 35.2, 60.1)$ MHz
$A_{max}^{(Si)} = (-96.6, -92.1, -83.7)$ MHz

quadrupole tensor: Intermediate regime

(f) Si_{Ba} ($q = -1$, $S = 1/2$)

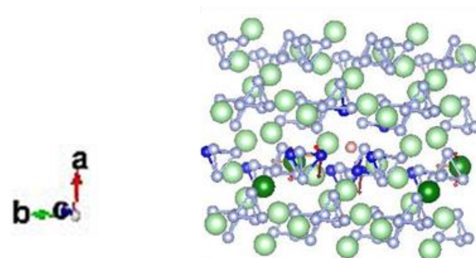

g-tensor : **strong anisotropy**, (1.936, 2.004, 2.134), $g_{av} = 2.025$

hyperfine tensor : **Large coupling** with **Si** and **Ba**
$A_{max}^{(Ba)} = (489, 491, 506)$ MHz
$A_{max}^{(Si)} = (-144, -151, -159)$ MHz

quadrupole tensor: **High** Field regime

The defects considered to likely to be formed in Ba-rich condition are following.

(a) V_{Si} ($q = -1, S = 1/2$)

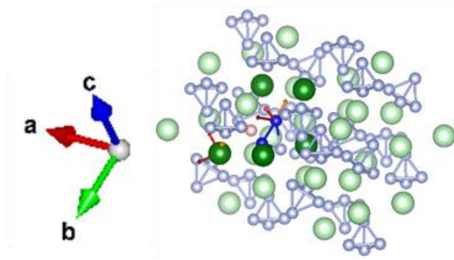

g-tensor : **less anisotropic**
$(1.974, 1.985, 2.001), g_{av} = 1.987$

hyperfine tensor : almost with **Ba**
$A_{max}^{(Ba)} = (95.7, 95.8, 107)$ MHz
$A_{max}^{(Si)} = (-2.8, -4.9, -83.7)$ MHz

quadrupole tensor: Depends on sites (**High** field regime)

(b) V_{Si} ($q = +1, S = 1/2$)

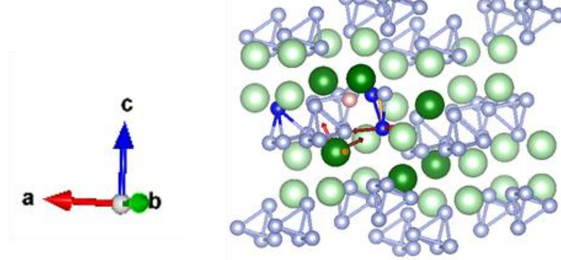

g-tensor : **less anisotropic**
$(2.013, 2.042, 2.047), g_{av} = 2.034$

hyperfine tensor : **large coupling** with **Si** and **Ba**
$A_{max}^{(Ba)} = (181, 182, 202)$ MHz
$A_{max}^{(Si)} = (-13.0, -16.4, -139)$ MHz

quadrupole tensor: Depends on sites (**High** field regime)

(c) Ba_i ($q = +1, S = 1/2$)

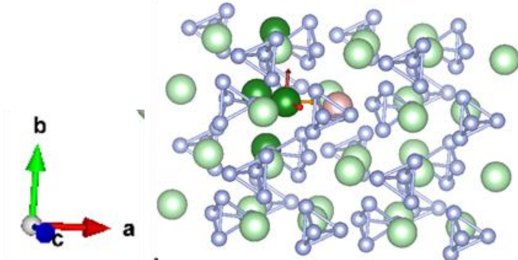

g-tensor : **less anisotropic**
$(1.951, 1.992, 1.996), g_{av} = 1.980$

hyperfine tensor : only with **Ba**
$A_{max}^{(Ba)} = (-42.6, -41.7, -37.8)$ MHz
$A_{max}^{(Si)} =$ --- MHz

quadrupole tensor: **Low** field regime

(d) Ba_i ($q = +3, S = 1/2$)

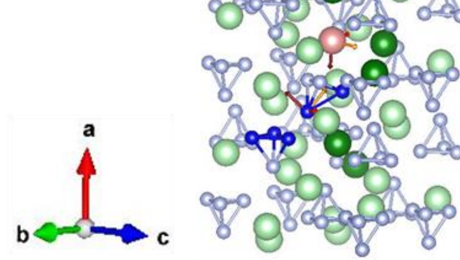

g-tensor : anisotropic
$(1.958, 2.027, 2.051), g_{av} = 2.012$

hyperfine tensor : quite large coupling
$A_{max}^{(Ba)} = (550, 551, 557)$ MHz
$A_{max}^{(Si)} = (-318, -325, -351)$ MHz

quadrupole tensor : Depends on sites (**High** field regime)

(f) Ba_{Si} ($q = +1, S = 1/2$)

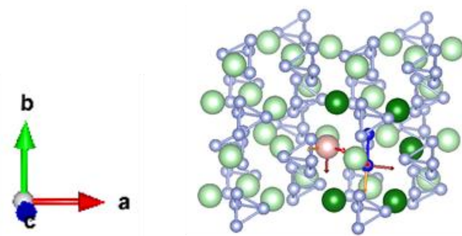

g-tensor : strong anisotropy,
$(1.958, 1.983, 2.023), g_{av} = 1.994$

hyperfine tensor : almost with **Ba**
$A_{max}^{(Ba)} = (-99.2, -94.3, -70.1)$ MHz
$A_{max}^{(Si)} = (-3.5, -6.0, -86.1)$ MHz

quadrupole tensor: Depends on sites (**High** field regime)

(f) Ba_{Si} ($q = +3, S = 1/2$)

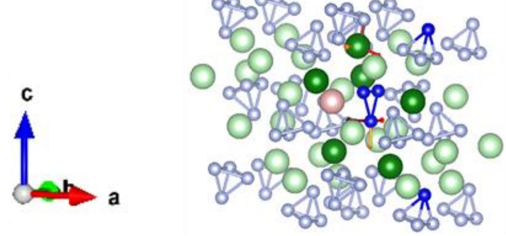

g-tensor : almost isotropic,
$(1.995, 2.031, 2.051), g_{av} = 2.026$

hyperfine tensor : $A_{max}^{(Ba)} = (51.9, 51.9, 53.5)$ MHz
$A_{max}^{(Si)} = (-21.0, -24.5, -142)$ MHz

quadrupole tensor: Intermediate regime

Table 5-25 Calculated EPR parameters considered in Si-rich condition: the principal values of g-tensor (g_{ii}), the average value g-tensor (g_{av}), the isotropic (a) and anisotropic (T_{ii}) parts of hyperfine tensor in a unit of MHz, the quadrupole coupling constant (K) in MHz and its asymmetry parameter (η), and the principal values of nuclear quadrupole tensor (Q_i) in MHz. Blue and green values in hyperfine columns express ^{29}Si and ^{135}Ba (and/or ^{137}Ba), respectively. Also, large anisotropic hyperfine couplings are emphasized in bold.

Model	(g_{11}, g_{22}, g_{33})	g_{av}	a_{iso} [MHz]	(T_{11}, T_{22}, T_{33}) [MHz]	K [MHz]	η
V_{Ba}(Q = -3) rd	(1.878, 2.023, 2.047)	1.983	+36	(-2, -2, 3)	-10	0.50
V_{Ba}(Q = -1) ox	(1.676, 1.969, 2.042)	1.896	+45.9	(-2.8, -3.3, 6.1)	8	0.66
			+9	**(16.7, 17.3, -34.0)**	-	-
			+4.3	(8.7, 9.3, -18.0)	-	-
			+0.9	(5.2, 5.2, -11.2)	-	-
			+0.6	(8.1, 8.8, -17.0)	-	-
			-1.9	(5.5, 6.0, -11.5)	-	-
			-2.9	(9.1, 9.7, -18.7)	-	-
			-10.2	(4.9, 5.6, -10.5)	-	-
			-13.6	(2.2, 2.5, -4.8)	-	-
Si_i (Q = -1) rd	(1.934, 1.989, 2.005)	1.976	-219	(1.3, 12.5, -13.8)	-	-
			-146	(9.8, 10.7, -20.5)	-	-
			-26.5	(-2.1, -3.1, 5.1)	21	0.60
			-14.7	(3.7, 5.1, -8.8)	-	-
			+5.5	(7.4, 8.0, -15.4)	-	-
			+11.2	**(28.6, 29.8, -58.4)**	-	-
			+22.4	(-0.6, -1.0, 1.6)	-5	0.42
			+56.6	(-2.6, -2.8, 5.4)	-15	0.03
			+57.3	(0.1, 0.4, -0.5)	14	0.26
			+97	(-2.3, -3.4, 5.7)	10	0.09
Si_i (Q = +1) ox	(1.933, 2.030, 2.078)	2.014	-27.6	(1.1, 2.8, -3.9)	-	-
			+4.5	(6.3,6.9, -13.2)	-	-
			+5.2	**(21.7, 23.1, -44.7)**	-	-
			+9.0	(9.8, 12.2, -22.0)	-	-
			+9.8	(13.9,14.1,-28.0)	-	-
			+10.6	(-3.3, -3.6, 6.9)	-17	0.94
Si_{Ba} (Q = -3) rd	(1.957, 2.003, 2.057)	2.006	-97.9	(-1.3, -5.8, 7.1)	-	-
			-20.6	(0.10, 0.53, -0.63)	-	-
			-2.0	**(16.3, 18.1, -34.4)**	-	-
			+0.23	(7.6, 8.4, -15.7)	-	-
			+11.7	**(17.4, 18.3, -35.6)**	-	-
			+16.1	(-6.1, -6.5, 12.6)	15.2	0.14
			+19.4	(-1.4, -2.0, 3.4)	11.0	0.82
			+26.6	(-8.2, -8.5, 16.7)	18.3	0.91
Si_{Ba} (Q = -1) ox	(1.936, 2.004, 2.134)	2.025	-143	(0.6, 7.4, -7.9)	-	-
			-37.9	**(21.2, 24.0, -45.2)**	-	-
			-30.3	(0.2, 1.3, -1.5)	-	-
			-24.1	(0.1, 0.6, -0.7)	-	-
			-11.4	(9.4, 10.8, -20.2)	-	-
			+46.1	(-4.7, -4.8, 9.6)	-7	0.22
			+485	(-4.1, -6.3, 10.4)	19	0.69

Table 5-26 Calculated EPR parameters considered in Ba-rich condition: the principal values of g-tensor (g_{ii}), the average value g-tensor (g_{av}), the isotropic (a) and anisotropic (T_{ii}) parts of hyperfine tensor in a unit of MHz, the quadrupole coupling constant (K) in MHz and its asymmetry parameter (η), and the principal values of nuclear quadrupole tensor (Q_i) in MHz. Blue and green values in hyperfine columns express ^{29}Si and ^{135}Ba (and/or ^{137}Ba), respectively. Also, large anisotropic hyperfine couplings are emphasized in bold.

Model	(g_{11}, g_{22}, g_{33})	g_{av}	a_{iso} [MHz]	(T_{11}, T_{22}, T_{33}) [MHz]	K [MHz]	η
V_{Si}(Q = -1) rd	(1.974, 1.985, 2.001)	1.987	-46.5	(-2.4, -3.5, 5.9)	-19.9	0.54
			+22.7	(**25.6, 27.6, -53.2**)	-	-
			+49.8	(-3.3, -3.8, 7.1)	13.9	0.36
			+92.0	(-3.6, -3.8, 7.4)	-11.5	0.24
V_{Si}(Q = +1) ox	(2.013, 2.042, 2.047)	2.034	-28.5	(-2.1, -2.4, 4.5)	18.8	0.82
			-28.0	(-0.9, -1.0, 1.9)	16.7	0.55
			+6.7	(6.1, 7.5, -13.7)	-	-
			+23.2	(-0.3, -0.7, 1.0)	11.9	0.79
			+26.8	(**39.7, 43.2, -82.9**)	-	-
			+37.5	(-0.7, -1.0, 1.6)	17.8	0.68
			+174	(-6.5, -7.1, 13.6)	38.4	0.36
Ba_i (Q = +1) rd	(1.951, 1.992, 1.996)	1.980	-7.8	(-8.5, -9.0, 17.5)	17.2	0.49
			-32.4	(0.3, 0.5, -0.9)	50.9	0.13
			-43.7	(-1.0, -1.9, 2.9)	84.5	0.04
Ba_i (Q = +3) ox	(1.958, 2.027, 2.051)	2.012	-312	(**318, -325, -351**)	-	-
			-45.4	(**-50.2, -52.7, -69.6**)	-	-
			-39.7	(**-55.1, -55.4, -102**)	-	-
			-18.2	(**-24.6, -26.3, -47.2**)	-	-
			+10.9	(**-1.4, -1.8, -39.0**)	-	-
			+18.4	(**19.1, 19.3, 21.7**)	46.5	0.03
			+24.6	(**30.2, 32.3, 51.3**)	-40.7	0.88
			+40.6	(**45.2, 45.4, 59.4**)	18.5	0.82
			+69.8	(-1.8, -2.1, 3.8)	17.9	0.20
			+78.7	(-3.7, -3.7, 7.4)	44.2	0.16
			+548	(-1.3, -3.1, 4.4)	54.0	0.31
Ba_{Si} (Q = +1) rd	(1.977, 1.983, 2.023)	1.994	106	(-6.4, -11.3, 17.8)	15.7	0.28
			-36.0	(-2.0, -2.7, 4.7)	-17.2	0.26
			+22.3	(**25.8, 28.4, -54.2**)	-	-
			+26.3	(-3.2, -3.6, 6.8)	13.8	0.47
			+71.3	(-3.1, -3.4, 6.5)	13.6	0.38
Ba_{Si} (Q = +3) ox	(1.995, 2.031, 2.051)	2.026	-52.2	(-6.0, -6.6, 12.6)	10.8	0.24
			-23.7	(-0.5, -0.6, 1.1)	-11.8	0.81
			-23.0	(-3.5, -4.0, 7.6)	13.6	0.03
			+4.0	(6.2, 6.3, -12.6)	-	-
			+7.6	(7.2, 8.8, -15.9)	-	-
			+17.1	(**38.1, 41.6, -79.7**)	-	-
			+43.0	(-1.2, -1.7, 2.8)	23.2	0.26
			+51.3	(-0.5, -0.6, 1.1)	-14.5	0.87
			+79	(-6.0, -6.6, 12.7)	49.0	0.14

5.6. General discussion

5.6.1. Comparison: experiments and computations

I compare the experimental results with the calculated ones by DFT.

Si-rich

In the Si-rich samples, I observed the two different paramagnetic centers as follows:

- Defect 1 [Si-rich]

g-tensor : g_1 = 1.993-1.998, g_2 = 2.012-2.014, g_3 = 2.025-2.030

- Defect 2 [Si-rich]

g-tensor : g_1 = 1.997, g_2 = 2.004-2.005, g_3 = 2.010-2.011

A peak at ± 20-40 MHz is observed by ED-NMR measurement. At g-value less than 2.01, both the Defect 1 and the Defect 2 overlap, and it is difficult to determine which center the ED-NMR spectrum is due to. On the other hand, from Fig. B-4 (Appendix), it is considered that the positions of g = 2.02 in Sample J are almost caused by the Defect 1. Therefore, I discuss the origin of the Defect1 first based on the position of the ED-NMR peak observed at that magnetic field position, −39 and 35 MHz. Compared to the result of DFT calculation in a defect model that is likely to be formed under Si-rich conditions, positively charged Si_i is given as the most probable candidate from the viewpoint of g-tensor. From the viewpoint of g-tensor, negatively charged Si_{Ba} is also a candidate, but a very large hyperfine tensor is expected in this defect model. Since such a large hyperfine interaction was not observed in real experiment, I can exclude Si_{Ba}^- as a candidate. On the other hand, considering even a defect model that is easily formed under Ba-rich conditions, it can be seen that positively charged Ba_{Si} also shows values that are in good

(a) Si_i (q = +1, S = 1/2)

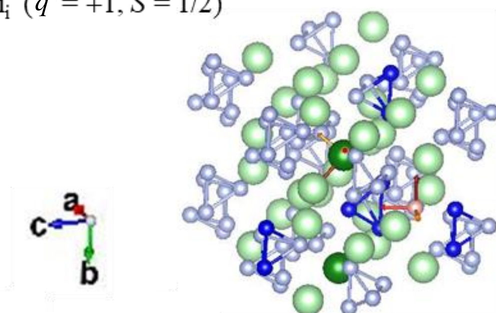

g-tensor : (1.933, 2.030, 2.078), g_{av} = 2.014

hyperfine tensor : almost with **Si**

$A_{max}^{(Ba)}$ = (13.9, 14.2, 24.5) MHz

$A_{max}^{(Si)}$ = (-16.5, -17.9, -84.3) MHz

quadrupole tensor: **Low** field regime

(b) Ba_{Si} (q = +3, S = 1/2)

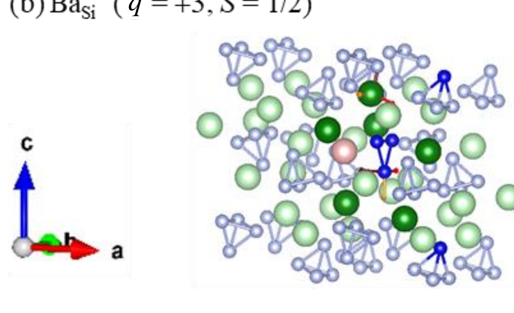

g-tensor : (1.995, 2.031, 2.051), g_{av} = 2.026

hyperfine tensor : $A_{max}^{(Ba)}$ = (51.9, 51.9, 53.5) MHz

$A_{max}^{(Si)}$ = (-21.0, -24.5, -142) MHz

quadrupole tensor: Intermediate regime

Fig. 5.6-1 Defect models of (a) interstitial Si (q = +1) and (b) Ba antisite substituted for Si (q = +3)

agreement with the experimental results.

For further identification, ED-NMR spectra were simulated based on the Hyperfine tensor and the quadrupole tensor obtained with these two defect models. I used a simulation routine developed by Cox *et al.*[169] That had previously successfully reproduced the ED-NMR spectrum of the nitroxide radical system. Figure 5.6-2(a) is obtained by inverting the actually measured ED-NMR spectrum. Thus, the sharp peak at $\Delta\nu = 0$ corresponds to an EPR allowed transition. On the other hand, it seems that a broad peak with its maximum at $\Delta\nu = 0$ is observed in $\Delta\nu = \pm 20$ MHz. In the ED-NMR measurement in Q-band reported by Prisner *et al.*,[170] the blind spot at $\Delta\nu = 0$ could be decreased up to $\Delta\nu_{1/2} \leq 5.1$ MHz by using Gaussian type pulse as HTA pulse as in this case. Considering that $\Delta\nu_{1/2}$ ~ 30-40 MHz, the possibility of an ED-NMR spectrum is sufficiently considered. In fact, the formation of a broad peak with its maximum at $\Delta\nu = 0$ was also confirmed from the simulation results of Si_i^+ and Ba_{Si}^{3+} (Fig. 5.6-2(b) and (c)). By the way, in the actual ED-NMR measurement, as shown in Table 5-16, clear peaks were observed at $\Delta\nu = -39, +35$ MHz. On the other hand, in the defect model considered this time, the appearance of a relatively sharp peak at $\Delta\nu \geq \pm 100$ MHz are expected. Even if the blind spot near $\Delta\nu = 0$ is considered, it is hard to say that the experimental results and the simulation results match. The spectrum may be due to another paramagnetic defect that could not be considered in this study. More detailed simulations and additional experiments are needed to identify defects in Si-rich samples.

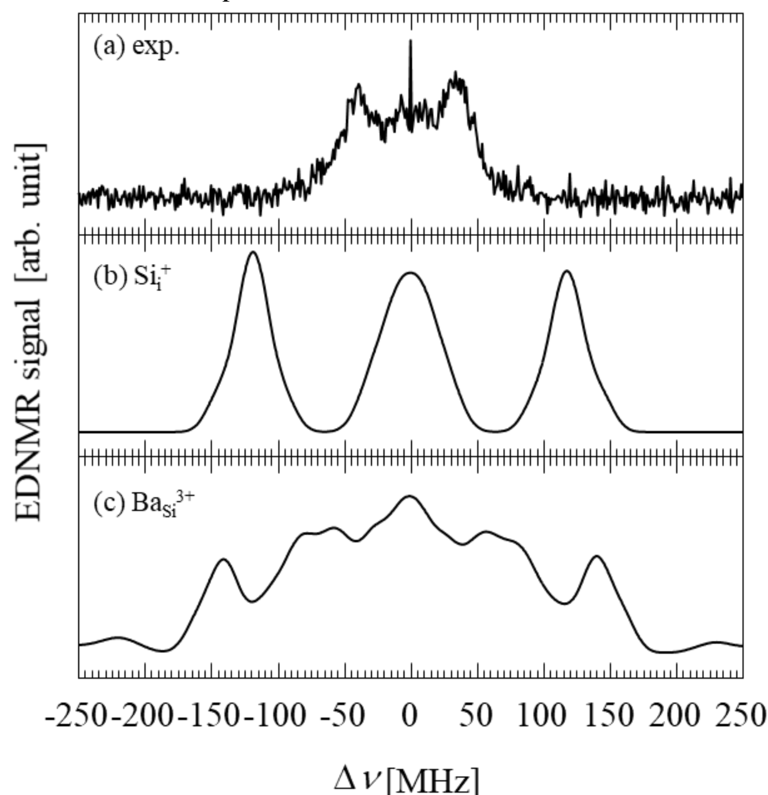

Fig. 5.6-2 (a) ED-NMR spectra of Sample J recorded at 1194 mT. Simulated ED-NMR spectra of (b) Si_i ($Q = +1$) and (c) Ba_{Si} ($Q = +3$).

Identification of the Defect 1 → nonconclusive yet

- ✓ *g*-tensor → Si_i^+ or Ba_{Si}^{3+}
- ✓ hyperfine tensor → no suitable defect model for the moment

Ba-rich

In the Ba-rich samples, I observed the three different paramagnetic centers as follow:

● Defect 3 [Ba-rich]

g-tensor : $g_1 = 1.844$, $g_2 = 1.910$, $g_3 = (1.930)$

● Defect 4 [Ba-rich]

g-tensor : tentative, $g_{av} \sim 1.975$ at X-band

● Defect 5 [Ba-rich]

g-tensor : $g_1 = 1.977$, $g_2 = 1.980$, $g_3 = 1.983\text{-}1.984$

In this discussion, I focus on the Defect 5 because I could observe enough visible hyperfine structures to compare with the calculated values. Judging from g-tensors, I pick two defect models as its candidate (Figs. 5.6-3).

(a) V_{Si} ($q = -1$, $S = 1/2$)

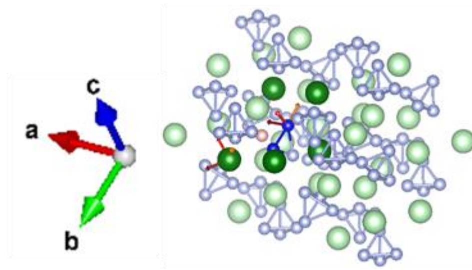

g-tensor : (1.974, 1.985, 2.001), $g_{av} = 1.987$

hyperfine tensor : almost with **Ba**

$A_{max}^{(Ba)} = (95.7, 95.8, 107)$ MHz

$A_{max}^{(Si)} = (-2.8, -4.9, -83.7)$ MHz

quadrupole tensor: Depends on sites (**High** field regime)

(b) Ba_i ($q = +1$, $S = 1/2$)

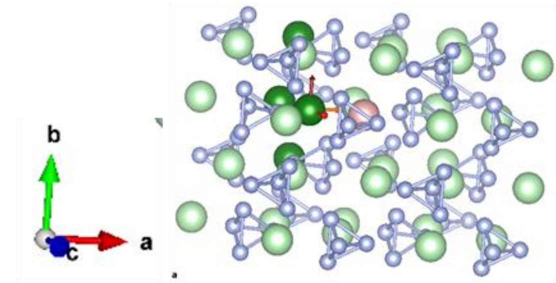

g-tensor : (1.951, 1.992, 1.9996), $g_{av} = 1.980$

hyperfine tensor : only with **Ba**

$A_{max}^{(Ba)} = (-42.6, -41.7, -37.8)$ MHz

$A_{max}^{(Si)} = ---$ MHz

quadrupole tensor: **Low** field regime

Fig. 5.6-3 Defect models of (a) Si vacancy ($q = -1$) and (b) interstitial Ba ($q = +1$)

Both models are considered to be formed in Ba-rich conditions. Similar way as the Si-rich, I simulated ED-NMR spectra for each model. Attention is first focused on Fig. 5.6-4(a). Comparing Fig. 5.6-4(b) with the experimental results, ED-NMR is observed by actual measurement at the position where the appearance of the ED-NMR peak is distant. On the other hand, the Ba-rich sample differs from the Si-rich sample in that the dependence on shot repetition time (srt) has been confirmed. In the sample with a shot repetition time of 1 ms, the peak of $\Delta\nu \sim \pm 45$ MHz expected for V_{Si}^- is relatively small, and it seems that it corresponds to the spectrum expected for Ba_i^+. Therefore, we focus on the results obtained with Ba-rich single crystal samples. As shown in Fig. 5.3-7 (a), a hyperfine structure with Ba at $|A| = 84$ MHz was observed in the single crystal sample. While such a large hyperfine component can be expected in V_{Si}^- in Fig. 5.6-3(a), it is about 40 MHz at the maximum in Ba_i^+ (Fig. 5.6-3(b)). Based on the above results, it can be said that the Defect 5 is most likely to be negatively charged V_{Si} at this time. However, as shown in Tables 5-6 and

5-7, at the current magnetic field position B_0 = 1209 mT (g ~ 1.982), T_1 and T_2 reflect at least two paramagnetic centers, and The possibility of two paramagnetic centers having close g-tensors cannot be completely excluded from the angle dependence of the sample (Figs. 5.3-6). More detailed identification should be confirmed by ED-NMR measurements in higher frequency bands (e.g., W-band to 94 GHz).

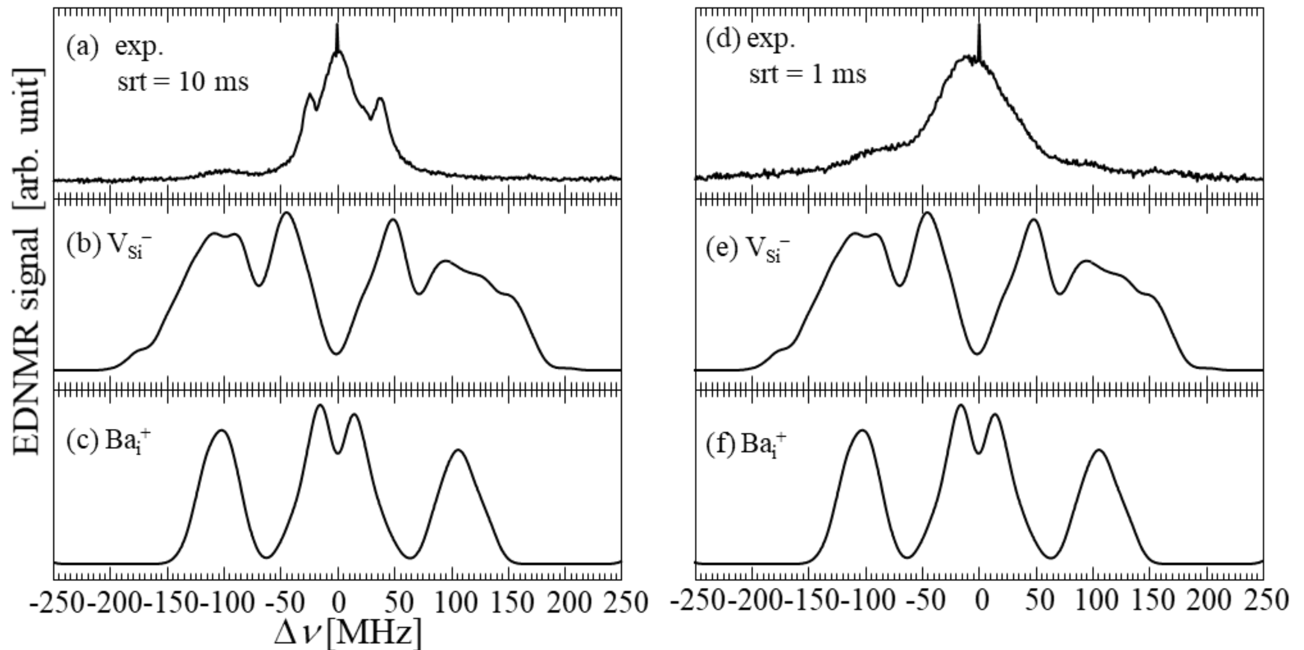

Fig. 5.6-4 (a) ED-NMR spectra of Sample J recorded at 1204 mT with shot repetition time, srt = 20 ms. Simulated ED-NMR spectra of (b) V_{Si} ($q = -1$) and (c) Ba_i ($q = +1$). (d) ED-NMR spectra of Sample J recorded at 1204 mT with shot repetition time, srt = 1 ms. Simulated ED-NMR spectra of (e) V_{Si} ($q = -1$) and (f) Ba_i ($q = +1$).

Identification of the Defect 5 → negatively charged Si vacancy, V_{Si}^-

- ✓ g-tensor → V_{Si}^- or Ba_i^+
- ✓ hyperfine tensor → V_{Si}^- or Ba_i^+
- ✓ single crystal → V_{Si}^-

Finally, through simulation of the ED-NMR spectrum of $BaSi_2$ based on the calculation result by DFT, it can be considered that it has the following two features:

① Possibility of ED-NMR broadening due to quadrupole interactions of Ba atom

② Asymmetric ED-NMR spectrum may be due to anisotropic hyperfine tensor

5.6.2. Comparison: film and bulk

At the end of this chapter, I discuss the origin of the paramagnetic center (the Defect B) observed in the film in chapter 4. As described in 4.6.1, the Defect B was suggested to be the defect that could significantly affect optical properties. The main purpose of this chapter was to reveal paramagnetic defects in $BaSi_2$ by using powder and single crystal of $BaSi_2$ bulk samples instead of the $BaSi_2$ epitaxial films. Therefore, I'd like to close this chapter with a discussion of this topic.

Figure 5.6-5 shows the EPR spectra of Samples D, I, and N. The red broken line indicate the position observed the EPR line with angle $\theta = 0$ (static magnetic field // *a* axis of the film). The *g* value of the film changed in the range of 2.003-2.010 as varying the angles. Also, the Defect B was considered to have longer relaxation time. Compared with the powder patterns of the Si-rich and the Ba-rich samples, the Defect B seems to correspond to those of the Si-rich samples. At the position of the red line, the two EPR lines are overlapped. From the anisotropy of g-tensor of the Defect 1 and 2, I suppose that the Defect B is ascribed to the Defect 2 while its behavior of relaxation, that is, the Defect 2 is more easily saturated than the Defect 1. However, relaxation times often depends on its spin concentrations. Unfortunately, the origin of the Defect 2 is still open.

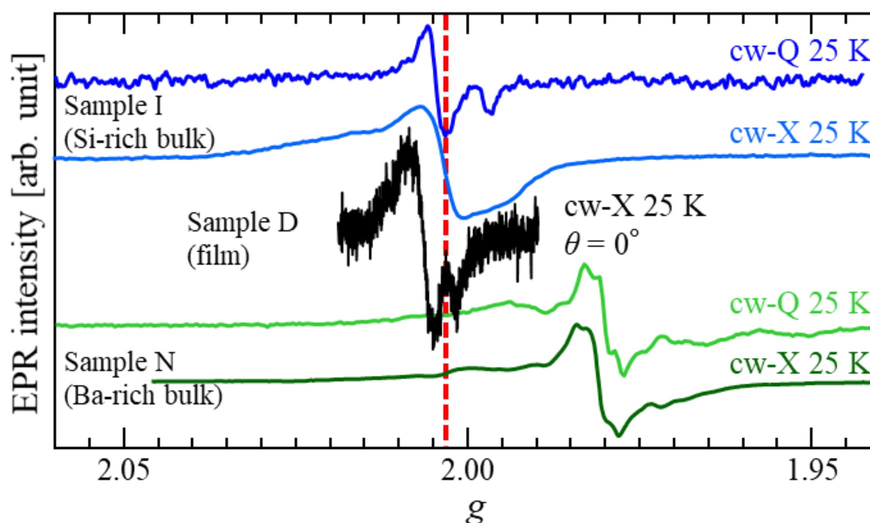

Fig. 5.6-5 Comparison the EPR line from the film with those of Si-rich and Ba-rich powder samples.

Chapter 6 Photoluminescence spectroscopy

EPR measurements provided microscopic information on defects in $BaSi_2$. However, it is difficult to determine their defect levels in the band gap by EPR. Therefore, I tried to determine the defect levels by photoluminescence (PL) spectroscopy, which is one of the most powerful methods for determination of the defect levels. A radiative defect model is also established by comparing the PL measurement results of samples having different atomic ratios with the defect levels previously reported. Furthermore, I paid special attention to the difference in formation of defects between the polycrystalline samples and thin-films by PL measurement.

6.1. Sample

I performed the PL measurements basically on the same samples as those used for the EPR measurements. The preparation and characterization of the polycrystalline sample are as summarized in Table 2-1 (the polycrystalline samples, sample I-N). Note that the polycrystalline samples before powdering were used. As thin film samples, undoped samples grown at different Si substrate temperatures during MBE growth were prepared. Samples O-AA with different deposition rate ratios (R_{Ba}/R_{Si}) were prepared (Table 6-1).

Table 6-1 Details of MBE growth conditions

<table>
<tr><th rowspan="2">Label</th><th colspan="5">MBE</th></tr>
<tr><th>T_S [°C]</th><th>R_{Si} (nm/min)</th><th>R_{Ba} (nm/min)</th><th>R_{Ba}/R_{Si}</th><th>Thickness (nm)</th></tr>
<tr><td>O</td><td rowspan="6">580</td><td rowspan="6">0.9</td><td>0.9</td><td>1.0</td><td rowspan="6">500</td></tr>
<tr><td>P</td><td>1.8</td><td>2.0</td></tr>
<tr><td>Q</td><td>1.8</td><td>2.2</td></tr>
<tr><td>R</td><td>2.0</td><td>2.6</td></tr>
<tr><td>S</td><td>2.8</td><td>3.1</td></tr>
<tr><td>T</td><td>3.6</td><td>4.0</td></tr>
<tr><td>U</td><td rowspan="7">650</td><td rowspan="7">0.9</td><td>0.4</td><td>0.4</td><td rowspan="7">500</td></tr>
<tr><td>V</td><td>0.8</td><td>0.9</td></tr>
<tr><td>W</td><td>1.1</td><td>1.2</td></tr>
<tr><td>X</td><td>1.4</td><td>1.5</td></tr>
<tr><td>Y</td><td>2.1</td><td>2.3</td></tr>
<tr><td>Z</td><td>2.6</td><td>2.9</td></tr>
<tr><td>AA</td><td>3.3</td><td>3.7</td></tr>
</table>

6.2. PL spectra of polycrystalline samples

I show the PL spectra of the polycrystalline samples measured at 8 K in Fig. 6.2-1. Among all the samples, relatively broad spectra were observed. The band gap of $BaSi_2$ is equal to 1.3 eV at RT. Also, there is a report showing that the band gap increased up to 1.4 eV at 8 K with decreasing temperature.[91] Therefore, all the observed peaks are

considered to be related to transitions containing defects levels. I confirmed that the spectral shape changed depending on the atomic ratios. In the most Si-rich sample, a very broad spectrum was observed in the energy range 0.7–1.0 eV. From the temperature dependence of the PL spectrum described later, it is considered that this broad spectra are superimposed with two spectra: P_1 having the maximum intensity at ~ 0.83 eV and P_2 having the maximum value at ~ 0.93 eV. As the atomic ratio changed from Si-rich to Ba-rich, P_3 (~ 1.03 eV) and P_4 (~ 1.12 eV) newly appeared. It should be noted that in the Ba-rich sample, the dominant P_1 and P_2 intensities were significantly decreased. In the present our PL setup, it is required to adjust the position of the lens for each measurement, so it is difficult to compare the absolute PL intensities precisely. However, as shown in Fig. 6.2-1, it was confirmed that the Si-rih sample tended to have a higher PL intensity. Since the order of the intensity differs between Samples I and N by one order of magnitude, it is inferred that P_1 and P_2 are transitions with high radiation intensity.

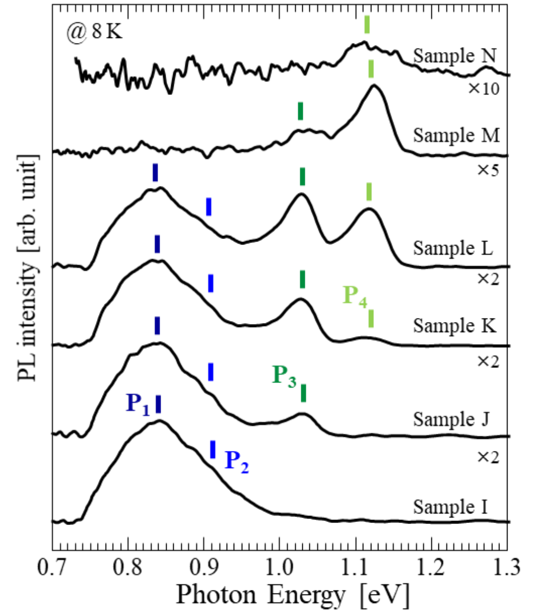

Fig. 6.2-1 PL spectra of polycrystalline Samples I-N. Four different transitions (P_1-P_4) were observed.

In order to get further information on the defect leves, I measured the PL spectra at different temperatures from 8-90 K on Sample I, K, and M (Figs. 6.2-2). As the PL transitions related to defects, (a) a transition between a donor (acceptor) level and a valence band (conduction band) or (b) a transition between a donor level and an acceptor level can be considered. In the case of (a), as the temperature rises, electrons (holes) trapped on the defect levels are thermally excited into the conduction band (valence band), so that the spectrum intensity increases. On the other hand, in the case of (b), the spectrum intensity decreases in the same scenario. However, since the spectra observed in this study were very broad, it was difficult to confirm the above-mentioned temperature dependence. According to Eagle,[183] a probability of transitions W_{BA} between electrons (holes) in the CB (VB) and holes (electrons) trapped by relatively shallow acceptor (donor) is given by,

$$W_{BA}(\hbar\omega) = A\left(\frac{\hbar\omega - E_g + E_a}{k_B T}\right)^{1/2} exp\left(-\frac{\hbar\omega - E_g + E_a}{k_B T}\right).$$

Here, E_a is the activation energy of the acceptors. From the equation, in the case of (a), we can also expect that a width of PL spectra become broader and a peak position shift toward high energy as increase of temperature. Therefore, using the PL peak position as a function of temperature, we tried to classify which of transitions (a) or (b) the PL spectrum observed is. The PL peak shift with the increase of temperature is generally several tens of meV.[184-186] In this measurement, it was mandatory to increase the measurable PL intensities by increasing the slit opening to 3 mm, so that there was no resolution of more than ten meV. I also paid attention to their very broad width of the spectra. In the case of (b), in theory, the transition between donors and holes as a function of the distance (r) between them can be observed at

$$\hbar\omega = E_g - (E_a + E_d) + \frac{e^2}{\epsilon r} - \frac{e^2 b}{\epsilon r^6}.$$

The E_d and ϵ are the activation energy of donor and the dielectric constant, respectively, and b is the constant. Hence, we can expect discrete spectra corresponding to the lattice parameter, making the detailed assignments possible in some materials.[187,188] However, we often observe a broad spectra because the r is too large to resolve the energy.

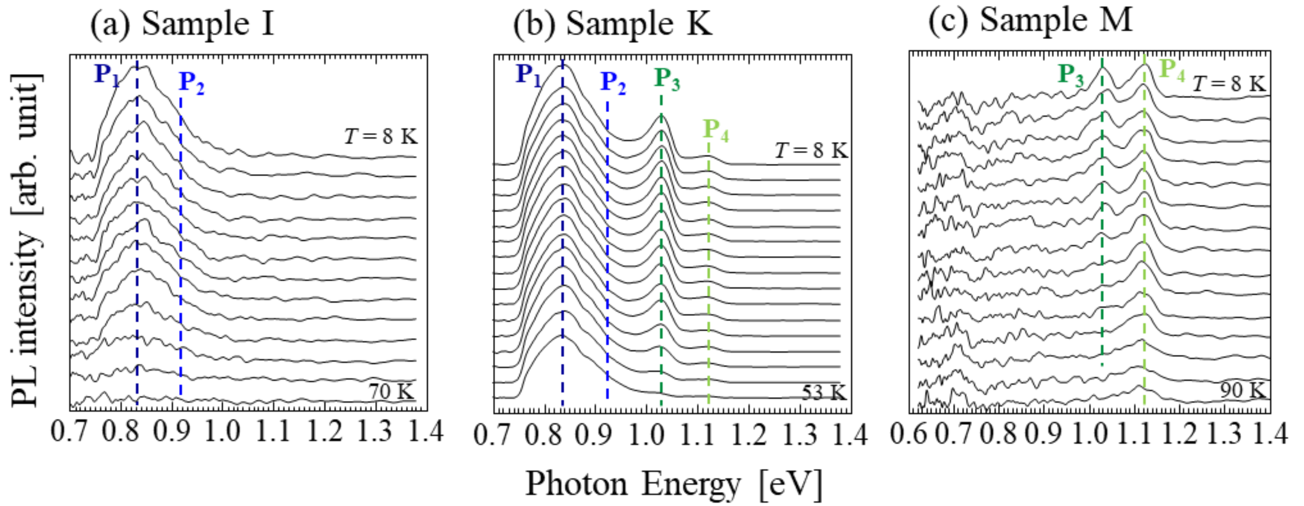

Fig. 6.2-2 Temperature dependence of PL spectra of (a)Sample I, (b) K, and (c) M.

The detailed classification of the transitions was confirmed by the excitation intensity dependence of each PL spectrum intensity. First, the experimental results were reproduced assuming four Gaussians. Fig. 6.2-3 shows the result of 8K as a typical fitting result.

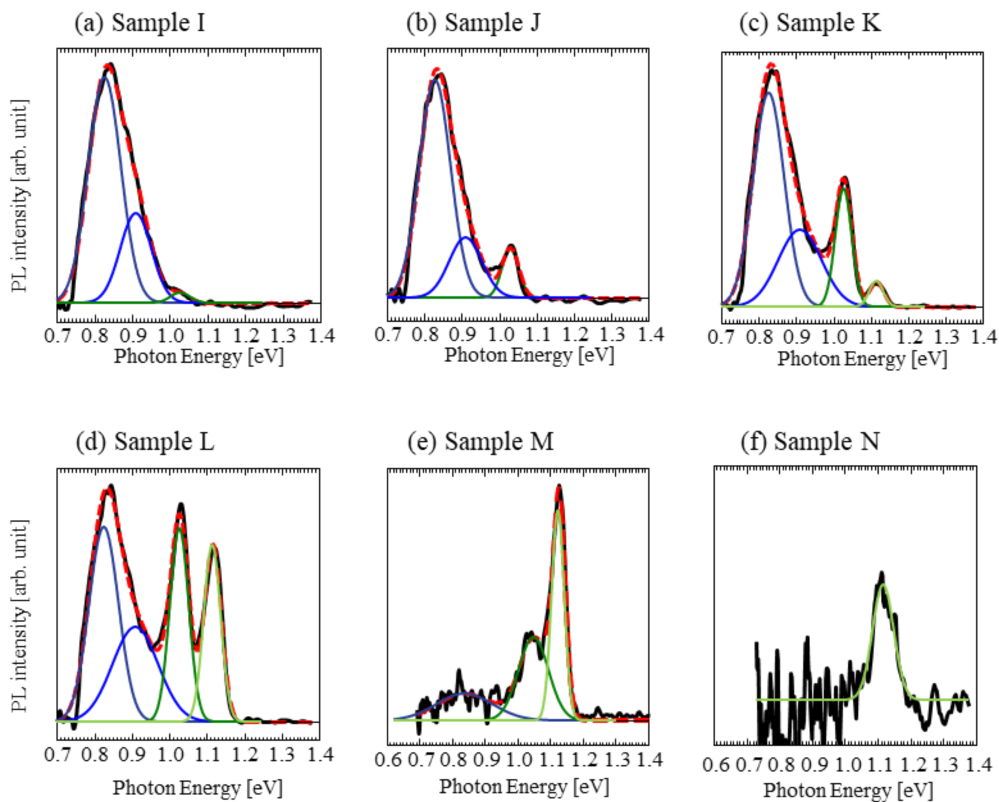

Fig. 6.2-3 Typical fitting results for samples I-N assuming four Gaussian curves are shown as a red broken line. Each PL spectrum contains four different transition denoted by P_1 (dark blue), P_2 (blue), P_3 (green), and P_4(light green).

Figures. 6.2-4 plots the intensity of P_1–P_4 peaks as a function of excitation intensity. In the case of the transition (b), electrons (holes) trapped by the defects are limited due to their densities, and therefore, the PL intensities are supposed to saturate with the increase of the excitation intensity. On the other hand, in the case of (a), since the valence band (conduction band) is related, the PL intensity increases in proportional to the excitation intensity. Hence, it is possible to classify which kind of transition exits by fitting the excitation intensity dependence using $I_{PL} \propto P_{exc}^{k}$. In the case of (a), $k = 1$, and in (b), $k < 1$.[186,189,190] From fig. 6.2-4, it was confirmed that $k < 1$ for P_1, P_2, P_3, and P_4, where $k = 0.52$, 0.57, 0.55, and 0.66, respectively. Thus, I concluded that all of the PL spectra observed this time are transitions between defect levels.

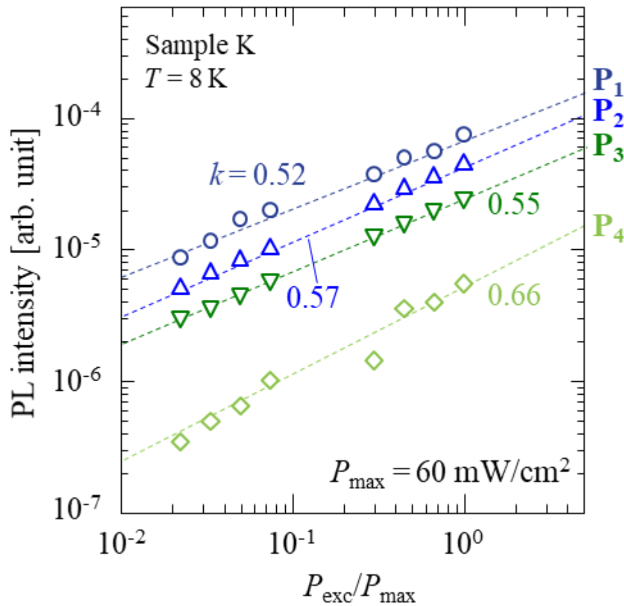

Fig. 6.2-4 Excitation intensity dependence of PL intensity at 8 K for sample K. All transitions follows $I_{PL} \propto P_{exc}^{k}$ ($k < 1$) as drawn by broken lines.

6.3. PL spectra of film samples

Figure 6.3-1(a) shows PL spectra of samples Q and W. The PL intensity increased in sample W, while sample W showed more intense photoresponse (PR) as seen in Fig. 6.3-1(b). In PL measurements, only radiative recombination process are possible to be observed. Therefore, such discrepancy between PL and PR intensities indicates that nonradiative and/or undetectable defects which are impossible to be detected by PL decreased in sample W. The defect level localized near the middle of the band gap, that is, deep defect levels often tend to be nonradiative. Also, I measured the PL spectra by using the detector in the range 800-1600 nm, so transitions between shallow donor (acceptor) defects levels are nondetectable. According to our previous first-principle calculations, a Raman peak originating from V_{Si} should appear at around 480 cm^{-1} (Appendix A). Because of a convolution with the most intense Raman peak of A_g mode in $BaSi_2$, I cannot decompose each spectrum at RT, yet I confirmed that its full-width at half maximum (FWHM) including a contribution of V_{Si} decreased in the film grown at $T_S = 650$ °C by 0.8 cm^{-1} compared with that in sample Q grown at $T_S = 580$ °C (Fig. 6.3-1(c) and its inset). As discussed in Ref. [97], the decrease of FWHM is correlated with the decrease of V_{Si}. Thus, I attribute the decrease of nonradiative (or undetectable) defects such as V_{Si} to an enhancement of PL intensity in sample W. The enhancement of PL intensity was observed among whole samples with different R_{Ba}/R_{Si}, which enables us to investigate radiative defects in the films with the whole range of R_{Ba}/R_{Si} (Fig. 6.3-2).

Figures 6.3-2(a)-(d) show temperature dependencies of PL spectra of samples V, X, Y, and AA grown at T_S = 650 °C. Although the variation of R_{Ba}/R_{Si} made their PL spectra look differently, I observed the four different transitions denoted as P_1, P_2, P_3, and P_4 in all samples. An example of the fitting result is shown in Fig. 6.3-3(e). The observed PL peaks (P_1-P_4) are located around 0.83, 0.95, 1.03, and 1.12 eV, respectively. Interestingly, I observed four PL peaks at almost the same energies as those observed in the films.

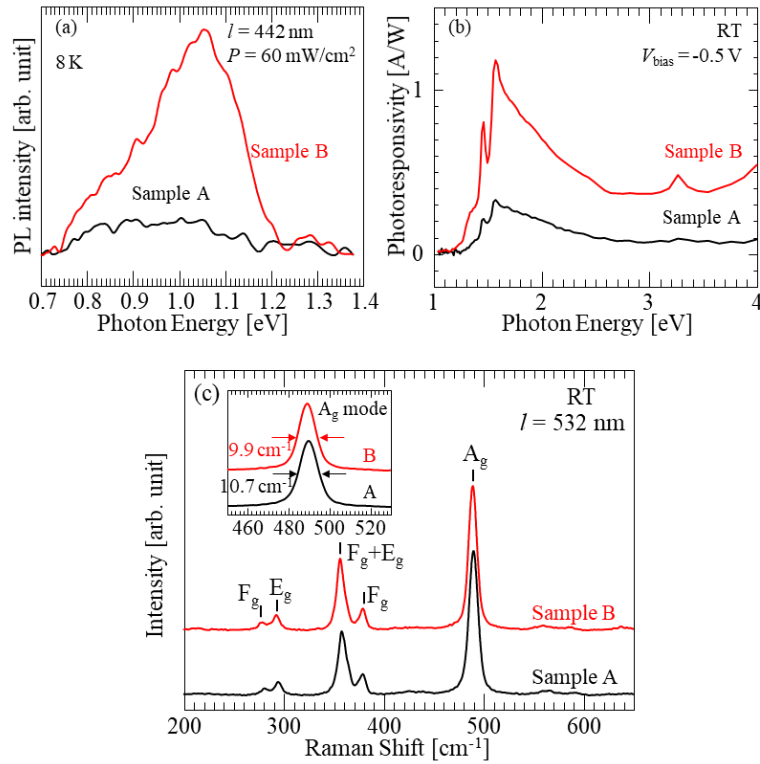

Fig. 6.3-1(a) PL and (b) PR spectra of samples A (TS = 580 ˚C) and B (TS = 650 ˚C). The PL spectra were measured at 8 K by a 442 nm laser light with an excitation power of 60 mW/cm2. The PR spectra were measured at RT under a bias voltage of –0.5 V applied to the front ITO electrode with respect to the back Al electrode. (c) Raman spectra of samples A and B. The decrease of FWHM of Ag mode indicates that the contribution of V_{Si} deceased in sample B as seen in the inserted figure.

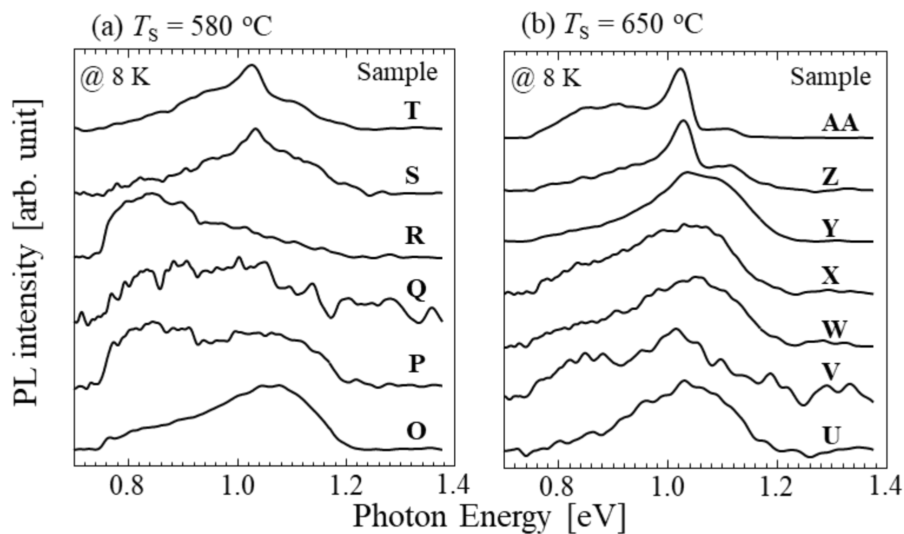

Fig. 6.3-2 PL spectra of $BaSi_2$ films grown at (a) T_S = 580 ˚C and (b) T_S = 650 ˚C

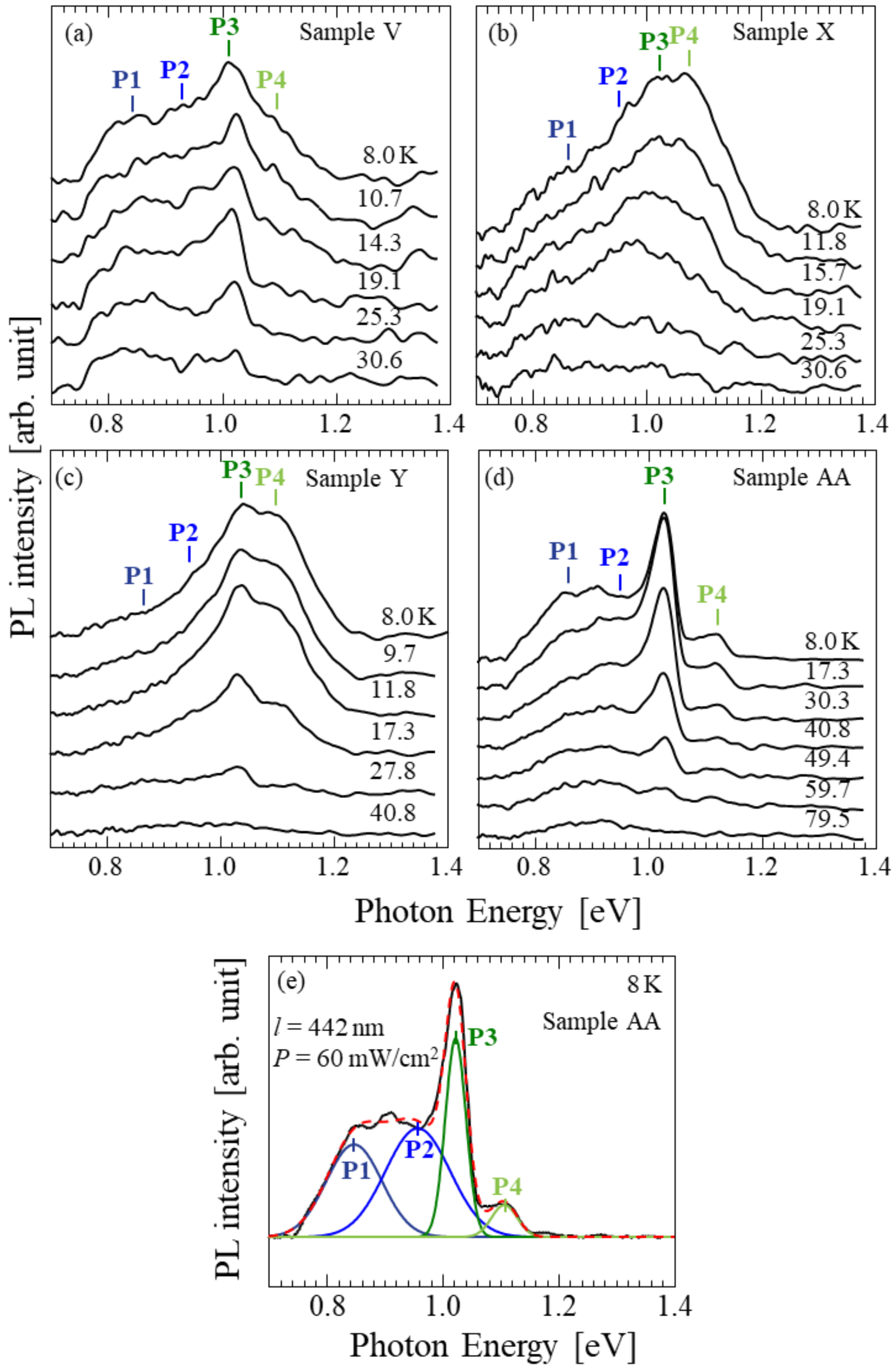

Fig. 6.3-3 Temperature dependence of PL spectra of (a) sample V, (b) sample X, (c) sample Y, and (d) sample AA. (e) A typical fitting result for sample AA assuming four Gaussian curves were shown as a red broken line. Each sample contains four different transition as denoted by P_1 (dark blue), P_2 (blue), P_3 (green), and P_4 (light green) in the figures.

6.4. Radiative defects model

Based on the obtained results, I discuss origins of each PL peak. Experimentally obtained defect levels are summarized in Table 6-2.

Table 6-2 Reported defect levels.

Defect level	Shape of sample	Measured by	Reference
$E_C – E_t = 0.26$ eV	Polycrystalline	resistivity	[80]
$E_C – E_t = 0.13$ eV	Polycrystalline	resistivity	[80]
$E_t – E_V = 0.27$ eV	film	DLTS	[84]

According to first-principle calculations,[106] V_{Si}, self-interstitial Si (Si_i), and Ba antisite for Si (Ba_{Si}) are considered as intrinsic defects in $BaSi_2$. Such defects are created with different concentrations under Si-rich and Ba-rich conditions. I compared relative PL intensity of each peak among the films and polycrystalline bulks in Fig. 6.4-1.

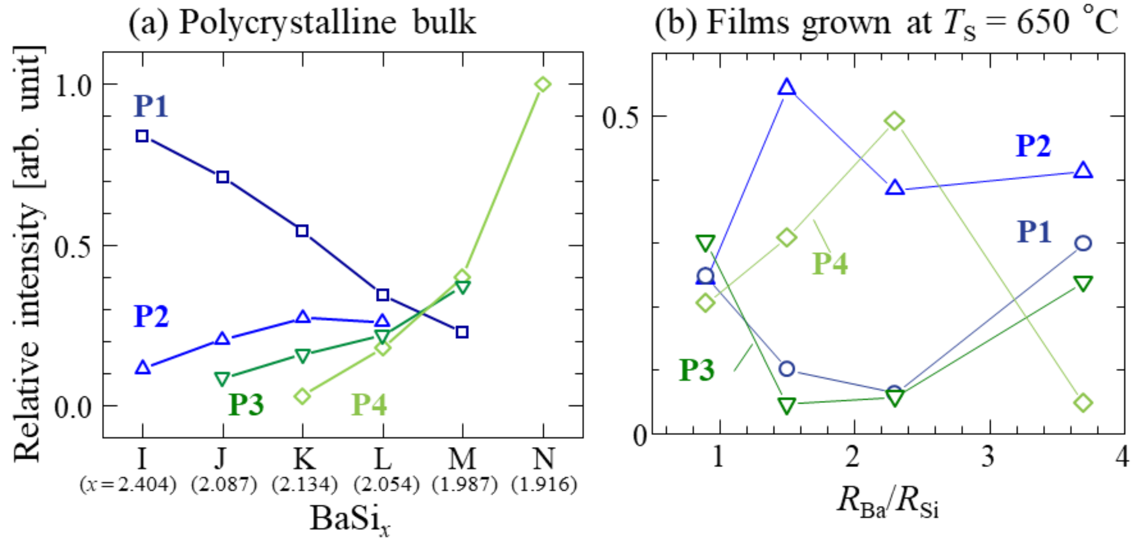

Fig. 6.4-1 Relative PL intensities of (a) the polycrystalline samples and (b) the film samples at 8 K, assuming four Gauss curves.

In the polycrystalline samples, the ratio of P_1 intensity increased with x while those of P_3 and P_4 decreased in Fig. 6.4-1(a). In contrast, rather complicated behavior was observed in the films in Fig. 6.4-1(b). One of the factors which make the R_{Ba}/R_{Si} dependence of P_1-P_4 intensity ratio complicated for the films is the diffusion of Si atoms from the Si substrate into grown layers. It was found from Rutherford backscattering spectrometry that the Ba/Si atomic ratio in a $BaSi_2$ film decreased when it approached the $BaSi_2$/Si interface for all the samples even though they were grown under a constant value of R_{Ba}/R_{Si} during the growth.[51] Besides we recently found that excess Si atoms in $BaSi_2$ films grown under Si rich conditions diffused out from the $BaSi_2$ layers and precipitated around the $BaSi_2$/Si interface, leading to the degradation of *a*-axis crystal orientation of $BaSi_2$ and quite rough $BaSi_2$/Si interfaces. Judging from these situations, I focus on the results of polycrystalline bulks in this study, where I can neglect such atomic distributions. Because Kumar *et al*. pointed out that V_{Si} were most likely to be formed in $BaSi_2$ even under Si-rich

conditions,[106] I suppose the most dominant PL peak, P_1, is related to V_{Si}. On the other hand, P_1 became most intense in sample I grown under Si-rich conditions. Hence, it is reasonable to assign Si_i as its counterpart. In the vicinity of stoichiometry, the intensity of P_1 decreased because of the decrease in the amount of V_{Si} and/or Si_i defects. In $BaSi_2$ epitaxial films passivated with atomic H, which might be consider to fill V_{Si}, the intensity of P_1 was decreased significantly (Fig. 6.4-2).[142,143] The fact that the carrier type changed from p-type to n-type around its stoichiometry in undoped $BaSi_2$ films supported this interpretation.[51] Thus, I conclude that a defect level of V_{Si} located at 0.26 eV below the conduction band minimum (CBM) as a donor level[89] and that of Si_i at 0.27 eV above the valence band maximum (VBM)[95] as had been suggested from the calculation.[106] P_2 is attributed to a transition between Si_i–related level and another donor level (0.13 eV)[89] so that its intensity also becomes intense as the Si ratio increased. Due to the lack of further information on defect levels, the origins of P_3 and P_4 peaks still remain unclear. However, judging from the tendency that both peaks increased under Ba-rich conditions, I speculate that Ba_{Si} seems to be responsible for them and it might be located at approximately 0.1 eV above the VBM. This assumption is considered reasonable because Ba_{Si} induces the defect level above the VBM according to the calculation.[106] Based on the above discussions, I propose a tentative model of radiative defects in $BaSi_2$ as shown in Fig. 6.4-3.

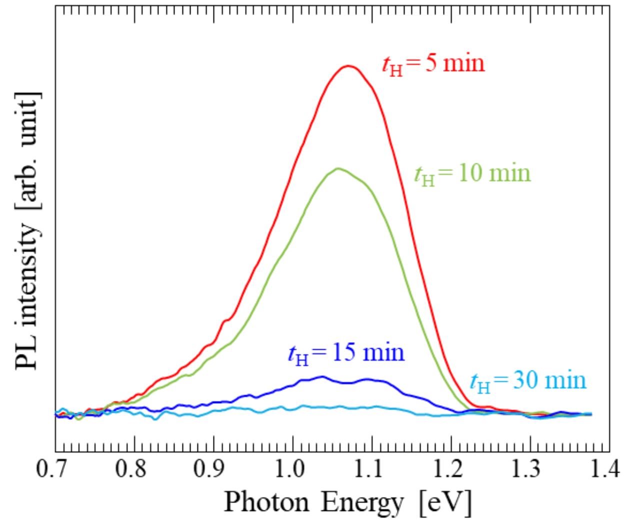

Fig. 6.4-2 PL spectra of $BaSi_2$ films (R_{Ba}/R_{Si} = 2.2) introduced atomic H for different supply durarions (t_H).

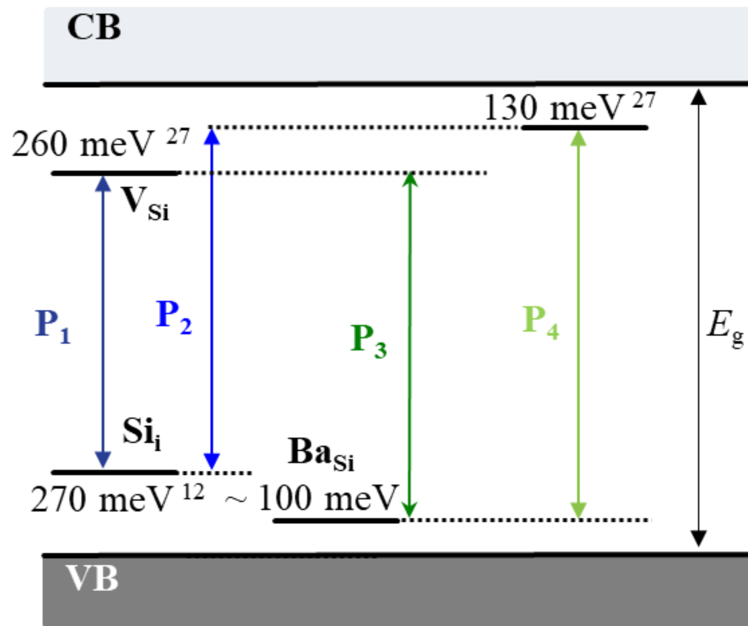

Fig. 6.4-3 A model of radiative defects in $BaSi_2$. Each assignment is discussed in the text.

6.5. Comparison with EPR spectra

Figures 6.5-1 (a) and (b) show the PL and EPR spectra of each bulk sample. First, we focus on the dominant PL spectra, P_1 and P_2, in Si-rich samples. This broad PL spectrum decreased in Ba-rich samples significantly. On the other hand, it can be seen that the paramagnetic centers, the Defect1 and the Defect2 observed in the Si-rich sample similarly decreased in the Ba-rich samples. From the radiative defect model (Fig. 6.4-3), I attributed P_1 to the transition between V_{Si} and Si_i. On the other hand, P_2 was assigned to the transition between Si_i and another donor level. Therefore, the Defect1 and the Defect2 originate from two of these three intrinsic properties. An origin of the Defect4 observed in Ba-rich samples may be assigned to defects that cause the P_3 or P_4 transition, or may be non-radiative defects that cannot be observed in PL. Considering that a positive correlation between the spin density of the Defect4 and the intensities of P_3 or P_4 in Samples M and N cannot be confirmed, I suppose that the Defect4 is likely to be the non-radiation defect for the moment.

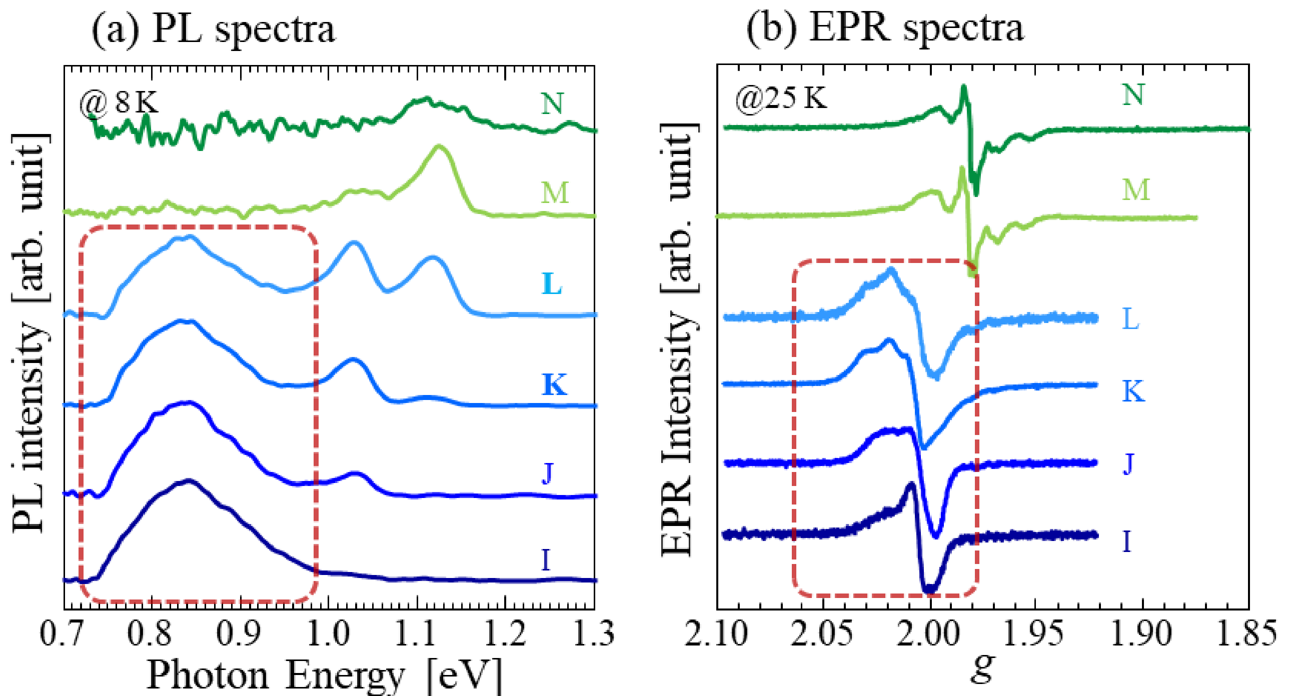

Fig. 6.5-1 (a) PL spectra of polycrystalline samples I-N and (b) EPR spectra of powder samples I-N measured at X-band. PL spectra and EPR scpectra surrounded by a red broken line show a positive correlation.

Next, we discuss the effects of introducing atomic H. As shown in Fig. 6.5-2 (a), a significant improvement in spectral sensitivity was confirmed for the thin film sample into which hydrogen was introduced. On the other hand, in the sample into which hydrogen was introduced, a decrease in the EPR line due to defects in the $BaSi_2$ thin film was confirmed (Fig. 6.5-2 (b)). In addition, when the PL spectra of the sample with and without hydrogen introduction are compared, a decrease in the P_1 and P_2 spectra can be confirmed in the sample into which hydrogen has been introduced. According to Figure 6.4-2, these PL transitions are caused by relatively deep defects. Thus, I conclude that the introduction of atomic hydrogen deactivates the relatively deeper defect in $BaSi_2$, resulting in that the significant improvement on PR was achieved.

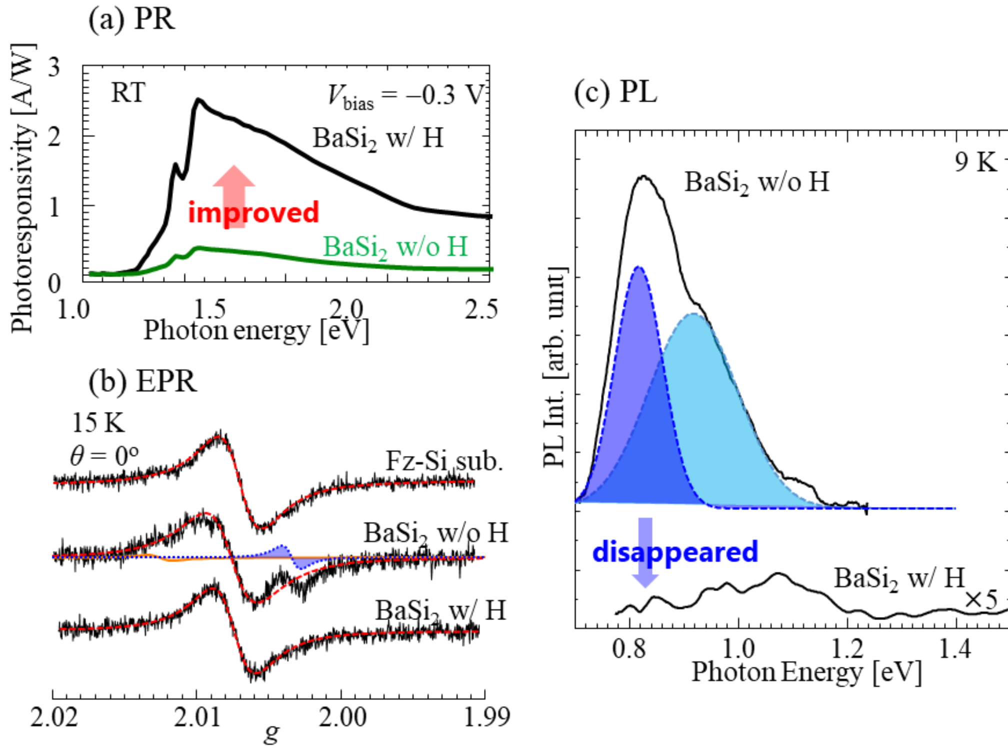

Fig. 6.5-2 (a) Photoresoponse improvement are observed in the film introduced atomic hydrogen (H). (b) EPR spectra of FZ-Si substrate, $BaSi_2$ epitaxial film without (w/o) and with (w/) atomic H. The EPR lines from the defects in $BaSi_2$ decreased in the films with atomic H. (c) PL spectra of sample B and G at 9 K. The sub-bandgap PL spectra disappeared after the introduction of atomic H.

6.6 Conclusion

Through the PL measurent of the $BaSi_2$ films and the pollycrystalline $BaSi_2$ samples with different atomic ratios of Ba and Si, I established the radiative defects model tentatively. The observed transitions and their origins are listed in Table 6-3.

Table 6-3 PL transitions observed in $BaSi_2$.

PL peak	Energy difference	Origin	Others
P_1	$(E_C - 0.26\ \mathrm{eV}) - (E_{V+} 0.27\ \mathrm{eV}) \sim 0.8$ eV	V_{Si} - Si_i	dominant in Si-rich
P_2	$(E_C - 0.13\ \mathrm{eV}) - (E_{V+} 0.27\ \mathrm{eV}) \sim 0.9$ eV	? - Si_{Si}	dominant in Si-rich
P_3	$(E_C - 0.26\ \mathrm{eV}) - (E_{V+} 0.10\ \mathrm{eV}) \sim 1.0$ eV	V_{Si} - Ba_{Si}	-
P_4	$(E_C - 0.13\ \mathrm{eV}) - (E_{V+} 0.10\ \mathrm{eV}) \sim 1.1$ eV	? - Ba_{Si}	-

Chapter 7 Total summary

My thesis focused on the investigation of intrinsic defects in $BaSi_2$ for defect control which is indispensable to design higher-η photovoltaic devices. The obtained results and the most significant contributions can be summarized as follows:

EPR study for $BaSi_2$ epitaxial films

I performed the electron paramagnetic resonance measurements on *a*-axis-orientated $BaSi_2$ epitaxial films grown on the Si substrate by molecular beam epitaxy. Through the EPR experiments, I successfully detect paramagnetic centers in the films (the Defect A: an isotropic center with $g = 2.00$, the Defect B: an anisotropic center with $g = 2.003$-2.010), which is pioneering results in $BaSi_2$. Also, I found that atomic hydrogens deactivate the centers. In other words, I considered that the Defect B can affect optical property significantly. Hence, aiming for further identification of the defects, I made full use of the conventional EPR techniques as well as multi-frequency EPR measurements. The only barrier to overcome was a paramagnetic center from the Si substrate. Since $BaSi_2$ is sensitive to moistures, it was impossible to apply a conventional technique to remove the center originating from the substrate. Therefore, I changed a strategy from the investigation of $BaSi_2$ films to $BaSi_2$ bulk samples.

EPR study for $BaSi_2$ bulks

I revealed that a deviation from stoichiometry produces five different paramagnetic defects in $BaSi_2$. First, I measured relaxation times (T_1 and T_2) by pulse EPR measurements and showed that paramagnetic centers possess different time orders of relaxation times. Based on these results, temperature dependence, microwave intensity dependence and multifrequency EPR measurements revealed the presence of at least two paramagnetic defects in Si-rich samples and at least three in Ba-rich samples.

In addition, I set up on further identification by evaluating hyperfine couplings of each defect by hyperfine spectroscopy using advanced EPR pulse sequence. HYSCORE revealed that all defects had a small hyperfine coupling of 2-3 MHz with ^{29}Si. Then, I continued to work on the hyperfine spectroscopy to obtain larger hyperfine coupling constants which correspond to deep defects that were interesting from the viewpoint of solar cell application. I performed the Davies ENDOR measurements, which are widely used for large hyperfine coupling. Although I successfully observed a broad spectrum with a maximum value of $|A/2| \sim 40$ MHz in the Ba-rich samples, a poor signal to noise ratio made detection of large hyperfine couplings difficult, especially, in the Si-rich samples. Therefore, I performed the ED-NMR measurements, which has been attracting attention as a new hyperfine coupling method in recent years. As a result, I succeeded in getting ED-NMR spectra with peaks at about 35 MHz for the Si-rich sample and about 35, 100, and 165 MHz for the Ba-rich sample.

I have also started EPR studies using single crystal samples to determine all the components of g-tensor and hyperfine tensor. Although it is necessary to determine the crystal axes by XRD in the future, I have already succeeded in obtaining an interesting angular dependence of the EPR spectra. In a rather short future (2-3 months), I will be able to have a complete list of all simple defects for $BaSi_2$. The EPR measurements on single crystal have such an awesome and tremendous potential.

Based on the above experimental results, each paramagnetic center was separated and simulated using Easyspin. In addition, the spin density of each paramagnetic center was evaluated using TEMPO as a standard sample. As mentioned earlier, the experimental results could be explained by assuming the presence of two different paramagnetic centers in the Si-rich sample and three in the Ba-rich sample.

Finally, I also tried to obtain EPR parameters by DFT calculation. The g-tensor, hyperfine tensor, and nuclear quadrupole tensor were calculated for a total of 12 defect models with different charge states for 6 different possible defects in $BaSi_2$. Now, the computations are going on very well with 2×2×1 supercell within the limited computational resources. Furthermore, the calculated results showed that each defect model possesses compatible g-tensors and hyperfine tensor, suggesting that I can establish defect models in $BaSi_2$ in near the future.

Combining all the above results, it was shown that a negatively charged Si vacancy (V_{Si}^-) can be identified in a Ba-rich sample as a specific defect model for the Defect 5. On the other hand, it was revealed that the EPR spectrum observed in the $BaSi_2$ thin-film (the Defect B) could correspond to the paramagnetic center observed in the Si-rich sample (the Defect 2). As for the origin of the Defect 2 is still under discussion.

Photoluminescence spectra of $BaSi_2$

Through photoluminescence (PL) spectroscopy, I tried to obtain information on defect levels that cannot be obtained by the conventional EPR measurements. Four corresponding PL peaks were observed for thin and bulk samples, suggesting that similar defects are present in both samples.

By combining EPR and PL, I also confirmed that the decrease in the EPR line originating from the Defect B, which was observed in the thin film sample into which atomic hydrogen was introduced, corresponded to the decrease in the PL peak of 0.8-0.9 eV. From the viewpoint of solar cell application, the significant improvement in optical properties of the sample with atomic hydrogen was due to the fact that defects located at relatively deep positions in the band gap were inactivated by hydrogen.

Table 7-1 summarize the defects in $BaSi_2$ revealed by this studies.

<table>
<tr><td rowspan="2"></td><td>Defect 1</td><td>Defect 2</td><td>Defect 3</td><td>Defect 4</td><td>Defect 5</td></tr>
<tr><td colspan="2">Si-rich</td><td colspan="3">Ba-rich</td></tr>
<tr><td>g-tensor</td><td>g_1 = 1.993-8,
g_2 = 2.012-4,
g_3 = 2.025-30</td><td>g_1 = 1.997,
g_2 = 2.004-5,
g_3 = 2.010-1</td><td>g_1 = 1.844,
g_2 = 1.910,
g_3 = 1.930</td><td>g_{av} ~ 1.975
at X-band</td><td>g_1 = 1.977,
g_2 = 1.980,
g_3 = 1.983-4</td></tr>
<tr><td>N_{spin}
[spins/cm^{-3}]</td><td>2.27–9.28
× 10^{16}</td><td>2.22–3.71
× 10^{16}</td><td>4.22–7.56
× 10^{16}</td><td>6.43 × 10^{17} –
1.11 × 10^{17}</td><td>8.97 × 10^{15} –
3.02 × 10^{17}</td></tr>
<tr><td>Origin</td><td>(Si_i^+?, Ba_{Si}^{3+}??)</td><td>?</td><td>?</td><td>?</td><td>V_{Si}^-</td></tr>
<tr><td>PL peak</td><td colspan="2">P_1 (0.8 eV) or P_2 (0.9 eV)</td><td colspan="2">N/A</td><td>Nonradiative?</td></tr>
</table>

Impact of this work and prospective

I had established the base of EPR study in $BaSi_2$. Unfortunately, full investigation and identification have not accomplished yet. However, now that this study has clarified the paramagnetic centers in $BaSi_2$, for example, EPR measurements using single crystal $BaSi_2$ will further clarify the nature of the defects. The most potential application of $BaSi_2$ is to solar cells, but recently its low thermal conductivity has raised expectations as a thermoelectric conversion material, too. I hope that the defect information identified through this research will be useful in that respect as well.

In the future, rapid scan EPR,[191] which has recently been remarkably developing, will provide a new perspective in addition to electrically-detected EPR as a means of directly observing defects in thin film samples. From a relation between defects and optical properties, EPR measurements on powder or single crystal $BaSi_2$ with atomic hydrogen introduced will provide more direct information on the effect of atomic hydrogen toward the defects. In addition, the present study confirmed the correlation between PL and EPR spectra to some extent, indicating that there is plenty of room for studying optically-detected-EPR experiments.[192,193]

Focusing on EPR spectroscopy, I hope that the ED-NMR used here could show its amazing potential for investigating hyperfine coupling in disorder systems such as powder samples. The development and improvement of a two-dimensional ED-NMR sequence using Chirp pulses reported recently by Jeschke *et al.*[194] will show further benefits of ED-NMR, as well as W-band ED-NMR. A ED-NMR spectra simulation combining with DFT calculation will also help us reveal the full picture of the defects in $BaSi_2$.

At the end

In my personal opinion, I have successfully demonstrated that EPR is very good spectroscopy to analyze the defects of $BaSi_2$. At the beginning of the EPR study of the film, it seemed difficult to characterize the defects in $BaSi_2$ by EPR. However, after the investigation on the bulk, I could obtain plenty of results. Moreover, the observed EPR line in the bulk agreed well with that observed in the films. I strongly recommend the “next” challenger to perform electrically-detected EPR on the films and also to continue ED-NMR measurements at the higher field, for instance, W-band.

Acknowledgement

This thesis and all experimental results have been completed thanks to a lot of supports. Here, I acknowledge all of them such as supervision of my Ph. D course, technical advice, research funds and equipment for experiments.

Supervision

My research activities in Ph.D course have been supervised by Prof. Takashi SUEMASU in the University of Tsukuba (UT), Dr. Serge GAMBARELLI in IRIG, DIESE, SyMMES, CEA-Grenoble, and Dr. Anne-Laure BARRA in LNCMI-Grenoble, CNRS. They helped me a lot to complete this thesis by discussing the direction of my research, writing papers, brushing up presentations, and admission processes for the universities. In particular, the double degree program (DDP) between UT and Université Grenoble Alpes (UGA), which I belong to, needed a lot of complicated processes. Thank you very much for supporting and leading me. I also acknowledge Prof. Katsuhiro AKIMOTO and Prof. Etienne GHEERAERT who are in charge of DDP and secretaries in UT, UGA and CEA. Without their help, I could not have such precious experiences as a researcher and an individual.

Scientific advice and experimental support

In Japan, I have been given lots of advice and impression from Prof. Takashi SYEMASU and Assoc. Prof. Kaoru TOKO for the growth and characterization technique of crystalline thin film by MBE. Prof. Yuzo OHNO, Assoc. Prof. Takahide UMEDA, Assoc. Prof. Takeaki SAKURAI in UT provided me kind advice and feedback of my research in several checkpoints in my PhD course and especially in the pre-defense. I also express my gratitude to Dr. Motoharu IMAI in the National Institute for Material Science (NIMS) who is one of the jury members of my Ph.D thesis. Prof. Haruhiko UDONO in the Ibaraki University and Mr. Masami MESUDA in the Toso Corp. provided us their precious bulk $BaSi_2$ samples. Without their kindness, I could not even start my work. I appreciate to Emeritus Prof. Junichi ISOYA in UT fruitful discussions from the viewpoints of his outstanding experiences. Regarding the results of Raman spectroscopy, Prof. Yoshikazu TERAI helped me to obtained interesting results. Asst. Prof. Kosuke O. HARA in the University of Yamanashi, gave me a new interest of $BaSi_2$. When I started to compute lattice vibrations by the first principle calculation, Prof. Norio Ohta in UTtaught me know-how.

In France, lots of researchers in SyMMES and LNCMI contributed to my research. In addition to my supervisors, Prof. Lionel DUBOIS, Ph.D Jean-Marie MOUESCA and Ph.D Vincent MAUREL in CEA-Grenoble provided me many hints to brush up my work from their great professionality. Also, I express great gratitude to Prof. Didier GOURIER in Insitut des sciences et technologies de Paris, who is one of the jury members of my Ph.D thesis. The discussions with Prof. GOURIER gave us novel and valuable insights. I appreciate their accessments during my Ph. D defense to Dr. Geneviève BLONDIN in CNRS-Grenoble and Dr. Matthieu JAMET in CEA-Grenoble. I also appreciate it to Dr. Michel BARDET in CEA-Grenoble to introduce me to Dr. GAMBARELLI. Without your introduction, I couldn' t work with him. I also appreciate to Mr. Christian LOMBARD and Mr. Jean-Francois JACQUOTD in CEA-Grenoble , who helped me not only develope new experimental setup but also design sample holders. Dr. Julia LENDON and Dr. Timothée CHAUVIRÉ in CEA-Grenoble helped me manipulate EPR

spectrometer and interpriate spectra. I appreciate it to Dr. Paul NÖEL in Eidgenössische Technische Hochschule Zürich that he helped me prepare the samples and gave me scientific advice.
comments and helpful suggestions.

Special thanks

I am now really satisfied with my Ph. D course in Tsukuba and Grenoble. The three years I spent there were and will be the most precious in my life. I did not imagine such wonderful experiences. I express great gratitude to all the people I worked with and met.

SUEMASU-sensei has given me a lot of opportunities since I started my Ph. D course. First of all, thank you very much for accepting me to your amazing laboratory. I am really glad that I was one of the members of my laboratory. I appreciate it to you that you gave me not only a good environment for researches but also a lot of advice.

Serge is one of the best benefactors in my French student life. Without you, I wouldn't decide to continue researches in a field of EPR. You are always working with a lot of enthusiasm. I respect you and want to become a researcher like you. I am honor to be one of your students. Thank you very much, Serge.

I also express my gratitude to Anne-Laure. The experiences of high-field EPR measurements were very impressive. Also, thank you very much for telling me about the beautiful mountains to visit. I have not visited all the mountains yet, but I will in the future.

TOKO-sensei taught me the attitude of a young researcher and also gave me a very nice opportunity for my next carrier. Thank you so much for all your advice and help.

As senior students in Japan, Dr. Ryota TAKABE and Dr. Tianguo DENG, and Dr. Toshiki GUSHI taught me how to manage research life in Suemasu-Toko laboratory. Especially, Gushi-san helped me live a life in Grenoble, too. Thank you very much.

I also thank Julia and Timothée for your kind teaching for EPR measurements in France. I look forward to seeing you at future EPR meetings in the future.

As junior students, Mr. Zhinhao XU, Mr. Mr, Suguru Yachi, Mr. Miftahullatif EMHA Bayu, Mr. Yudai YAMASHITA, Ms. Komomo KODAMA, Mr. Rhota SUGIYAMA, Mr. Shu SUGIYAMA, Mr. Taira NEMOTO, Mr. Sho AONUKI, Ms. Loise BENINCASA, Ms. Yurika HAKU, Mr. Ryuichi YOSHIDA, and Mr. Ryota KOITABASHI helped my experiments and lots of discussion and activated me by their own attitude for research. Thank you very much. Xu-san, I am sure that you can obtain interesting results in Canada. Yamashita-kun, your MBE techniques were outstanding. I wish that you all obtain nice results in the future.

Owing to all members of the Suemasu-Toko laboratory, I could enjoy my student life in Tsukuba. Thank you very much.

In France, thanks to all my friends in the laboratory. Also, I especially thank Mr. Damien DEJEAN and Jérôme NENICH. Without you guys, I couldn’t spend such a great daily life in Grenoble. Thanks a lot.

Finally, thank you very much, my parents, for watching me warmly so far.

February, 2020

Takuma SATO

Appendix

A. Raman spectroscopy and DFT calculations

Raman spectroscopy enables us to access to the atomic structure of defects in $BaSi_2$ with the help of first-principles calculation because vibrational frequencies are specific to a moleclue's chemical bonding and symmetry. There have been several defect studies using Raman spectroscopy such as Se vacancies in Cu(In, Ga)Se_2 and Si precipitations in β-$FeSi_2$ films.[195,196] However, there has been no such discussion about defects in $BaSi_2$ although there have been serveral rerpots on Raman spectra of $BaSi_2$ from both experimental and theoretical viewpoints so far.[69,123-125]

A.1. Sample

I carried out the Raman spectroscopy on the same film samples (denoted as Sample O-T in Table 6-1) as those used for the PL measurements in Chapter 6. Lattice constants of the films were measured by out-of-plane (θ-2θ) and in-plane (φ–$2\theta_\chi$) x-ray diffraction (XRD) measurements with a Cu Kα radiation source. I calculate the lattice constants from the XRD peak positions obtained from out-of-plane (a) and in-plane (b and c) XRD patterns by using the Nelson-Riley relationship.[122]

A.2. Lattice constants and residual stress

The peak shift of Raman spectrum $\Delta\omega$ is proportional to the magnitude of the residual stress σ_{res} in the film.[197,198] Hence I estimate σ_{res} by using lattice constants of sample . The lattice constants as a function of $R_{\mathrm{Ba}}/R_{\mathrm{Si}}$ are shown in Fig. A.2-1 (a). As can be seen in Fig. A.2-1 (a), a becomes larger as $R_{\mathrm{Ba}}/R_{\mathrm{Si}}$ increases, and then decreases with further increase in $R_{\mathrm{Ba}}/R_{\mathrm{Si}}$ after reaching a maximum in the vicinity of 2.2. On the other hand, b and c show the tendency opposite to a. From the obtained lattice constants, I evaluate the strain ε_{ii} in the directions of a, b, and c based on Eq. (1),

$$\epsilon_{ii} = \frac{d_{hkl} - d_{0_{hkl}}}{d_{0_{hkl}}} \quad (i = 1, 2, 3)\,, \tag{1}$$

where d_{hkl} and $d_{0\,hkl}$ is the measured lattice spacing and that of unstrained $BaSi_2$, respectively. As the lattice constants of relaxed sample, those of powdered XRD are used.[22] Following the Hooke's law, the residual stress in the film is obtained from the evaluated strain as,

$$\sigma_{ij} = s_{ijkl}\epsilon_{kl} \quad (i, j, k, l = 1, 2, 3)\,, \tag{2}$$

where s_{ijkl} are the compliance constants of single crystal $BaSi_2$, and the values calculated by Peng *et al.* are used for them.[125] Evaluation of the residual stress in the film by XRD is carried out assuming an in-plane stress condition ($\sigma_{11} = \sigma_{12} = \sigma_{13} = 0$) as applied to, for example, <111>-oriented Al thin films on a Si(001) substrate.[199] However, in this work, it was difficult to obtain diffractions of sufficient intensity from the asymmetric planes of $BaSi_2$. Hence, diffractions such as (0k0) and (00l) obtained in the in-plane XRD measurement were used. The stress $\sigma_{22}(\parallel \sigma_b)$ and $\sigma_{33}(\parallel \sigma_c)$ in the plane were roughly estimated by assuming that the principal axes of stress coincided with the crystal axes. Figure A.2-1 (b) shows the result of the calculated strain $\varepsilon_{11}(= \varepsilon_a)$ in the direction perpendicular to the film

from the obtained in-plane stress using Eq. (2). The R_{Ba}/R_{Si} dependence of the *a*-axis lattice constant of the $BaSi_2$ film on Si(111) can be qualitatively understood by the above model, that is, the in-plane stress model assumed the principal axes of stress coincides with the crystal axes. On the other hand, the residual stress σ_{res} in the film is expressed by the sum of thermal stress σ_{th}, intrinsic stress σ_{int}, and external stress σ_{ext} given by,

$$\sigma_{res} = \sigma_{th} + \sigma_{int} + \sigma_{ext}. \quad (3)$$

Using the following Eq. (4), I calculate the thermal stress.

$$\sigma_{th} = \frac{E_f}{a - \nu_f}(\alpha_f - \alpha_s)\,\Delta T, \quad (4)$$

where, α_s and α_f are the linear thermal expansion coefficients of Si and $BaSi_2$, and ΔT is the difference between the Si substrate temperature during MBE growth and room temperature. E_f and ν_f are the Young's modulus and Poisson's ratio of $BaSi_2$, respectively. I employ the values of 50 GPa and 0.201 reported by Imai *et al.*[200] for them. Figure A.2-1 (c) shows the R_{Ba}/R_{Si} dependence of the intrinsic stress σ_{int} subtracted the thermal stress σ_{th} from the in-plane residual stress σ_{res}. σ_b and σ_c are the intrinsic stresses in the *b*-axis and *c*-axis directions, respectively, assuming the external stress σ_{ext} = 0. Intrinsic stress is caused by extinction of point defects and/or vacancies,[201] formation of grain boundaries,[201] interface lattice mismatch between the substrate and the film.[202,203] There is not so much difference in the effect of grain boundary and lattice mismatch among the $BaSi_2$ films grown with different R_{Ba}/R_{Si} values. Therefore, I consider that the contribution of defects in un doped $BaSi_2$ films is mainly responsible for the variation of intrinsic stress on R_{Ba}/R_{Si}.

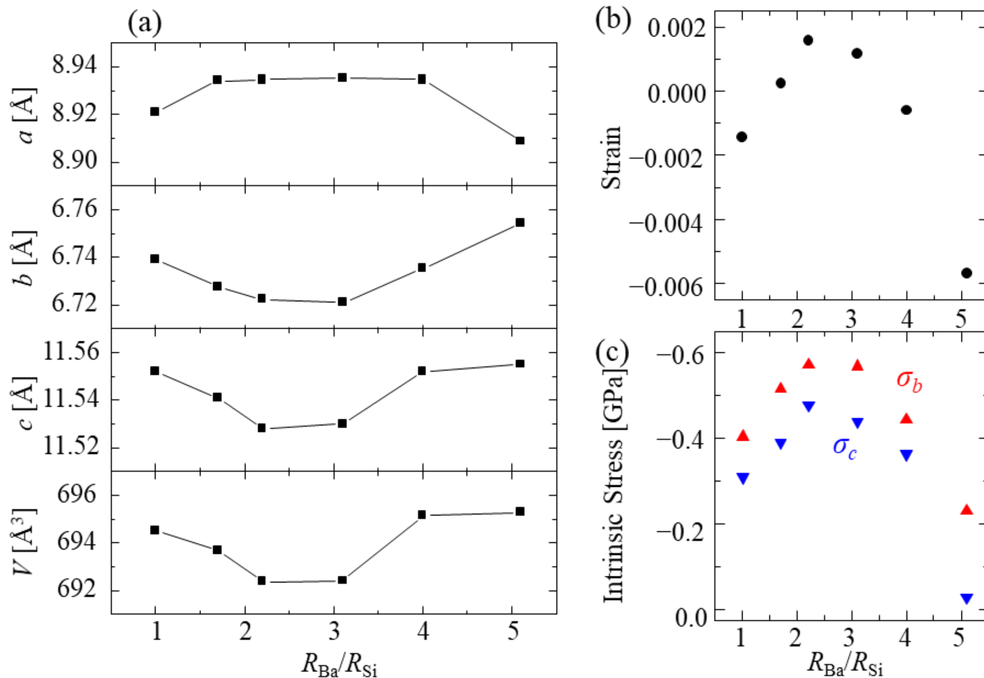

Fig. A.2-1 (a) Lattice constants as a function of R_{Ba}/R_{Si} for 600-nm-thick undoped $BaSi_2$ films. (b) Strain in the *a*-axis direction and (c) intrinsic stress in the *b*-axis and *c*-axis directions as a function of R_{Ba}/R_{Si}.

A.3. DFT Calculation: vibrational frequency

In order to discuss the effects of point defects mentioned in the previous Section on the Raman spectrum, I calculate the vibrational frequencies of $BaSi_2$ including point defects by first principles calculation.

A.3.1. Method

Two intrinsic point defects, Si vacancy (V_{Si}) and Ba substituted for Si antisites (Ba_{Si}), were introduced into one of the four Si(3) sites as previously reported.[51,106] I adopted a previously reported interstitial site, the fractional coordinate of which is (0.5841, 0.25, 0.2251), as an initial configuration for Si interstitials (Si_i).[174] The vibrational frequency calculation at Γ point was performed with QUANTUMN ESPRESSO code[175] within the framework of *ab initio* pseudopotential density functional perturbation theory.[204] I employed the norm-conserving pseudopotentials with generalized gradient approximation in Troullier-Martins type[205] and the cut-off energy of the plane-wave basis sets was 45 Ry. For *k* points in the Brillouin zone, a 3×4×2 Monkhorst-Pack mesh was used for a perfect crystal (with an orthorhombic cell). The estimated energy error in self-consistency was less than 10^{-14} a.u. Relaxation was performed until the total energy changed by less than 10^{-5} a.u. and the components of forces were smaller than 10^{-4} a.u. during geometry optimization.

Table A-1. Calculated Raman active optical phonon frequencies [cm^{-1}] of $BaSi_2$ at Γ point. The modes are categorized to external modes (ext) including the translation of Si cluster (t) and rotation of that (r), internal modes of Si cluster (int), and the modes of Ba. Their relative magnitudes of displacement are also shown as vs = very strong, s = strong, m = medium, and w = weak.

Freq. [cm-1]		Si	Ba	Freq. [cm-1]		Si	Ba
51.2	ext	m	s	134.7	ext(t,r)	s	-
52.7	ext	s	vs	141	ext(r)	s	w
63.4	ext(t)	s	vs	145.5	ext(t,r)	vs	w
64.1	ext(t,r)	m	s	149.8	ext(r)	vs	w
66.2	ext(t,r)	m	vs	154.8	ext(r)	vs	w
71	ext(r)	m	s	156.7	ext(r)	vs	m
71.7	ext(t,r)	m	s	267.9	int	s	-
73.3	ext(t,r)	w	vs	268.9	int	s	-
75.8	ext(t)	s	vs	282.3	int	vs	-
75.9	ext(r)	m	vs	286.7	int	vs	-
82	ext(t,r)	s	vs	361	int	vs	-
93.9	ext(r)	m	vs	362	int	vs	-
103.3	ext(r)	vs	w	364.6	int	vs	-
113.2	ext(r)	vs	-	365.1	int	vs	-
118.9	ext(t,r)	s	w	384.9	int	vs	-
124.1	ext(r)	s	w	387.6	int	vs	-
127.8	ext(t,r)	vs	w	499.8	int	vs	-
130.6	ext(t,r)	vs	w	502.5	int	vs	-

A.3.2. Computed results

First, I confirm the reproducibility of this calculation. Table A-1 shows the calculation results of the optical modes at the Γ point (q = (0,0,0)) in a $BaSi_2$ perfect crystal. The relative magnitudes of displacement of Si_4 cluster and Ba for each mode are also shown. As reported previously by Peng *et al.*,[125] lattice vibrations of Ba atoms is hardly observed at wavenumbers higher than 200 cm^{-1}, and all the calculated modes are internal vibrations of Si_4 clusters. On the other hand, the modes observed below 200 cm^{-1} are the external vibrations (rotation, translation) of the Si_4 clusters and/or the lattice vibrations of Ba. For comparison, Table A-2 summaries reported Raman peak positions due to a Si_4 cluster in $BaSi_2$.[69,123-125] Terai *et al.* also pointed out such feature of modes in the measurement of the angle dependencies of polarized Raman spectra of *a*-axis-oriented undoped $BaSi_2$ epitaxial films on Si(001).[127] Comparing the present calculated peak positions of Raman active modes to the experimental result in powdered $BaSi_2$, I confirm that the peak positions are almost reproducible (Table A-2).[124] In particular, with respect to the internal vibrations of Si_4 cluster, the reproductivity is within ± 2-3%. In Raman scattering experiments, the A_g modes at around 500 cm^{-1} as shown in Fig. A.3-1, are the most intense peak. Hereafter, I pay attention to the A_g modes of each

Table A-2. Reported experimental and theoretical Raman peak positions [cm^{-1}] due to a Si_4 cluster in $BaSi_2$. They are based on the results of powdered $BaSi_2$,[124] phonon density of states (DOS),[125] $BaSi_2$ film on Si(111) by vacuum evaporation,[69] and $BaSi_2$ film on Si(001) by MBE,[123] respectively.

Powdered $BaSi_2$[124]	Phonon DOS[125]	$BaSi_2$/Si(001)[69]	$BaSi_2$/Si(001)[123]
276	282	278	280
293	296	292	295
355	-	355	358
-	363	-	362
376	381	376	380
486	486	486	486

sample.

Table A-3. Calculated total energies [Ry] for compounds. V_{Si} or Ba_{Si} is introduced into one of the crystallographically inequivalent Si sites in unit cell.

Compunds	Total energy [Ry]
$Ba_8Si_{15}V_{Si(3)}$	−139.97
$Ba_8Si_{15}V_{Si(4)}$	−139.95
$Ba_8Si_{15}V_{Si(5)}$	−139.96
$Ba_8Si_{15}Ba_{Si(3)}$	−142.33
$Ba_8Si_{15}Ba_{Si(4)}$	−142.20
$Ba_8Si_{15}Ba_{Si(5)}$	−142.25

Table A-4. Fractional coordinates of three intrinsic defects as an initial configuration.

Intrinsic defects		Fractional coordinates		
		x	*y*	*z*
Si vacancy	$V_{Si(3)}$	0.424	0.25	0.091
Ba antisite	$Ba_{Si(3)}$	0.424	0.25	0.091
Si interstitial	Si_i	0.5841	0.25	0.2251
O interstitial	O_i	0.5841	0.25	0.2251

I next investigated the effect of point defects in $BaSi_2$ on the Raman peak position. Based on the report by Kumar *et al.*,[106] I adopted three native defects such as V_{Si}, Ba_{Si}, and Si_i. As shown in Fig. 2.2-1, $BaSi_2$ has three crystallographically inequivalent Si sites in the unit cell; Si(3) and Si(4) occupy the 4*c* site and Si(5) occupies the 8*d* site. Table A-3 shows the calculated total energy of compounds including one V_{Si} or Ba_{Si} into each Si site, which is described as $Ba_8Si_{15}V_{Si(3)}$, $Ba_8Si_{15}V_{Si(4)}$, $Ba_8Si_{15}V_{Si(5)}$, $Ba_8Si_{15}Ba_{Si(3)}$, $Ba_8Si_{15}Ba_{Si(4)}$, and $Ba_8Si_{15}Ba_{Si(5)}$.

From the viewpoint of total energy, both V_{Si} and Ba_{Si} seem to be easily introduced into the Si(3) site. On the other hand, there are 16 sites into which interstitial impurities can be introduced. According to Imai and Watanabe,[174] the most probable insertion sites are the 4*c* sites, where an impurity atom is surrounded by three Si atoms, one of which is at a peak of one Si-tetrahedron and the other two of which are composing an angle of the other Si-tetrahedron. Thus, we employed one of the 4*c* sites as the initial configuration of Si_i, the fractional coordinate of which is (0.5841, 0.25, 0.2251). Table A-4 shows the initial configurations of the three native point defects used to calculate the vibrational frequencies, whose positions correspond to those for the EPR parameter in Chapter 4. The calculated photon frequencies of A_g modes are shown in Tabel A-5 together with that of perfect crystal. I predict the local vibrational modes shown in Figs. A.3-2 (a)-(c) to emerge at certain wavenumbers presented in bold in Table A-5. The appearance of local vibrational modes by the introduction of point defects has been confirmed by Raman spectroscopy, for example in B doped bulk Si.[206] On the other hand, as shown in Table A-5, the peak position of the main peak (A_g mode) shown in Fig. A1.2-2 is expected to shift to lower wavenumbers because of the formation of native defects.

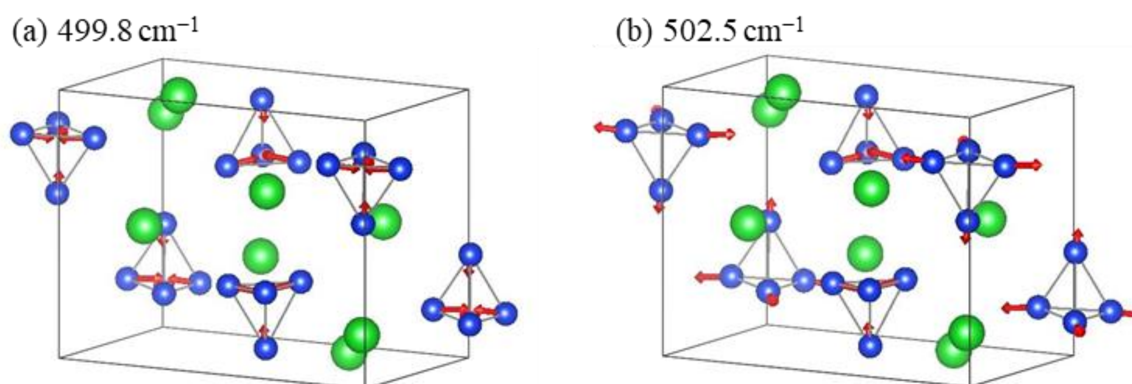

Fig. A.3-1 Raman active A_g modes calculated at Γ point in a $BaSi_2$ perfect crystal at (a) 499.8 cm^{-1} and (b) 502.5 cm^{-1}.

Table A-5. Calculated phonon frequencies of Raman active A_g modes. Frequencies in boldface are local vibrational modes (LVM).

Ba_8Si_{16}	$Ba_8Si_{15}V_{Si(3)}$	$Ba_8Si_{15}Ba_{Si(3)}$	$Ba_8Si_{16}Si_i$	$Ba_8Si_{16}O_i$
499.8	469.5	436.8 (LVM)	442.7	447.2
502.5	474.1	457.1	465.7	478.7
	477.1	472.1	477.1	484.7
	477.7 (LVM)	486.6	556.7 (LVM)	597.3 (LVM)

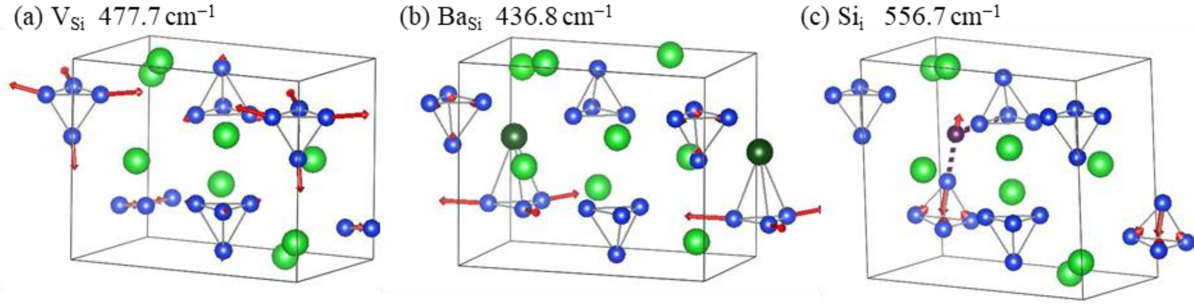

Fig. A.3-2 Local vibrational modes of (a) V_{Si}, (b) Ba_{Si}, and (c) Si_i.

A.4 Effects of intrinsic defects on Raman spectra

Based on the above discussions, I attempted to detect intrinsic defects by Raman spectroscopy in undoped $BaSi_2$ with different R_{Ba}/R_{Si}. Figures A.4-1 (a) shows the Raman spectra of undoped $BaSi_2$ in the range between 200 and 650 cm^{-1}. Peaks due to the internal vibration of Si_4 cluster can be observed at wavenumbers ranging from 250 to 500 cm^{-1}. Figure A4-1 (b) presents an enlarged view of the main peak due to the A_g mode at approximately 490 cm^{-1}. Figure A.4-1 (c) shows a plot of the peak wavenumber in Fig. A.4-1 (b) against R_{Ba}/R_{Si}, showing that it reaches a maximized at R_{Ba}/R_{Si} = 2.2. From the calculation results in Section A2, it is expected that the shift of this main peak to a lower wavenumber is ascribed to the influence of intrinsic defects.

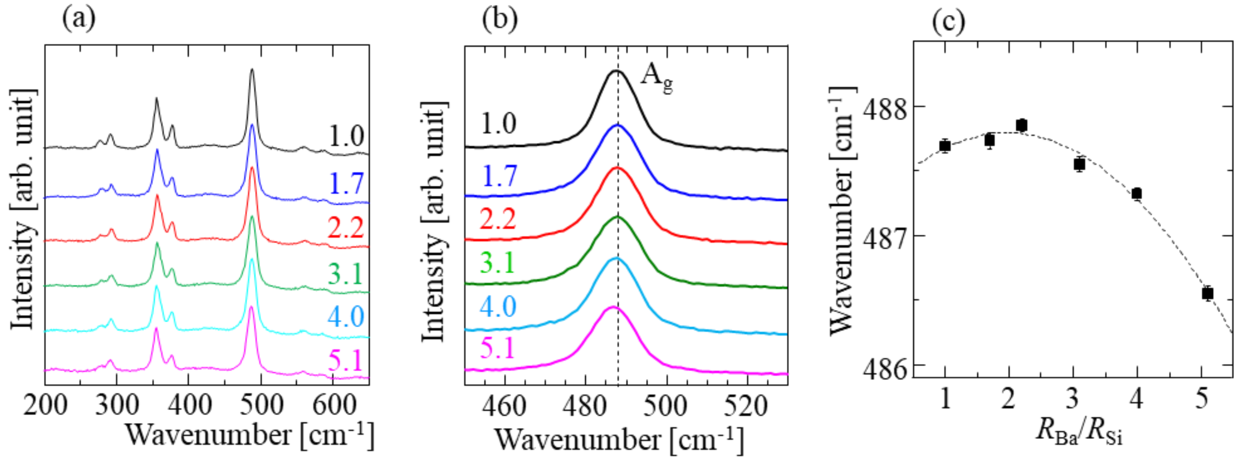

Fig. A.4-1 (a) Raman spectra of 600-nm-thick undoped $BaSi_2$ films with different R_{Ba}/R_{Si} values in the range of 200-650 cm $^{-1}$ at RT. (b) Raman spectra of Raman spectra of 600-nm-thick undoped $BaSi_2$ films with different R_{Ba}/R_{Si} in the range of 450-530 cm^{-1} at RT. (c) A main peak (A_g mode) position (shown in Fig. A4-1 (b)) as functions of R_{Ba}/R_{Si}.

Therefore, the shift of the main peak was examined from the viewpoint of atomic ratio of Ba to Si, N_{Ba}/N_{Si}, in these samples. Using the depth profile of N_{Ba}/N_{Si} obtained by RBS,[51] I calculated the N_{Ba}/N_{Si} in the film surface weighted by the optical absorption coefficient of $BaSi_2$ at a wavelength of the incident light λ = 532 nm used in this Raman measurement.

$$\frac{N_{Ba}}{N_{Si}} = \frac{\int N_{RBS}(z)e^{-\alpha z}dz}{\int e^{-\alpha z}dz}, \qquad (5)$$

where $N_{RBS}(z)$ is the measured N_{Ba}/N_{Si} at a depth z by RBS, and $\alpha = 3 \times 10^5$ cm^{-1} is used as the light absorption coefficient at λ = 532 nm. Substituting these values for Eq. (5), I calculated the weighted N_{Ba}/N_{Si} values to be 0.477,

0.499, and 0.510 for R_{Ba}/R_{Si} = 1.0, 2.2 and 4.0, respectively. Figure A.4.-2 plots the peak position of A_g mode of the present Raman spectra against weighted N_{Ba}/N_{Si}. From the viewpoint of stoichiometry, we consider that intrinsic defects in the film are least abundant at R_{Ba}/R_{Si} = 2.2 because it is the closest to stoichiometry (N_{Ba}/N_{Si} = 0.5).
Thus, the main peak shift in Fig. A.4-1 (c) is considered to reflect the influence of intrinsic point defects. In order to further confirm the validity of this interpretation, I discuss the appearance of local vibrational modes accompanying the formation of native defects shown in Figs. A.3-2 (a)-(c). First, I examine V_{Si}, which is most likely to occur according to Kumar *et al.*[106] Although the local vibrational mode of V_{Si} is expected to appear at approximately 480 cm^{-1} , it is very close to the peak position of the most intense peak of the A_g mode. Figure A.4-3 (a) shows the full width at half maximum (FWHM) of the peak intensity of A_g mode as a function of R_{Ba}/R_{Si}. The FWHM value increased with R_{Ba}/R_{Si}. Polarized Raman spectra measured at RT on samples prepared with R_{Ba}/R_{Si} = 1.0 and 5.1 are also shown in Fig. A.4-3 (b). One Lorentzian curve located at around 486 cm^{-1} is enough to reconstruct the measured spectrum at R_{Ba}/R_{Si} = 1.0. However, another Lorentzian curve located at around 480 cm^{-1} is necessary to reconstruct the experimental data at R_{Ba}/R_{Si} = 5.1. As the contribution of this peak increases with R_{Ba}/R_{Si} = 1.0, this peak is assumed to originate from V_{Si}. Also, we confirmed a positive correlation between the FWHM of A_g modes and the increase of S-parameter which become larger with increse of vacancy density in the field of the positron annihilation spectroscopy. I thus conclude that the number of V_{Si} increases with R_{Ba}/R_{Si}.

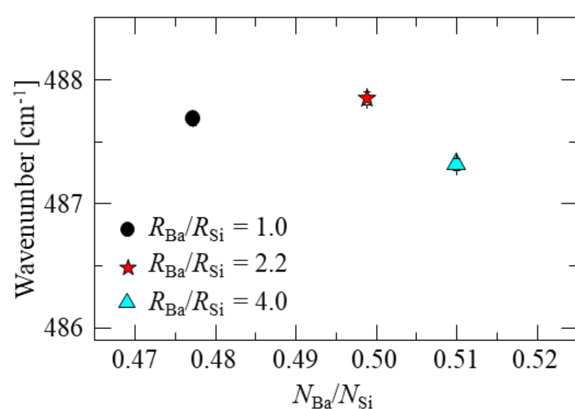

Fig. A.4-2 A main peak (A_g mode) position (shown in Fig. A.4-1 (b)) as a function of weighted N_{Ba}/N_{Si} for R_{Ba}/R_{Si} = 1.0, 2.2, and 4.0.

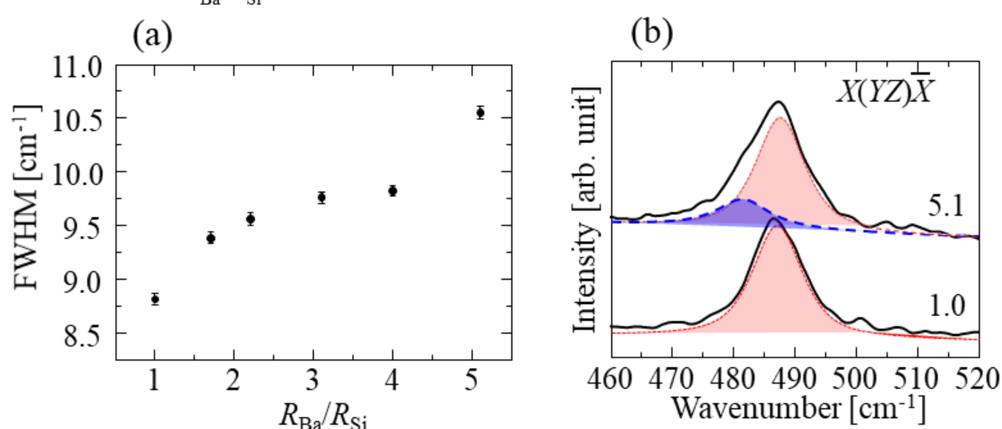

Fig. A.4-3 (a) FWHM values of the peak intensity at around 490 cm^{-1} as a function of R_{Ba}/R_{Si} at RT. (b) In the polarized Raman spectrum measured on the sample prepared with R_{Ba}/R_{Si}=5.1 (Ba rich condition), another Gaussian curve peaking at 480 cm^{-1} is necessary. I interpret it as being due to V_{Si} LVM.

Figure A.4-4 presents the highlighted Raman spectra of $BaSi_2$ films with different R_{Ba}/R_{Si} values. Additional peaks denoted by broken lines at 430, 560, and 590 cm^{-1} are observed. Figure A.4-5 presents the R_{Ba}/R_{Si} dependence of the peak intensity at 430 cm^{-1} normalized using the A_g mode intensity at 490 cm^{-1} . The dotted lines are guides to the eye. The peak intensity increases with increasing R_{Ba}/R_{Si}. In addition, the calculated phonon frequency caused by the vibrational mode of Ba_{Si} (436.8 cm^{-1}) shown in Table A-5 is close to this wavenumber. Hence, I interpret this broad peak as being due to the local vibrational mode of Ba_{Si}.

To investigate the other two Raman peaks at around 560 and 590 cm^{-1} in Fig. A.4-4, I measured the Raman spectrum at 78 K on the sample with R_{Ba}/R_{Si} = 2.2 as shown in Fig. A.4-6 (a). In the range between 560 and 600 cm^{-1} , three peaks appear at 561.3, 576.0, and 590.2 cm^{-1} . The wavenumbers 561.3 and 590.2 cm^{-1} almost double 279.8 and 296.6 cm^{-1}, respectively. Hence, there is a possibility that the second order vibrational modes were observed. However, this assumption is not valid because of the following reasons. Figure A.4-6 (b) shows the Raman spectra measured at 78 K on samples with different R_{Ba}/R_{Si} values. Note that the spectra were normalized using the peak intensity of the A_g mode at 490 cm^{-1}. As shown in Fig. A.4-6 (b), the signal intensities in the range between

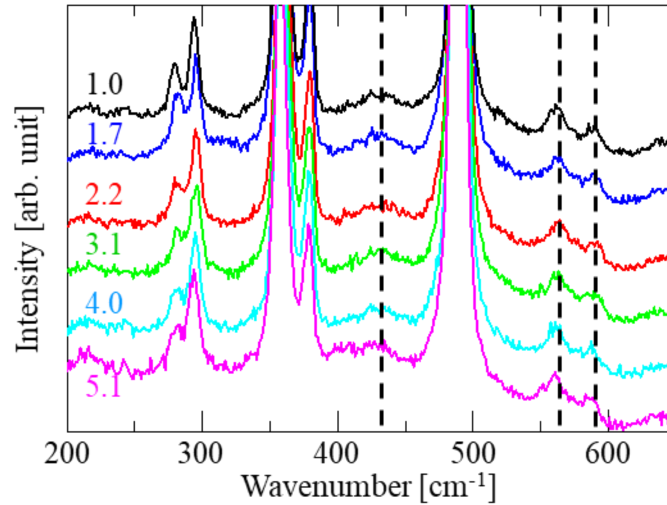

Fig. A.4-4 Highlighted Raman spectra of $BaSi_2$ films with different R_{Ba}/R_{Si} values. Additional peaks are observed along the broken lines.

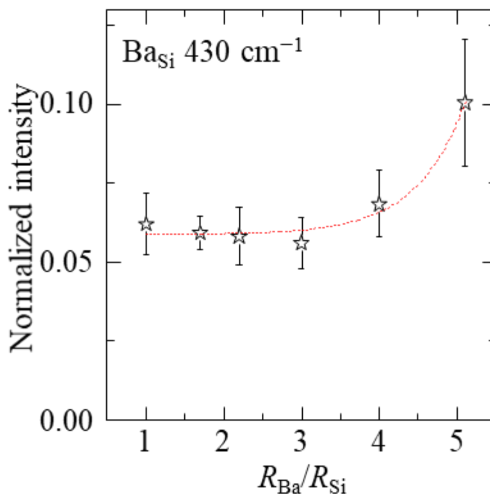

Fig. A.4-5 R_{Ba}/R_{Si} dependence of Raman peak intensity at around 430 cm^{-1} normalized using the A_g mode intensity at around 490 cm^{-1}. The dot lines are a guide to the eyes.

500 and 600 cm^{-1} are quite sensitive to R_{Ba}/R_{Si}, whereas there is not so much difference in the other range. Besides, they become higher as R_{Ba}/R_{Si} is deviated away from the vicinity of 2.2. These results suggest that the Raman peaks at around 560 and 590 cm^{-1} in Fig. A1.3-4 originate from defects. It is considered that Si_i is considered one of the origins because the calculated phonon frequency of Si_i (556.7 cm^{-1}) is close to 560 cm^{-1}. O_i (597.3 cm^{-1}) is also a candidate because it is close to 590 cm^{-1} , and the oxygen concentration in $BaSi_2$ films grown by MBE is more than 10^{19} cm^{-3} according to Ref. [207]. At present, I do not have sufficient data to discuss further. Thus, further studies are mandatory; however, I may reasonably conclude that Raman spectroscopy is an effective means to understand the presence of intrinsic point defects in $BaSi_2$.

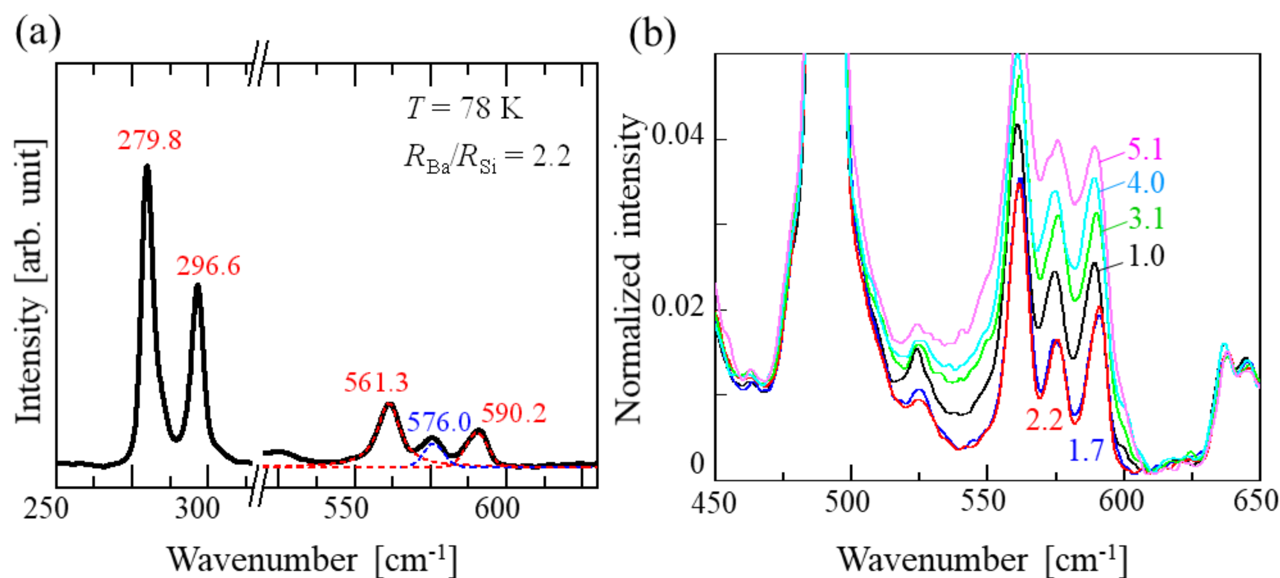

Fig. A.4-6 (a) Raman spectrum of sample with R_{Ba}/R_{Si} = 2.2 at 78 K. (b) Normalized Raman spectra of samples with different R_{Ba}/R_{Si} values at 78K.

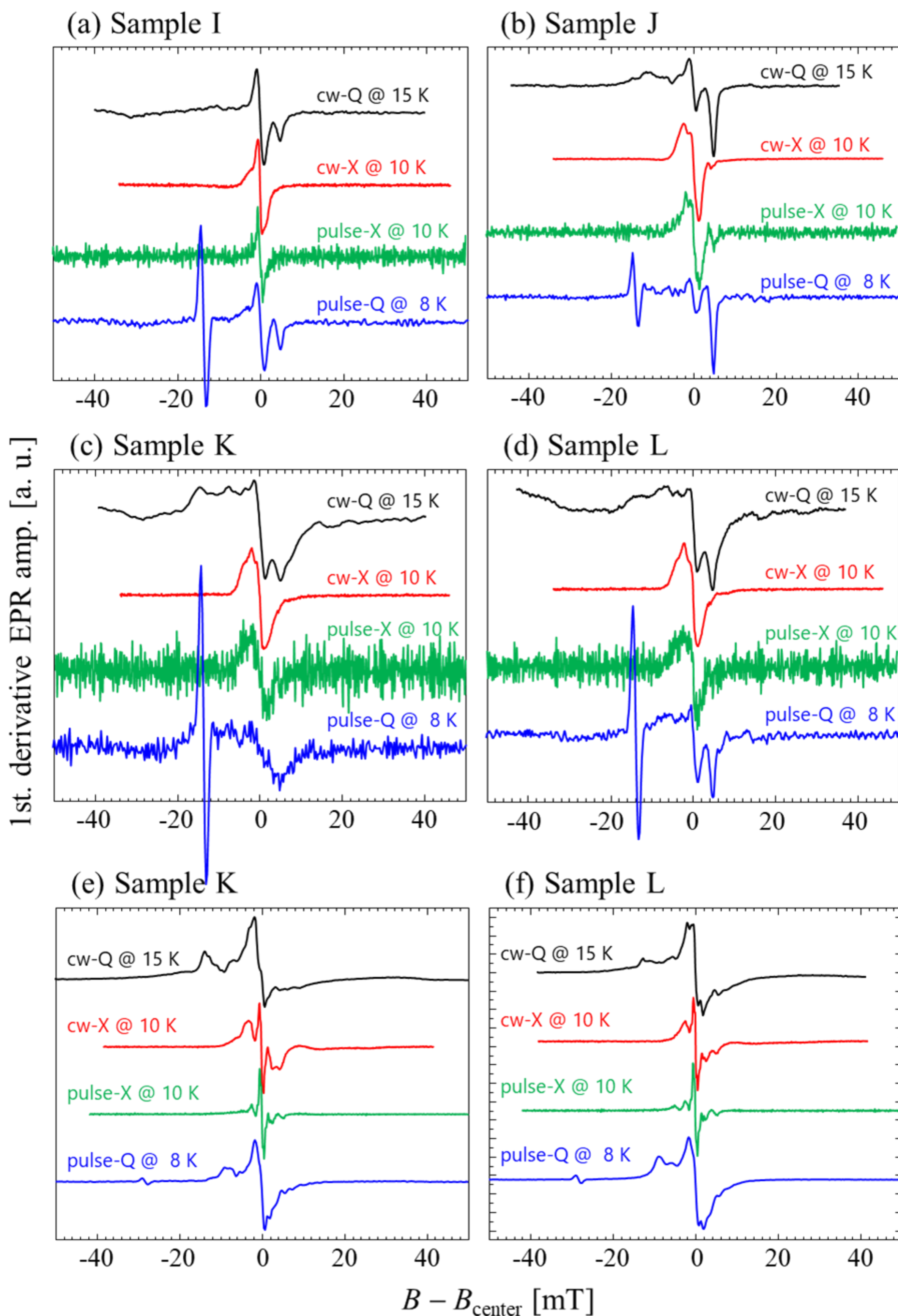

Fig. B-1 Comparison of EPR spectra of Sample I-J recorded by different EPR spectrometers.

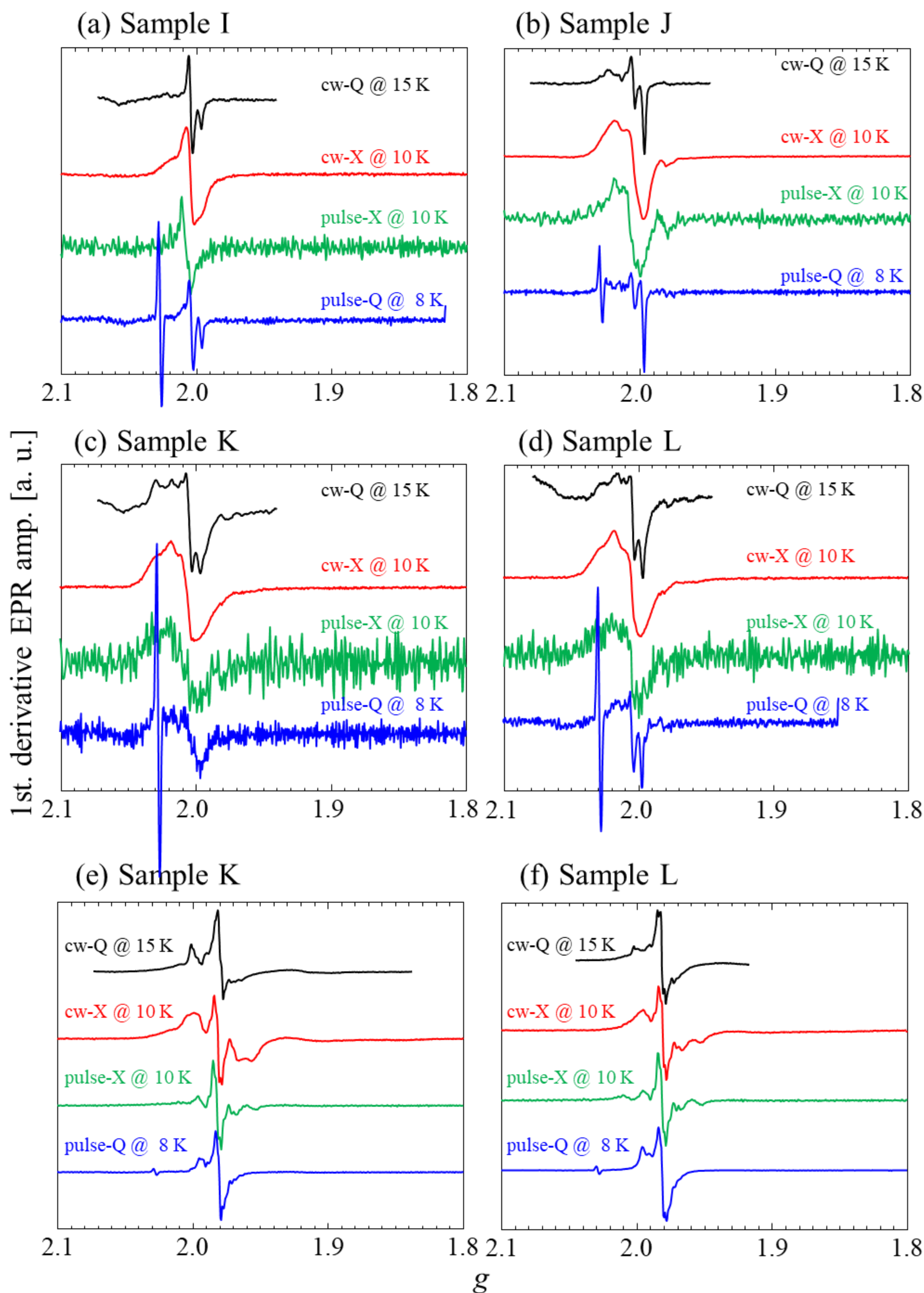

Fig. B-2 Comparison of EPR spectra of Sample I-J recorded by different EPR spectrometers.

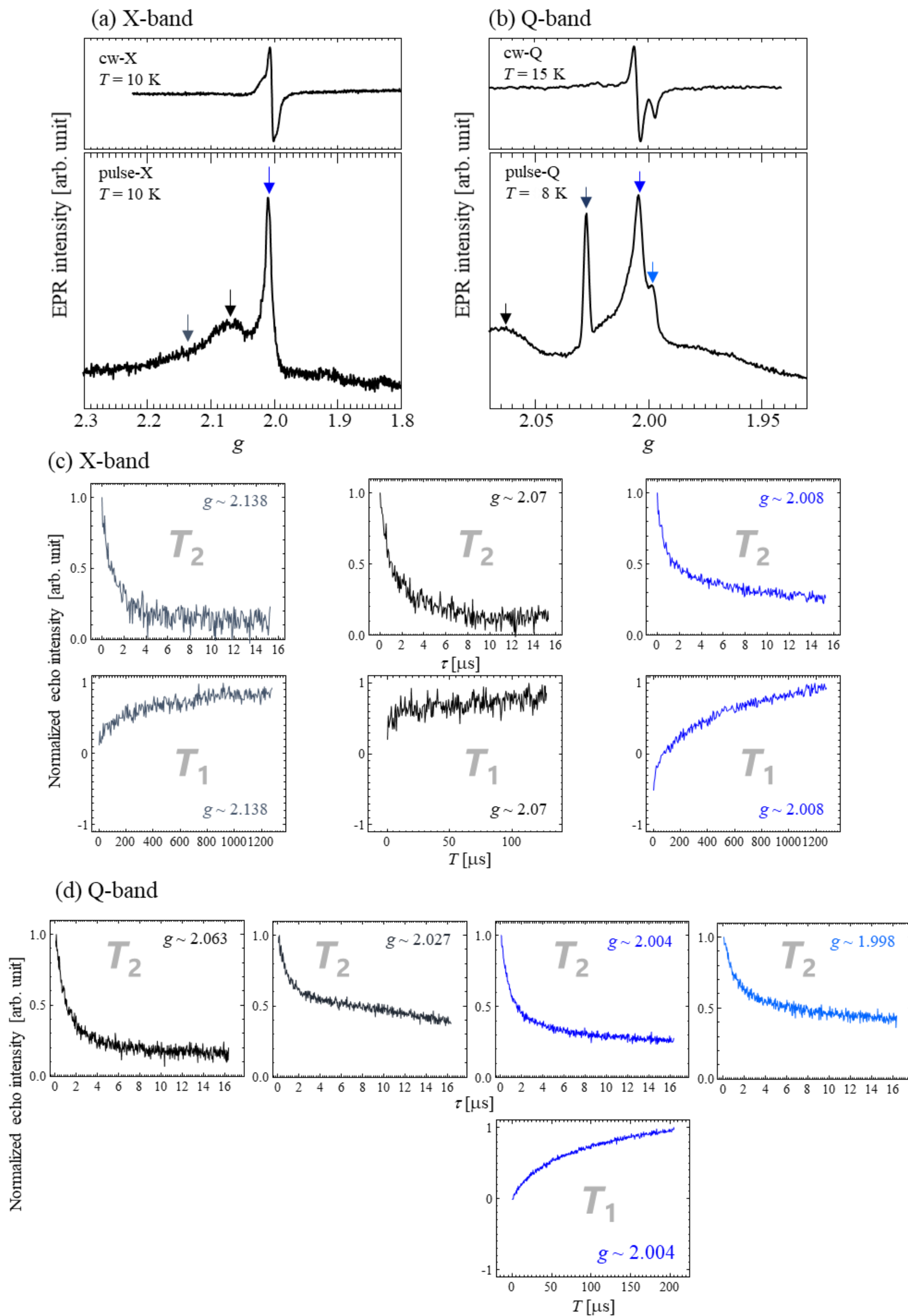

Fig. B-3 Experimental results of T_1 and T_2 in Sample I.

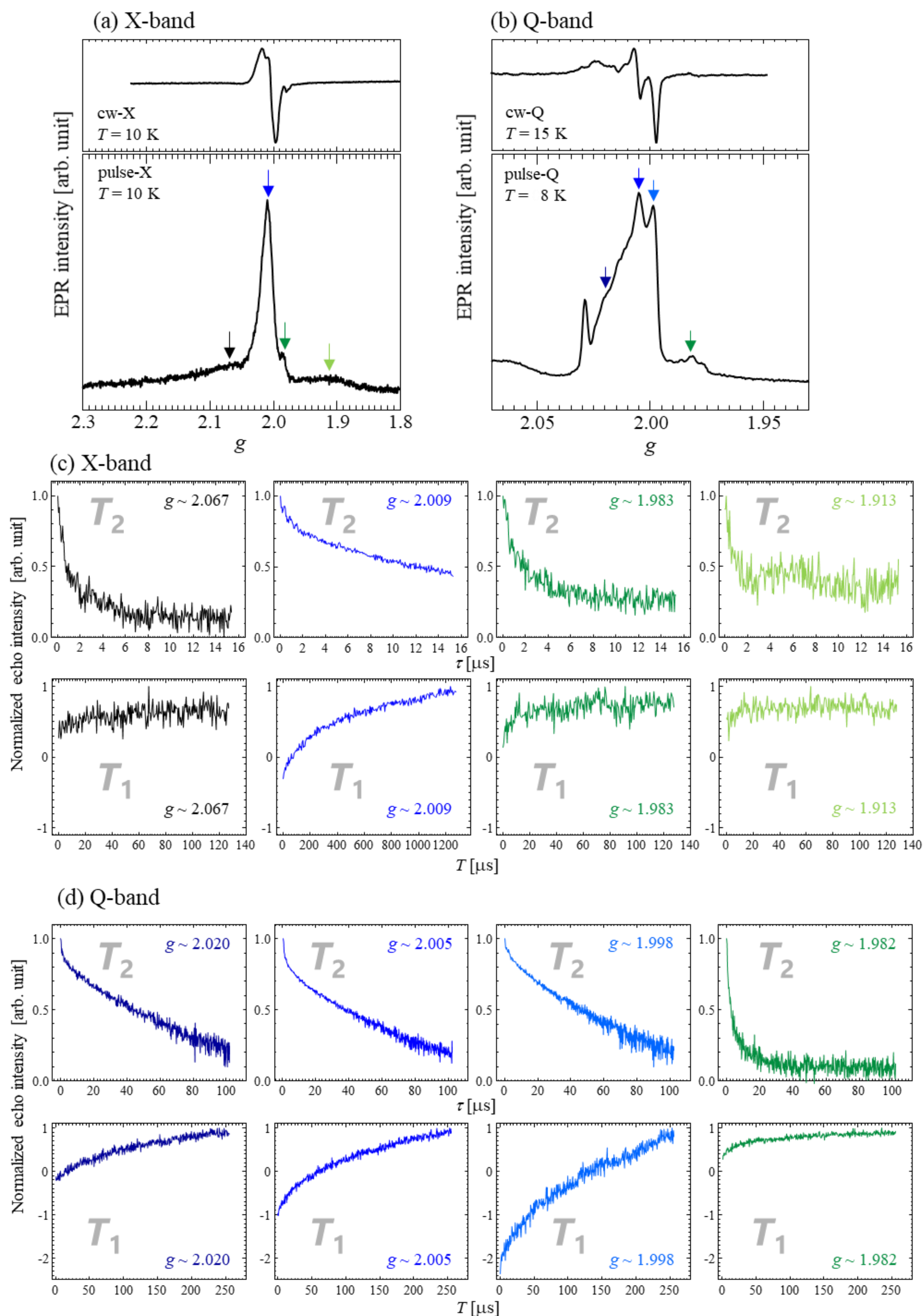

Fig. B-4 Experimental results of T_1 and T_2 in Sample J.

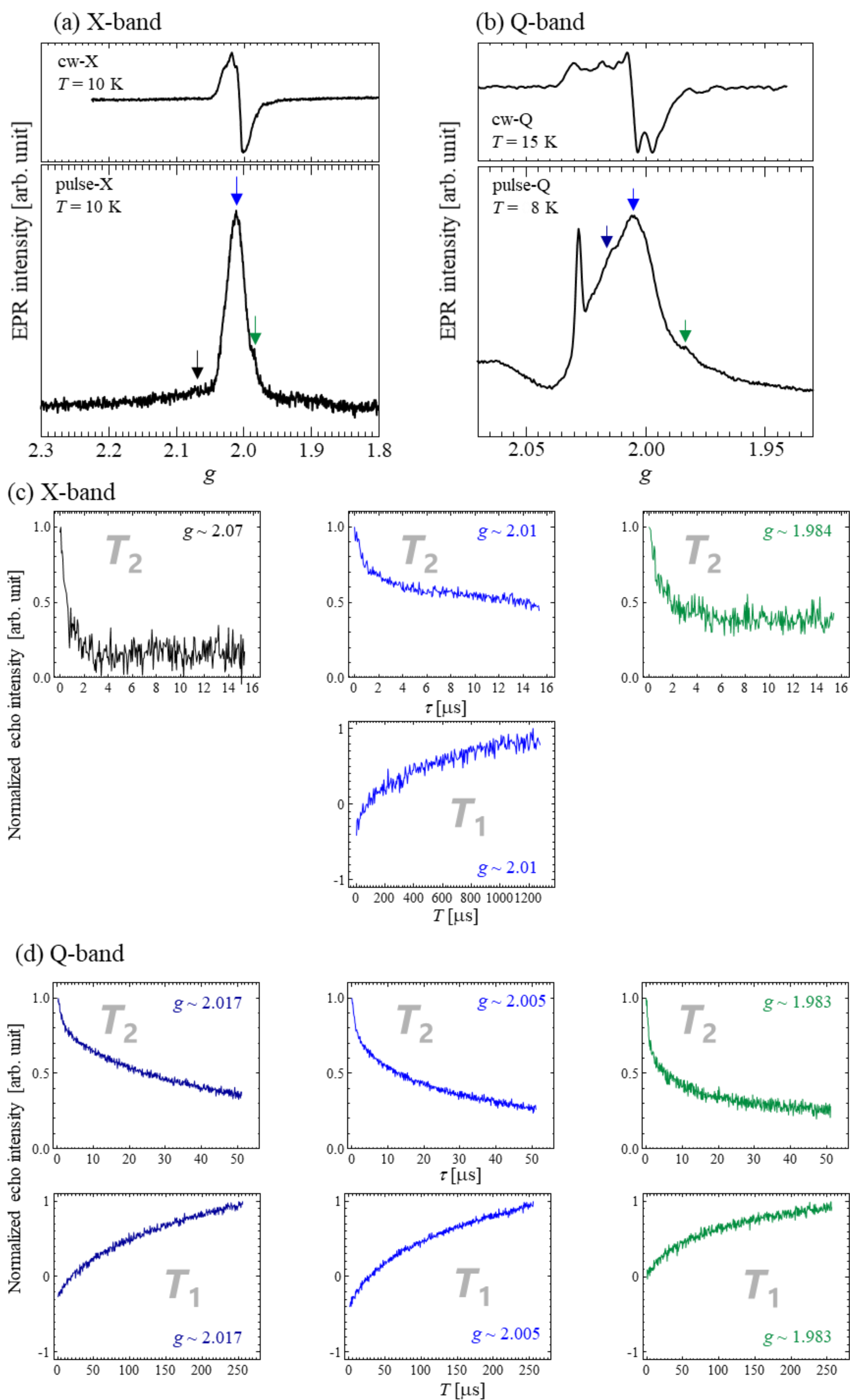

Fig. B-5 Experimental results of T_1 and T_2 in Sample K.

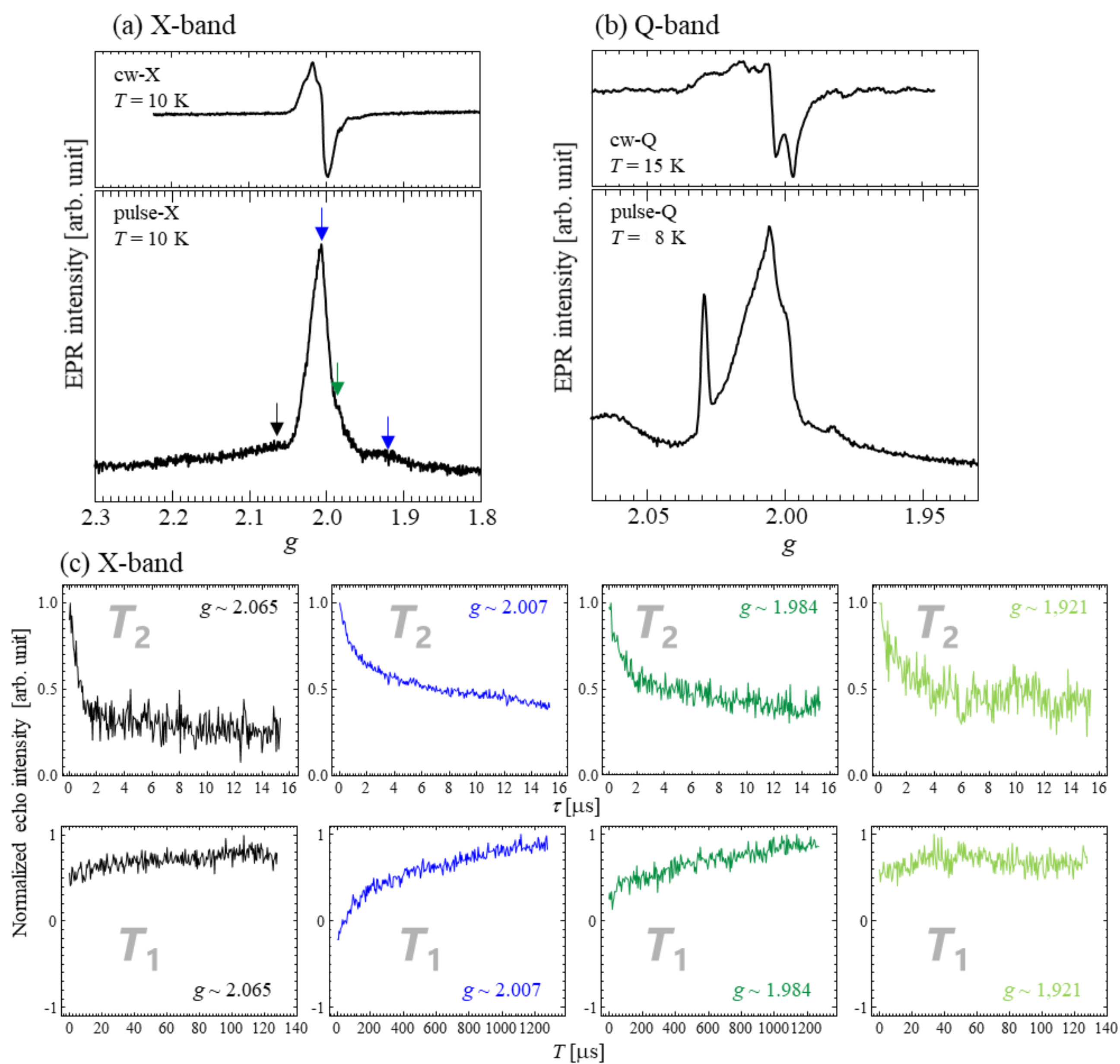

Fig. B-6 Experimental results of T_1 and T_2 in Sample L.

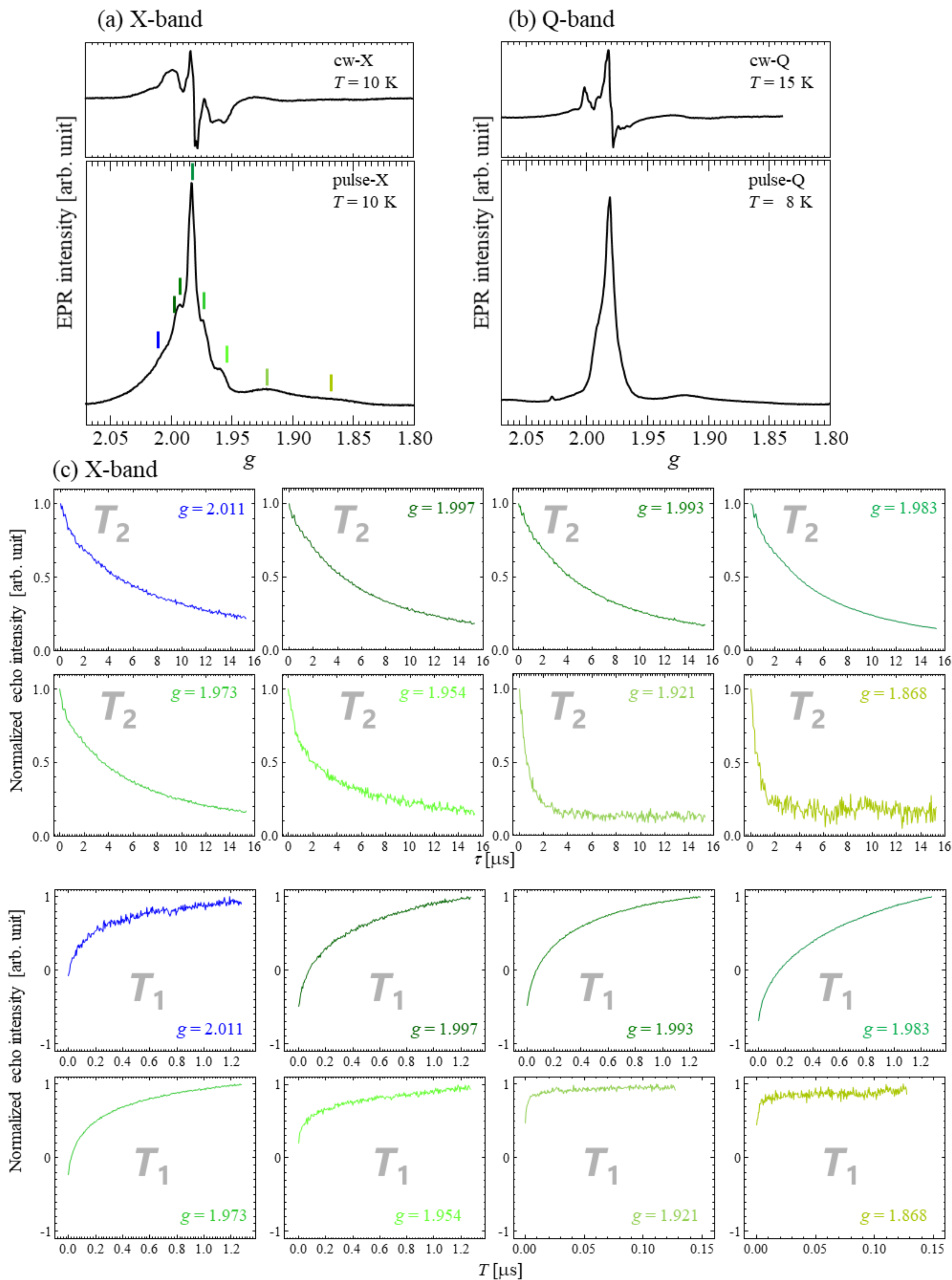

Fig. B-7 Experimental results of T_1 and T_2 in Sample M.

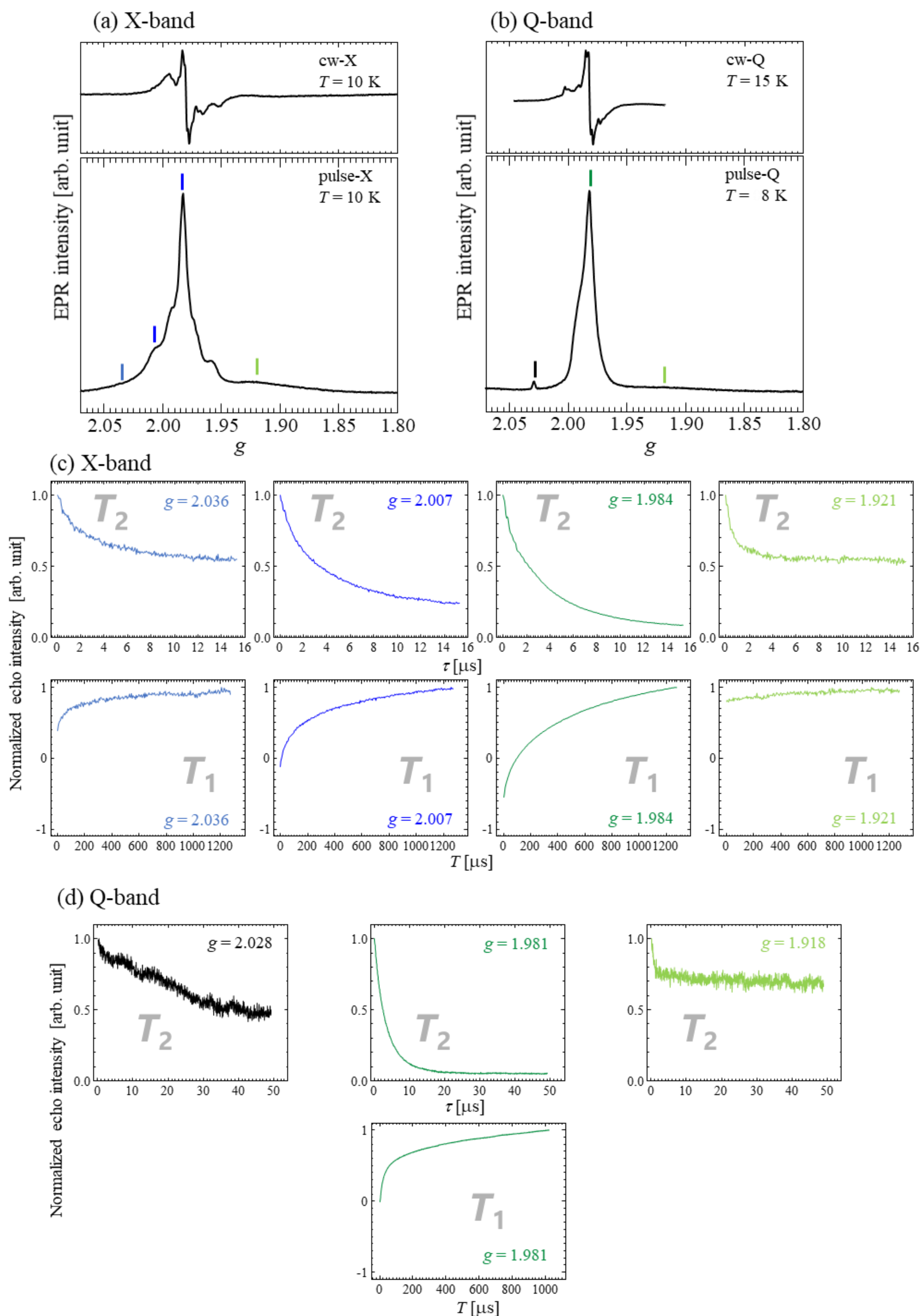

Fig. B-8 Experimental results of T_1 and T_2 in Sample N.

List of publications

Paper

1. Y. Yamashita, **T. Sato**, K. Toko, and T. Suemasu, "*Investigation of electrically active defects in undoped $BaSi_2$ light absorber layers using deep-level transient spectroscopy,*" Jpn. J. Appl. Phys. **57**, 75801(2018).
2. T. Deng, **T. Sato**, Z. Xu, R. Takabe, S. Yachi, Y. Yamashita, K. Toko, and T. Suemasu, "*p-$BaSi_2$/n-Si heterojunction solar cells on Si(001) with conversion efficiency approaching 10%: comparison with Si(111),*" Appl. Phys. Express **11**, 062301 (2018).
3. Z. Xu, K. Gotoh, T. Deng, **T. Sato**, R. Takabe, K. Toko, N. Usami, and T. Suemasu, "*Improving the photoresponse spectra of $BaSi_2$ layers by capping with hydrogenated amorphous Si layers prepared by radio-frequency hydrogen plasma,*" AIP Advances **8**, 055306 (2018).
4. R. Takabe, T. Deng, K. Kodama, Y. Yamashita, **T. Sato**, K. Toko, and T. Suemasu, "*Impact of Ba to Si deposition rate ratios during molecular beam epitaxy on carrier concentration and spectral response of $BaSi_2$ epitaxial film,*" J. Appl. Phys. **123**, 045703 (2018).
5. **T. Sato**, H. Hoshida, R. Takabe, K. Toko, Y. Terai and T. Suemasu, "*Detection of local vibrational modes of point defects in undoped $BaSi_2$ light absorber layers by Raman spectroscopy,*" J. Appl. Phys. **124**, 025301 (2018).
6. Y. Yamashita, **T. Sato**, K. Toko, A. Uedono, and T. Suemasu, "*Simple way of finding Ba to Si deposition rate ratios for high photoresponsivity in $BaSi_2$ films by Raman spectroscopy,*" Appl. Phys. Express **12**, 055506 (2019).
7. **T. Sato**, C. Lombard, Y. Yamashita, Z. Xu, L. Benincasa, K. Toko, S. Gambarelli, and T. Suemasu, "*Investigation of native defects in $BaSi_2$ epitaxial films by electron paramagnetic resonance,*" Appl. Phys. Express **12**, 061005 (2019).
8. L. Benincasa, H. Hoshida, T. Deng, **T. Sato**, Z. Xu, K. Toko, Y. Terai, and T. Suemasu, "Investigation of defect levels in $BaSi_2$ epitaxial films by photoluminescence and the effect of atomic hydrogen passivation," Journal of Physics Communications **3**, 075005 (2019).
9. **T. Sato**, Y. Yamashita, Z. Xu, K. Toko, S. Gambarelli, M. Imai, and T. Suemasu, "*Correlation of native defects between epitaxial films and polycrystalline $BaSi_2$ bulks based on photoluminescence spectra,*" Appl. Phys. Express **12**, 111001 (2019).
10. Y. Yamashita, **T. Sato**, N. Saitoh, N. Yoshizawa, K. Toko, and T. Suemasu, "*Three-step growth of highly photoresponsive $BaSi_2$ light absorbing layers with uniform Ba to Si atomic ratios,*" J. Appl. Phys. **126**, 215301 (2019).
11. T. Deng, Z. Xu, Y. Yamashita, **T. Sato**, K. Toko, and T. Suemasu, "*Modeling the effects of defect parameters on the performance of a p-$BaSi_2$/n-Si heterojunction solar cell,*" Solar Energy Materials and Solar Cells **205**, 110244 (2020).
12. T. Nemoto, S. Matsuno, **T. Sato**, K. Gotoh, M. Mesuda, H. Kuramochi, T. Toko, N. Usami, and T. Suemasu, "*Drastic enhancement of photoresponsivity in C-doped $BaSi_2$ films formed by radio-frequency sputtering,*" Japanese Journal of Applied Physics **59**, SFFA06 (2020).
13. Y. Yamashita, **T. Sato**, K. Toko, and T. Suemasu, "*Effects of molecular beam epitaxy growth conditions on grain size and lattice strain in $BaSi_2$ epitaxial films,*" To be published in Japanese Journal of Applied Physics.

14. L. Benincasa, Z. Xu, T. Deng, **T. Sato**, K. Toko, and T. Suemasu, "*Effects of boron and hydrogen doping on the enhancement of photoresponsivity and photoluminescence of $BaSi_2$ epitaxial films,*" To be published in Japanese Journal of Applied Physics.

International conferences

1. T. Deng, **T. Sato**, Z. Xu, R. Takabe, S. Yachi, Y. Yamashita, K. Toko and T. Suemasu, "*Investigation of p-$BaSi_2$/n-Si heterojunction solar cells on Si(001) and comparison to those on Si(111)*" 7th World Conference on Photovoltaic Energy Conversion, A7-572, Hawaii, USA, June 13 (2018).
2. Y. Yamashita, **T. Sato**, K. Toko, and T. Suemasu, "*Formation of low defect density $BaSi_2$ light absorbers for solar cell applications*" 60th Electric Materials Conference, O10, California, USA, June 27 (2018).
3. Y. Yamashita, **T. Sato**, K. Toko, T. Suemasu, "*Deep level transient spectroscopy characterization of undoped $BaSi_2$ light absorbers*," 2018 International Conference on Solid State Devices and Materials (SSDM 2018), E-4-04, Tokyo, Japan, Sept. 12, 2018.
4. T. Deng, Z. Xu, Y. Yamashita, K. Kodama, **T. Sato**, K. Toko and T. Suemasu, "*Investigation of $BaSi_2$ homojunction solar cells on a p+-$BaSi_2$/p+-Si tunnel junction towards $BaSi_2$/Si tandem solar cells,*" 2018 International Conference on Solid State Devices and Materials (SSDM 2018), F-5-03, Tokyo, Japan, Sept. 12, 2018.
5. Y. Yamashita, **T. Sato**, R. Takabe, T. Suemasu, "*Formation of lowest defect density $BaSi_2$ light absorbers for high efficiency homojunction solar cell applications,*" Tsukuba Global Science Week Interdisciplinary Workshop on Science and Patents 2018, IWP043, Tsukuba, Sept. 21, 2018.
6. T. Deng, **T. Sato**, Z. Xu, R. Takabe, S. Yachi, Y. Yamashita, K. Toko and T. Suemasu, "*Towards $BaSi_2$ homojunction solar cells on Si(001),*" 4th International Asian School Conference on Physics and Technology of Nanostructured Materials (ASCO-NANOMAT), III.24.01o, Vladivostok, Russia, Sept. 24, 2018.
7. Y. Yamashita, **T. Sato**, K. Toko, T. Suemasu, "*Characterization of Defect Levels in $BaSi_2$ by DLTS and Significant Improvement of Photoresponsivity by Increasing Growth Temperature*," MRS Spring Meeting and exhibit ES20.07.18, Phoenix, USA, April 24, 2019.
8. **T. Sato**, Y. Yamashita, Z. Xu, L. Benincasa, K. Toko, S. Gambarelli, T. Suemasu, "*Electron paramagnetic resonance spectra of $BaSi_2$ epitaxial films and bulk samples*," The 5th Asia-Pacific Conference on Semiconducting Silicides and Related Materials, Sun-a-O5, Miyazaki, Japan, July 21, 2019.
9. L. Benincasa, H. Hoshida, T. Deng, **T. Sato**, Z. Xu, K. Toko, Y. Terai, and T. Suemasu, "*Investigation of defect levels in undoped-$BaSi_2$ epitaxial films and the effect of atomic hydrogen passivation by photoluminescence measurement,*" The 5th Asia-Pacific Conference on Semiconducting Silicides and Related Materials, Sun-a-O8, Miyazaki, Japan, July 21, 2019.
10. Y. Yamashita, **T. Sato**, K. Toko, T. Suemasu, "*Molecular Beam Epitaxy of High-quality Undoped $BaSi_2$ Light Absorbers using Threestep Growth Method*," The 5th Asia-Pacific Conference on Semiconducting Silicides and Related Materials, Sun-a-O11, Miyazaki, Japan, July 21, 2019.
11. T. Suemasu, Z. Xu, **T. Sato**, J. Nakamura, A. Koda, K. Shimomura, "*Investigation of hydrogen states in semiconducting $BaSi_2$ by muon spin rotation,*" Materials Research Meeting 2019, E3-13-p02, Yokohama, Japan,

Dec. 13, 2019.

Domestic conferences

1. **<u>佐藤 拓磨</u>**, 髙部涼太, 小玉 小桃, 都甲 薫, 末益 崇 "DLTS 法による $BaSi_2$ エピタキシャル膜内の欠陥評価" 第 78 回応用物理学会秋季学術講演会 7p-PB4-9, 福岡, September 8 (2017).
2. **<u>佐藤 拓磨</u>**, 山下 雄大, 都甲 薫, 末益 崇 "$BaSi_2$ エピタキシャル膜ラマンスペクトルの膜厚および Ba/Si 体積レート比依存性" 第 65 回応用物理学会春季学術講演会 19a-F202-8, 東京, March 19 (2018).
3. T. Deng, **<u>T. Sato</u>**, Z. Xu, R. Takabe, S. Yachi, Y. Yamashita, K. Toko, and T. Suemasu "*Investigation on p-$BaSi_2$/n-Si heterojunction solar cells using a Si(001) substrate*" 第 65 回応用物理学会春季学術講演会 19a-F202-1, 東京, March 19 (2018).
4. 山下 雄大, **<u>佐藤 拓磨</u>**, 都甲 薫, 末益 崇, "DLTS 法を用いた undoped $BaSi_2$ 光吸収層の欠陥評価" 第 15 回「次世代の太陽光発電システム」シンポジウム PB-39, 札幌, July 12 (2018).
5. 山下 雄大, **<u>佐藤 拓磨</u>**, 都甲 薫、上殿 明良、末益 崇 "MBE 法により成長した $BaSi_2$ 光吸収層中の点欠陥評価" 第 79 回応用物理学会秋季学術講演会 19p-436-15, 名古屋, Sept. 19 (2018).
6. **<u>佐藤 拓磨</u>**, Gambarelli Serge, 山下 雄大, 末益 崇 "電子スピン共鳴による $BaSi_2$ 薄膜の欠陥評価" 第 79 回応用物理学会秋季学術講演会 19p-436-16, 名古屋, Sept. 19 (2018).
7. L. Benincasa, H. Hoshida, T. Deng, **<u>T. Sato</u>**, K. Toko, Y. Terai, T. Suemasu "*Investigation of defect levels in undoped-$BaSi_2$ epitaxial films by PL measurement*" 第 79 回応用物理学会秋季学術講演会 20a-PA4-2, 名古屋, Sept. 20 (2018).
8. L. Benincasa, H. Hoshida, T. Deng, **<u>T. Sato</u>**, K. Toko, Y. Terai and T. Suemasu "*Study of the origin of defect levels in undoped-$BaSi_2$ epitaxial films by PL measurement*" 第 66 回応用物理学会春季学術講演会 E 10a-PB2-10, 東京, March 10 (2019).
9. 山下 雄大, **<u>佐藤 拓磨</u>**, 倉持 豪人, 都甲 薫, 末益 崇 "三段階成長法による $BaSi_2$ 光吸収層の高品位エピタキシャル成長" 第 66 回応用物理学会春季学術講演会 11p-W834-7, 東京, March 11 (2019).
10. **<u>佐藤 拓磨</u>**, G. Serge, A. L. Barra, 末益 崇 "電子スピン共鳴によるバルクおよび薄膜 $BaSi_2$ 内の欠陥の調査" 第 66 回応用物理学会春季学術講演会 11p-W834-18, 東京, March 11 (2019).
11. Z.Xu, **<u>T. Sato</u>**, J. Nakamura, A. Koda, K. Shimomura, T, Suemasu "*Investigation of hydrogen states in semiconducting $BaSi_2$ by muon spin rotation*" 第 80 回応用物理学会秋季学術講演会 20P-E303-5, 札幌, Sept. 20 (2019).
12. 根本 泰良, **<u>佐藤拓磨</u>**, 召田 雅実, 倉持豪人, 都甲 薫, 末益 崇 "スパッタリング法による C-doped $BaSi_2$ の作製と特性評価" 第 80 回応用物理学会秋季学術講演会 20P-E303-1, 札幌, Sept. 20 (2019).
13. 伯 ゆりか, **<u>佐藤 拓磨</u>**, 山下 雄大, 都甲 薫, 末益 崇 "$BaSi_2$ におけるポストアニールが光学特性に及ぼす影響 " 第 80 回応用物理学会秋季学術講演会 21a-PA3-5, 札幌, Sept. 21 (2019).

Reference

[1] R. Perez and M. Perez, IEA SHC Solar Update (2009).

[2] D. M. Chapin, C. S. Fuller, and G. L. Pearson, J. Appl. Phys. **25**, 676 (1954).

[3] J. Del Alamo, J. Eguren, and A. Luque, Solid-state Electronics **24**, 415 (1981).

[4] A. Kaminskia, B. Vandellea, A. Favea, J.P. Boyeauxa, Le Quan Namb, R. Monnab, D. Sartib, and A. Laugiera, Sol. Energy Mater. Sol. Cells **72**, 373 (2002).

[5] A. G. Aberle, Prog. Photovolt: Res. Appl. **8**, 473 (2000).

[6] J. Schmidt, A. Merkle, R. Brendel, B. Hoex, M. C. M. van de Sanden and W. M. M. Kessels, Prog. Photovolt: Res. Appl. **16**, 461 (2008).

[7] O. Kluth, B. Rech, L. Houben, S. Wieder, G. Schöpe, C. Beneking, H. Wagner, A. Löffl, and H.W. Schock, Thin Solid Films **351**, 247 (1999).

[8] J. Müller, B. Rech, J. Springer, M. Vanecek, Solar Energy **77**, 917 (2004).

[9] H. Savin, P. Repo, G. von Gastrow, P. Ortega, E. Calle, M. Garín, and Ramon Alcubilla, NATURE NANOTECHNOLOGY **10**, 624 (2015).

[10] F. Granek, M. Hermle, D. M. Huljić, O. Schultz-Wittmann, and S. W. Glunz, Prog. Photovolt: Res. Appl.**17**, 47 (2009).

[11] K. Masuko, M. Shigematsu, T. Hashiguchi, D. Fujishima, M. Kai, N. Yoshimura, T. Yamaguchi, Y. Ichihashi, T. Mishima, N. Matsubara, T. Yamanishi, T. Takahama, M. Taguchi, E. Maruyama, and S. Okamoto, IEEE J. Photovoltaics **4**, 1433 (2014).

[12] K. Yoshikawa, H. Kawasaki, W. Yoshida, T. Irie, K. Konishi, K. Nakano, T. Uto, D. Adachi, M. Kanematsu, H. Uzu, and K. Yamamoto, Nature Energy **2**, 17302 (2017).

[13] Renewables 2018 Global Status Report, REN21 (2018).

[14] S. Philipps, Photovoltaics Report, Fraunhofer ISE (2018).

[15] M. A. M. Al-Alwani, A. B. Mohamad, N. A. Ludin, A. A. H. Kadhum, and K. Sopian, Renew. Sust. Energy Rev. **65**, 183 (2016).

[16] P. K. Nayak, G. Garcia-Belmonte, A. Kahn, J. Bisquert, and D. Cahen, Energy Environ. Sci. **5**, 6022 (2012).

[17] W. Shockley and H. J. Queisser, J. Appl. Phys. **32**, 510 (1961).

[18] K. Chakrabarty and S. N. Singh, Solid-St. Electron. **39**, 577 (1996).

[19] Priyanka, M. Lal, S.N. Singh, Sol. Ener. Mater. Sol. Cells **91**, 137 (2007).

[20] P. Singh, S.N. Singh, M. Lal, and M. Husain, Sol. Ener. Mater. Sol. Cells **92**, 1611 (2008).

[21] W. Shockley and W. T. Read Jr., Phys. Rev. **87**, 835 (1952).

[22] T. Goebel, Y. Prots, and Frank Haarmann, Z. Kristallogr. NCS **224**, 7 (2009).

[23] S. M. Kauzlarich, *Chemistry, Structure and Bonding of Zintle Phase and Ions*, First ed. Wiley-VCH, New York, 1996.

[24] W. B. Jensen, J. Chem. Educ. **61**, 191 (1984).

[25] R. O. Jones and D.Hohl, J Chem. Phys. **92**, 6710 (1990).

[26] M. Imai, M. Kumar, N. Umezawa, Scripta Materialia **172**, 43 (2019).

[27] M. Pani and A. Palenzona, J. Alloys Compounds **454** L1 (2008).

[28] G. Bruzzone and E. Franceschi, J. Less-Common Metals, **57**, 201 (1978).

[29] W. Rieger and E. Parthé, Acta. Cryst. **22**, 919 (1967).

[30] E. A. Leon-Escamilla and J. D. Corbett, J. Solid State Chem. **159**, 149 (2001).

[31] U. Aydemir, A. Ormeci, H. Borrmann, B. Böhme, F. Zürcher, B. Uslu, T. Goebel, W. Schnelle, P. Simon, W. Carrillo-Cabrera, F. Haarmann, M. Baritinger, R. Nesper, H. G. Schnering, and Y. Grin, Z. Anorg. Allg. Chem., **634**, 1651 (2008).

[32] S. Yamanaka, E. Enishi, H. Fukuoka, and M. Yasukawa, Inorg. Chem. **159**, 149 (2001).

[33] D. B. Migas, V. L. Shaposhnikov, and V. E. Borisenko, Phys. Status Solidi (b) **244**, 2611 (2007).

[34] M. Kumar, N. Umezawa, and M. Imai, Appl. Phys. Express **7**, 071203 (2014).

[35] K. Toh, T. Saito, and T. Suemasu, Jpn. J. Appl. Phys. **50**, 068001 (2011).

[36] K. Morita, M. Kobayashi, and T. Suemasu, Thin Solid Films **515**, 8216 (2007).

[37] Y. Imai and A. Watanabe, Intermetallics **18**, 1432 (2010).

[38] T. Nemoto, S. Matsuno, T. Sato, K. Gothoh, M. Mesuda, H. Kuramochi, K. Toko, N. Usami, and T. Suemasu, Jpn. J. Appl. Phys. **59**, SFFA06 (2020).

[39] T. Gokmen, O. Gunawan, and D. B. Mitzi, J. Appl. Phys. 114, 114511 (2013).

[40] A.A. Al-Ghamdi, S. A. Khan, A. Nagat, M. S. Abd El-Sadek, Optics & Laser Technology **42**, 1181 (2010).

[41] A. Polman, M. Knight, E. C. Garnett, B. Ehrler, and W. C. Sinke, Science **352**, 6283 (2016).

[42] L. Yu, R. S. Kokenyesi, D. A. Keszler, and A. Zunger, Adv. Energy Mater. **3**, 43 (2013).

[43] W.-J. Yin, T. Shi, and Y. Yan, Adv. Mater. **26**, 4653 (2014).

[44] M. Baba, K. Toh, K. Toko, N. Saito, N. Yoshizawa, K. Jiptner, T. Sekiguchi, K. O. Hara, N. Usami, and T. Suemasu, J. Cryst. Growth **348**, 75 (2012).

[45] M. Baba, K. Watanabe, K. O. Hara, K. Toko, T. Sekiguchi, N. Usami, and T. Suemasu, Jpn. J. Appl. Phys. **53**, 078004 (2014).

[46] K. O. Hara, N. Usami, K. Toh, M. Baba, K. Toko, and T. Suemasu, J. Appl. Phys. **112**, 083108 (2012).

[47] K. O. Hara, N. Usami, K. Nakamura, R. Takabe, M. Baba, K. Toko, and T. Suemasu, Appl. Phys. Express **6**, 112302 (2013).

[48] T. Suemasu and N. Usami, J. Phys. D: Appl. Phys. **50**, 023001 (2017).

[49] Y. Imai and A. Watanabe, Intermetallics **15**, 1291 (2007).

[50] S. Aonuki, Y. Yamashita, K. Toko, and T. Suemasu, Jpn. J. Appl. Phys. **59**, SFFA01 (2020).

[51] R. Takabe, T. Deng, K. Kodama, Y. Yamashita, T. Sato, K. Toko, and T. Suemasu, J. Appl. Phys. **123**, 045703 (2018).

[52] M. Ajmal Khan, K. O. Hara, W. Du, M. Baba, K. Nakamura, M. Suzuno, K. Toko, N. Usami, and T. Suemasu, Appl. Phys. Lett. **102**, 112107 (2013).

[53] M. Takeishi, Y. Matsumoto, R. Sasaki, T. Saito, and T. Suemasu, Phys. Procedia **11**, 27 (2011).

[54] M. Kobayashi, K. Morita, and T. Suemasu, Thin Solid Films **515**, 8242 (2007) 8242.

[55] Z. Xu, T. Deng, R. Takabe, K. Toko, and T. Suemasu, J. Cryst. Growth **471**, 37 (2017) 37.

[56] R. Takabe, M. Baba, K. Nakamura, W. Du, M. A. Khan, S. Koike, K. Toko, K. O. Hara, N. Usami, and T.

Suemasu, Phys. Status Solidi (c) **10**, 1753 (2013).
[57] K. O. Hara, Y. Hoshi, N. Usami, Y. Shiraki, K. Nakamura, K. Toko, and T. Suemasu, Thin Solid Films **557**, 90 (2014).
[58] M. Kobayashi, Y. Matsumoto, Y. Ichikawa, D. Tsukada, and T. Suemasu, Appl. Phys. Express **1**, 051403 (2008).
[59] R. A. McKee, F. J. Walker, J. R. Conner, and R. Raj, Appl. Phys. Lett. **63**, 2818 (1993).
[60] Y. Inomata, T. Nakamura, T. Suemasu, and F. Hasegawa, Jpn. J. Appl. Phys. **43**, 4155 (2004).
[61] Y. Inomata, T. Nakamura, T. Suemasu, and F. Hasegawa, Jpn. J. Appl. Phys. **43**, L478 (2004).
[62] K. Toh, K. O. Hara, N. Usami, N. Saito, N. Yoshizawa, K. Toko, and T. Suemasu, J. Cryst. Growth **345**, 16 (2012).
[63] M. Baba, K. Toh, K. Toko, K. O. Hara, N. Usami, N. Saito, N. Yoshizawa, and T. Suemasu, J. Cryst. Growth **378**, 193 (2013).
[64] S. Matsuno, R. Takabe, S. Yokoyama, K. Toko, M. Mesuda, H. Kuramochi, and T. Suemasu, Appl. Phys. Express **11**, 071401 (2018).
[65] S. Matsuno, T. Nemoto, M. Mesuda, H. Kuramochi, K. Toko, and T. Suemasu, Appl. Phys. Express **12**, 021004 (2019).
[66] K. Yamaya, Y. Yamaki, H. Nakanishi, and S. Chichibu, Appl. Phys. Lett. **72**, 235 (1998).
[67] C. Thi Trinh, Y. Nakagawa, K. O. Hara, R. Takabe, T. Suemasu, and N. Usami, Mater. Res. Express **3**, 076204 (2016).
[68] K. O. Hara, Y. Nakagawa, T. Suemasu, and N. Usami, Jpn. J. Appl. Phys. **54**, 07JE02 (2015).
[69] K. O. Hara, C. T. Trinh, K. Arimoto, J. Yamanaka, K. Nakagawa, Y. Kurokawa, T. Suemasu, and N. Usami, J. Appl. Phys. **120**, 045103 (2016).
[70] K. O. Hara, K. Arimoto, J. Yamanaka, and K. Nakagawa, J. Mater. Res. **33**, 2297 (2018).
[71] K. O. Hara, K. Arimoto, J. Yamanaka, and K. Nakagawa, Jpn. J. Appl. Phys. **59**, SFFA02 (2020).
[72] T. Suemasu, Jpn. J. Appl. Phys. **54**, 07JA01 (2015).
[73] T. Suemasu, K. Morita, M. Kobayashi, M. Saida, and M. Sasaki, Jpn. J. Appl. Phys. **45**, L519 (2006).
[74] D. Tsukahara, S. Yachi, H. Takeuchi, R. Takabe, W. Du, M. Baba, Y. Li, K. Toko, N. Usami, and T. Suemasu, Appl. Phys. Lett. **108**, 152101 (2016).
[75] S. Yachi, R. Takabe, H. Takeuchi, K. Toko, and T. Suemasu, Appl. Phys. Lett. **109**, 072103 (2016).
[76] S. Yachi, R. Takabe, K. Toko, and T. Suemasu, Jpn. J. Appl. Phys. **56**, 05DB03 (2017).
[77] T. Deng, T. Sato, Z. Xu, R. Takabe, S. Yachi, Y. Yamashita, K. Toko, and T. Suemasu, Appl. Phys. Express **11**, 062301 (2018).
[78] S. Michael, A.D. Bates, M.S. Green, Silvaco ATLAS as a solar cell modeling tool, in: 2005 31st IEEE Photovoltaic Specialists Conference, 2005, pp. 719–721.
[79] T. Deng, Z. Xu, Y. Yamashita, T. Sato, K. Toko, and T. Suemasu, Sol. Energ. Mater. Sol. Cells **205**, 110244 (2020).
[80] K. Kodama, R. Takabe, T. Deng, K. Toko, and T. Suemasu, Jpn. J. Appl. Phys. **57**, 050310 (2018).
[81] T. Saito, Y. Matsumoto, R. Sasaki, M. Takeishi, and T. Suemasu, Jpn. J. Appl. Phys. **49**, 068001 (2010).
[82] T. Saito, Y. Matsumoto, M. Suzuno, M. Takeishi, R. Sasaki, T. Suemasu, and N. Usami, Appl. Phys. Express **3**,

021301 (2010).
[83] T. Suemasu, T. Saito, K. Toh, A. Okada, and M. A. Khan, Thin Solid Films **519**, 8501 (2011).
[84] Y. Yamashita, S. Yachi, R. Takabe, T. Sato, M. E. Bayu, K. Toko, and T. Suemasu, Jpn. J. Appl. Phys. **57**, 025501 (2018).
[85] K. Kodama, Y. Yamashita, K. Toko, and T. Suemasu, Appl. Phys. Express **12**, 041005 (2019).
[86] T. Deng, Tsukuba, University of Tsukuba, 2019, Ph. D. thesis.
[87] J. Evers and A. Weiss, Mat. Res. Bull. **9**, 549 (1974).
[88] M. Imai and T. Hirano, J. Alloys Compd. **224**, 111 (1995).
[89] T. Nakamura, T. Suemasu, K. Takakura, F. Hasegawa, A. Wakahara, and M. Imai, Appl. Phys. Lett. **81**, 1032 (2002).
[90] S. Kishino, T. Imai, T. Iida, Y. Nakaishi, M. Shinada, Y. Takanashi, and N. Hamada, J. Alloys Compd. **428**, 22 (2007).
[91] T. Suemasu, K. Morita, and M. Kobayashi, J. Cryst. Growth **301-302**, 680 (2007).
[92] H. Takeuchi, W. Du, M. Baba, R. Takabe, K. Toko, and T. Suemasu, Jpn. J. Appl. Phys. **54**, 07JE01 (2015).
[93] S. Yachi, R. Takabe, T. Deng, K. Toko, and T. Suemasu, Jpn. J. Appl. Phys. **57**, 042301 (2018).
[94] Y. Yamashita, T. Sato, M. E. Bayu, K. Toko, and T. Suemasu, Jpn. J. Appl. Phys. **57**, 075801 (2018).
[95] Y. Yamashita, T. Sato, N. Saitoh, N. Yoshizawa, K. Toko, and T. Suemasu, J. Appl. Phys. **126**, 215301 (2019).
[96] T. Sato, H. Hoshida, R. Takabe, K. Toko, Y. Terai, and T. Suemasu, J. Appl. Phys. **124**, 025301 (2018).
[97] Y. Yamashita, Y. Takahara, T. Sato, K. Toko, A. Uedono, and T. Suemasu, Appl. Phys. Express **12**, 055506 (2019).
[98] R. Krause-Rehberg and H. S. Leipner, *Positron Annihilation in Semiconductors, Solid-State Sciences* (Springer, Berlin, 1999) Vol. 127.
[99] O. Isabella, Recent advancements in the development and characterization of $BaSi_2$ for photovoltaic applications, The 5th Asia-Pacific Conference on Semiconducting Silicides and Related Mterials, 21st of July, Miyazaki, Japan, 2019.
[100] H. Hoshida, T. Suemasu, and Y. Terai, Ba/Si flux ratio dependence of photoreflecrance spectra in $BaSi_2$ epitaxial films, The 79th JSAP Autumn Meeting, 20a-PA4-3, 20th of September, Nagoya, Japan, 2019.
[101] R. Takabe, K. Nakamura, M. Baba, W. Du, M. A. Khan, K. Toko, M. Sasase, K. O. Hara, N. Usami, and T. Suemasu, Jpn. J. Appl. Phys. **53**, 04ER04 (2014).
[102] K. Toh, K. O. Hara, N. Usami, N. Saito, N. Yoshizawa, K. Toko, and T. Suemasu, Jpn. J. Appl. Phys. **51**, 095501 (2012).
[103] M. Baba, S. Tsurekawa, K. Watanabe, W. Du,1 K. Toko, K. O. Hara, N. Usami, T. Sekiguchi, and T. Suemasu, Appl. Phys. Lett. **103**, 142113 (2013).
[104] R. Takabe, K. O. Hara, M. Baba, W. Du, N. Shimada, K. Toko, N. Usami, and T. Suemasu, J. Appl. Phys. **115**, 193510 (2014).
[105] M. Baba, K. Nakamura, W. Du, M. A. Khan, S. Koike, K. Toko, N. Usami, N. Saito, N. Yoshizawa, and T. Suemasu, Jpn. J. Appl. Phys. **51**, 098003 (2012).
[106] M. Kumar, N. Umezawa, W. Zhou, and M. Imai, J. Mater. Chem. A **5**, 25293 (2017).

[107] D.Tsukahara, M. Baba, S. Honda, Y. Imai, K. O. Hara, N. Usami, K. Toko, J. H. Werner, and T. Suemasu, J. Appl. Phys. **116**, 123709 (2014).

[108] J. Evers, J. Less-Commom Metals **58**, 75 (1978).

[109] M. Imada, A. Fujimori, and Y. Tokura, Rev. Mod. Phys. **70**, 1039 (1998).

[110] T. Goebel, A. Ormmeci, O. Pecher, and F. Haarmann, Z. Anorg. Allg. Chem. **638**, 1437 (2012).

[111] S. Scharge, F. Kraus, S. Stegmaier, A. Schier, and T. F. Fassler. Angew. Chem. Int. Ed. **50**, 3630 (2011).

[112] EasySpin, Nuclear isotope database, http://easyspin.org/easyspin/documentation/isotopetable.html.

[113] M. Neumeier, F. Fendt, S. Gärtner, C. Kosh, T. Gärtner, N. Korber, and R. M. Gschwind, Angew. Chem. Int. Ed. **52**, 4483 (2013).

[114] L. M. Scherf, O. Pecher, K. J. Griffith, F. Haarmann, C. P. Grey, and T. F. Fassler, Eur. J. Inorg. Chem. 4674 (2016).

[115] B. M. Nolan, T. Henneberger, M. Waibel, T. F. Fässler, and S. M. Kauzlarich, Inorg. Chem. **54**, 396 (2015).

[116] T. F. Fässler, M. Hunziker, M. E. Spahr, H. Lueken, and H. Schilder, Z. Anorg. Allg. Chem. **626**, 692 (2000).

[117] J. M. Goicoechea and S. C. Sevov, J. Am. Chem. Soc. **126**, 6860 (2004).

[118] M. Waibel and T. F. Fässler, Inorg. Chem. **52**, 5861 (2013).

[119] Y. Inomata, T. Nakamura, T. Suemasu, and F. Hasegawa, Jpn. J. Appl. Phys. **43**, 4155 (2004).

[120] R. Takabe, S. Yachi, W. Du, D. Tsukahara, H. Takeuchi, K. Toko, and T. Suemasu, AIP Advances. **6**, 085107 (2016).

[121] R. Takabe, H. Takeuchi, W. Du, K. Ito, K. Yoko, S. Ueda, A. Kimura, and T. Suemasu, J. Appl. Phys. **119**, 165304 (2016).

[122] J. B. Nelson and D. P. Riley, Proc. Phys. Soc. **57**, 160 (1945).

[123] Y. Terai, H. Yamaguchi, H. Tsukamoto, N. Murakoso, M. Iinuma, and T. Suemasu, Jpn J. Appl. Phys. **56**, 05DD02 (2017).

[124] M. Somer, Z. Anorg. Allg. Chem. **626**, 2478 (2000).

[125] H. Peng, C. L. Wang, J. C. Li, R. Z. Zhang, M. X. Wang, Y. Sun, and M. Sheng, Phys. Lett. A **374**, 3797 (2010).

[126] K. O. Hara, N. Usami, Y. Hoshi, Y. Shiraki, M. Suzuno, K. Toko, and T. Suemasu, Jpn. J. Appl. Phys. **50**, 121202 (2011).

[127] H. Hoshida, T. Suemasu, and Y. Terai, Defect Diffusion Forum **386**, 43 (2018).

[128] Y. Nishi, Jpn. J. Appl. Phys. **10**, 52 (1971).

[129] P. J. Caplan, J. N. Helbert, B E. Wagner, and E. H. Poindexter, Surf. Sci. **54**, 33 (1976).

[130] K. L. Brower, Appl. Phys. Lett. **43**, 1111 (1983).

[131] A. Stersmans, J. Braet, J. Witters, and R. F. Dekeersmaecker, Surf. Sci. **141**, 255 (1984).

[132] A. Stesmans and V. V. Afanas'ev, J. Appl. Phys. **83**, 2449 (1998).

[133] L. Skuja, J. Non-Crystalline Solids, **239**, 16 (1998).

[134] P. M. Lenahan and J. F. Conley Jr., J. Vac. Sci. Technol. B **16**, 2134 (1998).

[135] T. Umeda, M. Nishizawa, T. Yasuda, J. Isoya, S. Yamasaki, and K. Tanaka, Phys. Rev. Lett. **86**, 1054 (2001).

[136] B. P. Lemke and D. Haneman, Phys. Rev. B **17**, 1893 (1978).

[137] H. J. von Bardeleben, J. L. Cantin, H. Vrielinck, F. Callens, L. Binet, E. Rauls, and U. Gerstmann, Phys. Rev. B **90**, 085203 (2014).

[138] H. Kaftelen, K. Ocakoglu, R. Thomann, S. Tu, S. Weber, and E. Ergem, Phys. Rev. B **86**, 014113 (2012).

[139] P. Burner, A. D. Sontakke, M. Salaün, M. Bardet, J.-M. Mouesca, S. Gambarelli, A.-L. Barra, A. Ferrier, B. Viana, A. Ibanez, V. Maurel, and I. Gutier-Luneau, Angew. Chem. Int. Ed. **56**, 13995 (2017).

[140] G. Charron, E. Malkin, G. Rogez, L. J. Batchelor, S. Mazerat, R. Guillot, N. Guihéry, A.-L. Barra, T. Mallah, and H. Bolvin, Chem. Eur. J. **22**, 16850 (2016).

[141] A.-L. Barra, L. C. Brunel, and J. B. Robert, Chem. Phys. Lett. **165**, 107 (1990).

[142] Z. Xu, K. Gotoh, T. Deng, T. Sato, R. Takabe, K. Toko, N. Usami, and T. Suemasu, AIP Advances **8**, 055306 (2018).

[143] Z. Xu, D. A. Shohonov, A. B. Filonov, K. Gotoh, T. Deng, S. Honda, K. Yoko, N. Usami, D. B. Migas, V. E. Borisenko, and T. Suemasu, Phys. Rev. Materials 3, 065403 (2019).

[144] J. I. Pankove and N. M. Johnson, *Hydrogen in Semiconductor,* Academic, New York, 1991.

[145] A. Stesmans, Phys. Rev. B **61**, 8393 (2000).

[146] K. Murakami, R. Shirakawa, M. Tsujimura, N. Uchida, N. Fukata, and S. Hishita, J. Appl. Phys. **105**, 054307 (2009).

[147] A. Stesmans, J. Braet, J. Witters, R. F. Dekeersmaecker, Surf. Sci. **141**, 255 (1984).

[148] K. Lips, P. Kanschat, and W. Fuhs, Sol. Energy & Sol. Cells **78**, 513 (2003).

[149] J. P. Campbell, P. M. Lenahan, C. J. Cochrane, A. T. Krishnan, S. Krishnan, IEEE Trans. Device and Materials Reliab. **7**, 540 (2007).

[150] T. Umeda, K. Okonogi, K. Ohyu, S. Tsukada, K. Hamada, S. Fujieda, Y. Mochizuki, Appl. Phys. Lett. **88**, 253504 (2006)

[151] A. Schnegg, J. Behrends, M. Fehr, and K. Lips, Chem. Phys. Phys. Chem. **14**, 14418 (2012).

[152] C. Meier, J. Behrends, C. Teutloff, O. Astakhov, A. Schnegg, K. Lips, and R. Bittl, J. Mag. Res. **234**, 1 (2013).

[153] T. Maly, F. MacMillan, K. Zwicker, N. Kashani-Poor, U. Brandt, and T. Prisner, Biochem **43**, 3969 (2004).

[154] R. Dastvan, B. Bode, M. P. R. Karuppiah, A. Marko, S. Lyubenova, H. Schwalbe, and T. Prisner, J. Phys. Chem. B **114**, 13507 (2010).

[155] D. Goldfarb and S. Stoll, *EPR Spectroscopy: Funcamentals and methods*, John Wiley & Sons, Inc., New York, 2018.

[156] D. S. Marlin, E. Bill, T. Weyhermuller, E. Bothe, and K. Wieghardt, J. Am Chem. Soc. **127**, 6095 (2005).

[157] H. Quast, W. Nüdling, G. Klemm, A. Kirschfeld,.P. Neuhaus, W. Sander, D. A. Hrovat, and W. T. Borden, J. Org. Chem. **73**, 4956 (2008).

[158] N. Mizuochi, S. Yamasaki, H. Takizawa, N. Morishita, T. Oshima, H. Itoh, and J. Isoya, Phys Rev. B **66**, 235202 (2002).

[159] S. Beraina, S. Gambarelli, T. Mitra, B. Tsukerblat, A. Müller, and B. Barbara, Nature **453**, 203 (2008).

[160] J. A. Fee, D. Sanders, C. E. Slutter, P. E. Doan, R. Aasa, M. Karpefors, and T. Vanngard, Biochem. Biophys. Res. Commun. **212**, 77 (1995).

[161] L. G. Rowan, E. L. Hahn, and W. B. Mims, Phys Rev. A **137**, 61 (1965).

[162] P. Höfer, A. Grupp, H. Nebenführ, and M. Mehring, Chem. Phys. Lett. **132**, 279 (1986).

[163] G. Feher, Phys. Rev. **103**, 834 (1956).

[164] P. Schosseler, T. Wacker, and A. Schweiger, Chem. Phys. Lett. **224**, 319 (1994).

[165] E. R. Davies, Phys. Lett. A **47**, 1 (1974).

[166] W. B. Mims, Proc. R. Soc. London Ser. A **283**, 452 (1965).

[167] N. Cox , A. Nalepa, M.-E. Pandelia, W. Lubitz, and A. Savitsky, Methods Enzymol. **563**, 211 (2015).

[168] N. Cox, W. Lubitz, and A. Savitsky, Molecular Physics **111**, 2788 (2013).

[169] N. Cox, A. Nalepa, W. Lubitz, and A. Savitsky, J. Magn. Reson. **280**, 63 (2017)

[170] T. Hetzke, A. M. Bowen, and T. F. Prisner, Appl. Magn. Reson. **48**, 1375 (2017).

[171] S. Stoll and A. Schweiger, J. Mag. Res. **178**, 42 (2006); http://easyspin.org/

[172] G. R. Eaton, S. S. Eaton, D. P. Barr, and R. T. Weber, *Quantitative EPR*, Springer Wien New York, New York, 2010.

[173] D. Cordischi, M. Occhiuzzi, and R. Dragone, Appl. Magn. Reson. **16**, 427 (1999).

[174] Y. Imai and A. Watanabe, Intermetallics **19**, 1102 (2011).

[175] P. Giannozzi, S. Baroni, N. Bonini, M. Calandra, R. Car, C. Cavazzoni, D. Ceresoli, G. L. Chiarotti, M. Cococcioni, I. Dabo, A. Dal Corso, S. de Gironcoli, S. Fabris, G. Fratesi, R. Gebauer, U. Gerstmann, C. Gougoussis, A. Kokalj, M. Lazzeri, L. Martin-Samos, N. Marzari, F. Mauri, R. Mazzarello, S. Paolini, A. Pasquarello, L. Paulatto, C. Sbraccia, S. Scandolo, G. Sclauzero, A. P. Seitsonen, A. Smogunov, P. Umari, and R. M. Wentzcovitch, J. Phys.: Condens. Matter **21**, 395502 (2009).

[176] P. Giannozzi, O. Andreussi, T. Brumme, O. Bunau, M. Buongiorno Nardelli, M. Calandra, R. Car, C. Cavazzoni, D. Ceresoli, M. Cococcioni, N. Colonna, I. Carnimeo, A. Dal Corso, S. de Gironcoli, P. Delugas, R. A. DiStasio Jr., A. Ferretti, A. Floris, G. Fratesi, G. Fugallo, R. Gebauer, U. Gerstmann, F. Giustino, T. Gorni, J. Jia, M. Kawamura, H.-Y. Ko, A. Kokalj, E. Küçükbenli, M. Lazzeri, M. Marsili, N. Marzari, F. Mauri, N. L. Nguyen, H.-V. Nguyen, A. Otero-de-la-Roza, L. Paulatto, S. Poncé, D. Rocca, R. Sabatini, B. Santra, M. Schlipf, A. P. Seitsonen, A. Smogunov, I. Timrov, T. Thonhauser, P. Umari, N. Vast, X. Wu and S. Baroni, J. Phys.: Condens. Matter **29**, 465901 (2017).

[177] J. P. Perdew, K. Burke, and M. Ernzerhof, Phys. Rev. Lett. **77**, 3865 (1996).

[177] We used Si.pbe-mt_gipaw.UPF and Ba.pbe-tm-gipaw-dc.UP, which coded by A. Dal Corso.

[178] C. M. Ruiz, X. Fontané, A. Fairbrother, V. Izquierdo-Roca, C. Broussillou, S. Bodnar, A. Pérez-Rodríguez, and V. Bermúdez, Appl. Phys. Lett. **102**, 091106 (2013).

[179] G. Pacchioni, Solid State Sci. **2**, 161 (2000).

[180] C. D. Valentin, G. Pacchioni, A. Selloni, S. Livraghi, and E. Giamello, J. Phys. Chem. B **109**, 11414 (2005).

[181] M. Fehr, A. Schnegg, B. Rech, K. Lips, O. Astakhov, F. Finger, G. Pfanner, C. Freysoldt, J. Neugebauer, R. Bittl, and C. Teutloff, Phys. Rev. B **84**, 245203 (2011).

[182] C. Freysoldt, B. Grabowski, T. Hickel, J. Neugebauer, G. Kresse, A. Janotti, and C. V. Walle, Rev. Mod. Phys. **86**, 253 (2014).

[183] D. M. Eagle, J. Phys. Chem. Solids **16**, 76 (1990).

[184] D. J. Ashen, P. J. Dean, D. T. J. Hurle, j. B. Mullin, A. M. White and P. D. Greene, J. Phys. Chem. Solids **36**,

1041 (1975).

[185] M. Ozeki, K. Nakai, K. Dazai, and O. Ryuzan, Jpn. J. Appl. Phys. **13**, 1121 (1974).

[186] A. Bauknecht, S. Siebentritt, J. Albert, and M. Ch. Lux-Steiner, J. Appl. Phys. **89**, 4391 (2001).

[187] F. A. Trumbore and D. G. Thomas, Phys. Rev. **137**, A1030 (1965).

[188] W. J. Choyke and L. Patrick, Phys. Rev. B **2**, 4959 (1970).

[189] J. I. Pankove, *Optical Processes in Semiconductors* Dover, New York, 1975.

[190] T. Schmidt, K. Lischka, and W. Zulehner, Phys. Rev. B **45**, 8989 (1992).

[191] J. Möser, K. Lips, M. Tseytlin, G. R. Eaton, S.S. Eaton, and A. Schnegg, J. Mag. Reson. **281**, 17 (2017).

[192] T. Wimbauer, M. S. Brandt, M. W. Bayerl, N. M. Reinacher, M. Stutzmann, D. M. Hofmann, Y. Mochizuki, and M. Mizuta, Phys. Rev. B **58**, 4892 (1998).

[193] P. Neumann, I. Jakobi, F. Dolde, C. Burk, R. Reuter, G. Waldherr, J. Honert, T. Wolf, A. Brunner, J. H. Shim, D. Suter, H. Sumiya, J. Isoya, and J. Wrachtrup, Nano Lett. **13**, 2738 (2013).

[194] N. Wili and G. Jeschke, J. Mag. Reon. **289**, 26 (2018).

[195] C. M. Ruiz, X. Fontané, A. Fairbrother, V. Izquierdo-Roca, C. Broussillou, S. Bodnar, A. Pérez-Rodríguez, and V. Bermúdez, Appl. Phys. Lett. **102**, 091106 (2013).

[196] M. Iinuma, H. Tsukamoto, N. Murakoso, H. Yamaguchi, and Y. Terai, JJAP Conf. Proc. **5**, 011106 (2017).

[197] S. J. Fonash, J. Appl. Phys. **44**, 4607 (1973).

[198] C. H. Hsueha and S. Lee, Composites B **34**, 747 (2003).

[199] M. F. Doerner and S. Brennan, J. Appl. Phys. **63**, 126 (1988).

[200] M. Imai, Jpn. J. Appl. Phys. **50**, 101801 (2011).

[201] H. S. Story and R. W. Hoffman, Proc. Phys. Soc. B **70**, 950 (1957).

[202] J. D. Finegan and R. W. Hoffman, J. Appl. Phys. **30**, 597 (1959).

[203] J. H. van der Merwe, Philos. Mag. **7**, 1433 (1962).

[204] S. Baroni, S. d Gironcoli, and P. Giannozzi, Rev.Mod. Phys. **73**, 515 (2001).

[205] We used Si.pbe-mt_fhi.UPF, Ba.pbe-mt_fhi.UPF, B.pbe-mt_fhi.UPF and Sb.pbe-mt_fhi.UPF from http://www.quantum-espresso.org.

[206] C. P. Herrero and M. Stutzmann, Phys. Rev. B **38**, 12668 (1988).

[207] W. Du, R. Takabe, S. Yachi, K. Toko, and T. Suemasu, Thin Solid Films **629**, 17 (2017).